# Modeling perfusable human brain microvasculature: Multimodal investigation of cerebrovasculature in dementia, trauma and development.

Yu Jung Shin

A dissertation

submitted in partial fulfillment of the

requirements for the degree of

Doctor of Philosophy

University of Washington

2024

Reading Committee:

Ying Zheng, Chair

Andy Shih

Alexander Smith

Program Authorized to Offer Degree:

Bioengineering

University of Washington

**Abstract**

Modeling perfusable human brain microvasculature: Multimodal investigation of cerebrovasculature in dementia, trauma, and development.

Yu Jung Shin

Chair of the Supervisory Committee:

Ying Zheng

Department of Bioengineering

The brain vasculature is a dense, hierarchical network responsible for ensuring the transport of oxygen and metabolic precursors essential for normal neurological function. Unlike blood vessels in other organ systems, the brain vasculature is uniquely characterized by the neurovascular unit (NVU), a specialized vascular subunit composed of dynamic cellular interactions between endothelial cells and perivascular cells, including mural cells, astrocytes, and glial cells. These components work together to tightly regulate the blood-brain barrier (BBB), a semi-permeable barrier critical for maintaining brain homeostasis. The integrity of the BBB is maintained through the formation of tight junctions, a continuous basement membrane, and the expression of

transmembrane proteins that facilitate the selective transport of molecules and metabolites. This tightly regulated barrier effectively sequesters neurotoxic substances, preventing them from entering the brain parenchyma.

Dysfunction of the NVU plays a key role in the pathogenesis of numerous cerebrovascular diseases. Therefore, understanding the mechanisms regulating the BBB under normal conditions, as well as its pathophysiological alterations in disease states, is essential for advancing our knowledge of cerebrovascular diseases and developing effective therapeutic interventions. However, most studies to date have relied on animal models, which fail to fully capture the complexities of human cerebrovascular biology and often exhibit intrinsic molecular differences in cerebrovascular development and disease progression. Recent advances in engineered brain vasculature models and human stem cell technologies provide promising opportunities to overcome species-specific differences and enhance our ability to study human brain microvasculature with greater accuracy.

This body of work presents the development of a 3D perfusable brain microvascular model that enables spatiotemporal investigation of vascular changes in response to perfused stimuli. Each chapter explores increasing complexity of the 3D perfusable brain microvessel model, employing the model to study cerebrovascular dysfunctions in neurodegenerative diseases and culminating in the creation of a novel brain vascular model that mimics the hierarchical vascular bed found in the brain. The first section focuses on the use of stem-cell-derived cortical neurons and the perfusion of conditioned media from differentiated cortical neurons to study endothelial dysfunctions in Alzheimer's disease (AD). This work highlights the potential of perfusing disease-mimicking stimuli, such as amyloid beta (Aβ) peptides, to examine how brain endothelial dysfunction manifests in brain microvessels. Through this study, we demonstrated that a familial AD genotype-

dependent increase in Aβ levels can trigger pro-inflammatory and pro-thrombotic responses within cerebral microvessels, which may exacerbate AD pathology even before clinical symptoms appear.

The second section challenges the functionality of 3D perfusable microvessels as an endothelial barrier model, specifically for investigating BBB integrity and its breakdown in traumatic brain injury (TBI). By perfusing fluorescent particles through these microvessels after inducing TBI-mimicking BBB disruption, the model serves as a screening platform to identify potential therapeutic targets for TBI-induced endothelial barrier dysfunction. Specifically, this study explored the role of kinase inhibitors—known to be heavily implicated in endothelial barrier modulation—as therapeutic agents. Furthermore, by incorporating a machine-learning-based kinase regression model, a novel kinase target for barrier restoration was identified. This work highlights the feasibility of leveraging functional parameters derived from 3D microvascular models within a systems biology framework for therapeutic discovery and screening.

Finally, recognizing the need for more complex and physiologically relevant models of brain vasculature, the last section presents the development of a novel brain vascular model using human induced pluripotent stem cell (hiPSC)-derived vascular organoids. These organoids integrate astrocytes, neurons, and hemodynamic stimuli to create hierarchical vascular networks that replicate the molecular signatures of the BBB, advancing the field of vascular engineering. By mimicking both the cellular diversity and geometric organization of the brain vasculature, this sophisticated model offers a more comprehensive platform for investigating neurovascular interactions and cerebrovascular disease mechanisms.

In summary, this work leverages advanced brain vascular engineering techniques to generate physiologically relevant models of brain vasculature and conduct multifaceted investigations into endothelial dysfunction in Alzheimer’s disease and traumatic brain injury (TBI). Additionally, it

presents an innovative model of the hierarchical brain vasculature, incorporating relevant neurovascular cell types and replicating the complex hierarchical vascular bed found in the brain. This model serves as a novel platform for investigating the mechanisms underlying cerebrovascular diseases.

# Table of contents

# List of Figures

# List of Supplementary Figures

# Acknowledgement

"Reflecting on the Ph.D. journey, I'm reminded of the proverb, 'It takes a village to raise a child' — only in this case, it takes a village to graduate a Ph.D. student. I have grown immensely from the many lessons I learned from my friends, family, and advisors, who have provided unwavering support, critical feedback, and, most importantly, heartfelt love. To everyone in my village: I would not be here without your love, belief, and encouragement.

During my Ph.D., I have transformed from a young and naïve scientist into a more mature and logical one. I am forever grateful to my advisor, Dr. Ying Zheng, for all the opportunities she has provided — the techniques, projects, and discussions that have been pivotal for my growth as a scientist. You gave me the opportunity to work in your lab during the darkest point of my Ph.D., and you always listened to my interests and helped shape my project accordingly. Your incredible scientific insights and guidance have been invaluable. I am grateful to have spent the last five years with such an empathetic and innovative mentor. I am also fortunate to have had wonderful supervisory committee members: Andy Shih, Jennifer Davis, Jessica Young, and Alec Smith. You have provided invaluable guidance and extremely helpful directions for my project throughout my Ph.D. I am especially thankful for their constant encouragement to consider the biological significance of my work and potential next steps.

To all of my immediate collaborators — Dr. Jessica Young, Kira Evitts, Dr. Alexis Kaushansky, Dr. Joe Smith, and Dr. Ling Wei — you have provided me with invaluable input and resources. I gained a wide range of skills because of each of you, from working with stem cell-derived neurons to applying machine learning-based regression models. You were inspirational, encouraging, and incredibly helpful, especially in moments when I doubted the direction of my projects. The discussions I had with all of you were another pivotal part of my scientific growth.

To all of my lab members, I feel incredibly lucky to have been part of such a family-like environment. Kira, you are the best thing that happened to me during my Ph.D. I'm truly grateful for our friendship. From all

the coffee sessions where we brainstormed our projects to the therapy sessions you held for me during challenging times — I wouldn't be completing my Ph.D. in one piece without you. Ariana and Rachel, I have so many fond memories with you, from our Amsterdam trip to the late-night lab sessions. Thank you for being part of some of my most cherished memories in the Zheng lab. Nicole and Caitlin, thank you for teaching me all the fundamental skills I needed in the Zheng lab. Sam, thank you for your constructive feedback, especially from a medical perspective, and for all the Korea-related conversations that lifted my spirits. To all the other lab members I did not mention by name — you mean so much to me. The discussions we shared and the help you provided were instrumental in completing my thesis.

To all of my previous research mentors, thank you for nurturing my aspirations as a scientist. Dr. Jeremy Chae, thank you for teaching me how to conduct scientific research during my undergraduate years. You were the first to show me how to perform experiments, and those lessons laid the foundation for my scientific journey. Dr. Daniele Gilkes, thank you for taking in an engineering student and introducing me to biological research. My experience in your lab was crucial in helping me determine the focus of my scientific interests.To Ines Godet, thank you so much for your invaluable guidance and feedback, both during my time in the Gilkes lab and beyond. You are an inspirational person, both in and out of work. Working with you solidified my decision to pursue a Ph.D., and I'm always grateful to have a mentor just a few years ahead of me who can teach me what to look out for.

To all of my friends from Seattle whom I met during my Ph.D., thank you for supporting me through my lowest moments. I am grateful to have met so many wonderful people here. From coffee sessions, dinners, and board game nights — you were the highlight of my Ph.D. journey. Alex Ochs, thank you for being a true friend and cohort buddy. I appreciate you always checking in, grabbing coffee with me, and lending your ear when I was going through tough times. Rongyu Zhang, we went through every step of the Ph.D. together — from the qualifying exam to the general exam and defense. I cherish our study sessions and the vacations we took, hiking and traveling to New York. I'm so glad I found another best friend during my

Ph.D. To Juyoung, Justin, Namu, Kyunghoon, and Junghyun — thank you for the dinners, early morning coffee sessions that got me to the lab, and for always cheering me up throughout my Ph.D.

To all of my friends outside of Seattle — my Thanksgiving crew — I am extremely lucky to have a friend group that continues to meet annually despite our geographical challenges. All the late-night chit-chats have given me the energy to work long hours in the lab. To my friends in Korea, thank you for always being there to listen when I return home. Even though it may be hard to relate, your willingness to hear me out means the world. Your support has helped me stay positive and relentless throughout this journey.

To my brother, Ho Joong — you are one of the hardest-working people I know. I am always inspired by your work ethic whenever I visit Korea. Seeing your dedication energizes me and motivates me to return and work even harder. To my mother, Ji Hye — you are the reason I am here today. You always encourage me to dream big, reach for the stars, and not fear failure. You taught me to rise from the ashes. But most importantly, you remind me that if I fail, there is always a home to return to. Your words are why I can continue to grow as a person and as a scientist. Last but certainly not least, to my father, Yung Jae — I am always grateful for your wisdom. You remind me to maintain an open perspective, to look beyond the obvious options, and to appreciate life and those around me. You emphasize that I am running a marathon, not a 100-meter sprint. The reason I have so many supporters and friends is because you taught me the importance of living a life outside of work and cherishing every moment.

# Thesis Research Aims Overview

**Aim 1: To investigate the role of amyloid beta peptides (Aβ) from the Alzheimer's disease (AD) neuronal secretome on human brain microvascular endothelial cell (HBMEC) activation in a 3D perfusable cerebrovascular model.**

1.1 Characterize conditioned media (CM) from AD and isogenic wild-type (WT) control human induced pluripotent stem cell (hiPSC)-derived neurons (hiPSC-CN), and investigate endothelial activation in a 2D culture of HBMECs.

1.2 Perfuse CM in 3D brain microvessels to investigate von Willebrand Factor (vWF) fiber formation, platelet binding, and immune cell trafficking in response to the AD neuronal secretome.

1.3 Assess the specific role of Aβ in eliciting endothelial activation and vWF fiber formation in 3D brain microvessels.

**Aim 2: To develop a 3D brain endothelial barrier (BEB) model to investigate kinase targets that stabilize endothelial barrier properties in traumatic brain injury (TBI) via kinase regression (KiR).**

2.1 Perfuse patient-derived TBI plasma and thrombin in 3D BEB microvessels to mimic and characterize TBI-associated endothelial barrier disruption.

2.2 Screen the barrier-modulating activity of selected kinase inhibitors (KIs) to identify kinase targets that influence endothelial junctions and HBMEC barrier function.

2.3 Generate and validate kinase targets predicted by KiR, and investigate their effects on endothelial cell (EC) barrier function in a 3D TBI microvessel model.

**Aim 3: To engineer hiPSC-derived vascular organoids microvessels (hVOMVs) and shape their vascular cell fate and architecture toward a novel perfusable cerebrovascular model.**

3.1 Investigate the role of the neurovascular parenchyma in the acquisition of the brain vascular phenotype in hiPSC-derived vascular organoids (hVOs) using a co-culture model.

3.2 Engineer perfusable hVOs and assess the role of perfusion and hemodynamic stimuli in vascular maturation, remodeling, and hierarchical network formation.

3.3 Characterize the cell fate changes in perfusable hVOMVs via single-cell transcriptomics.

# Chapter 1: Introduction

*Part of this chapter is adapted from review papers: **Shin YJ** et al. IJSC 2023 DOI:10.15283/ijsc23086, and Mandrycky, Howard, Rayner and **Shin** et al. JMCC 2021)*

## 1.1 Developmental signaling in vasculature towards hierarchical blood vessels

Vasculature is a closed hierarchical network of arteries, veins, and interconnecting capillaries that specifies in different tissues. Vascular development initiates during embryogenesis through the intricate coordination of critical regulators that drive vessel formation, stabilization, branching, and pruning. Two major processes are involved in vascular development, vasculogenesis and angiogenesis. During vasculogenesis, mesodermal precursors (ETV2＋, FLK1＋) differentiate into angioblasts, forming an early primitive vascular plexus before specifying into the dorsal aorta, cardinal vein and subsequently arteriovenous blood vessels[1] (Figure 1.1, left upper panel). New vessels further develop via angiogenesis and vascular remodeling into a hierarchical vascular network. Each crucial step of differentiation and remodeling necessitates the integration of both chemical and mechanical signals, which trigger morphogenic behaviors (Figure 1.1, right upper panel). One of the critical signaling pathways driving initial vascular development and angiogenesis is the vascular endothelial growth factor (VEGF) signaling pathway. Maintaining a balanced level of VEGF is particularly crucial for establishing a proper vascular network. Studies conducted on rodents have demonstrated that the absence of a single VEGF allele can lead to abnormal vessel development and lethality in mouse embryos[2] whereas overexpression of VEGF results in embryonic lethality[3] in mice. VEGF comprises various classes with different homo dimeric ligands, with VEGF-A playing the most critical role in promoting angiogenesis and developing nascent vessels. VEGF-A isoforms exert their activity by interacting with kinase

tyrosine receptors on endothelial cells (ECs), namely VEGF receptor 1 and VEGF receptor 2 (VEGFR2). VEGFR2, expressed on vascular endothelium, is the most predominant receptor involved in VEGF signaling[3]. Upon binding of VEGF-A, receptor dimerization occurs, leading to the phosphorylation of tyrosine residues and initiation of signaling pathways that regulate angiogenesis, endothelial proliferation, survival, migration, and vascular permeability[4].

Another critical component for vascular development is biomechanical stimuli. Hemodynamic flow and pressure induce crucial signals for maturing and stabilizing the vasculature into hierarchical networks. One critical mechanosensitive signaling pathway involved in this process is Notch, which plays a versatile role throughout blood vessel development. In the early stages of development, Notch is essential for expanding vessels from the vascular plexus[5]. Deletion of Notch1 in transgenic mice before E9.5 results in embryonic lethality, while deletion at the 8-week or later stage leads to the loss of cell-cell junctions and the absence of mechanosensing in arteries[6,7]. Notch signaling is also heavily involved in angiogenic expansion of vascular beds during the formation of tip and stalk cells in angiogenic sprouts. During angiogenic sprouting, two types of cells emerge: tip cells located at the sprout's leading edge and stalk cells adjacent to the tip cells, which proliferate and form new blood vessels. Angiogenesis is initiated in response to VEGF gradients, which activate the Notch receptor delta-like 4 (DLL4) via VEGFR2[6]. Activation of DLL4 in tip cells leads to their transition from a proliferative state to a migratory state. Subsequently, the interaction between DLL4 and Notch ligand receptor in tip cells activates Notch signaling and triggers the translocation of the Notch intracellular domain, suppressing the tip cell phenotype[7] (Figure 1.1, left lower panel). Downstream of VEGFR2 and Notch signaling in tip-stalk cross is the 6-phosphofructo-2-kinase/fructose-2, 6-bisphosphatase (PFKFB3) gene, which is responsible for stimulating glycolytic activity in cells. ECs exhibit high glycolytic activity,

generating approximately 85% of their ATP through glycolysis. This is consistent with ECs having a smaller mitochondrial volume fraction (5%) than other cell types. Studies have shown that PFKFB3 activity is increased in response to sprout promoting signals such as VEGF, while PFKFB3 activity is significantly reduced in response to sprout limiting signals such as DLL4[8]. Silencing of PFKFB3 leads to immobile filopodia, quiescent tip cells, and decreased proliferation in stalk cells suggesting that PFKFB3 is important for regulating glycolysis and cytoskeletal organization, which are crucial for promoting functional angiogenesis[9].

Following vasculogenesis and angiogenesis, the newly formed vessel network undergoes stabilization to establish an intact vasculature with the assistance of mural cells that surround the abluminal lining of ECs[10]. The platelet derived growth factor-B (PDGF-B) – PDGF receptor β (PDGFRβ) pathway and Angiopoietin (ANG)-TIE pathway are two crucial pathways implicated in vascular stabilization and the maintenance of vascular homeostasis. PDGFRβ is predominantly expressed in mural cells, including vascular smooth muscle cells and pericytes, and is primarily involved in regulating the proliferation and recruitment of these mural cells towards nascent vessels[11]. PDGF signaling plays a fundamental role in vessel development, as the deletion of PDGF results in the failure of mural cell recruitment and leads to embryonic lethality. In the presence of VEGF-A signals, ECs enhance the expression of PDGF-B, which interacts with PDGFRβ on mural cells and initiate signaling cascades involved in proliferation and migration, such as phosphoinositide 3- kinase (PI3K), extracellular regulatory kinase 1/2, and mitogen-activated protein kinase[11] (MAPK). Conditional inactivation of PDGF-B secretion by ECs prevents the migration and proliferation of mural cells, suggesting that ECs are the primary source of PDGF-B required for vascular stabilization[12].

The orchestra of VEGF[13], Notch[14] and other signaling pathways such as Hedgehog[15] and Wnt/β-catenin[16] govern the arteriovenous specification during development. VEGF acts as the primary driver of arterial specifications through direct stimulation of DLL4/Notch[13] or indirect stimulation of ETS factors[17]. Different VEGF isoforms also preferentially direct vessels towards arteriovenous specification. In mice designed to express single VEGF isoform, VEGF164 was sufficient to direct arterial specification, and VEGF188 was necessary for venular development[18]. Arterial fate is also driven by the activation of transcription factors (TFs) Forkhead box (FOX) C1 and FOX C2, which leads to increased expression of DLL4/Notch and downstream signals such as Ephrin-B2 (EFNB2) and HEY/ HES[19] (Figure 1.1, right panel). In contrast, venous specification is marked by the expression of COUP transcription factor 2 (COUP-TFII), which is required to suppress the Notch signaling pathway[20]. This suggests that vessels are programmed to follow arterial fate during hierarchical vessel formation, and the repression of Notch signaling is important for hierarchical vessel formation. However, studies show that vessels are not locked into its "pre-determined" arteriovenous subtypes but rather respond to hemodynamic forces that alter expression profile towards arterial or venous subtypes[21,22].

Moreover, cell cycling influences EC fate determination in arteriovenous specification (Figure. 1.1, right upper panel). The Notch and COUP-TFII signaling pathways play crucial roles in the arterial differentiation of ECs by influencing cell cycling and metabolism rather than directly regulating arterial and venous fate determinants[20]. Studies in various model systems, such as the retina and developing heart, have revealed that shear stress-induced Notch signaling leads to cell cycle arrest and the expression of arterial specification genes[23,24]. On the other hand, COUP-TFII inhibits arterial differentiation by activating cell cycle genes. Epigenetic studies have supported the connection between cell cycle genes and COUP-TFII's inhibitory effects[25,26]. Proliferating ECs

exhibit a bias towards venous fate, as indicated by the expression of venous EC genes. Recent research has demonstrated that ECs in the late G1 state respond more to arterial specification signals[27]. Additionally, arterial pre-specification has been observed in different vascular beds, involving low proliferative rates, high Notch activity, and VEGF-extracellular signal-regulated kinases signaling.

Our body has meticulously mapped out the signaling pathways that govern and sustain vascularization throughout development and homeostasis. A deeper comprehension of the intricate interactions among these signaling pathways in both spatial and temporal contexts offers us opportunities to enhance vasculature construction in vivo, regulate appropriate vascularization in engineered tissues in vitro, and facilitate vascular regeneration in vivo.

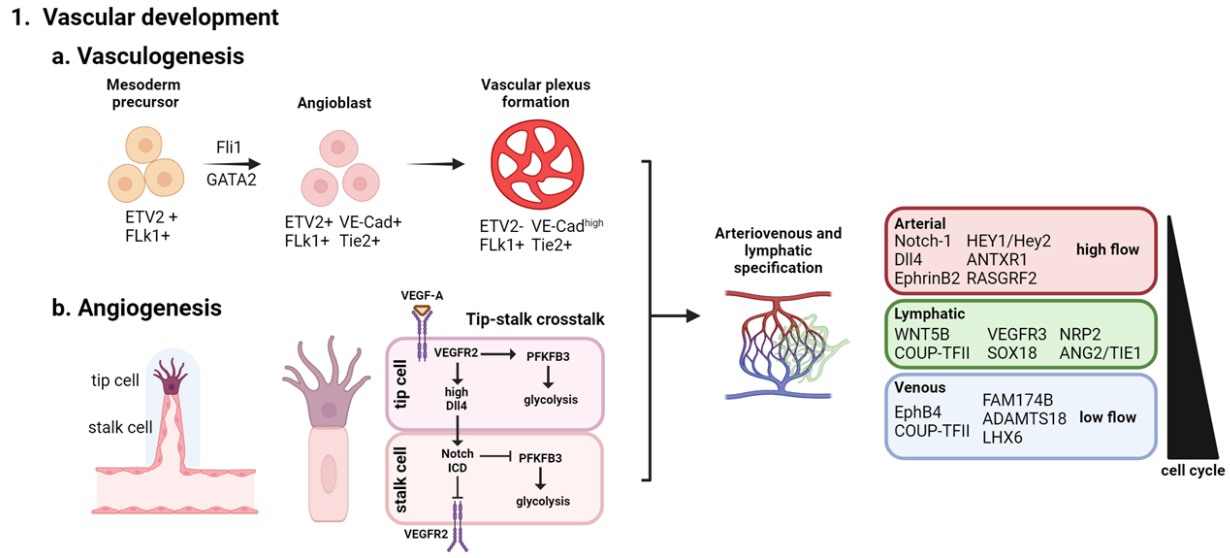


**Figure 1.1 The development of vascular endothelial cells (ECs) in arteriovenous specification and angiogenesis.**

Vasculogenesis occurs as ECs emerge from mesodermal precursors that differentiate into angioblasts and form the vascular plexus. From the primitive vascular plexus, ECs undergo arteriovenous specification and angiogenesis to form a multitude of vascular networks (top left panel). Arterial and venous specification in developing vasculature is driven by Notch and COUP transcription factor 2 (COUP-TFII) signaling. High flow initiates Notch activation, inducing downstream signals such as HEY/HES and EphrinB2 for arterial priming. COUP-TFII primes vasculature toward venous and lymphatic differentiation, where downstream activation of Ephrin type-B receptor 4 (EPHB4) leads to venous EC differentiation, and vascular endothelial growth factor receptor 3 (VEGFR3) leads to lymphatic EC differentiation (left panel). Angiogenesis begins as tip cells are activated by a gradient of VEGF signals, which induces

the delta-like 4 (DLL4)/Notch pathway and initiates migration. Adjacent stalk cells receive Notch signaling from the tip cells and initiate proliferation for tube morphogenesis (bottom left panel).

## 1.2 Organ specific endothelial cells and molecular signature of endothelial heterogeneity.

Microvasculature exhibits remarkable anatomical and functional diversity across different organs, reflecting adaptation to the specific metabolic and physiological demands of each tissue. Dense capillary networks in the heart and brain, for example, support high metabolic demands by facilitating rapid nutrient and oxygen exchange (Figure 1.2). Unique glomerulus capillaries in kidneys filter blood into Bowman's space, with efferent vessels extending into the peritubular region to wrap around the tubules to support the filtration, reabsorption and secretion. In the lungs, pulmonary microvasculature wraps around the alveoli to participate in the gas exchange whereas bronchial microvasculature supports tissue metabolism. In the liver, the portal vein connects with liver sinusoids and connects with hepatic arteries. In addition to organ-specific vascular architecture, ECs demonstrated significant heterogeneity in structure and function across various tissues between and within organs. Microvasculature in the brain, heart, and lungs have continuous ECs linked by tight junctions. Brain ECs form an increased presence of tight junction proteins such as claudins and occludins, as well as drug efflux transporters like glycoproteins and multi-drug resistance-associated proteins[28] to create the blood-brain barrier (BBB), a critical mediator of cerebral homeostasis. These features contribute to tightening transcellular gaps and restricts the transport of molecules from the bloodstream to the brain parenchyma. However, a specialized subset of ECs in the choroid plexus capillaries are fenestrated, allowing for the clearance of metabolites from the ventricles into the cerebrospinal fluid. Liver and marrow ECs form discontinuous sinusoids that facilitate transfer of large proteins and cells. Kidney and intestine

ECs, on the other hand, have fenestrated structure, with or without diaphragm, to facilitate solute transport and optimize the filtration and absorption processes. In particular, glomerular ECs have open fenestrae that allow larger blood proteins to pass through the filtration barrier, while peritubular ECs possess fenestral diaphragms that facilitate the transfer of fluids and solutes for reabsorption. These specialized endothelial cell types are essential for meeting the localized needs of each tissue, supporting specific functions and adapting to the microenvironmental demands of each vascular bed. (Figure. 1.2)

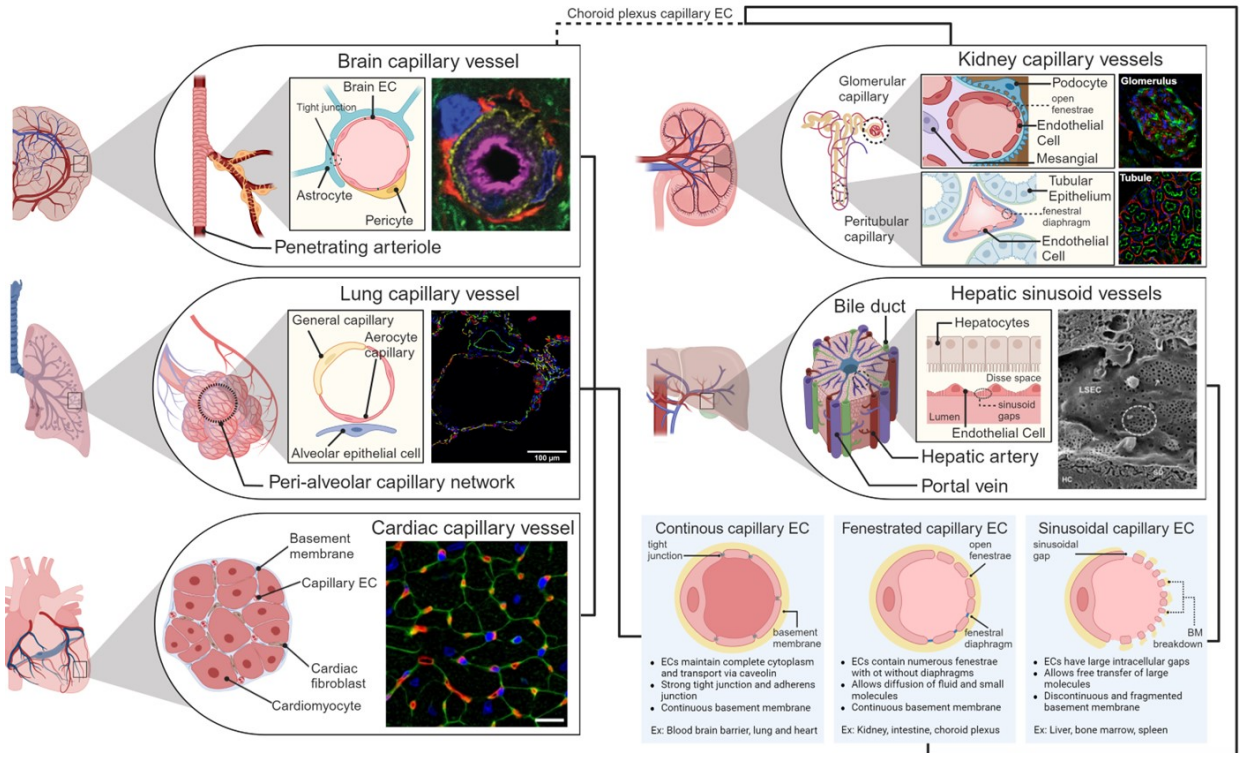


**Figure 1.2 Heterogeneity in tissue-specific capillary networks and endothelial cell morphology.**

A schematic representation of organ-specific microvasculature and structural phenotype of capillary ECs (bottom; right). Brain capillary network (top; left) extends from penetrating arterioles and form neurovascular unit with brain capillary ECs (magenta, lectin), pericytes (gold, platelet derived growth factor beta), astrocyte (red, glial fibrillary acidic protein) and neurons (green, NeuroChrom). Image adapted from Lochhead et al.[29] with permission (CC BY 4.0). Majority of brain capillary ECs are found in blood brain barrier with continuous EC structure apart from choroid plexus capillary ECs found that the blood-cerebrospinal fluid (CSF) barrier which are fenestrated with lack tight junctions to facilitate waste clearance toward the CSF. Lung capillary network (middle, left) within alveolus is comprised of aerocyte capillary ECs specialized in facilitating gas exchange and leukocyte trafficking and general capillary ECs responsible for vasomotor tone and capillary homeostasis. Lung capillaries (green; PECAM1, DAPI; nuclei) express genes coding gas-exchange related enzymes (CA4; red) Image adapted from Schupp et al.[30] with permission (CC BY-NC-ND 4.0). Dense cardiac capillary networks (bottom; left) vascularize the myocardium with one capillary (red; cd31) supporting one myocyte (green; WGA). Image adapted from Schimmel et al.[31] and Droste et

al.[32] with permission (CC BY 4.0). Kidney capillary networks (top; right) shows intra-organ specificity with glomerular capillary ECs (top insert; green; EMCN) comprised of open fenestrae adjacent to podocytes (top insert; red; nephrin) to facilitate selective filtration of plasma protein. Image adapted from Rodriguez et al.[33] with permission (CC BY 4.0). Peritubular capillary ECs (bottom insert; red; CD34) comprised of pvlap+ ECs with fenestral diaphragms that enable reabsorption of smaller solutes and water into adjacent epithelial tubules (bottom insert; Green; phalloidin). Image adapted from Kumaran et al.[34] with permission. Liver sinusoidal capillaries (middle; right) line between central vein to hepatic artery and portal veins and are comprised of ECs with large sinusoidal gaps (SP; dotted line circles) with large holes for filtration of lipoproteins and drug clearance. Image adapted from Szafranska et al.[35] with permission (CC BY 4.0).

Recently, the development of multimodal omics tools has allowed for transcriptional and epigenetic insights into the heterogeneity of ECs across organs. Organism wide investigations using single-cell RNA sequencing (scRNAseq), notably the Tabula Muris dataset, which provides single cell transcriptomic profiles of ECs from 12 major organs, has revealed both similarities and disparities in the transcriptomes of ECs among these organs[36,37]. Interestingly, studies have shown that lymphatic ECs across different organ systems share a similar transcriptomic profile, while blood vascular ECs exhibit heterogeneity[37]. Within the vascular hierarchy, capillary ECs display the most distinctive transcriptomic profile compared to arteries and veins, which share similar transcriptomic signatures across different tissues. Major organs with highly specialized vasculature, such as the brain, liver, kidney and lung, also exhibit distinct EC signatures, demonstrating intra-organ EC heterogeneity[37–39] as well as zone-specific[40–43] gene expression profiles within the tissue. In contrast, tissues such as adipose, skeletal muscle and aorta show overlapping gene clusters. While the developmental trajectories of ECs are similar across the organs, the regulation of WNT and Mitogen-activated protein kinases signaling pathways plays a crucial role in determining tissue-specific gene expression patterns[37]. Furthermore, scRNA-seq of ECs across organs has revealed sexual dimorphism, particularly in the heart, brain and lung, where the non-sex-linked gene Lars2 is enriched in male murine ECs. This data suggests an additional layer of EC heterogeneity: sex-specific EC transcriptome in major organs[37].

From an epigenetic perspective, the incorporation of Assay for Transposase-Accessible Chromatin sequencing in multi-omic studies of ECs has enabled further investigation into the TF motifs that regulate the distinct EC transcriptome[44]. Given that ECs share a common developmental pathway during embryonic development, the ETS TF family was found to be globally enriched in all EC subtypes. Further examination of motif enrichment in the commonly expressed TFs in ECs revealed distinct patterns of enrichment corresponding to each EC subtypes[44]. Given that ECs share a common developmental pathway during embryonic development, the ETS TF family was found to be globally enriched in all EC subtypes. Further examination of motif enrichment in the commonly expressed TFs in ECs revealed distinct patterns of enrichment corresponding to each EC subtypes[44]. In the brain, TFs such as FOX, TCF/LEF and ZIC were identified, all of which are known to regulate WNT signaling, an important pathway involved in blood-brain barrier development and angiogenesis. In the liver, GATA TF families were enriched, which aligns with previous findings implicating the importance of GATA4 in hepatic EC development. In the kidney, Homeobox TF families were strongly enriched, confirming other scRNA-seq findings that show high expression of homeobox transcripts such as Irx3, Hoxa7, Pbx1, and Meis2.

Overall, comparative analysis of scRNA-seq data suggests a strong correlation between parenchymal and EC gene expression. Therefore, it is crucial to understand EC niche interactions, as they play a critical role in maintaining region-specific EC signatures. In fact, primary ECs harvested from tissues and cultured in vitro often lose the transcriptomic and phenotypic signature observed in vivo[38]. This suggests that ECs possess their own tissue-specific gene expression, but cell-cell and cell-extracellular matrix (ECM) niche interaction are critical for maintaining their heterogeneity. This highlights the need to incorporate relevant cell types for modeling organ-specific vascularture in vitro.

## 1.3 Blood brain barrier and its implications in neurovascular diseases.

The brain vasculature is uniquely characterized by the blood-brain barrier, a semi-permeable barrier essential for maintaining neural homeostasis. The cells that make up the neurovascular unit—including endothelial cells, mural cells, astrocytes, neurons, and glial cells—work together to tightly regulate the BBB. This regulation is achieved through the enhanced expression of tight junction proteins, which allow endothelial cells to form a more restrictive barrier. Additionally, the BBB's function is supported by the formation of a continuous basement membrane and the expression of specialized transmembrane transporter proteins such as efflux proteins (P-glycoprotein, and multidrug resistance-associated proteins and ATP binding cassette proteins). These features collectively limit the influx of neurotoxic molecules into the brain parenchyma and actively expel harmful substances, preserving the brain's microenvironment.

Dysfunction of the BBB is implicated in the pathogenesis of numerous cerebrovascular diseases. Vascular dysfunctions in the brain arise from a combination of vascular rarefaction, dysregulation of blood flow to the brain, systemic inflammation from traumatic injuries, genetic predisposition to vascular malformations, and aberrant neuronal and glial activity in neurodegenerative diseases. For instance, in Alzheimer's disease (AD), alterations in the neurovascular unit (NVU) contribute to BBB damage through the deposition of amyloid-beta (Aβ) plaques, leading to endothelial dysfunction. Approximately 90% of late-onset Alzheimer's disease patients exhibit cerebral blood flow alterations and vascular rarefaction in response to the accumulation of Aβ plaques and the formation of neurofibrillary tangles.[45] Subsequently, decreased cerebral blood flow results in decreased Aβ clearance and an inability to support neuronal function in the brain parenchyma[46].

Similarly, in trauma-induced cerebral (TIC) vasculopathy, abnormal coagulation and endotheliopathy lead to increased morbidity and mortality. The pathophysiology behind TIC is

complex, involving many mechanisms that trigger both hemorrhagic and hypercoagulative responses. Within 6 hours of TIC onset, uncontrolled hemorrhage disrupts the blood-brain barrier, triggering inflammatory responses and release of EC and platelet activation molecules. In the late TIC stage, the hypercoagulable state dominates, leading to excessive clotting and the formation of thromboembolisms.[47] The mechanism of TIC primarily involves the imbalance of the coagulation pathway—the interplay between activation and coagulation feedback via a compensatory reaction that exacerbates inflammatory responses. Thrombin possesses a multifaceted role in BBB breakdown, having an ambivalent role and initiating both pro- and anti-coagulation pathways as well as pro- and anti-inflammatory pathways. In early TIC, thrombin may induce activation of protein C, endothelial PAR-1 cleavage, and glycocalyx shedding, which leads to loss of endothelial junctions[40]. On the other hand, excessive stimulation of platelets by thrombin can result in calcium mobilization within platelets and drive pro-coagulative states[48].

Finally, inherited genetic disorders such as Moyamoya disease, Fabry's disease, Marfan syndrome, or Cerebral autosomal-dominant arteriopathy with subcortical infarcts and leukoencephalopathy (CADASIL) leads to debilitating cerebrovascular dysfunctions.[49] CADASIL and Marfan syndrome results in defective vascular smooth muscle cell development and accumulation of osmiophilic deposits along the vascular wall. Moyamoya and Fabry's disease led to cerebral endotheliopathy, leading to malformation and occlusion of brain microvessels.

Majority of the cerebrovascular dysfunctions accompany a rare genetic mutation, co-morbidity with neurological disorder, and/or imbalance of clotting cascade. However, the lack of appropriate human brain-specific vascular models prevents the study of neurovascular disease mechanisms. Therefore, there is a strong need for a perfusable human brain vascular models to study such disease etiology.

## 1.4 Engineering strategies for modeling organ-specific perfusable microvascular networks

Investigation of brain vascular development in homeostasis and disease requires a human model of the brain vasculature. The previous sections have discussed the intricate signaling processes involved in blood vessel development, as well as how the body programs blood vessels in each organ to meet their specific metabolic demands. The discussion also explored the use of scRNA-seq and its transformative impact on understanding the human brain vasculature, particularly in the context of neurodegenerative diseases, while emphasizing the necessity of a faithful human model of the brain vasculature. Given the inaccessibility of human brain tissue, it becomes imperative to develop in vitro models of the brain vasculature. In this section, I will review the state-of-the-art models of the vasculature and the various engineering strategies employed to create physiologically relevant models of the human vasculature.

### *1.4.1 Self-assembled vascular models*

The initial process of vasculogenesis (also called tubulogenesis) has been modeled with direct cell-in-gel culture systems, by embedding endothelial cells in cell-remodelable 3D matrices like collagen, fibrin, or Matrigel[50,51]. Once encased in these ECM hydrogels, ECs can create lumens via either intracellular or extracellular mechanisms and form connective vascular tubes[50]. Vacuoles develop in ECs and then fuse with those in neighboring cells to form an intracellular lumen[52]. In addition, membrane invagination occurs at the junctions of neighboring ECs to hollow out the space between cells and create a lumen between them[53].

Extensive studies have utilized this direct cell-in-gel culture system to define factors and conditions which coax endothelial cells into luminal structures that connect and remodel following biophysical and biochemical cues[54,55]. Pericytes can be embedded in the bulk gel and recruited to

support the developing vessel tube by stimulating basement membrane matrix assembly [56]. Since then, multiple organ-on-a-chip (OOC) devices have been developed to further elucidate the role of biochemical and biophysical signals on tubulogenesis. For example, the Kamm group has developed microfluidic vasculogenesis devices with multiple culture compartments, which allowed for the inclusion of stromal cells or pericytes, and the flexibility of modifying growth factors, extracellular matrices, cellular composition, and imposing shear flow in parallel with the vasculogenic compartment[57]. Using this system, they identified that angiopoietin-1 was a critical factor in the formation of stable and perfusable vessels with direct mural-EC cell-cell contacts (Figure. 1.3 **A**). In a different microfluidic model developed by the Lee group, series of microtissue chambers containing self-assembled vascular networks, are connected between long microfluidic channels with full control of interstitial flow and mass transport. Using such an OOC device, Hsu and colleagues showed that interstitial flow across a cell-in-gel mixture could stimulate vasculogenesis[58]. This technique was then applied to create a higher throughput multi-channel platform for drug screening applications by the Hughes group[59] (Figure. 1.3 **B**) and used to develop various vascularized microphysiological systems[60–62]. Self-assembled vascular networks have also been useful in identifying the role of endothelial cells and other vascular cells in supporting vascularization, tissue regeneration and OOC development[63–65].

### *1.4.2 Vascular organoids and vascularized organoids*

In the past decade, organoids, self-organizing 3D multicellular structures derived from hiPSCs, have revolutionized biomedical research, as reviewed previously[66–68]. These human organoids recreate organ architecture and physiology in remarkable detail, offering unique opportunities for regenerative medicine and translational research. Many organoids have been developed including kidney[69,70], intestine[71], brain[72], liver[73,74], lung[75], heart[76], and many other organs. However, one of

the significant challenges hindering their full potential is the lack of an integrated vascular network, essential for sustaining larger and more complex organoid structures. Organoids can develop to sizes where passive diffusion of oxygen and nutrients is insufficient, often resulting in the formation of necrotic cores. Addressing this limitation requires innovative strategies to incorporate vascular networks within organoids. Induction of vascularization in parenchymal organoids using chemical factors such as VEGF promotes the differentiation and proliferation of ECs, leading to the formation of a vascular network. For instance, increased levels of VEGF generated by podocytes led to de novo renal vasculature within kidney organoids[77] (Figure. 2.1 **C**). Similarly, vascular structures within kidney[78] and cerebral[79] organoids could be achieved by adding recombinant human VEGF to organoid cultures. These studies highlight the potential of chemical induction for vascularization, although precise control remains a challenge (Figure. 2.1 **C**).

In addition to vascularization strategies in parenchymal organoids, recent report by Wimmer et al. demonstrated the development of human vascular organoids (hVOs) from human induced pluripotent stem cells (hiPSCs) with an organized vascular network[80]. By aggregating hiPSCs in 3D suspension culture, hVOs can be differentiated using growth factors and small molecules into organized endothelial and perivascular populations. These can be further matured and compacted in a collagen-Matrigel hydrogel to allow for sprouting and vascular network formation by VEGF and FGF stimulation. After compaction, hVOs displayed an organized vascular network with endothelial cells (CD31+) forming connective lumens and coated with COL IV+ basement membrane and PDGFR-β + pericytes, and αSMA+ mural cells (Figure. 2.1 **D**). There are also cell populations at similar differentiation stage including mesenchymal stem cells (CD90+ CD73+ CD44+) and hematopoietic cells (CD45+), suggesting simultaneous development of vascular and

hematopoietic cell populations in hVOs. When transplanted in immunodeficient mice, the hVOs showed successful host integration[80]. Notably, transplanted hVOs matured to form perfusable hierarchical vascular networks containing branching arteries and veins as well as capillary networks enveloped with mural cells and basement membranes. This is likely the first demonstration of hierarchical vascular network formation in an implanted graft. In recent studies, this same group showed that hVOs can be directly infected with SARS-CoV-2 isolates, express viral RNA, shed progeny virus and substantially resist infection under the introduction of human recombinant soluble ACE2[81]. The faithful recapitulation of human vasculature by hVOs promises in-depth understanding of vascular associated changes in human context and its application as a drug screening platform for treating diseases accompanying vascular complications.

Beyond hVOs, organoids have been developed to study organ development and model many organ-specific diseases[67]. The immediate milestone in these self-assembled culture models is to establish functional vascularization and perfusion. Endeavors have been made to promote vascular formation in organoids via endogenous growth factors[77,82], and reprogramming[63,83]. One remaining but critical challenge is the lack of luminal perfusion in these self-assembled vascular structures. A recent effort led by Homan et al. managed to incorporate flow around cultured organoids, which promoted vascular network formation in the kidney organoids (Figure. 2.1 **E**)[78], though luminal perfusion remains to be achieved. A perfusable vasculature is needed for the long-term culture and development of these self-assembled systems in vitro. Once that is achieved, these culture systems could be used to trace the formation of organ-specific endothelial and mural cell populations in vitro, and to model the complex organ-specific vascular physiology and pathology. It is expected that engineering tools, such as microfluidic and bioprinting techniques presented in the following

sections, would be needed to help bridge these gaps and advance our understanding of vascular biology.

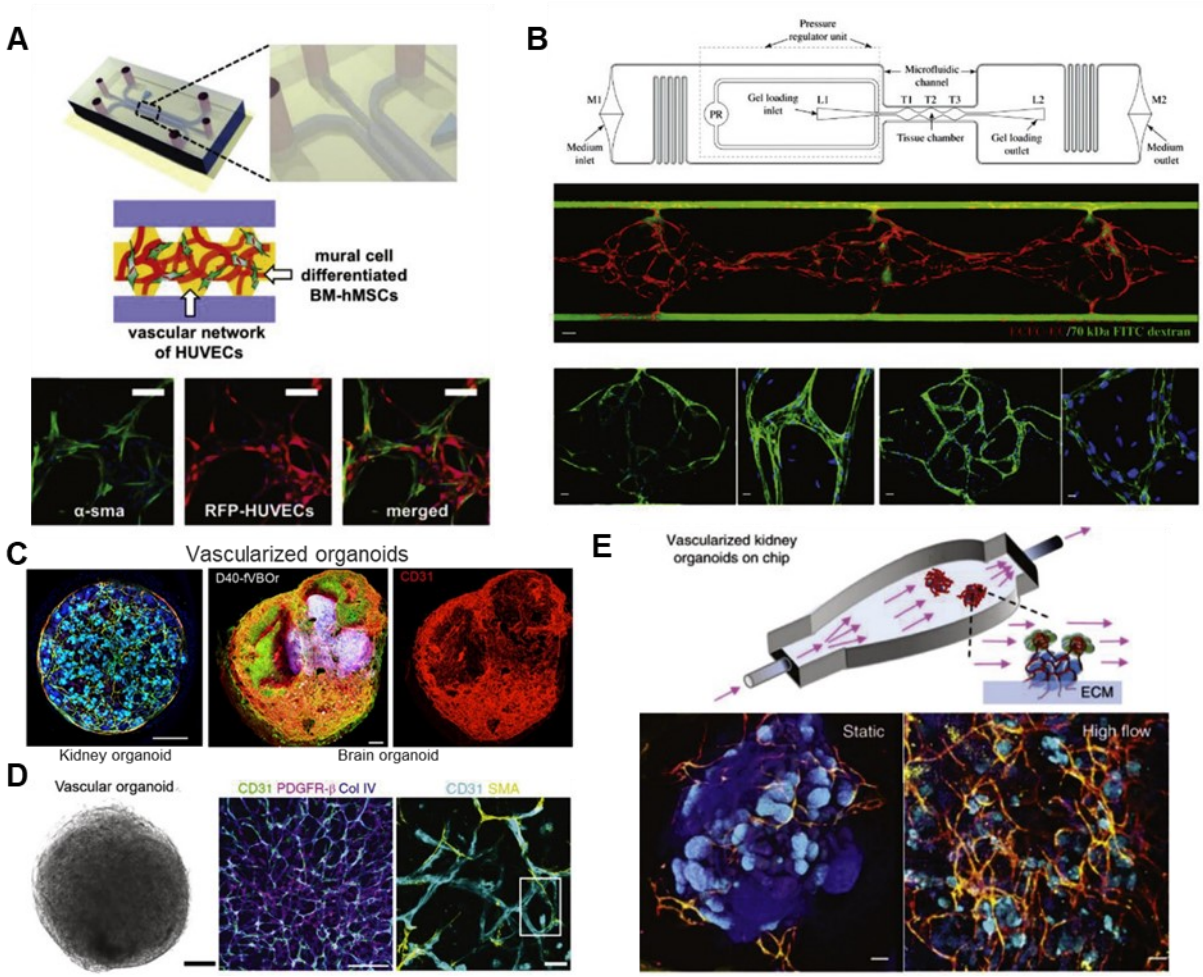


**Figure 1.3 Overview of 3D self-assembled microvascular tissues.**

(A) Endothelial cells and mural cells embedded in a fibrin matrix and supported by perfusion self-assemble into perfusable networks with close contact between cell types. Adapted from Jeon et al.[84] . (B) Controlled interstitial flow and mass transport in a microfluidic design (top) across EC-laden hydrogels stimulates vasculogenesis and the formation of perfusable vascular networks. Adapted from Phan et al.[59]. Middle panel: three tissue chambers with red for ECs and green for perfusion of 70 kDa FITC-Dextran. Bottom panels: staining of claudin-5 (left two), and VE-Cad (right two). (C) Vascularized kidney (left) and brain (right) organoids. Kidney organoids formed de novo generated blood vessels by inducing VEGF-producing podocytes within kidney organoids. Image adapted from Low et al.[77] with permission. Brain organoids were combined with vascular organoids to form a vascularized brain organoid. Image adapted from Sun et al.[85] (CC BY 4.0) with permission. (D) Vascular organoids after 15 days of differentiation compact into a sphere comprised of CD31 expressing endothelial cells that are enveloped with mural cells (PDGFR-β, SMA) and basement membrane (COL IV). Adapted from Wimmer et al.[80]. (E) Using microfluidics to deliver flow through vascularized kidney organoids enhanced vascular network formation as well as maturation of kidney organoid parenchyma. Adapted from Homan et al.[78].

### *1.4.3 Patterning perfusable microvascular networks*

Beyond the fundamental study of vascular biology itself, introducing vasculature into OOC systems is critical for the development of functional tissue and the study of biologic processes including vascular-parenchymal and blood-vessel interactions[86]. Perfusion through the vasculature is necessary for the nutritional support of parenchymal tissue, with tissues generally needing to be located within a few hundred microns of a vascular lumen[87]. In addition to transport and hemodynamic-related phenomenon, vascular cells themselves guide the development and behavior of parenchymal and perivascular cells and are intimately involved in biological processes like inflammation, hemostasis, and wound healing[88–90]. The function of organs such as the heart, kidney, lungs, liver, or spleen is dependent on continuous perfusion, which is required for truly modeling the behavior of such organs.

An ideal vascularized OOC would include precise three-dimensional cellular arrangement, high vascular density, close apposition of vasculature and parenchyma, organ-specific function, cell-remodelable extracellular matrix materials, in vivo-like hemodynamics, hierarchical and multicellular blood vessels, and multiple organ-specific cell types. Current OOC systems generally focus on a limited number of these features and achieving them all simultaneously remains an outstanding challenge for the field. Various patterning techniques have been used to generate perfusable vasculature. The prepatterned approach involves the creation of hollow lumens within a bulk material followed by the introduction of endothelial cells. Methods for prepatterning vascular channels in OOC systems range from relatively planar microfluidic approaches, to lithographic or molding approaches within cell-remodelable hydrogels, to direct-writing strategies with full 3D control such as 3D printing or laser degradation[91,92].

Most molding structures are based on simple mandrel or needle removal (Figure. 1.4 **A** i), but

in the body, blood vessels bend and twist through 3D space with varying curvature and torsion. ECs cultured in a new spiral microvessel system with controlled diameter, curvature, and torsion[93] showed distinct changes in their phenotype and transcriptional profiles compared with straight vessels (Figure. 1.4 **A** ii). Additionally, a photoannealing approach has been developed in living microtissue, presenting a scalable strategy to engineer capillary-rich tissues. This work demonstrates that cell-laden microgels coated with ECs can be photoannealed into a monolithic tissue with interconnected pores, which is compatible with perfusion[94]. These models added new parameter space for better mimicking vascular structures in vivo and supporting angiogenesis toward tumors and homogeneous perfusion to cardiac tissue[93] (Figure. 1.4 **A** iii).

For more complex structure, techniques such as stamp-based molding have been developed. Lithographically patterned molds were used to create geometrically complex engineered vessels by imprinting channels into liquid collagen hydrogels[95]. This approach has been used to model the bone marrow niche[96], create implantable cardiac vascular patches[97,98], and mimic brain microvessels for studying cerebrovascular diseases[99,100]. By assembling two patterned collagen slabs across a thin collagen membrane and seeding channels with renal tubular epithelial cells and ECs, respectively, this method emulates the human renal vascular-tubular unit, supporting blood perfusion and albumin resorption[101]. These micropatterns can also be stacked to increase vascular density and generate thick, multilayered cardiac constructs (Figure. 1.4 **A** iv) [102,103]. Despite these advancements, molding techniques are often confined to layered structures, limiting their applications.

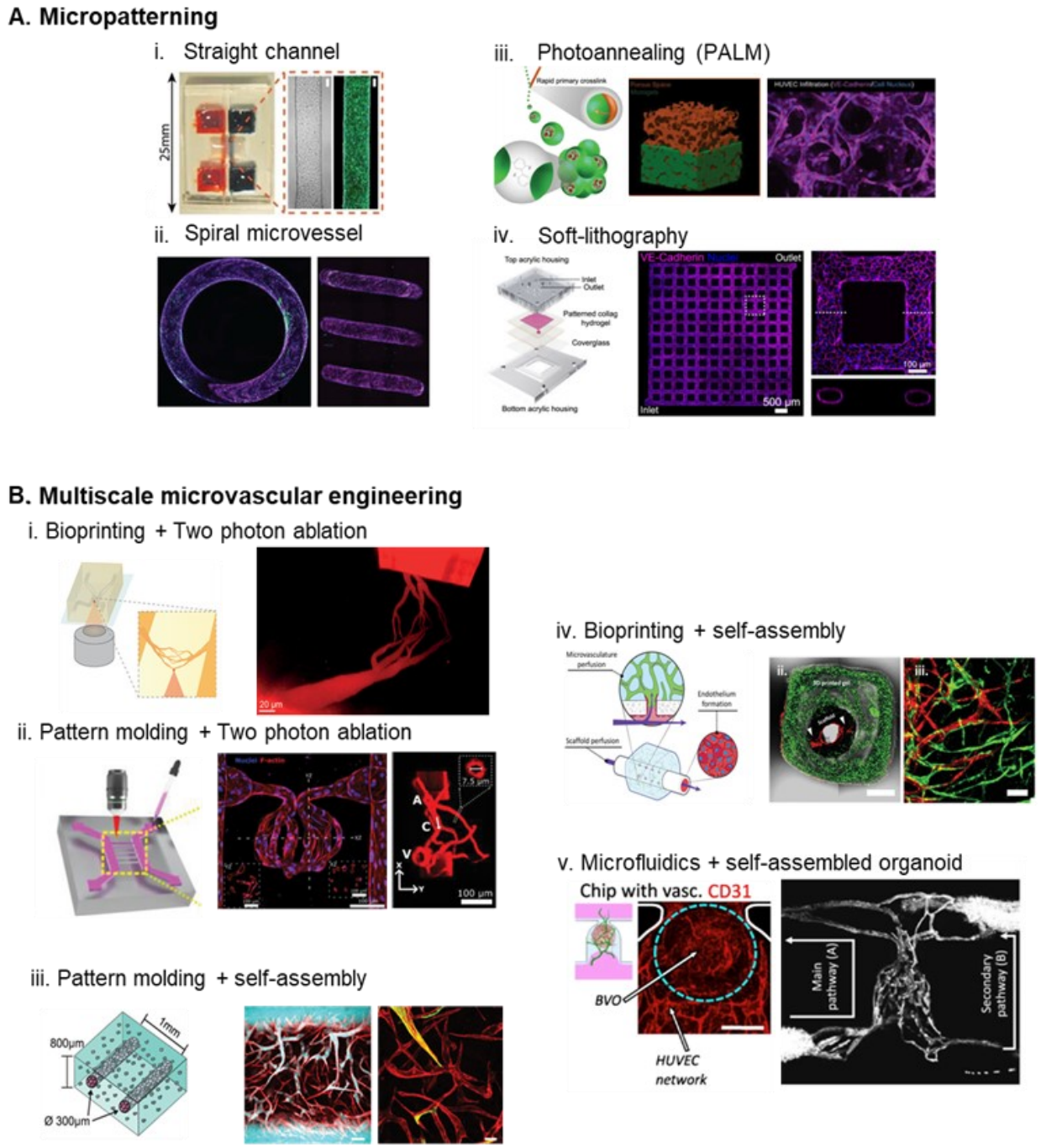


**Figure 1.4 Microvascular patterning and multiscale vascular network engineering approaches.**

Schematic representations of the fabrication strategy and/or representative immunofluorescent images are presented for (A) micropatterned, and (B) multiscale engineered microvessels. (A) Micropatterned vascular engineering strategies. (i) Fabrication of straight channel. Image adapted from Nguyen et al.[104] with permission; copyright 2013 National Academy of Sciences. (ii) Fabrication of spiral channel. Image adapted from Mandrycky et al.[93] with permission (CC BY-NC 4.0). (iii) Cell-laden microgel photoannealed monolithic construct toward vascularized capillary network. Image adapted from Schot et al.[94] (CC BY 4.0). (iv) Micropatterned vascular construct fabricated via soft lithography–based collagen injection molding approach. Image adapted from Howard et al.[105] with permission

(CC BY-NC-ND 4.0). (B) Examples of multiscale vascular networks formed by a combination of prepatterning and self-assembly approaches. (i) Organotypic capillary network generated using two-photon ablation of small capillary–sized vessels from a mesoscale microfluidic conduit generated via volumetric printing. Image adapted from Rizzo et al.[106] with permission (CC BY-NC 4.0). (ii) Glomerular and brain capillaries generated via two-photon ablation from a soft lithography–based microfluidic device. Image adapted from Rayner et al.[107] with permission (CC BY-NC-ND 4.0). (iii) HUVECs and fibroblast-laden hydrogel cast in a microfluidic device with two parallel macrochannels patterned using needles and endothelialized with HUVECs. Macrovessel sprouts were anastomosed with self-assembled microvessels, forming a multiscale vascular network. Image adapted from Song et al.[108] with permission; copyright 2020 John Wiley & Sons. (iv) Bioprinted and self-assembled vascular construct assembled with endothelium ECs (dTomato-ECs, red) and printed microvascular ECs (ZsGreen-ECs, green). Image adapted from Szklanny et al.[109] with permission (CC BY-NC-ND 4.0). (v) Complex multiscale vascular network generated from vascular organoids within a microfluidic chip. Image adapted from Quintard et al.[110] (CC BY 4.0).

### *1.4.4 Combination of self-assembly and pre-patterning approaches*

Native macro- and mesovessels, including arteries, veins, arterioles, and venules, are highly capable of sprouting and anastomosis with self-assembled capillaries[111,112]. Patterned perfusable vasculatures can connect with self-assembled networks to generate interconnected multiscale vascular networks (Figure. 1.4 **B**). Recent work has shown success in macrovessel sprouts anastomosing with self-assembled microvessels[97,108,113] (Figure. 1.4 **B** i-iii). This results in thick and mechanically robust engineered tissue. Upon implantation, these tissues exhibit extensive host vessel penetration and significantly increased blood perfusion compared with control microvascular grafts[97,102,111]. Similarly, multiscale perfusable tissues with interconnected vascular networks have been achieved using multimaterial DLP bioprinting[113,114] or by combining DLP bioprinting with vasculogenic and angiogenic sprouts[115]. These studies illustrate how combining precise patterning and the flexibility of self-assembly results in stable, perfusable hierarchical vasculature, which is difficult to achieve with either approach alone.

The ultimate goal of vascularized tissue engineering is to enhance the survival, integration, and functionality of engineered tissues upon implantation. The ability to directly anastomose the engineered vascular networks with the host bloodstream is crucial for immediate perfusion. Zohar

et al.[116] fabricated an implantable biodegradable macrovessel surrounded by a cylindrical microchannel array, called an angiotube, designed to support physiological flow distribution and enable integration with living capillaries. The engineered microchannels guides ECs to form patent microvessels that sprout in accordance with the channel orientation. The angiotube was wrapped with hydrogel embedded with a mixture of endothelial and support cells, which self-assembled into a microvascular network. The endothelialized angiotube sprouted and anastomosed with the surrounding capillary network, forming a patent hierarchical vascular network suitable for direct anastomosis with the host vasculature[116]. Further developments led a new two-staged 3D bioprinting approach to create an implantable multiscale vascular network (Figure. 1.4 **B** iv). A 3D-printed scaffold seeded with ECs created a macrovessel that sprouted and anastomosed with surrounding 3D bioprinted soft tissue containing self-assembled capillaries. Using a cuffing microsurgery approach, the engineered tissue was directly anastomosed with a rat femoral artery, promoting seamless integration of the implant with host vasculature. The bioprinted vascular network also supported the functionality of cardiomyocytes[109].

Self-assembled organoids have been connected for perfusion, either through luminal flow or interstitial fluid flow[110,117], to enhance their functionality and structural integrity. 3D microfluidic devices, fabricated with two-photon SLA, supported organoid culture by enabling long-term perfusion of multimillimeter-scale engineered tissues[118] (Figure. 1.4 **B** v). Integrating advanced microvascular patterning with organoids provides long-term survival, growth, and function, improving outcomes for regenerative medicine and disease modeling.

## 1.5 Future Directions

OOC devices have been applied to a wide range of research questions, spanning basic endothelial biology to disease modeling and drug discovery. Essential to these approaches is the extent to which different vascular features and compartments are modeled and the tailoring of device designs to the research question at hand. In the slow progression from simple to complex models, simplified systems targeting only some biophysical or biochemical cues have provided great insight into core aspects of endothelial biology. Laminar flow chambers, for example, have revealed fundamental mechanisms of endothelial mechanotransduction. Similarly, cell-in-gel OOCs provided new insights into the mechanisms of angiogenesis and potential strategies to induce vascular growth (or inhibit it in the case of tumorigenesis) in living or engineered tissues. In totality, however, these works as well as a variety of in vivo studies have demonstrated a wide range of factors which may influence vascular function. Recent work has increasingly reinforced the concept of vascular heterogeneity, going beyond long appreciated organ-specific or vessel-size-specific identities. Determining which populations are most important to incorporate into a given OOC device will be critical and depend on the study goals. Developing highly accurate tissue OOCs for disease modeling and drug testing, for example, may be sensitive to the presence of the full complement of native vascular phenotypes.

The question of what level of complexity to model extends beyond the varieties of endothelial cells to include. Recent work by our lab and others have highlighted additional levels of heterogeneity in the vasculature resulting from differences in hemodynamic factors. Laminar fluid flows with secondary flow characteristics can induce unique transcriptional profiles in endothelial cells[93]. This finding suggests the complex 3D geometries found in the native vasculature may lead to more diverse endothelial responses to flow than were previously thought. The functional

consequences of these differences and their role in health and disease, if any, remain an open question which OOC systems are poised to provide new insight into. On the other hand, many critical vascular phenomena occur at the smallest vessels – capillaries of 5–10 μm, which scale remains an engineering limit since most existing OOC technologies have resolution at the order of 100 μm or more. The development of robust capillary scale engineered vessels has enabled new investigations into the dynamics of vascular interactions like those between malaria infected red blood cells and endothelial cells when exposed to controlled flow. The inclusion of these capillary structures in OOC platforms may be crucial for studies of vascular interactions with different blood components, including altered RBCs, immune cells, platelets, and others. In these capillary vessels, the blood cells and blood vessels are of nearly the same caliber. Such close interactions may contribute to disease progression and their modulation may be core to a variety of therapeutic approaches.

Another important element is the original source of cells. Cell lines or isolated primary cells have so far been the predominant cell source in OOCs, but advances in stem cell technology have made a greater variety of cell types available to researchers. As a result, the prospect of patient-specific OOC systems populated with cells differentiated from patient-derived stem cells for applications in precision medicine has become more tenable[119]. Protocols for the differentiation of the many different endothelial subtypes are not yet available, but recent advances in vascular organoids[120] suggest renewable sources of these cells may be on the horizon. Incorporating these patient-derived cells into disease modeling OOC may provide new insight into the mechanisms of disease and the safety and efficacy of new therapeutic approaches.

In summary, existing vascular engineering technologies allow us to build vasculatures over the full range of diameters, curvatures, and potentially densities of blood vessels found in living organisms.

Incorporating those technologies into a single engineered system encompassing the entire range of structures and cell types, however, remains an immense outstanding challenge. It is then important to define the goal of research projects, and wisely choose the appropriate OOC for approaching biological questions as well as drug and disease modeling. This approach has proven fruitful, but future advances are poised to further add to OOC device complexity and their ability to accurately replicate human physiology to gain a deeper understanding of vascular biology and to serve as powerful testbeds for modeling diseases and developing novel therapeutics.

In this body of work, we utilize a soft-lithography and collagen injection molding approach to generate a 3D perfusable model for investigating endothelial dysfunction in neurodegenerative disease. Our focus is to create brain-specific microvessels with the ability to introduce intraluminal perfusate and study endothelial activation and barrier changes in response to stimuli. Therefore, we emphasize generating a complete 3D lumen with minimal barrier leakage and incorporating relevant geometry to better investigate endothelial responses to the perfusate. We then build upon this existing model to create a more physiologically relevant representation of brain vasculature by incorporating relevant neurovascular cell types (i.e., astrocytes and cortical neurons) and human induced pluripotent stem cell-derived vascular organoids to introduce a hierarchical vascular network.

# Chapter 2: Amyloid Beta Peptides (Aβ) from Alzheimer's Disease Neuronal Secretome Induce Endothelial Activation in a Human Cerebral Microvessel Model

*Parts of this chapter has been published in the following manuscript: Shin YJ* and Evitts*, et al. "Amyloid beta peptides (Aβ) from Alzheimer's disease neuronal secretome induce endothelial activation in a human cerebral microvessel model" Neurobiology of disease, 2023. DOI: 10.1016/j.nbd.2023.106125)*

## 2.1 Abstract

In Alzheimer's disease (AD), secretion and deposition of amyloid beta peptides (Aβ) have been associated with blood-brain barrier dysfunction. However, the role of Aβ in endothelial cell (EC) dysfunction remains elusive. Here we investigated AD mediated EC activation by studying the effect of amyloid beta peptide (Aβ) secreted from human induced pluripotent stem cell-derived cortical neurons (hiPSC-CN) harboring a familial AD mutation ($Swe^{+/+}$) on human brain microvascular endothelial cells (HBMECs) in 2D and 3D perfusable microvessels. We demonstrated that increased Aβ levels in $Swe^{+/+}$ conditioned media (CM) led to stress fiber formation and upregulation of genes associated with endothelial inflammation and immune adhesion. Perfusion of Aβ-rich $Swe^{+/+}$ CM induced acute formation of von Willebrand factor (VWF) fibers in the vessel lumen, which was attenuated by reducing Aβ levels in CM. Our findings suggest that Aβ peptides can trigger rapid inflammatory and thrombogenic responses within cerebral microvessels, which may exacerbate AD pathology.

## 2.2 Introduction

Alzheimer's disease (AD) is a progressive neurodegenerative disease and the most common form of dementia[121,122]. Based on patient's genetic predisposition and the age of onset, AD has been

categorized into different types: Sporadic AD accounts for the vast majority of AD cases with patients often exhibiting symptoms later in life; By comparison, familial AD accounts for <5% of AD cases but is associated with stronger symptoms and earlier onset[123,124]. The neuropathological hallmarks of AD include the deposition of extracellular amyloid beta (Aβ) plaques, primarily of the Aβ 1–42 isoform[125], formation of intracellular neurofibrillary tangles[126], and progressive loss of neurons and synapses[127].

Although decades of research have been devoted to understanding the mechanisms of AD development and potential treatments, only a few FDA-approved agents for the treatment of AD are available and no long-term disease-modifying treatments are available[128]. Existing AD research has primarily focused on dysfunctions of cell types in the central nervous system (CNS) such as neurons, astrocytes, and microglia, but growing evidence suggests a role for vascular dysfunction in the development and progression of AD[128]. >90% of patients with Alzheimer's disease (AD) have been found with amyloid deposits along their cerebral vasculature, a condition known as cerebral amyloid angiopathy[129–132] (CAA). Such amyloid deposits are known to derive from the pathogenic cleavage of amyloid precursor protein (APP) into insoluble Aβ fragments that oligomerize into amyloid fibrils and plaques[133]. Aberrant vascular morphology (increased tortuosity of vessels, increased presence of string vessels, thinning of vessel walls, etc.), degeneration of vessels in affected brain regions, and decreased cerebral blood flow (CBF) are also apparent in AD[46]. However, the driving factors for vascular malformations present in AD pathogenesis remain unclear.

In vivo, brain microvessels form a vast and complex hierarchical network to regulate transport of nutrients and prevent toxic pathogens and metabolites from entering the CNS. As the interface between circulation and brain tissue, endothelial cells (ECs) play a critical role in building a strong

blood-brain barrier (BBB). In their healthy state, brain ECs express tight junction proteins to limit the diffusion of molecules into the brain;[134] when activated in response to pro-inflammatory signals, brain ECs exhibit (1) loss of vascular integrity, (2) increased expression of adhesion molecules, such as intercellular adhesion molecule 1 (ICAM-1) and vascular cell adhesion molecule 1 (VCAM-1), (3) upregulation of human leukocyte antigen molecules, (4) exocytosis of Weibel-Palade bodies (WPB) containing P-selectins and von Willebrand Factor (VWF), indicating a prothrombotic state following endothelial injury, (5) increased secretion of cytokines (IL-8, IL-12), and (6) assembly of stress fibers[135–137].

In patients with AD, serum and plasma analysis showed increases in plasma concentration of VWF and soluble endothelial adhesion proteins including E-selectin, P-selectin, ICAM-1 and VCAM-1[46,138–142], suggesting EC activation and systemic inflammation. Activation of the endothelium would convert the normally unreactive endothelial surface into an adhesive surface capable of binding platelets and leukocytes, and possibly also erythrocytes. These vascular activation events could initiate the coagulation cascade, leading to microvascular occlusion in brain microvessels[89]. In addition, enhanced expression of other adhesion molecules such as ICAM-1 and VCAM-1 would assist the rolling and firm adhesion of leukocytes to EC surface, promoting extravasation of immune cells into the brain parenchyma[143,144]. Neutrophil recruitment to the CNS via adhesion molecules is also known to promote activation of microglia and astrocytes inducing neuronal damage[145].

Despite the debilitating nature of vasculopathies in AD, studies of human AD-mediated vascular dysfunction are limited as it is challenging to study cellular function non-invasively in the human brain. In vitro cultures of EC monolayers have shown that exogenously applied Aβ peptides led to nuclear and mitochondrial DNA damage, cell death, increased BBB permeability and increased

monocyte adhesion on ECs[128,135,146,147]. In bovine aortic EC cultures, Aβ 1–42 was found to induce endothelial dysfunction by raising intracellular calcium levels via calcium-permeable Aβ channels[148]. These 2D in vitro studies, however, lack proper vascular architecture, lack in vivo flow characteristics, and apply exogenous Aβ at micromolar doses, which is higher than the average concentration, at picomolar levels, of Aβ measured in the human brain[149]. It remains elusive to what extent Aβ peptides drive human brain microvascular injuries and dysfunctions in AD conditions.

Transgenic mouse models of AD are often utilized to show cerebrovascular phenotypes, however, not all the models show the same aberrations and they do not always occur at the same time[150]. For example, decreased vessel density, a common vascular alteration in human AD, is observed in only one of the ten most common AD mouse models, and depending on the mouse line, the onset of vascular amyloid deposition can occur anywhere between 3 months and 24 months of age[150]. Furthermore, these animal models often have non-physiologic expression of a number of AD-related transgenes. Hence there is a critical need to evaluate the role of Aβ in AD-associated vascular dysfunction in a system that structurally and functionally mimics human brain vasculature and includes accurate Aβ levels.

More recently, advances in microfluidic-based techniques enabled modeling of the 3D BBB with perfusable lumens that can recapitulate the biochemical and biophysical perturbations occurring in cerebral blood vessels[151,152]. Culturing ECs under flow improves EC homogeneity, homeostatic control, EC alignment with flow, vascular development, and EC proliferation[97,153,154]. In primary HBMECs, flow has also been shown to increase the tightness of junctions in vascular models, which significantly decreased EC permeability, better reflecting the highly impermeable barrier of the in vivo BBB[155]. Hence, 3D perfusable human cerebral vascular models provide timely

opportunities for studying the responses of human brain ECs and microvessels to the increased levels of secreted Aβ in AD in physiological and pathological-relevant conditions.

In this study, we utilized primary HBMECs and established a 3D perfusable human brain microvessel platform to study AD-associated endothelial activation. We modeled the AD response by perfusing these microvessels with neuronal secretomes, collected as conditioned medium (CM) from human neuronal cultures. These neurons were differentiated from human induced pluripotent stem cells (hiPSCs), that harbor the APP Swedish mutation KM670/671NL (APPSwe). This mutation increases Aβ secretion by enhancing amyloidogenic APP cleavage by β-secretase 1 (BACE1) and is causative for early-onset familial AD[156,157] (Haass et al., 1995; Young et al., 2018). Cells with AD mutations, including the Swedish mutation, have been used to study blood-brain barrier (BBB) changes in AD and CAA[158,159]. One recent study demonstrated that conditioned media (CM) collected from hiPSC-derived APPSwe neurons led to increased permeability in 2D monolayers of proliferating brain ECs, while WT CM did not affect permeability[160], suggesting that this CM study can recapitulate features of BBB dysfunction seen in AD brain.

We compared the endothelial alterations induced by treatment with CM from cortical neuron cultures differentiated from APPSwe hiPSCs (hiPSC-CNs) and their isogenic wild-type (WT) control cell lines. In 2D, treatment of HBMECs with CM from AD hiPSC-CNs led to cytoskeletal reorganization and upregulation of genes involved in immune cell interaction with ECs. In 3D flow-directed brain microvessels, perfusion of CM from APPSwe hiPSC-CNs elicited acute endothelial activation and formation of transluminal VWF fibers, suggesting the initiation of thrombotic microangiopathy within the luminal space. By showing reduced endothelial activation to CM from neurons deficient in APP expression (APPKO), or from APPSwe cells treated with a β-secretase inhibitor (BACEi), we demonstrated the pivotal role of Aβ in EC activation. Our

findings highlight that increased Aβ levels secreted by AD neurons lead to endothelial activation in brain microvessels. This suggests that Aβ has a direct role in eliciting acute hemostasis and vascular inflammation in the cerebrovasculature of AD patients.

## 2.3 Materials and Methods

### *2.3.1. Endothelial cell culture*

Human brain microvascular endothelial cells (HBMECs) (CC# ACBRI 376 V; Cell systems) at passage number 3–6 were used for all experiments. HBMECs were maintained in culture flasks coated with Attachment Factor (CC# 4Z0–210; cell systems) and fed growth medium (GM) (CC# 3202; EGM-2 MV Microvascular Endothelial Cell Growth Medium-2 BulletKit (CC# 3156; EBM-2 Basal Medium), 5% fetal bovine serum (FBS), hydrocortisone, human fibroblast growth factor-beta (hFGF-B), vascular endothelial growth factor (VEGF), R3-insulin-like growth factor-1 (R3-IGF-1), ascorbic acid, human epidermal growth factor (hEGF), GA-1000 (gentamycin and amphotericin)). Cells were maintained at 37 °C in a 5% CO2 incubator and media was replaced every 3 days.

### *2.3.2 Cell lines and hiPSC neuronal differentiation*

To generate AD mimicking neurons from hiPSCs we used previously established gene-edited hiPSC lines heterozygous ($Swe+^{/WT}$) and homozygous ($Swe^{+/+}$) for the APP Swedish mutation as well as the parental control ($Swe^{WT/WT}$) described in Young et al.[157]. These cell lines were generated from a previously published and characterized CV background human induced pluripotent stem cell line[161]. This is a male cell line with an APOE ε3/ε4 genotype[162]. A previously published APP knockout (APPKO) line was used as an additional control for conditioned media (CM) experiments[157]. This cell line was made from a parental APP duplication hiPSC line and was

engineered using CRISPR/Cas9 genome editing to lack APP production. Neurons from these cell lines were differentiated from hiPSCs using dual-SMAD inhibition techniques as previously described[161,163]. For the experiments presented here, we started with neural precursor cells (NPCs) previously differentiated from hiPSCs and frozen. NPCs for all the APPSwe lines ($Swe^{+/WT}$, $Swe^{+/+}$, $Swe^{WT/WT}$) and the APPKO line were thawed and plated on a Matrigel (Growth factor reduced basement membrane matrix; CC# 356231; Corning) coated 6-well plates. NPCs were cultured in Basal Neural Maintenance Media (BNMM) + FGF (1:1 DMEM/F12 + Glutamine (CC# 11320–033; Gibco) and Neurobasal media (CC# 21103–049; Gibco), 0.5% N2 Supplement (CC# 17502–048; Gibco), 1% B27 Supplement (CC# 17504–044; Gibco), 0.5% GlutaMax (CC# 35050061; Thermo Fisher Scientific), 0.5% insulin-transferrin-selenium (CC# 41400045; Thermo Fisher Scientific), 0.5% NEAA (CC# 11140050; Thermo Fisher Scientific), 0.2% b-mercaptoethanol (CC# 21985023, Life Technologies) + 20 ng/mL FGF (R&D Systems, Minneapolis, MN)). The NPCs were allowed to reach 70% confluence for 1–3 days with media changes every other day. Once the NPCs were sufficiently confluent, cells were dissociated with Accutase (CC# 07930, STEMCELL Technologies) and passaged into Matrigel-coated 10 cm culture plates for neural differentiation. 24 h after replating, the cells were switched to Neural Differentiation media (BNMM +0.2 mg/mL brain-derived neurotrophic factor (CC# 450–02; PeproTech) + 0.2 mg/mL glial-cell-derived neurotrophic factor (CC# 450–10; PeproTech) + 0.5 M dbcAMP (CC# D0260; Sigma Aldrich). Media was changed twice a week for 21 days at which point the differentiation is considered finished. Cells were maintained at 37 °C in a 5% CO2 incubator.

*2.3.3 Conditioned media preparation*

Following 21 days of differentiation, Neural Differentiation media was refreshed and was then kept on the cells for at least 72 h with no media change to generate conditioned media (CM) for 2D and 3D treatment experiments. After 72 h, the media was collected and stored at 4 °C for short-term storage and -20 °C for long-term storage. To generate CM from BACEi treated APPSwe neurons, neurons were dissociated from 10 cm plates using Accutase following 21 days of differentiation and split into 3 wells of a Matrigel-coated 6 well plate. This was repeated for all cell lines. At least 3 days later, neurons were treated with either 25 nM β-secretase inhibitor (CC# HY-13240; BACEi LY2886721; MedChemExpress) or dimethyl sulfoxide (DMSO, as vehicle control) or left untreated every 24 h 72 h with no media change. After 72 h of treatment, media from untreated, DMSO, and BACEi treated neurons was harvested for perfusion through microvessels, treatment in 2D, and quantification of Aβ1–40 and Aβ1–42 peptides secreted by neurons.

### *2.3.4 Immunoprecipitation of Aβ*

For immunoprecipitation of Aβ from our CM, 4 µg/mL of mouse anti-Aβ 6E10 antibody (CC# 803001, BioLegend) was added to CM samples from the $Swe^{+/+}$ and $Swe^{WT/WT}$ lines as previously described[164–166]. Media containing the antibody was incubated tilting, overnight at 4 °C. 50 µl of M-280 Sheep Anti-Mouse IgG Dynabeads™ (CC# 11202D, Invitrogen) for every 4 µg of antibody were added to each CM sample according to the manufacturer's instructions and the samples were incubated tilting at 4 °C for 1 h. The Dynabeads™ covalently coupled to 6E10 labeled Aβ were removed from the media using a magnet according to the manufacturer's instructions. Supernatant was removed from the magnetically separated beads and CM lacking Aβ was collected and stored at -80 °C for downstream analysis and perfusion through engineered microvessels.

### *2.3.5 Amyloid beta measurements*

Aβ1–40 and Aβ1–42 peptides were measured using the methods previously described by Young et al[167]. Conditioned media collected from the $Swe^{+/+}$, $Swe^{+/WT}$, $Swe^{WT/WT}$, and APPKO cell lines after a 3-week differentiation were frozen at -80 °C until use. The media was run on an Aβ Triplex ELISA plate (CC# 151200E-2; MesoScale Diagnostics).

### *2.3.6 Meso-Scale Discovery (MSD) U-PLEX platform to measure extracellular levels of cytokines and chemokines*

Pro-inflammatory proteins in the media were measured using the MSD U-PLEX platform (MesoScale Diagnostics). For this assay, conditioned media collected from the $Swe^{+/+}$, $Swe^{+/WT}$, $Swe^{WT/WT}$, and APPKO cell lines after a 3-week differentiation were frozen at -80 °C until use. 25 µl of media was used to run an MSD U-plex assay as per manufacturer's protocol and MSD Quick plex SQ120 instrument was used to detect analytes. This MSD U-Plex plate detected a panel of pro-inflammatory cytokines including IL-1β, IL-6, IL-8, IFN-β, TNF-α, IL-15, IFN-α2a and chemokines including Eotaxin, and IP-10, known to be elevated in AD patients.

### *2.3.7 Total and phospho-tau measurements*

Samples were prepared by plating differentiated neurons from the $Swe^{+/WT}$, $Swe^{+/+}$, $Swe^{WT/WT}$ and APPKO lines in a 96 well plate at 300,000 cells per well. Conditioned media and cell lysate were harvested and pooled from six wells per line. Conditioned media was incubated on the cells for at least 72 h prior to collection. pTau (Thr231) and tTau levels were measured in these samples using pTAUThr231/tTAU ELISA plates (CC# K15121D-1, Meso Scale Discovery).

### *2.3.8 3D cerebral microvessel fabrication*

Engineered microvessels were fabricated using soft lithography and injection molding techniques previously described by Zheng et al[95]. Briefly, type I rat tail collagen was dissolved in 0.1% acetic acid at a stock concentration of 15 mg/mL[95]. The collagen was neutralized and diluted to 7.5 mg/mL on ice with 1 M NaOH (20 mM final), 10× M199 (CC# 11825015; Thermo Fisher Scientific), and EGM-2MV. A microfabricated polydimethylsiloxane (PDMS) stamp was used to define a double-grid vessel network with a feature height of 150 μm. Collagen was molded around this PDMS stamp. A flat collagen gel was also generated. After gelation at 37 °C, the channels were incubated with the flat collagen gel to generate closed off microchannels that can be perfused and seeded with endothelial cells (ECs). These two gels merged through additive bonding upon incubation at 37 °C. Once the gel was fabricated, HBMECs were lifted from culture flasks with trypsin (CC# MT-25-052-CI; Thermo Fisher Scientific) and resuspended in GM at a concentration of 7–10 × $10^6$ cells/mL. Using a gel loading pipette tip, 10 μL of this cell suspension is injected into the inlet of the microvessel and allowing them to circumferentially attach to the collagen gel under static conditions for 1 h prior to the start of gravity-driven flow. Microvessel constructs were cultured under gravity-driven flow for 5–7 days with media replenishment approximately every 12 h.

*2.3.9 Conditioned media treatment*

For the treatment of HBMECs with CM in 2D, HBMECs were plated at a density of 0.03 M/well in a glass bottom chamber slide (CC# 80827, Ibidi) and allowed to recover for 48 h prior to treatment. Prior to treatment, the cells were washed with EBM-2 basal media (serum-free) for 5 mins. Then, 250 μL of CM per well was then added to the cells for 8 h, following which the cells were fixed in 4% PFA. To treat our engineered microvessels in 3D, vessel fabrication was performed as described above. Following vessel fabrication and culture for 5–7 days under gravity-

driven flow, the vessels were treated with CM from all of our APPSwe lines and CM from BACEi treated neurons. Vessels were washed with EBM-2 basal media (serum-free) for 20 mins. Vessels were then perfused with CM for 1 h. Media was replenished every 20 mins to continue gravity-driven flow throughout the duration of treatment. Following 1 h of perfusion, the vessels were fixed with 4%PFA for 20 mins for downstream analysis and washed with phosphate buffered saline (PBS) three times for 20 mins each. For RNAseq analysis, vessels were treated for 8 h with media replenished every 2 h.

*2.3.10 RNA isolation and RNAseq analysis*

RNA was collected from two different culture subtypes (2D cultures and 3D microvessels) for three different media conditions (unconditioned BNMN media, conditioned control media and conditioned $Swe^{+/+}$ media). RNA from 2D cultures was collected following media treatment from 24 well plates by addition of RLT lysis buffer and pipette homogenization. RNA from 3D vessels was collected by perfusion of RLT lysis buffer in the inlets and collection of the lysates in the outlets. Lysates from three wells in 2D cultures were pooled as one sample replicate, and two vessels from 3D cultures were pooled as one replicate. Total RNA was isolated from the lysate using on-column digestion of genomic DNA via RNeasy Micro Kit (CC# 74004; Qiagen). RNA quality was assessed using High sensitivity RNA TapeStation 4200 (Agilent Technologies) and total RNA samples with RNA integrity number > 8 were used to proceed to library preparation. For sequencing, cDNA preparation was performed using Takara SMART-Seq v4 Ultra Low Input RNA Kit (SMARTv4), library preparation using Illumina Nextera XT DNA Library Prep Kit (Nextera XT) and sequenced with Illumina NovaSeq 6000 (paired-end 50 cycles). Sequenced reads were aligned using STAR2 aligner and gene-level raw counts was obtained using STAR2's internal

quantification method. Gene ontology analysis was performed using iDEP.951 for pathway analysis of differentially expressed genes.

### *2.3.11 Isolated platelet and peripheral blood mononuclear cell (PBMC) perfusion in microvessels.*

Whole blood was drawn from normal healthy donors into a blood collection tube (BD, CC# 364606; Vacutainer) containing 1.5 mL of acid citrate dextrose (ACD). Platelets were isolated from whole blood using an existing protocol provided by the manufacturer. Briefly, collected blood was centrifuged at 200 g for 20 min (acceleration 4; deceleration 0) at room temperature for platelet-rich plasma (PRP) extraction. PRP was subsequently centrifuged at 1200 g for 10 min to obtain pellets containing the isolated platelets. Pellets were resuspended in CGS buffer containing 120 mM NaCl, 13 mM Sodium Citrate and 30 mM Glucose supplemented with Prostaglandin E1 (sigma P5515-1MG) at 1:10,000 (vol: vol) to inhibit aggregation of platelets. Isolated platelets rinsed in CGS/PGE1 buffer were counted under a bright-field microscope using a hemocytometer and centrifuged again using the previous setting. Pellets were resuspended carefully in Tyrode's buffer containing 5.5 mM glucose, 10 mM HEPES, 138 mM NaCl, 12 mm HaHCO3, 2.9 mM KCL and 0.36 mM NaH2PO4 and stained with CD41a (CC# 555467; BD) conjugated with phycoerythrin (PE) for 30 min. Following staining, platelet concentration was adjusted to $5 \times 10^7$ platelets/mL by supplementing an additional Tyrode's buffer.

Isolated platelets were perfused in conditioned media treated microvessels to assess the functional activation of endothelial cells. CD41a labeled isolated platelets were perfused in HBMEC microvessels treated with conditioned media for 1 h through transfer pipettes to avoid shear-induced activation. Approximately 150 µl of platelets resuspended in Tyrode's buffer was pipetted into the inlets of microvessels and incubated at 37 °C for 20 min. Following platelet treatment,

vessels were washed three times, each rinse for five minutes, to eliminate residual unbound platelets within the vessel lumen. Immediately after the wash step, microvessels were fixed in 4% paraformaldehyde solution and rinsed with PBS three times. Platelet adhesion analysis was performed after performing immunofluorescent staining of VWF and confocal imaging.

PBMCs were also isolated from freshly drawn blood samples collected in ACD blood collection tube (BD CC# 364606; Vacutainer). PBMCs were isolated using density gradient centrifugation in a 50 mL SepMate tube (StemCell Technologies) following manufacturer's protocol. PBMCs were stained with pan-leukocyte marker CD45 (CC# 555485; BD biosciences) for live imaging of leukocyte adhesion on Swe+/+ CM treated HBMEC microvessel for 1 h.

*2.3.12 Scanning electron microscopy imaging of platelet bound VWF fibers*

$Swe^{+/+}$ perfused microvessels were fixed in ½ strength Karnovsky's fixative (2% paraformaldehyde and 2.5% glutaraldehyde) overnight at 4 °C. The top and bottom layers of the collagen matrices were gently teased apart and rinsed with 0.1 M cacodylate buffer. Samples were dehydrated with graded series of alcohols and critical point dried (Autosamdri, Tousimis Corp). Microvessel layers were sputter coated with Au/Pd alloy (Denton Desk IV, Denton Vacuum) and imaged using a JSM 6610 LV scanning electron microscope (JEOL) at an accelerating voltage of 5 kV.

*2.3.13 Flow cytometry analysis*

To characterize vascular cell adhesion molecule 1 expression on the surface of endothelial cell following CM treatment, multiparameter FACS analysis of CM treated human brain endothelial cells was performed. BD FACS Canto II was used to analyze VCAM-1 positive cells using FTIC-anti-VCAM-1 antibody (CC# ab24853; Abcam) and the number of positive cells were quantified

using with FlowJo software (Tree Star). Unstained controls were used to compensate and adjust voltage.

### *2.3.14 Immunofluorescent staining and image analysis*

At the end of each experimental time point, both microvessels and 2D endothelial cultures were fixed with 4% paraformaldehyde for 20 min and washed with PBS three times. For immunofluorescent staining of microvessels, reagents were perfused through the microchannels through the inlet of the acrylic jigs. PBS containing 2% bovine serum albumin (BSA) was used to block microvessels and 2D cultures for analysis of extracellular VWF. Following 1 h of blocking, fluorescein isothiocyanate (FITC) conjugated VWF antibody (1:100; Abcam CC# ab8822) was added to samples for 1 h at room temperature and washed three times with PBS before proceeding to stain with the remaining antibody of interest. Treatment with 2% BSA with 0.1% Triton-x preceded before staining with antibodies including CD41a (CC# 555467; BD), phalloidin (CC# A12380; Thermo Fisher), CD144 (CC# 136008; BioLegend) for cell permeabilization and blocking non-specific binding. All stained microvessels and 2D cultures were imaged using Yokogawa W1 spinning disk confocal microscope or Leica SP8 laser confocal microscope. For microvessels, the entire collagen construct was imaged using a 5 by 5 large z stack image stitch (10% blending stitch) under a 10× objective with a z-step size of 5.5 μm. 3D reconstruction and cross-sectional images of the microvessels were rendered using ImageJ software.

### *2.3.15 VWF fiber quantification*

VWF fibers were quantified into two distinct wall-fiber and transluminal fiber categories. Transluminal fibers were quantified from fibers formed cross-sectionally within the microchannels and are characteristically thicker and straighter than wall fibers. Wall fibers were quantified from

string fibers found circumferentially on the endothelial surface and are smaller and tortuous by nature. For classification of the number of fibers found in each group, stitched z stack Images of each vessel were divided into three layers: top, center lumen and bottom. The top and bottom layers were constructed from compilation of initial and final 4 z-stacks (~20 μm) of each image construct respectively. The luminal layer was constructed from compiled z stack images excluding the initial and final 4 layers.

#### *2.3.16 Statistical analysis*

Statistical analysis of fiber quantification was performed with either one-way ANOVA or two-way ANOVA for comparison between groups followed by Tukey's or Šídák's post hoc test for multiple comparisons between groups. Statistical analysis on the RNAseq was conducted with Fischer's Exact test. Significance was defined as a value of $p < 0.05$. For all imaging experiments the data was analyzed in a blinded manner. Statistical analysis was performed using GraphPad Prism software. Information on statistical details of individual experiments can be found in the respective figure legends.

### 2.4 Results

#### *2.4.1 APPSwe hiPSCs-CNs secretes Aβ in a genotype-dependent manner*

To investigate the effect of AD neuron derived paracrine signaling on HBMECs, we differentiated hiPSCs from an established cell line harboring the APPSwe mutation into cortical neurons (CNs)[157,159] (Figure. 2.1 **A** and **B**). Following a previously published[161,163] protocol, neural progenitor cells (NPCs) were first differentiated from hiPSCs for 3 weeks, followed by another 3 weeks of differentiation into neurons. At the end of the 3-week differentiation, CNs were enriched in the cultures, as marked by robust immunofluorescent staining for the neuron marker MAP2

(Figure. 2.1 **B**). hiPSC lines homozygous ($Swe^{+/+}$) and heterozygous ($Swe^{+/WT}$) for the APPSwe mutation were used to generate hiPSC-CNs (Figure. 2.1 **A**). Control hiPSC-CNs were made using the parental wild type ($Swe^{WT/WT}$) line for the APPSwe lines, and an APP knock out (APPKO) cell line was used as an additional control [157,167]. After 3-weeks of differentiation, CM was collected from hiPSC-CN cultures and measured for their Aβ 1–42 and 1–40 levels using an ELISA assay (Figure 3.1 **C**). CM collected from $Swe^{+/+}$ and $Swe^{+/WT}$ hiPSC-CNs showed increased Aβ 1–42 and 1–40 levels compared to controls, with the highest mean in the $Swe^{+/+}$ line for Aβ 1–42 (487 pg/mL) and 1–40 levels (5431 pg/mL). The $Swe^{+/WT}$ line showed significantly lower Aβ 1–42 (137 pg/mL) and Aβ 1–40 (1033 pg/mL) levels compared to $Swe^{+/+}$, but significantly higher than that collected from the $Swe^{WT/WT}$ (Aβ 1–42 at 50 pg/mL and 1–40 at 385 pg/mL). These results confirm that the APPSwe neurons secrete increased levels of Aβ and may be a viable way to mimic paracrine signals from neurons in the AD brain.

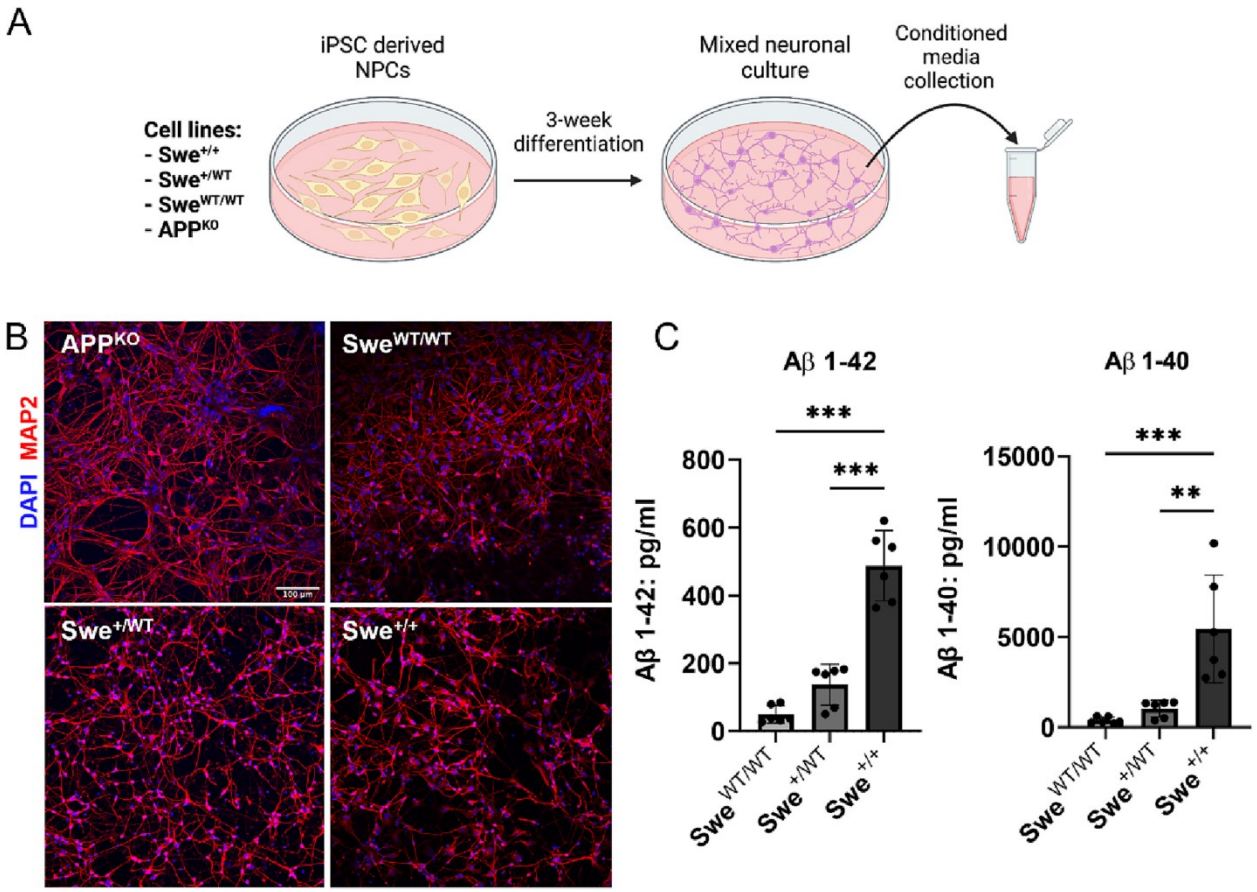


**Figure 2.1 Condition media (CM) collection and characterization of hiPSC-CN cultures.**

(A) Schematic overview of CM obtained from neuronal cultures. $Swe^{+/+}$ (homozygous) and $Swe^{+/WT}$ (heterozygous) CNs were differentiated from hiPSCs harboring the APP Swedish mutation. For our controls, CNs were differentiated from an isogenic control line, $Swe^{WT/WT}$, and a line that has CRISPR knockout of the APP gene, APPKO. (B) Immunofluorescent (IF) images of cortical neurons differentiated from APPKO, $Swe^{WT/WT}$, Swe+/WT, and $Swe^{+/+}$ hiPSCs show enriched staining for cortical neurons (MAP2, red). Scale bar: 100 μm (C) ELISA quantification of CM shows increased levels of Aβ expression in APPSwe CNs. n = 3 biological replicates. Error bars, mean ± SEM. *p < 0.033, **p < 0.002, and ***p < 0.001 by one-way ANOVA with Tukey's correction for multiple comparisons test.

### *2.4.2 Paracrine signaling from neurons induces endothelial activation and cytoskeletal reorganization in 2D monolayer culture*

Under stress, endothelial cells may be activated, which leads to the formation of stress fibers[137]. We next treated HBMECs in a 2D monolayer (Figure. 2.2 **A** i) with CM obtained from hiPSC-CN cultures to evaluate the paracrine effect of neurons on HBMECs. Four media groups were tested to assess endothelial activation after a 6-h treatment: $Swe^{+/+}$ CM, $Swe^{+/WT}$ CM, $Swe^{WT/WT}$ CM, and unconditioned media (UCM). Upon treatment with $Swe^{WT/WT}$ CM, HBMECs exhibited quiescent cytoskeletal structures characterized by a cortical actin rim around the peripheral junctions (Figure. 2.2 **A** i and ii; arrows). In comparison, $Swe^{+/+}$ CM and $Swe^{+/WT}$ CM treated HBMECs showed reorientation of actin fibers into elongated stress fibers with increased cell polarity (Figure. 2.2 **A** iii and iv; arrowheads), suggesting their activated state. In particular, $Swe^{+/+}$ CM treated HBMECs show significant retraction of endothelial cells (Figure. 2.2 **A** iv; arrowheads), characterized by degradation of vascular endothelial cadherin (VECAD) junctions in areas of retraction (Figure. 2.2 **A** viii; asterisk), and increased gap formation between adjacent ECs.

### *2.4.3 RNA sequencing (RNAseq) reveals endothelial activation signatures in CM treated HBMECs*

To understand the transcriptomic changes in endothelial cells following CM treatment, we sequenced RNA collected from 2D HBMECs that were treated with two batches of $Swe^{+/+}$ CM, $Swe^{WT/WT}$ CM, and UCM. Principal component analysis (PCA) showed that individual UCM, $Swe^{WT/WT}$, and $Swe^{+/+}$ CM treated groups clustered together (Figure. 2.2 **B**). In particular, the UCM cluster is distinctly separated from the $Swe^{WT/WT}$ and $Swe^{+/+}$ clusters, suggesting that neuronal secretomes had a large effect on EC function compared to UCM. Clusters also form within the same media batch groups, with distinct cluster presentations for $Swe^{WT/WT}$ and $Swe^{+/+}$ groups. Batch-to-batch variation appeared to exist in the CM obtained, leading to overlaps among clusters,

which is likely due to the inherent heterogeneity of hiPSC-CNs and secretome production for analysis of RNAseq, we combined both batches for unbiased representation of transcriptomes that were differentially expressed between $Swe^{WT/WT}$ and $Swe^{+/+}$ treated ECs. Results showed 10 genes that were differentially expressed between HBMECs treated with $Swe^{WT/WT}$ CM and $Swe^{+/+}$ CM (Figure. 2.2 **C**). This includes upregulation of genes associated with endothelial adhesion molecules: SELE (~7-fold change), VCAM-1 (~6-fold change) and ICAM-1 (~3-fold change) (Figure. 2.2 **D** and **E**). CCL2 and SDCBP2 were also upregulated, which supports the presence of higher levels of inflammatory cytokines in $Swe^{+/+}$ CM. Down-regulated genes include: INPP5J, TSPYL5, SOCS3 and PDZD7 (Figure. 2.2 **C** and **D**). Downregulation of the TSPYL5 gene, known to be associated with endothelial proliferation and tube formation, suggests angiogenic ability may be attenuated in ECs with AD exposure[168]. GO term and KEGG pathway analysis showed up-regulation of pathways related to leukocyte adhesion, cellular extravasation, and endothelial inflammation (Figure. 2.2 **F**). 24-h treatment of HBMECs with $Swe^{+/+}$ CM and $Swe^{WT/WT}$ CM confirmed increased VCAM-1 expression on the endothelial surface upon stimulation with $Swe^{+/+}$ CM (Supplementary Figure. S2.1).

Overall, both phenotypic and transcriptomic analyses of HBMECs suggest that ECs are activated by neuronal secretomes in AD CM through cytoskeletal reorganization, and transcriptional alteration. These data indicate that paracrine signaling from AD neurons elicits a pro-inflammatory, pro-thrombotic, and anti-angiogenic environment in brain ECs.

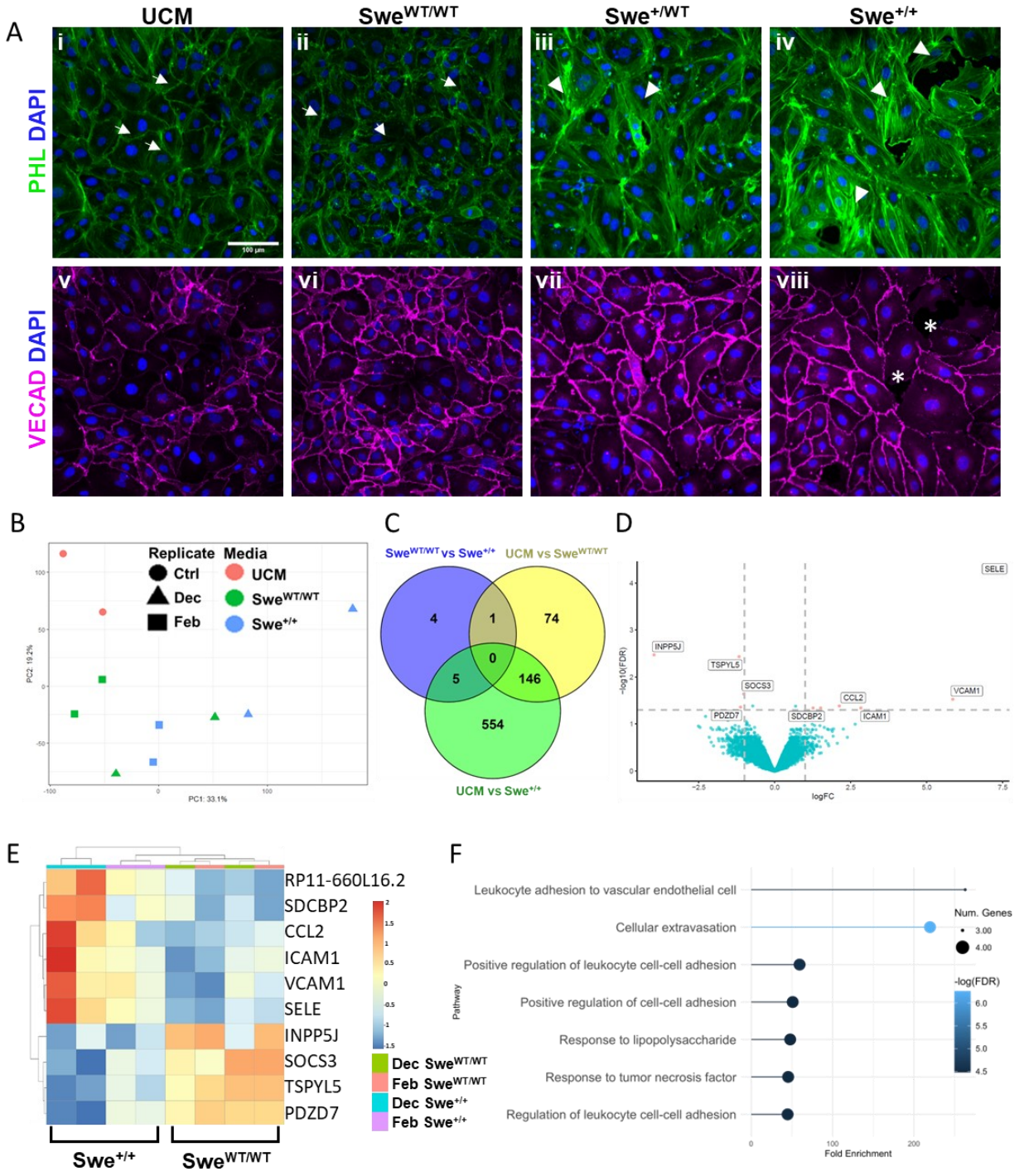


**Figure 2.2 Cytoskeletal and transcriptomic changes in 2D HBMEC cultures after CM treatment.**

(A) Representative IF images of 2D cultured (i-viii) HBMECs treated with CM media. 2D cultures exposed to UCM (i) and Swe$^{WT/WT}$ (ii) media maintain cortical actin cytoskeletal staining (Phalloidin, green) as denoted by white arrows (i and ii), (iii) Swe$^{+/WT}$ CM treatment shows endothelial retraction and f-actin stress fiber formation (Phalloidin, green) (iii) which is intensified in Swe$^{+/+}$ treatment (iv) as denoted by white arrow heads. Representative images from n = 3 biological replicates. 2D HBMEC IF staining shows good vascular endothelial cadherin junction (VECAD, magenta) in (v) UCM, (vi) Swe$^{WT/WT}$, (vii) Swe$^{+/WT}$ CM treated HBMECs. Regional loss of VECAD is observed in Swe$^{+/+}$ CM

treated HBMECs. (viii; asterisk) Scale bar: 100 μm (B) PCA of RNA-seq data from HBMECs treated with three media types (UCM, $Swe^{WT/WT}$ and $Swe^{+/+}$) in 2D. (C) Venn diagram showing the overlap of genes significantly changed by CM media treatment. 10 genes were differentially expressed between $Swe^{WT/WT}$ and $Swe^{+/+}$ CM treatment. (D) Volcano plot showing DEGs between, $Swe^{WT/WT}$ treated media and $Swe^{+/+}$ treated media. (E) Heatmap of log counts per million (CPM) values for genes that were identified to be significant in $Swe^{+/+}$ treated HBMECs. (F) Gene Ontology terminology analysis for biological processes involved in upregulated genes in $Swe^{+/+}$ CM treated HBMECs.

### *2.4.4 $Swe^{+/+}$ conditioned media induces endothelial activation in 3D flow-mediated engineered cerebral microvessels*

The endothelium in vivo forms an intact lumen and 3D network structure, responding to flow and cytokines synchronically. When activated, the endothelium is known to release granules, such as VWF, which can extend and multimerize into large fibers, under flow, to bind platelets and other blood cells[152]. Such activation denotes a shift of the endothelium toward a prothrombotic phenotype and has been shown as a signature phenomenon in 3D microvessels[152]. We examined whether $Swe^{+/+}$ CM would induce rapid activation of 3D flow-mediated engineered cerebral microvessels. Using the engineered microvessel method previously developed by our lab[95], we created devices with a double grid geometry (8 × 8) for microvessels with a feature height of 150 μm (Figure. 2.3 **A**) and seeded with HBMECs at a concentration of $7 \times 10^6$ cells/mL. After culture for 5–7 days under gravity-driven flow, a continuous and confluent endothelium was established in 3D engineered cerebral microvessels (Figure. 2.3 **A**).

We then perfused cerebral microvessels with different CM for 1 h under gravity-driven flow (Figure. 2.3 **A**) and evaluated the formation of VWF fibers in the vessel lumen. Treatment of vessels with $Swe^{+/+}$ media led to the formation of large transluminal VWF fibers throughout the vessels (Figure. 2.3 **B** (green) and **C**), which was not observed upon perfusion with CM from the $Swe^{WT/WT}$ line or UCM. The extended VWF fibers in the vessel lumen expose binding sites for platelets, which could initiate thrombosis in vessels[169]. We next perfused washed platelets isolated

from whole blood, stained for the platelet marker CD41a, through the microvessels. Upon perfusion, platelets readily bound to VWF fibers in the $Swe^{+/+}$ condition, but there was minimal binding in vessels with no VWF fibers (UCM and $Swe^{WT/WT}$) (Figure. 2.3 **B** (red)). Using VWF staining and platelet perfusion, two types of VWF fibers were identified in perfused microvessels, including transluminal fibers, seen as large fibers in the center of the vessel lumen, and wall fibers, as small fibers found on the wall of the vessels that are marked by platelet strings (Supplementary Figure. S2.2). Brightfield and scanning electron microscopy of the $Swe^{+/+}$ CM treated microvessels showed that large aggregates of platelets are bound to ultra-large transluminal VWF fibers whereas single platelet binding occurred on wall string fibers. Quantification of wall and transluminal fibers in vessels perfused with $Swe^{+/+}$ CM showed a significant increase in transluminal and total fibers, and a trend toward increased wall fiber formation across several replicates compared to controls (UCM and $Swe^{WT/WT}$) (Figure. 2.3 **E**). Furthermore, we observed that in brain microvessels perfused with $Swe^{+/+}$ CM, leukocytes were able to bind to the endothelial surface and initiate a tethering and rolling response. This suggests that endothelial cells were activated by CM with higher Aβ concentrations which facilitated immunoadhesion within the microvessels (Figure. 2.4). These results suggest that perfusion of engineered microvessels with CM with high Aβ levels can induce EC activation and VWF fiber formation that is not present in vessels perfused with CM from cell lines with low Aβ production.

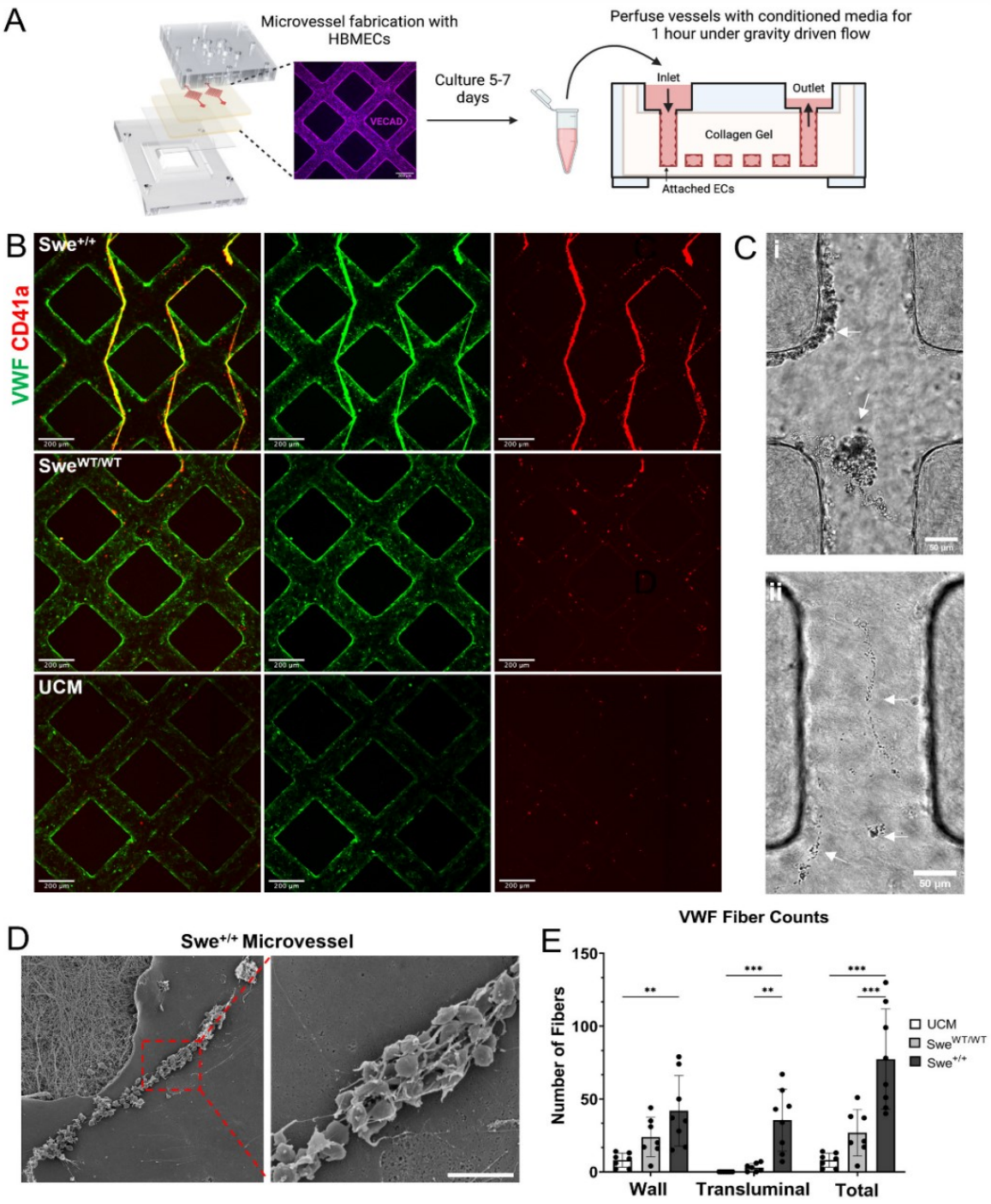


**Figure 2.3 Perfusion of CM stimulates VWF release in 3D engineered cerebral microvessels**

Schematic illustrating engineered microvessel fabrication and treatment of vessels with CM. (B) Representative images of microvessels treated with CM (bottom: unconditioned base media (UCM), middle: $Swe^{WT/WT}$, and top: $Swe^{+/+}$). $Swe^{+/+}$ CM perfusion causes VWF fiber formation (VWF, green) and induces binding of washed isolated platelets (CD41a, red). By comparison little to no VWF fiber formation or platelet binding occurs in UCM and $Swe^{WT/WT}$ CM treated microvessels. Scale bar: 200 µm. (C) Brightfield images of platelets binding to VWF fibers in engineered cerebral microvessels. Platelets bound to both (i) transluminal fibers and (ii) wall fibers. Arrows indicate platelet binding and aggregation. Scale bar: 50 µm. (D) SEM image of microvessels containing a wall VWF fiber with

bound platelets. Platelets are bound in a mesh of VWF fibers present on the luminal surface of microvessels. Scale bar: 5 μm. (E) Quantification of VWF fibers formed upon perfusion of engineered cerebral microvessels with CM. n = 4 biological replicates. Error bars, mean ± SEM. *p < 0.05, **p < 0.01, and ***p < 0.001 by two-way ANOVA with Tukey's correction for multiple comparisons test.

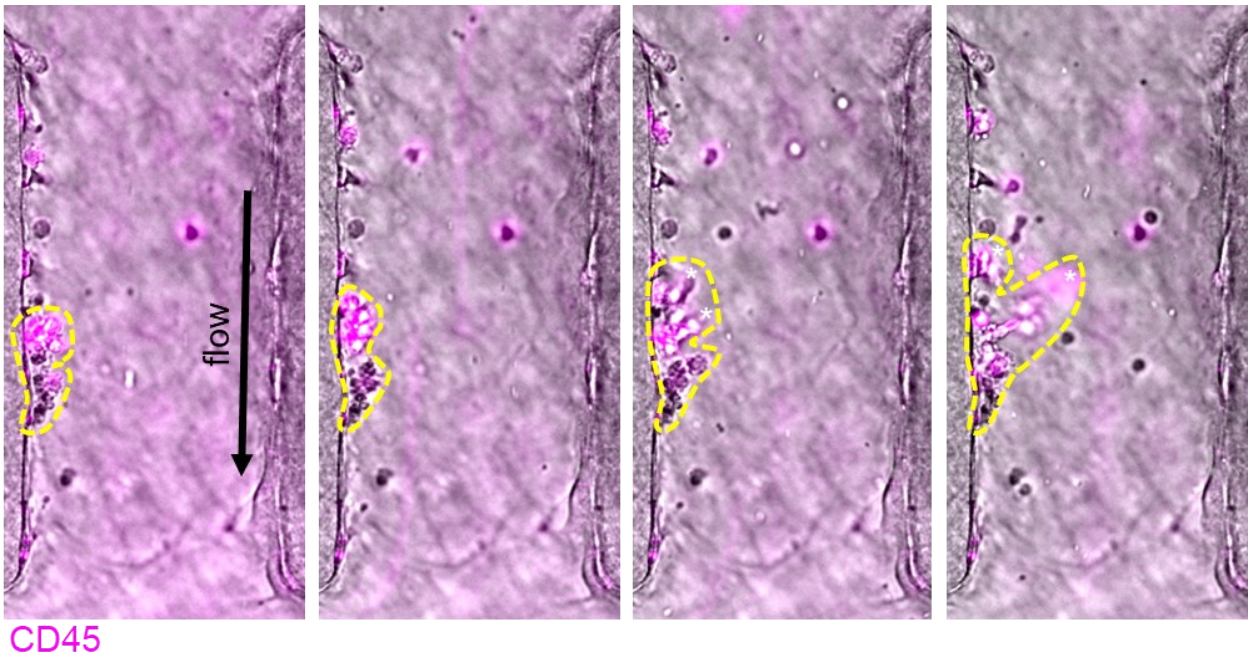


**Figure 2.4 Leukocyte tethering and rolling in Swe$^{+/+}$ CM treated microvessels.**

Time-lapse images show a cluster of isolated leukocytes bound to activated HBMEC microvessels under flow (black arrow). The leukocytes tether and roll (yellow dashed outline) on activated ECs against the direction of flow.

### *2.4.5 Knocking out APP and inhibiting the beta-secretase enzyme BACE1 with a small molecule inhibitor (BACEi) attenuate endothelial cell activation and VWF release*

To test whether the increased level of Aβ in our APPSwe CM is a driving factor for endothelial activation, we perfused microvessels with CM from Swe$^{+/+}$, Swe$^{+/WT}$, and Swe$^{WT/WT}$ hiPSC-CNs treated with a BACE1 inhibitor (BACEi). BACEi inhibits BACE1 function and prevents the amyloidogenic cleavage of APP into Aβ$^{170,171}$ (Figure. 2.5 **A**). CM was collected from cultures of hiPSC-CNs after treatment with either BACEi (25 nM) or vehicle control (DMSO) for 72 h (Figure. 2.5 **B**). ELISA measurements showed a statistically significant 44% decrease in Aβ 1–42 levels (DMSO: 170 pg/mL, BACEi: 75.4 pg/mL) and 45% decrease in Aβ 1–40 levels (DMSO: 1504 pg/mL, BACEi: 683 pg/mL) in Swe$^{+/+}$ BACEi treated cultures compared to DMSO controls

(Figure. 2.5 **C**). In $Swe^{+/WT}$ cultures, BACEi treatment led to a statistically significant 38% decrease in both Aβ 1–42 (DMSO: 101 pg/mL, BACEi: 38.1 pg/mL) and 1–40 (DMSO: 794 pg/mL, BACEi: 298 pg/mL) levels compared to controls. In $Swe^{WT/WT}$ cultures, BACEi treatment led to a 28% reduction in Aβ 1–42 levels (DMSO: 32.4 pg/mL, BACEi: 9.14 pg/mL) and 26% reduction in Aβ 1–40 levels (DMSO: 264 pg/mL, BACEi: 69.1 pg/mL).

Furthermore, perfusion of cerebral microvessels with $Swe^{+/+}$ and $Swe^{+/WT}$ BACEi CM led to the formation of only a few VWF fibers, in contrast to the significantly larger number of fibers in $Swe^{+/+}$ and $Swe^{+/WT}$ DMSO CM conditions (Figure. 2.5 **D**). Quantification of the fiber number in each media condition confirms this consistent and significant decrease across multiple replicates in BACEi treated conditions compared to the corresponding DMSO controls (Figure. 2.5 **F**). In our $Swe^{WT/WT}$ control line, there was little to no fiber formation in both the BACEi and DMSO conditions as expected (Figure. 2.5 **D**).

To test whether VWF fibers would form in the presence of neuronal secretomes but in the complete absence of Aβ or other components of amyloidogenic APP processing, CM was collected from APPKO hiPSC-CNs (Young et al., 2018). Analysis of Aβ 1–42 and 1–40 levels showed that CM from the APPKO line did not secrete detectable levels of Aβ peptides as expected (Figure. 2.5 **C**). When APPKO CM was perfused through brain microvessels, no transluminal VWF fibers were observed in the vessel lumen (Figure. 2.5 **E** and **F**).

Notably, the number of VWF fibers in the HBMEC microvessels appears to have a positive linear correlation with the levels of Aβ 1–42, across all the media groups (Figure. 2.5 **G**). For example, $Swe^{+/+}$ DMSO CM had Aβ 1–42 levels of 170 pg/mL and led to maximal fiber production of, on average, 45 VWF fibers per vessel. In contrast, $Swe^{+/WT}$ DMSO CM had 41% less Aβ 1–42 (101 pg/mL) and 46% less average VWF fiber production (24 VWF fibers per vessel) compared to

Swe$^{+/+}$ DMSO CM, demonstrating a strong correlation between Aβ 1–42 levels and VWF fiber production (Figure. 2.5 **G**).

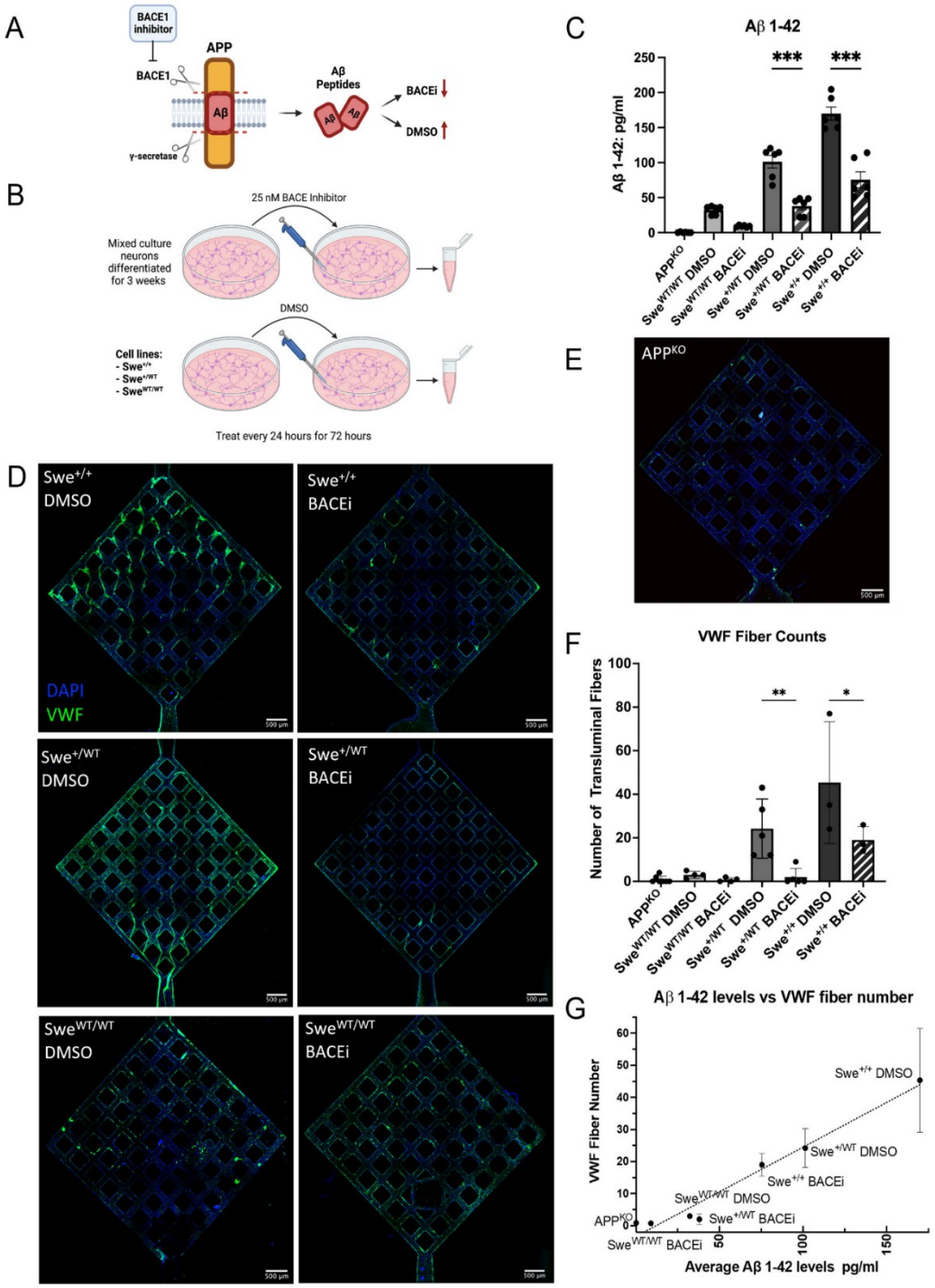


**Figure 2.5 CM collected from BACE1 inhibitor (BACEi) treated neurons or APPKO neurons cause reduced VWF fiber formation in 3D microvessels**

(A) BACEi mechanism of action. BACEi inhibits BACE1 cleavage of APP and results in decreased production amyloidogenic Aβ peptides. (B) Schematic overview showing CM collection from APPSwe neurons treated with BACEi or a DMSO vehicle control. BACEi CM and DMSO control CM were collected from CN differentiated from $Swe^{WT/WT}$, $Swe^{+/WT}$, and $Swe^{+/+}$ hiPSCs. (C) ELISA measurements confirm the reduction of pathogenic Aβ 1–42 production in BACEi and APPKO conditions compared to the DMSO control. n = 3 biological replicates per condition. (D) Representative immunofluorescent images of 3D microvessels after perfusion with CM collected from $Swe^{WT/WT}$ neurons treated with DMSO (bottom left), $Swe^{WT/WT}$ neurons treated with BACEi (bottom right), $Swe^{+/WT}$ neurons treated with DMSO (middle left), $Swe^{+/WT}$ neurons treated with BACEi (middle right), $Swe^{+/+}$ neurons treated with DMSO (top left), and $Swe^{+/+}$ neurons treated with BACEi (top right). BACEi CM results in a significant reduction in transluminal VWF fiber formation (VWF, green). Scale bars: 500 μm. (E) Representative IF image of 3D microvessels after perfusion with CM collected from APPKO neurons. VWF transluminal fibers are absent from microvessels. Scale bars: 500 μm. (F) Quantification of transluminal fibers present in the microvessels. The number of transluminal fibers is significantly reduced in BACEi CM treated microvessels compared to the number of fibers formed in DMSO CM treated microvessels. n = 4 biological replicates. (G) Association between average Aβ 1–42 peptide levels and average VWF fiber number. Dotted black line is a linear least squares regression fit to the data points that shows a strong positive linear correlation (R-squared = 0.966, P value <0.001). All plots: error bars, mean ± SEM. *p < 0.05, **p < 0.01, and ***p < 0.001 by two-way ANOVA with Tukey's correction for multiple comparisons test (C), linear regression (G), or one-way ANOVA with Šídák's correction for multiple comparisons test.

Next, we performed immunoprecipitation (IP) of Aβ peptides in $Swe^{+/+}$ and $Swe^{WT/WT}$ CM to investigate whether the presence of Aβ peptides in $Swe^{+/+}$ was necessary for inducing EC activation and VWF fiber formation in engineered brain microvessels. Aβ peptides in $Swe^{WT/WT}$ and $Swe^{+/+}$ CM were precipitated using the anti-Aβ 6E10 antibody. An ELISA assay following IP confirmed successful removal of Aβ peptides from $Swe^{+/+}$ and $Swe^{WT/WT}$ CM (Figure. 2.6 **A**). Next, control $Swe^{WT/WT}$ and $Swe^{+/+}$ CM (control CMs) and immunoprecipitated $Swe^{WT/WT}$ and $Swe^{+/+}$ CM (IP CMs) were perfused in engineered brain microvessels. VWF staining in the microvessels revealed a reduced number of fibers formed in $Swe^{+/+}$ IP CM compared to its $Swe^{+/+}$ control CMs (Figure. 2.6 **B**). Furthermore, perfusion of both $Swe^{WT/WT}$ control and IP CMs resulted in a lack of VWF fibers, further supporting that Aβ peptides were an important component of the CM for inducing EC activation and VWF fiber formation (Figure. 2.6 **B**). Taken together, the number of fibers formed in BACEi treatment, APPKO CM perfusion and Aβ-depleted CM

perfusion relative to Aβ peptide levels suggest that Aβ is an essential component of the CM for inducing EC activation and VWF fiber formation in engineered cerebral microvessels.

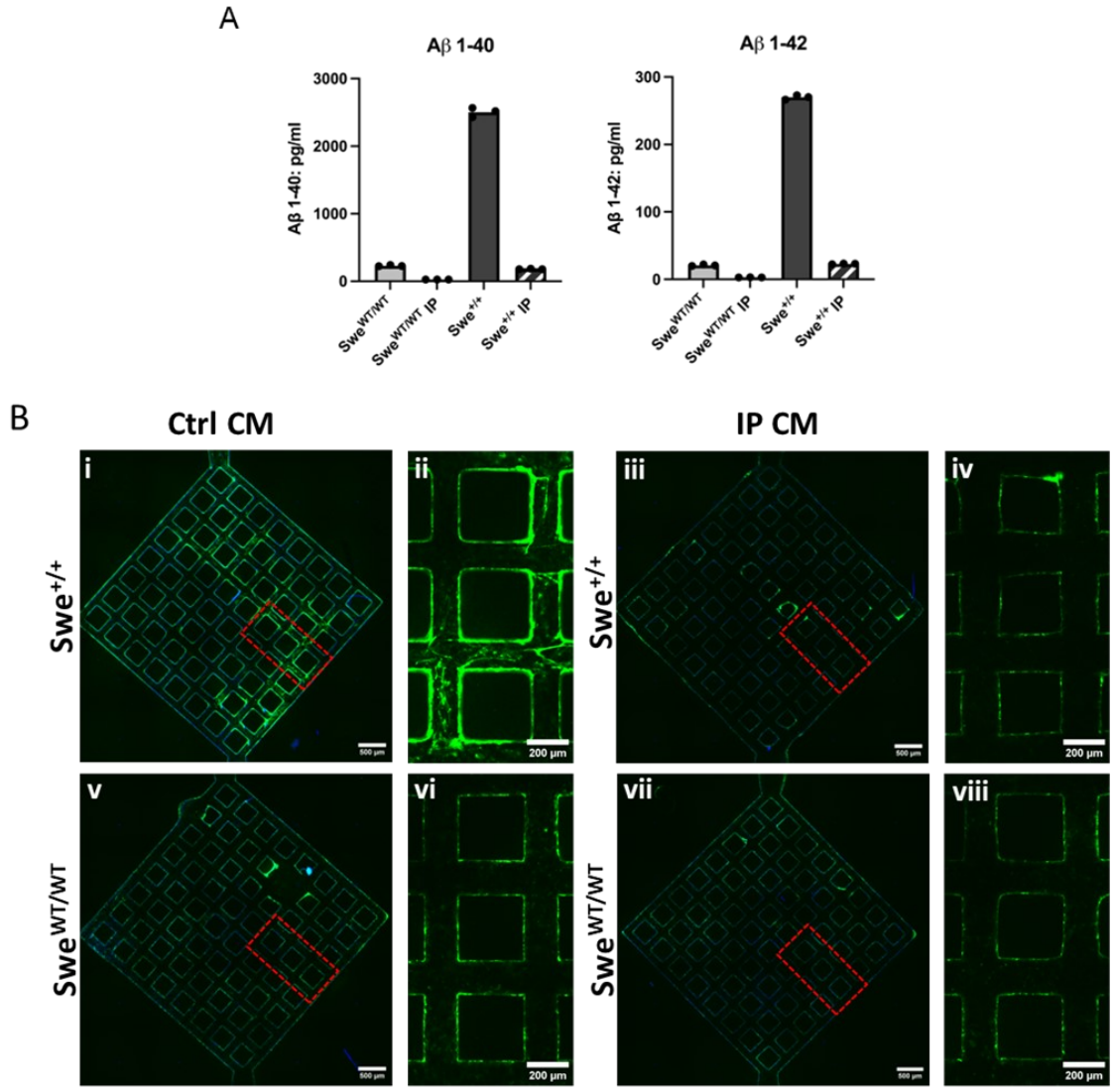


**Figure 2.6 Immunoprecipitation of Aβ in CM shows decreased Aβ levels in IP CMs and decreased vWF fiber formation in 3D microvessels.**

(A) ELISA results show removal of Aβ in immunoprecipitated $Swe^{WT/WT}$ and $Swe^{+/WT}$ CM (IP CM), compared to their control $Swe^{WT/WT}$ and $Swe^{+/+}$ CM (ctrl CM), leads to reduction in Aβ 1-40 and Aβ 1-42 levels. (B) Perfusion of ctrl CM (i,ii,v and vi) and IP CM (iii, iv, vi and viii) shows vWF fiber formation in $Swe^{+/+}$ Ctrl CM perfused microvessel (i and ii) which is absent in $Swe^{+/+}$ IP CM perfused microvessels (iii and iv). Red dotted box denotes zoomed in regions shown in ii, iv, vi and viii.

### *2.4.6 Analysis of pro-inflammatory cytokines and pTau from the neuronal secretome further supports increased Aβ levels as a primary factor in endothelial cell activation*

To determine whether secretion of pro-inflammatory cytokines into our CM acts as a confounding factor driving EC activation, independent of Aβ, we performed a multiplexed cytokine ELISA assay. We screened untreated CM from APPKO, $Swe^{WT/WT}$, $Swe^{+/WT}$, and $Swe^{+/+}$ hiPSC-CNs and CM from DMSO and BACEi treated $Swe^{WT/WT}$, $Swe^{+/WT}$, and $Swe^{+/+}$ hiPSC-CNs. APPKO CNs were not treated with DMSO or BACEi due to the lack of APP production and therefore were not included in those analyses. Our cytokine panel included 9 pro-inflammatory cytokines and chemokines: TNF-α, IP-10, IL-8, IL-6, IL-15, IL-1β, IFN-β, IFN-α2a, and Eotaxin.

We observed that there was no trend toward increased cytokine secretion in untreated $Swe^{+/+}$ and $Swe^{+/WT}$ CM as compared to $Swe^{WT/WT}$, or APPKO for any of the measured cytokines (Figure. 2.7). This suggests that the increased number of VWF fibers observed in microvessels treated with Swe+/+ and Swe+/WT CM was not driven by the cytokines present in CM. Surprisingly, for the majority of cytokines, IP-10, IL-8, IL-6, IFN-β, IFN-α2a, and Eotaxin, the highest cytokine levels were observed in our control CM ($Swe^{WT/WT}$ or APPKO). Additionally, across all measured cytokines, we saw no trend suggesting BACEi CM had decreased cytokine levels compared to DMSO CM (Figure. 2.7).

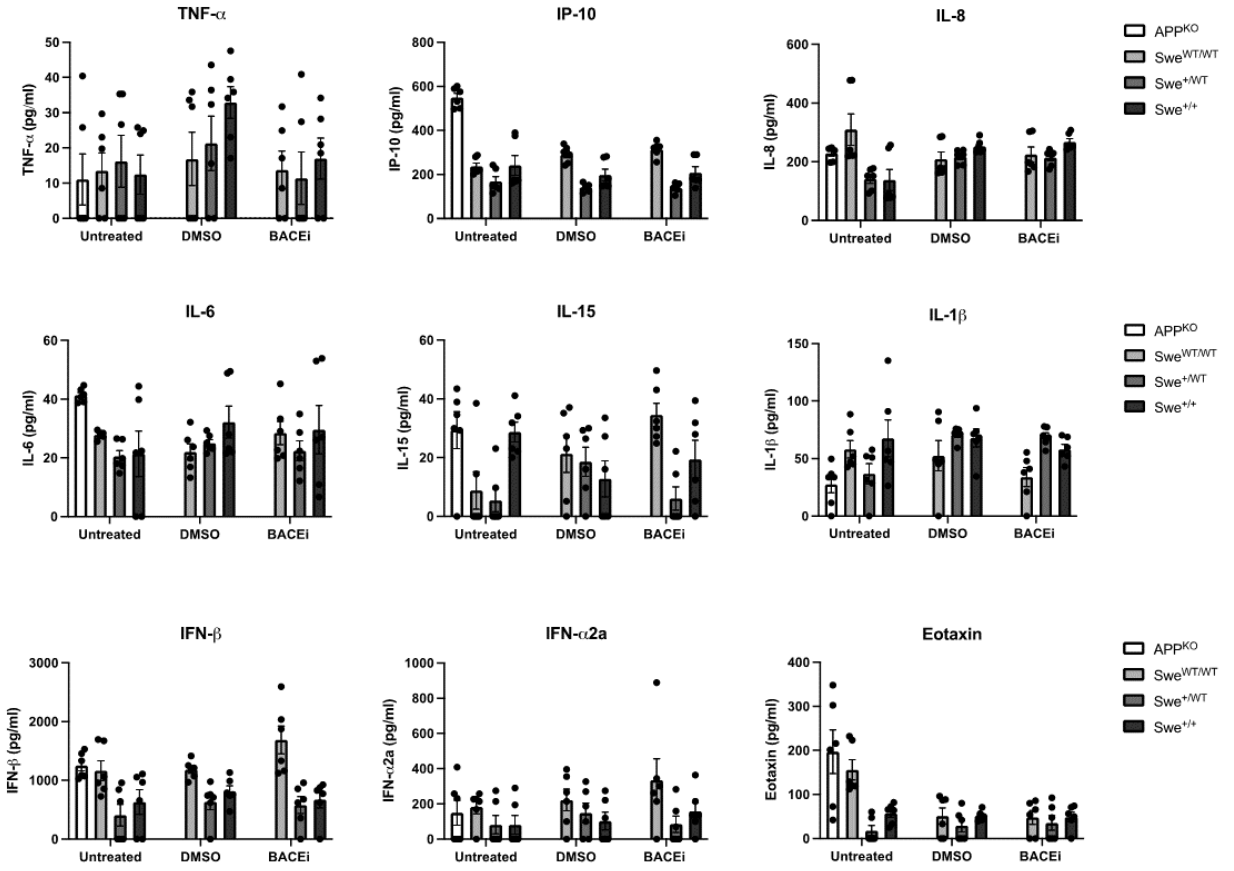


**Figure 2.7 ELISA measurement of pro-inflammatory cytokines reveals no correlation between cytokine secretion and APPSwe genotype or BACEi treatment**

A multiplexed ELISA assay was used to test CM for levels of 9 pro-inflammatory cytokines: (A) TNF-α, (B) IP-10, (C) IL-8, (D) IL-6, (E) IL-15, (F) IL-1β, (G) IFN-β, (H) IFN-α2a, and (I) Eotaxin. Cytokine levels were measured in untreated APPKO, $Swe^{WT/WT}$, $Swe^{+/WT}$, and $Swe^{+/+}$ CM. Cytokine secretion was also measured in CM from DMSO and BACEi treated $Swe^{WT/WT}$, $Swe^{+/WT}$, and $Swe^{+/+}$ hiPSC-CNs (APPKO CNs were not treated with DMSO or BACEi and were not included). Across all cytokines, CM from the untreated group did not show an increase in cytokine levels with increasing APPSwe mutation copy number ($Swe^{WT/WT}$ vs. $Swe^{+/WT}$ vs. $Swe^{+/+}$). In DMSO vs. BACEI CM conditions, across all cytokines, there is no observed decrease in cytokine levels in BACEi CM compared to DMSO CM levels. N=3 biological replicates and two technical replicates per condition. Error bars, mean ± SEM.

To rule out secreted phosphorylated tau (pTau) as a potential driver of the EC activation, we performed a pTau and total Tau (tTau) ELISA assay to quantify pTau levels in our CM. We screened media from APPKO, $Swe^{WT/WT}$, $Swe^{+/WT}$, and $Swe^{+/+}$ hiPSC-CNs. We found that pTau secretion into the CM was negligible for all of the measured lines and the levels of pTau within CM did not

correlate with the EC activation we observed in microvessels treated with $Swe^{+/+}$ and $Swe^{+/WT}$ CM (Figure. 2.8).

Overall, we conclude that that the APPSwe mutation does not drive increased pro-inflammatory cytokine secretion from neuronal cultures, treatment of CNs with a BACEi does not lead to reduced cytokine secretion, and pTau secretion in conditioned media is negligible across all lines and does not correlate with EC activation. Taken together, our results suggest that the endothelial activation observed in our studies is strongly correlated to the Aβ levels in neuronal secretomes.

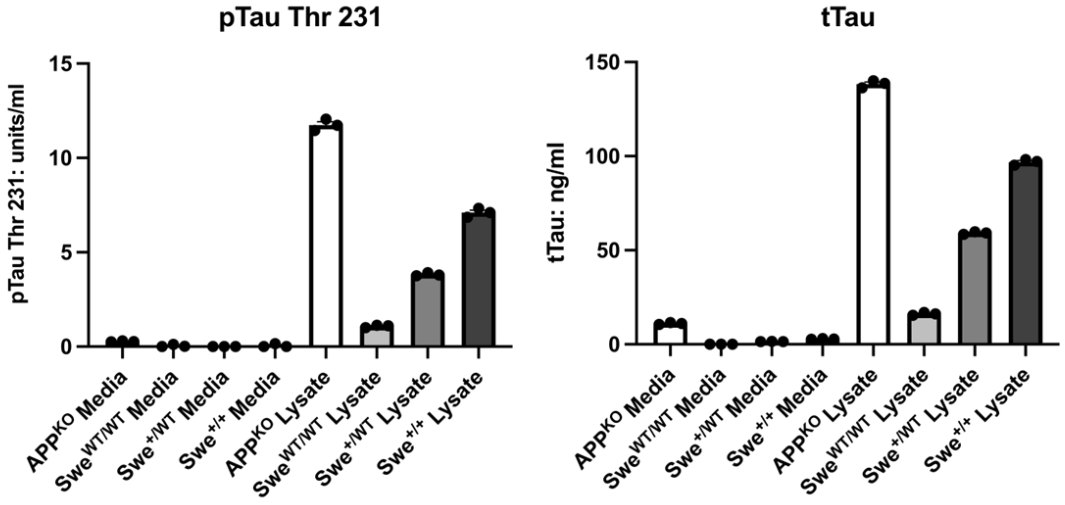


**Figure 2.8 ELISA measurement of pTau and tTau levels in CM and lysates demonstrates minimal pTau secretion into CM across all cell lines.**

pTau levels were measured in APPKO, $Swe^{WT/WT}$, $Swe^{+/WT}$, and $Swe^{+/+}$ CM and cell lysates using a pTau Thr231/tTau ELISA (left panel). In all cell lines screened, there was negligible secretion of pTau measured in the CM. Differences in pTau levels in cell lysates are explained by the corresponding levels of tTau from each measured line (right panel). N=3 technical replicates per condition. Error bars, mean ± SEM.

## 2.5 Discussion and Conclusion

AD research has traditionally been focused on neuronal and glial dysfunction. Despite evidence of vascular contributions that precede the clinical diagnosis of AD, endothelial alteration in AD has been relatively poorly explored, partly due to the lack of proper humanized models. In this study, we used hiPSC-derived neurons harboring the APPSwe mutation, together with primary HBMECs and engineered 3D brain microvessels to investigate AD-associated vascular dysfunction. We validated that $Swe^{+/+}$ mutation led to a higher concentration of Aβ deposition in CM compared to $Swe^{WT/WT}$ control. The measured Aβ levels were in the picomolar range, which is more physiologically relevant than micromolar concentrations of exogenous Aβ peptides often applied[146–148]. We demonstrated that these AD-mimicking CM caused transcriptomic and phenotypic upregulation of adhesion molecules in HBMECs. Perfusion of this high Aβ-containing $Swe^{+/+}$ CM in 3D microvessels elicited rapid endothelial activation, following 1-h treatment of brain microvessels, characterized by the formation of prothrombotic VWF fibers and leukocyte binding on vessel lumen. Inhibiting Aβ production in APPSwe with a BACE1 inhibitor or APPKO attenuated the endothelial activation.

Our findings show a threshold level of neuronally secreted Aβ peptide that leads to endothelial cell activation and acute VWF release and fiber formation. This process could serve as an early source of vascular dysfunction in AD. Measuring plasma Aβ as a biomarker for AD has produced conflicting results in the literature throughout the different stages of AD pathogenesis[172–175]. Although plasma and CSF levels of Aβ are decreased in some AD patients compared to healthy individuals[176,177], the majority of FAD patients develop CAA, a condition characterized by Aβ deposits along the small vessels in the brain[131]. This suggests an increase in circulating Aβ levels at or prior to the disease onset, which may increase endothelial activation, induce pro-coagulative

states, disrupt cerebral blood flow and increase immune cell activation, all of which can further induce deposition of Aβ in cerebral blood vessels. The increased deposition of Aβ, as Aβ fibrils and plaques along the vessel wall, could be a reason for the decreased plasma and CSF Aβ.

Our results suggest that neuronally derived Aβ peptides can drive the EC activation and dysfunction in otherwise healthy vessels. We show that the APPSwe mutation in our hiPSC-CNs led to increased Aβ 1–42 and Aβ 1–40 peptide secretion in a genotype-dependent manner (Figure. 2.1 **C**). Because the amounts of Aβ we measure from our CM are in the ng/mL concentrations, this suggests that even small amounts of pathogenic Aβ peptides may lead to significant changes in vascular structure and function, which can occur early in disease progression, prior to the formation of higher-order Aβ assemblies. Our observations support increasing evidence that vascular dysfunction may precede the onset of pathophysiological and cognitive symptoms in AD[46]. Our results also support that Aβ peptides may be involved early in AD pathogenesis.

AD-related changes in brain vasculature are associated with responses to inflammatory signals, oxidative stress, adaptive immune responses, and upregulation of endothelial adhesion molecules[36,41,178–180]. In particular, endothelial VCAM-1 expression[180] and increased binding of lymphocytes to VCAM-1 in the brains of AD patients[181] emphasize the role of endothelial adhesion molecules in AD. Using RNAseq, we revealed that endothelial cells respond to paracrine signals from neurons of $Swe^{+/+}$ FAD mutation by enhancing expression of genes associated with inflammatory responses and immunoadhesion. E-selectin, ICAM-1 and VCAM-1, precursor genes for adhesion molecules in endothelial cells, were significantly upregulated in HBMECs treated with $Swe^{+/+}$ CM. Increased expression of adhesion molecules can recruit circulating leukocytes in inflamed vessel lumens and assist infiltration of immune cells to the CNS compartment. Facilitating neutrophil recruitment to the CNS via adhesion molecules can promote activation of

microglia and astrocytes and initiate neuroinflammation and neuronal damage[182]. CCL2 was also significantly upregulated in $Swe^{+/+}$ CM treated HBMECs which can elicit endothelial retraction and breakdown of the blood-brain barrier, allowing for the accumulation of neurotoxic chemokines and plasma proteins[183]. Our transcriptional analysis highlights the molecular connection between pathogenic Aβ levels, vascular inflammation, and hemodynamic dysfunction. As vascular inflammation manifests in the early stages of AD neuropathology, the inflammation cycle may exacerbate AD pathology and augment cognitive impairment.

We showed, for the first time, that perfusion of Aβ-rich CM through 3D human brain microvessels can promote acute release of VWF from endothelium and formation of ultra-large transluminal fibers in the 3D vessel lumen. We show a strong linear correlation between Aβ levels in the CM and the number of transluminal VWF fibers in 3D microvessels. Perfusion of $Swe^{+/+}$ CM with high Aβ concentrations led to large VWF fiber formation and high level of platelet binding. Attenuated Aβ 1–42 and Aβ 1–40 levels in CM with BACE1 inhibition in APPSwe CNs significantly reduced VWF fiber formation in 3D human brain microvessels. CM from APPKO CNs with no detectable secretion of Aβ 1–42 and Aβ 1–40, correspondingly led to no transluminal VWF fiber formation in vessels. Pro-inflammatory cytokine levels in our APPSwe CM did not increase in a genotype-dependent manner or decrease upon BACEi treatment, suggesting that proinflammatory cytokine secretion is not a key driver of the EC activation we observed. These data demonstrate a strong correlation between concentrations of Aβ, endothelial VWF release, and endothelial activation in human brain microvessel models.

VWF is a multimeric protein that is released from WPB either constitutively from quiescent ECs, or acutely during acute activation of ECs[136,184]. Upon release from WPB, VWF unfurls its multimeric structures into elongated strings under flow, exposing crosslinking sites to bind

platelets and assemble into its ultra-large fiber structure[185]. Although how Aβ initiates WPB exocytosis is not in the scope of this work, past studies shed light on possible calcium-dependent mechanisms of Aβ induced WPB release. Transient exposure of Aβ 1–40 has been linked with disruption of calcium homeostasis in brain endothelial cells[186,187]. Short-term treatment of Aβ in rat brain endothelial cells has been found to increase mitochondrial and cytosolic calcium release[188], which could promote exocytotic formation and exocytosis of WPBs[189,190]. Release of VWF leads to fiber formation within the vessel lumens that attract platelets, bind directly to P-select glycoprotein ligan-1 on polymorphonuclear leukocytes, and recruit leukocytes for subsequent diapedesis and promote inflammatory and thrombotic events[191,192]. By comparing the perfusion outcomes of $Swe^{+/+}$ CM with $Swe^{WT/WT}$, $Swe^{+/WT}$ and that with BACEi treatment and APPKO media, our results demonstrated that Aβ peptides are an important component of the CM leading to EC activation. Future human studies are needed for remaining questions such as whether there is an Aβ concentration threshold below which EC activation will not occur and above which EC dysfunction will be initiated. Understanding the minimum Aβ peptide levels required to cause EC dysfunction could help inform therapeutic strategies for AD. Overall, the results of our study have enhanced our understanding of the role of Aβ in the EC dysfunction in AD.

We have established a 3D perfusable cerebral vascular model here to investigate luminal dysfunction caused by trophic factors released from brain parenchyma in AD patients. The simplicity of only including ECs in our 3D brain vascular model allows us to identify how ECs are specifically regulated by the pathogenic Aβ released from brain parenchyma of AD patients. ECs are known to be equipped with the abluminal expression of Aβ efflux transporters such as low-density lipoprotein receptor-related protein 1 and 2 mediate elimination of Aβ from brain

parenchyma to the plasma[193,194]. Moreover, BBB breakdown accompanying AD progression facilitates introduction of CNS secreted pathogenic Aβ peptides on the luminal side of ECs[195].

There are several limitations remaining in this study. Here, we posit that BACEi inhibition and subsequent Aβ reduction leads to diminished endothelial activation. It is also believed that other cleavage products generated through the amyloidogenic cleavage of APP may be inhibited by BACE1 inhibition (secreted APPβ (sAPPβ), β carboxyterminal fragment (βCTF), and amino-terminal APP intracellular domain (AICD)). The effect of these fragments on the endothelium has not been studied[170,196,197] and was not examined here. This should be evaluated in future studies to better understand the effect of other APP cleavage products on endothelial cell function. In addition to Aβ 1–40 and Aβ 1–42, truncated fragments of Aβ such 4–40 and 4–42, may also be contributing to the EC activation we observed. Further work to interrogate which fragments of Aβ specifically drive EC activation, would be beneficial in expanding our understanding of Aβ mediated vascular activation. Furthermore, although we have only investigated paracrine signaling from cortical neurons with APPSwe mutation, investigation of CM obtained from BBB relevant cell types like astrocytes and microglia could provide an extensive understanding of the role of other CNS cell types in AD vascular dysfunction. While we utilized the FAD APPSwe mutation, 90% of AD patients are suffering from a sporadic form of the disease and FAD is rare. Genetic studies of SAD have identified approximately two dozen associated candidate genes[161,197]. Incorporating these genes into the model described here could help advance our understanding of vascular changes in sporadic AD. Finally, future studies should incorporate all relevant cell types present in the BBB. Building a comprehensive BBB model and investigating cell type specific effects on the endothelium will lead to an in-depth understanding of how cerebrovascular dysfunction occurs in AD patients.

## 2.6 Supplementary Figure

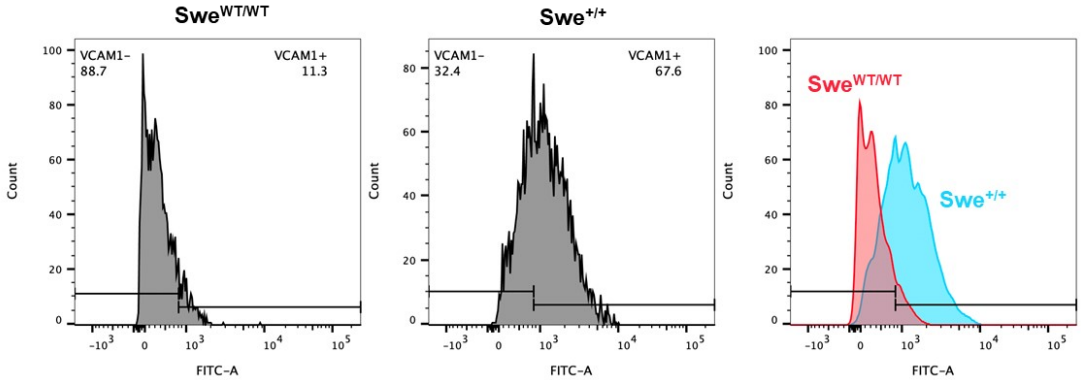


**Supplementary Figure S2.1 Flow cytometry analysis of VCAM-1 (FITC) expression on HBMECs.**

2D HBMECs treated with $Swe^{WT/WT}$ CM and $Swe^{+/+}$ CM at 37 °C for 24 hours were stained with VCAM-1 analyzed with flow cytometry. HBMECs treated with $Swe^{+/+}$ CM results in enhanced expression of VCAM-1.

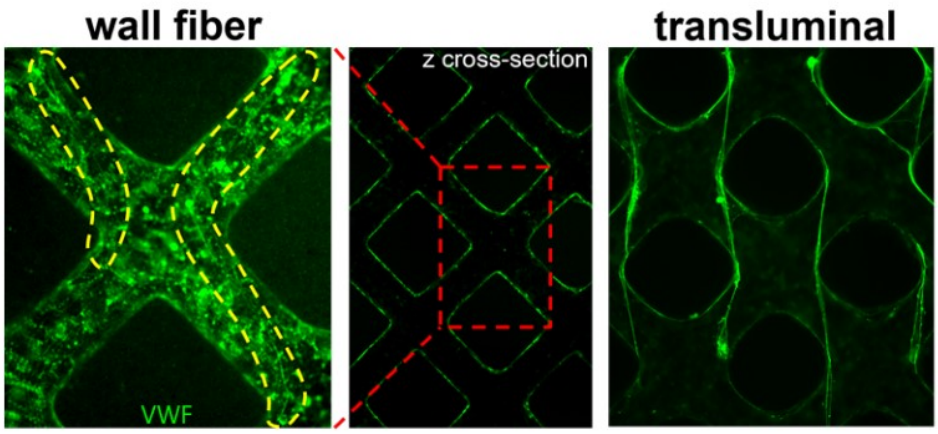


**Supplementary Figure S2.2 Identification of wall and transluminal fibers following CM perfusion in microvessels.**

Wall fibers are classified as fibers found on the surface of endothelial cells that line the microvessels. Transluminal fibers are classified as thick fibers present across the lumen of the microvessels.

# Chapter 3: Predictive Identification of Kinase Targets for Endothelial Barrier Stabilization in Traumatic Brain Injury Using a 3D Perfusable Brain Endothelial Barrier Model.

## 3.1 Abstract

Traumatic brain injury (TBI), Traumatic brain injury (TBI), a sudden external trauma to the brain, is a leading cause of death in young adults. TBI-associated coagulopathy is a significant risk factor for secondary brain damage, initiating with the rapid deterioration of the blood-brain barrier (BBB). Stabilizing the brain endothelial barrier, therefore, represents a crucial strategy to reduce neuroinflammation in TBI. In this study, we employed a kinase regression (KiR) model and 3D-engineered brain endothelial barrier (BEB) microvessels to identify key kinase targets that modulate barrier integrity following TBI. We treated BEB microvessels with 12 kinase inhibitors (KIs) previously linked to barrier modulation, measuring permeability coefficients and applying these results in KiR analysis to pinpoint kinases that protect or disrupt BBB function. By perfusing serum samples from TBI patients, we simulated BBB breakdown in engineered brain microvessels and observed that barrier-protective KIs restored cadherin junctions lost due to TBI plasma exposure. Our findings demonstrate that kinase polypharmacology and regression modeling can efficiently identify kinase targets that rapidly stabilize the BBB, as shown by improved barrier function in predicted kinase inhibitors within our thrombin- and TBI plasma-treated BEB model. We further show that 3D microvessels can facilitate drug screening and validation with a focused selection of compounds, providing a promising approach for drug repurposing in BBB protection.

## 3.2 Introduction

Brain microvascular endothelial cells are a central component of the blood-brain barrier (BBB), responsible for providing a higher level of barrier modulation through intercellular tight junctions and adherens junctions that limit paracellular transport, and endothelial transporters that selectively restrict transcytosis. The brain endothelial barrier (BEB) necessitates precise regulation of the flux of solutes and macromolecules from the plasma into the central nervous system (CNS) parenchyma, as many circulating factors and constituents of blood plasma are neurotoxic and can lead to injury and degeneration of various CNS cell types. Activation of endothelial cells, whether caused by direct insults to the BBB — such as physical trauma — or by heightened inflammatory signals within the brain's vasculature, can lead to substantial endothelial dysfunction, compromise the integrity of the BEB, and result in edema in the brain parenchyma.

Traumatic brain injury (TBI) is a devastating condition caused by external physical trauma to the brain, leading to both primary and secondary cerebral and systemic injuries. TBI is categorized into two phases: primary injury, which results in physical damage to the brain's structure, causing hemorrhage and contusion, and secondary injury, characterized by cerebral edema and inflammation, which is a high-risk factor for further brain damage. Secondary injury begins with the rapid deterioration of the BBB. Acute coagulopathy and endotheliopathy from secondary injury are particularly associated with poor clinical outcomes in TBI patients. One of the many factors that exacerbate secondary injury is the disruption of the BBB, which occurs within a few hours of the primary injury and is a major risk factor for high mortality and morbidity. Therefore, stabilizing the brain endothelial barrier is crucial for reducing secondary brain damage and neuroinflammation in TBI. However, despite emerging treatment strategies showing promise in modifying BBB-mediated injury, there is a lack of accepted therapeutic protocols for preventing

or treating secondary damage resulting from BBB breakdown. Further research into BBB breakdown following TBI may identify novel targets for clinical intervention.

The kinase signaling pathway is a key regulator of endothelial barrier permeability. Kinases are involved in both barrier-restorative and barrier-strengthening pathways, making it challenging to identify specific kinase targets that selectively promote barrier restoration. For example, Src family kinases (SFKs) play a dual role in barrier modulation; the phosphorylation of VE-cadherin (VECAD), a major adherens junction protein in endothelial cells, leads to the internalization and destabilization of junctions in response to inflammatory signals. However, certain SFKs also contribute to barrier restoration following thrombin-mediated activation of endothelial cells and are activated by barrier-strengthening mediators like sphingosine-1-phosphate. Additionally, kinases regulate cell-matrix junctions through focal adhesion kinase, which modulates integrin interactions with the extracellular matrix (ECM) and influences endothelial actomyosin structural changes. The contrasting roles of various kinase families in endothelial barrier regulation emphasize the need to understand their specific contributions more deeply. This is particularly important because many kinase pathways are involved in both the disruption and stabilization of endothelial barriers. Determining the precise roles of individual kinases in barrier function is complex, as some kinases can be activated by both barrier-strengthening and barrier-weakening stimuli. Therefore, a systems biology approach may be necessary to delineate these roles accurately.

The kinase regression (KiR) approach, which employs machine learning algorithms to identify kinase pathways based on specific biological phenotypes, has gained significant traction in recent years. This method relies on experimental kinase activity profiling, in which a panel of kinase inhibitor compounds is screened against recombinant protein kinases. KiR facilitates a detailed

interrogation of kinase pathways. Although KiR assays have been used in 2D models to investigate endothelial properties — particularly in response to inflammatory signals and their phosphorylation dynamics over time — their application in 3D vessel models, including functional parameters such as permeability and validation of predicted targets in disease-specific contexts, remains unexplored. This computational biology-driven approach, using machine learning to identify kinase pathways, is increasingly favored for its potential to advance research in more complex biological systems.

In this chapter, we integrate tissue engineering and computational approaches to combine a functional experimental readout, the permeability index, with a kinase regression model based on kinase activity profiling. This integration allows us to predict kinase targets that will stabilize the endothelial barrier. We first engineer a functional BEB model to investigate barrier integrity in response to pharmacological agents and injury-inducing molecules, quantifying changes in BEB integrity through a permeability assay. The permeability index is then incorporated into an elastic net-regularized kinase regression model to predict and test new classes of kinase inhibitors that may enhance barrier integrity following TBI-mimicking injury. Our approach identifies six potential kinase inhibitors with barrier-stabilizing effects. Furthermore, our findings reveal that at least two classes of these drugs are effective in mitigating the injury response and reducing endothelial activation in response to both thrombin and patient plasma, suggesting their therapeutic potential.

## 3.3 Methods

### *3.3.1 Human brain microvascular endothelial cell (HBMEC) culture*

Primary HBMECs (Cell Systems, Cat# ACBRI 376, passage 3) were cultured in EGM-2 Basal Medium (CC-3156) supplemented with EGM-2MV Microvascular Endothelial Cell Growth Medium SingleQuots (Lonza, CC-4147) at 37°C and 5% CO2. HBMECs were maintained as monolayers in tissue culture flasks coated with Attachment Factor (CC# 4Z0–210; cell systems) with media replacement every 3 days until seeding in 3D microvessels. HBMECs were used within passage number 4-7 for all experiments.

### *3.3.2 3D brain endothelial barrier (BEB) model fabrication*

The 3D BEB model was fabricated by engineering microvessels seeded with HBMECs, as previously reported (Zheng et al., 2012). Briefly, microvessels were fabricated using soft lithography and collagen injection molding, utilizing a hexagon network PDMS stamp (channel diameter: 100 μl). A 7.5 mg/ml collagen solution was prepared using a 15 mg/ml stock of rat tail collagen I reconstituted in 0.1% acetic acid. The stock collagen solution was diluted, neutralized, and solute-balanced to a working solution of 7.5 mg/ml collagen using 1N NaOH, 10x Mx199 media, and EGM2-MV.

Fabrication of the microvessels was performed by injecting the working collagen solution into the gel-loading portion of an acrylic jig. The top acrylic jig was placed on a hexagon-branched patterned polydimethylsiloxane (PDMS) stamp to generate a negative pattern on the gelled collagen. To generate a flat-bottomed collagen piece, the working collagen solution was injected on top of the bottom acrylic jig containing a glass coverslip and pressed down with a flat PDMS stamp. Both the top and bottom jigs were incubated at 37°C for 1 hour to allow the collagen to

crosslink. Following gelation, the respective PDMS stamps were removed from each acrylic jig. The top acrylic jig, containing the negative pattern of the PDMS, was placed on top of the bottom acrylic jig containing the flat collagen layer, and the two were screwed together to form a seal. The assembled acrylic jig was placed on cotton to elevate the inlet side of the microvessel jig. EGM2-MV media was then applied to the inlet jig to allow perfusion through the network. The assembled acrylic jig was incubated at 37°C for 1 hour to allow further crosslinking between the top and bottom collagen layers prior to seeding with HBMECs.

To generate the BEB model, the assembled microvessels were seeded with HBMECs by trypsinizing cells from tissue culture flasks. Cells were collected in EGM2-MV media at a concentration of 7-10 x $10^6$ cells/mL. A 10 µl cell suspension was perfused through the inlet of the microvessels. Seeded microvessels were incubated at 37°C and 5% $CO_2$. The medium was refreshed every 12 hours to allow for gravity-driven flow through the microvessel networks. The BEB microvessels were fed twice daily for 7 days before use in perfusion studies.

*3.3.3 Plasma, thrombin and kinase inhibitor preparation and permeability measurements*

Permeability measurements were conducted on resting and injured D7 BEB microvessels after treatment with TBI patient plasma, normal plasma, thrombin, and/or kinase inhibitors. One day prior to the permeability measurements, D6 BEB microvessels were perfused with 70 kDa FITC-dextran (100 mg/mL in EGM-2MV growth media) or 500 kDa TRITC-dextran (100 mg/mL in EGM-2MV growth media) to assess the permeability of the microvessels prior to kinase inhibitor (Selleck Chemicals) treatments, establishing a baseline measurement of the permeability of engineered BEB microvessels. Permeability measurements were obtained by perfusing the dextran solution through the BEB microvessels with a hydrostatic pressure drop (~1 mmHg). Dextran

diffusion across the BEB barrier was imaged using a fluorescent microscope (Nikon Eclipse Ti2) for 1 minute at 1-second intervals at 2-minute and 5-minute time points after dextran perfusion.

On the day of the assay, BEB microvessels were equilibrated by incubating them with serum-free EGM2-MV media for 20 minutes. Kinase inhibitor and dimethyl sulfoxide (DMSO) vehicle control solutions were prepared from 1 mM stock KIs and diluted to a final concentration of 1 μM in serum-free EGM2-MV media. For permeability measurements of 12 KIs and vehicle control in resting BEB microvessels, prepared solutions were perfused in equilibrated BEB microvessels for 2 hours, after which dextran solution (100 mg/mL in serum-free EGM-2MV growth media) was applied and imaged immediately. KIs were applied to both leaky and intact BEB microvessels to investigate the barrier-modulating effects of KIs in resting BEB microvessels.

For permeability measurement of KIs with BEB perturbation, an additional step was included prior to the 2-hour KI treatment. Thrombin activation was induced for 15 minutes with 0.5 U/mL or 1 U/mL thrombin in serum-free EGM2-MV media. Perturbations mimicking patient conditions were conducted using TBI patient plasma and normal pooled plasma. Plasma samples were thawed and immediately applied to the inlets of the BEB microvessels, then perfused for 2 hours or 6 hours. After perturbation of the BEB microvessels, dextran permeability was measured by perfusing a 70 kDa FITC-dextran solution. Prior to the 2-hour KI treatment, the dextran solution was washed out with serum-free EGM2-MV media for 15 minutes to minimize the diffusion of leftover dextran during KI incubation. Preparation and application of KIR-predicted KIs were conducted in the same manner as the initial 12 screened KIs. At the end of the permeability assay, all of the vessels were washed with PBS, fixed in 3.7% paraformaldehyde (PFA), and stored at 4°C for immunofluorescent analysis.

*3.3.4 Permeability analysis*

Permeability analysis was conducted from sequential fluorescent images of dextran diffusion across endothelial barrier into the collagen spaces. Permeability images generated from center straight channel was imported into ImageJ for analysis of dextran diffusion across the collagen lumen. Region of interest (ROI) from same positions of the microvessels were selected and lumen diameter, x and y coordinates of the ROI, angle of image rotation and center of horizontal axis for ROI were imported into excel sheet for parameter annotation for subsequent MATLAB analysis.

Analysis of endothelial permeability at the collagen interface was obtained by estimating the K (um s-1) as a function of parameters obtainable from fluorescent images and known variables. These parameters include: intensity of fluorescent solution, $\boldsymbol{i_0}$, initial background intensity $\boldsymbol{i_{initial}}$, intensity at the outer collagen spaces,$\boldsymbol{i_{col,\ intensity}}$ in the center straight channel, $\boldsymbol{i_{lumen}}$, diffusivity of 70kDa and 500kDa dextran, $\boldsymbol{D_{dextran}}$, and time t). From on previous study measuring membrane permeability of a tubular structure with unsteady state diffusion experiment. The membrane permeability was calculated by initially plotting for natural logarithm of R against time constant tau (dimensionless time), which is defined as fraction of dextran remaining in the lumen of the microvessels after time t. The asymptotic value of the graph was assumed to be related to the first root of alpha of Stevenson equation. Using MATLAB, alpha was solved for using polyfit junction to find asymptotic value of alpha. The permeability coefficient was obtained by implementing the diffusivity coefficient of 70kDa dextran, the radius of lumen, the calculated value alpha which was implemented into Bessel functions.

Additional parameter, permeation index, was also calculated to provide a dimensionless parameter for KIR regression analysis. Permeation index was necessary for measuring the subtle changes occurring in thrombin injured vessels where the initial leakage at 2 min was already substantive

and the change in fluorescent intensity as R became less reliable. Permeation index represents the distance FITC dextran particle traveled outside of collagen luminal space. We defined an arbitrary distance delta_x which is the corresponding x value for 2/3 of maximum fluorescent intensity (y value) obtained from center lumen. For analysis, delta_x value obtained from both boundaries were averaged and divided by the length of the lumen size to generate a dimensionless parameter.

*3.3.5 Immunofluorescence staining and microscopy*

At the end of the experimental time point, 3D microvessels were fixed in situ with 3.7% paraformaldehyde (PFA) for 20 minutes and washed three times with Dulbecco's phosphate-buffered saline (DPBS). Microvessels were then incubated in blocking buffer consisting of 2% bovine serum albumin and 0.1% Triton-X in DPBS for 1 hour. Following the 1-hour blocking step, microvessels were stained with primary antibodies overnight at 4°C. A combination of primary antibodies was used to stain the microvessels. For vessels stained with conjugated primary antibodies and phalloidin only, 1:100 APC anti-human VECAD (eBioscience, 17-1449-42) and 1:100 Alexa Fluor 488 phalloidin (Invitrogen, A12379) or 1:100 Alexa Fluor 594 phalloidin (Invitrogen, A12381) were incubated overnight at 4°C. Staining of additional antibodies, Zo-1 and Claudin 5, was conducted by staining primary-secondary antibodies first, followed by an additional step of staining primary-conjugated antibodies. In all staining procedures, the final step included overnight nuclei staining with 1:200 Hoechst 33342 (Thermo Fisher, CC-H1399). After every antibody staining step, the microvessels were washed three times, every 20 minutes, with DPBS and stored at 4°C until imaging. Immunofluorescence images were obtained using Yokogawa W1 spinning disk confocal microscopes (Nikon Ti2). Z-stack images were obtained using a 10x objective (z-step size: 5 μm) to provide an overall view of the microvessels in the center channel. A 20x objective was used to generate z-stack images (z-step size: 2 μm) of the top

and bottom layers for further analysis of endothelial cell (EC) cytoskeletal and junctional states. Fiji (ImageJ) software was used to generate an orthogonal view of the microvessels using source images obtained with the 10x objective, and maximum projection images of the top and bottom layers of ECs were generated from images obtained with the 20x objective.

*3.3.6 VECAD Quantification*

Maximum projection images of VECAD images were analyzed using previously published application developed for quantifying VECAD junctions. Quantification of % punctate and % discontinuous was obtained using JanaP (Junction Analyzer Program). MIP images were imported into the program and manually traced for cell boundaries to quantify edge-localized VECAD junctions. % punctate was defined as the percent of cell perimeter presenting punctate junctions and % discontinuous was defined as percent of cell perimeter presenting both punctate and perpendicular junction. More than 150 cells were sampled for VECAD quantification of 12 kinase inhibitors treated in thrombin activated vessels. More than 80 cells were sampled for VECAD quantification of 6 kinase inhibitors predicted from KIR.

*3.3.7 Scanning electron microscopy (SEM) and Transmission electron microscopy (TEM)*

BEB microvessels were fixed with ½ strength Karnovsky's fixative (2.5% glutaraldehyde, 2% PFA in 0.1 M sodium cacodylate buffer, pH 7.3) by perfusing the inlet of the microvessels for 20 minutes at room temperature, followed by a second fixation with fresh ½ strength Karnovsky's fixative for an additional 1 hour. The collagen construct containing 3D BEB microvessels was removed from its acrylic housing device and stored in 6-well plates immersed in ½ strength Karnovsky's fixative at 4°C.

For TEM sample preparation, the collagen construct was rinsed with 0.1 M cacodylate buffer, treated with 1% osmium tetroxide for 2 hours at 4°C, rinsed with cacodylate buffer, dehydrated

through a graded series of alcohols and propylene oxide, and embedded in Eponate12 resin (Ted Pella, Inc, Redding, CA). Ultrathin sections (70 nm) were cut using a Leica EM UC7 ultramicrotome, contrasted with uranyl acetate and lead citrate, and imaged on a ThermoFisher Talos L120c transmission electron microscope at 120 kV. Digital images were acquired with a Ceta 16M CMOS 4k x 4k digital camera system.

For SEM sample preparation, the bottom collagen layer containing BEB microvessels was peeled off, leaving open lumen channels for top-down imaging. Microvessels containing open lumen channels were rinsed with 0.1 M cacodylate buffer, dehydrated through a graded series of alcohols, and critical point dried (Autosamdri, Tousimis Corp, Rockville, MD). Samples were then mounted on stubs and sputter-coated with gold/palladium (Denton Desk IV, Denton Vacuum, Moorestown, NJ). Samples were imaged on a JSM 6610 LV scanning electron microscope at 5 kV (JEOL, Tokyo, Japan).

*3.3.8 KI regression analysis*

The elastic net regularization algorithm used for this study was published previously (Dankwa et al., 2021). The kinase regression (KiR) approach exploits the polypharmacology of a small panel of kinase inhibitors and makes predictions on kinases important for specific cellular phenotypes and the effect of untested kinase inhibitors on the phenotypes based on the linear combination of the contributions of kinases to the phenotypes (Gujral et al., 2014). For this study, permeability of 3D microvessels upon KI treatment was used as the phenotypic readout for KiR. The permeability of KI-treated vessels (pKI) was normalized to their permeability prior to KI treatment (pT) as (pKI-pT)/pT. The normalized permeability, along with the biochemical data of the panel of 12 kinase inhibitors against 291 recombinant protein kinases, were input into the elastic net regularization algorithm with a condition-specific cross-validation strategy. The glmnet package

(https://github.com/bbalasub1/glmnet_python, version 2.2.1) in Python (https://www.python.org, version 3.7.6) was used to perform elastic net regularization, with the elastic net mixing parameter of 0.8.

*3.3.10 Statistical Analysis*

All statistical analysis was performed using GraphPad Prism version. One-way ANOVA followed by student's t test for permeation index quantification. Statistical analysis of VECAD quantification was obtained by non-parametric one-way ANOVA test followed by ad-hoc Dunnett's test. Statistical significance was defined as a value of $p < 0.05$. For all imaging and permeability quantification, data was analyzed in a blinded manner.

## 3.4 Results

### *3.4.1 Perfusable human brain endothelial cell barrier models for screening kinase inhibitors for EC barrier modulation*

To generate a model of the human brain endothelial barrier for studying barrier integrity using fluorescent dextran perfusion, we developed a 3D perfusable microvessel model using soft-lithography and collagen injection molding techniques. The BEB model was created using a hexagonal network (diameter of 100 μm) with a straight center channel (diameter of 150 μm), mimicking the gross brain vascular network and penetrating arteries found in the human brain (Figure 3.1 **A**). Each hexagonal network contained an inlet and an outlet to allow the direct seeding of human brain microvascular endothelial cells (HBMECs), which formed fully lumenized microvessels with a robust endothelial barrier after 7 days of culture. Immunofluorescent staining of D7 BEB microvessels with tight junction proteins, such as claudin-5 and occludin, in HBMECs forming the BEB demonstrated successful modeling of brain microvessels (Figure 3.1 **B**). Additionally, staining for vascular endothelial cadherin (VECAD) in the 3D BEB model confirmed the presence of robust endothelial junctions as well as the formation of intact lumenized microvessels (Figure 3.1 **C**).

To comprehensively investigate changes in the brain endothelial barrier, a platform that enables perfusion of stimuli and measurement of permeability at the barrier-ECM interface is essential. Fluorescein-dextran perfusion in our BEB model demonstrates the feasibility of using barrier permeability — a functional barrier readout — to investigate the effects of perfusates on endothelial junctions and barrier integrity. The use of a hexagonal network structure with a straight center channel allowed us to utilize the center channel for analyzing dextran permeation across the endothelial barrier into the collagen matrix. Perfusion of 70 kDa fluorescein isothiocyanate (FITC)-dextran (Figure 3.1 **D**; green) and 500 kDa tetramethylrhodamine (TRITC)-dextran

(Figure 3.1 **D**; red) through the D7 BEB microvessels demonstrated intact barrier formation for both molecular weights. The permeation index for both 70 kDa and 500 kDa dextran suggested that the D7 BEB barrier was able to maintain integrity for at least 70 kDa molecules (Figure 3.1 **E**). Thereafter, 3D HBMEC microvessels were used throughout this study to assess endothelial barrier function in response to kinase inhibitors and activation stimuli such as thrombin and TBI plasma.

Kinase inhibitors (KIs) demonstrate polypharmacological effects by activating and inhibiting diverse kinase targets across the kinome. Kinase signaling plays a critical role in regulating both paracellular and transcellular endothelial permeability. We aimed to explore the polypharmacological impact of KIs on endothelial barrier function, regulated by multiple kinase targets. By screening KIs in our microvessels and quantifying permeability based on the barrier-protective or barrier-disruptive effects of individual KIs, and obtaining a permeability index, we performed kinase regression analysis to identify novel classes of KIs (Figure 3.1 **F**). To optimize and minimize the number of KIs required for effective screening and regression analysis of endothelial barrier function, we conducted a predictive analysis with 28 KIs from a prior study that used kinase regression modeling to identify key targets for barrier stabilization[198]. This analysis revealed that screening 10 KIs from the 28 KIs used in the 2D analysis produced the least variability and most accurate predictions for barrier-relevant kinase families (Figure 3.1 **G**). Based on the prediction analysis, we selected 10 KIs and included two additional BCR-ABL-targeting KIs, which were not included in the previous study but have been shown to enhance barrier regulation in 2D cultures of endothelial cells (Figure 3.1 **H**).

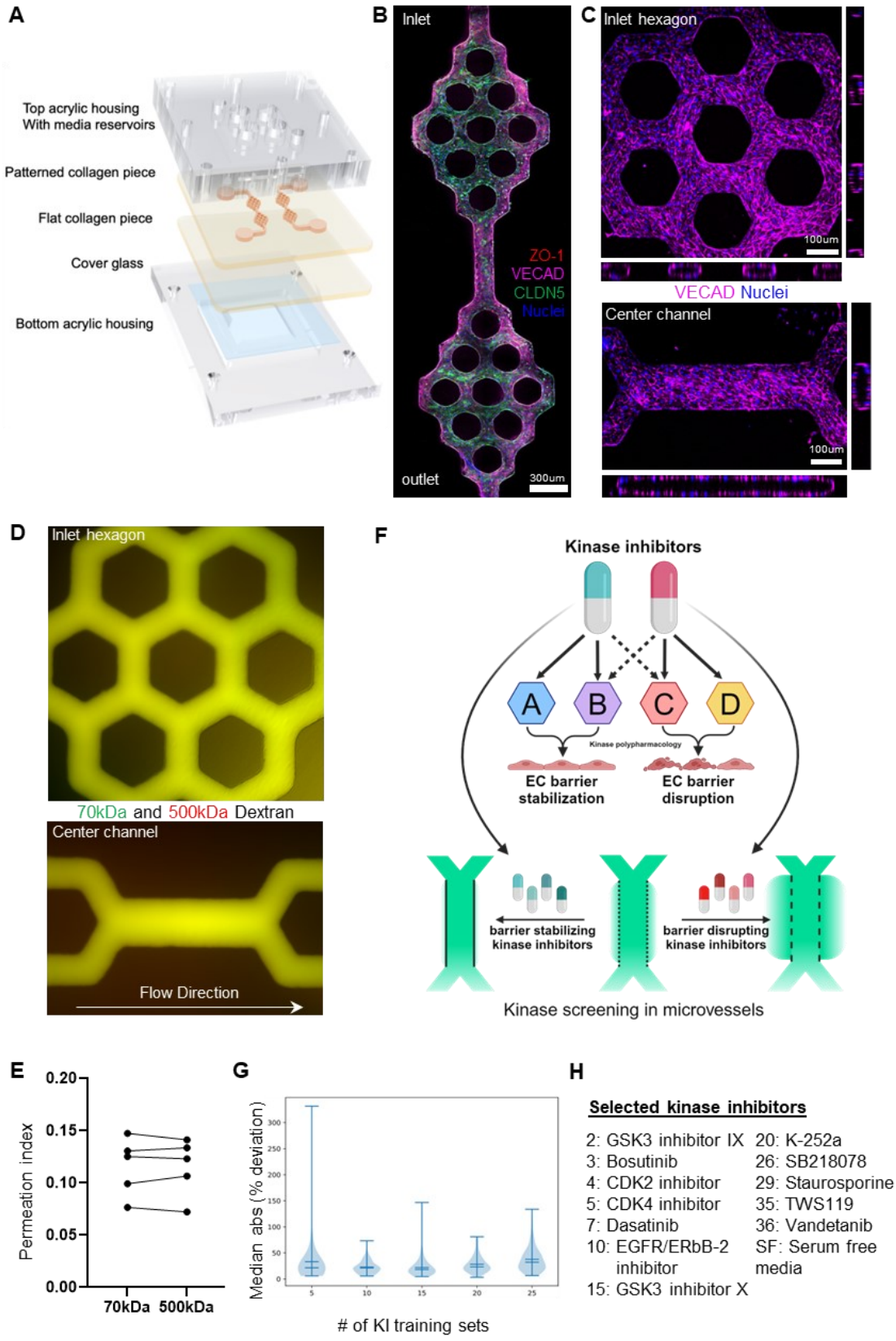


**Figure 3.1 3D perfusable brain endothelial barrier (BEB) model for screening EC barrier modulating kinase inhibitors.**

(A) Schematic diagram of 3D microvessels generated with hexagon network structure mimicking the brain vascular network with penetrating arteries. (B) Immunofluorescence image of HBMEC seeded microvessels stained for tight junction proteins occludin (ZO-1; red) and claudin (CLDN5; green) and vascular endothelial cadherin junction (VECAD; magenta). (C) Orthogonal projection of VECAD stained BEB microvessels shows round and intact lumen formation with robust junction formation after 7 days of culture. (D) Perfusion of 70kDa (FITC) and 500kDa (TRIT-C) dextran in D7 BEB microvessels. Each dextran remains within the lumen showing the formation of intact EC barrier in our BEB model. (E) Quantification of permeability for 70kDA and 500kDa; data points conjoined by lines represent same microvessels. (F) Schematic overview of kinase screening in 3D BEB microvessels for permeability measurement and KIR regression. (G) Prediction analysis determining number of KIs needed to provide least variable results in KIR from 28 previously screened KIs in 2D. (H) List of 10 KIs identified from prediction analysis and additional 2 FDA approved BCR-ABL targeting KIs known to impact EC barrier property used to screen in 3D BEB model.

### *3.4.2 Evaluating the effect of selected kinase inhibitors on endothelial barrier regulation in resting 3D BEB microvessels*

To investigate the polypharmacological effects of kinase inhibitors (KIs) on brain endothelial barrier regulation, we screened 12 selected KIs in a 3D blood-brain endothelial barrier (BEB) model. BEB microvessels were fabricated 7 days before the perfusion experiments. On Day 6, baseline permeability measurements were taken to assess barrier integrity prior to KI screening. To evaluate each KI for its protective and restorative potential, we tested them on microvessels with both intact and compromised endothelial barriers, categorized by baseline permeability. On the day of permeability imaging, the 3D BEB microvessels were equilibrated in serum-free culture media to minimize pharmacological effects from the serum environment. Each of the 12 KIs was then applied to the microvessels for 2 hours, after which permeability was assessed by perfusing 70 kDa FITC-dextran immediately following KI treatment (Figure 3.2 **A**).

The residual activity profiles of 12 kinase inhibitors were previously examined by Anastasia et al.[199], revealing the polypharmacological effects of these inhibitors. The residual activity analysis indicated a wide range of kinase inhibition and activation targets (Figure 3.2 **B**). Although the BCL-ABL drugs vandetanib and dasatinib exhibited similar activity profiles, the kinase inhibitors

Staurosporine, K252a, and SB218078 displayed comparable inhibition targets and activities despite differing primary targets. Notably, while SB218078 is a known Chk1 inhibitor, Staurosporine and its synthetic analog K252a share overlapping activity, suggesting that proposed inhibition targets may not fully capture the inhibitors' broader kinase reactivity, which could yield alternative biological outcomes.

To evaluate the effects of kinase inhibitors (KIs) on the integrity of the blood-brain endothelial barrier (BEB) in microvessels, we measured permeability by quantifying the diffusion of fluorescent dextran particles across the endothelial barrier (Figures 3.2 **C** and **D**). After a 2-hour KI perfusion, fluorescent imaging of dextran diffusion showed varying degrees of barrier disruption and restoration (Figures 3.2 **C** and **D**). Notably, the CDK4 inhibitor (Figures 3.2 **C** i and ii), the EGFR/ErbB-2 inhibitor (Figures 3.2 **C** iii and iv), and TWS119 (a GSK3 inhibitor; Figures 3.2 **C** v and vi) demonstrated barrier restoration within 2 hours in resting vessels (Figure 3.2 **C**). In contrast, dasatinib (Figures 3.2 **D** i and ii) and the PKC inhibitors K252a (Figures 3.2 **D** iii and iv) and Staurosporine (Figures 3.2 **D** v and vi) led to increased barrier disruption in 3D microvessels (Figure 3.2 **D**). Overall, permeability quantification revealed that barrier-disruptive KIs significantly increased dextran permeation compared to the DMSO control, while only CDK4 inhibitors showed a significant increase in dextran permeability relative to the control (Figure 3.2 **E**).

Additionally, staining of microvessels following a 2-hour treatment with the barrier-restorative KI, TWS119, revealed thick, intact VECAD coverage along cell boundaries (Figures 3.2 **F** i-ii) with cortical actin structures, indicative of a more quiescent endothelial cell phenotype (Figure 3.2 F iii). In contrast, barrier-exacerbating KI treatments led to disrupted VE-cadherin (VECAD) junctions (Figure 3.2 **G** i). Specifically, treatment with K252a resulted in a loss of VECAD (Figure

3.2 **G** ii) in microvessels and increased endothelial cell activation, as indicated by heightened stress. fiber formation within the endothelial cytoplasm (Phalloidin; green) (Figure 3.2 **G** iii).

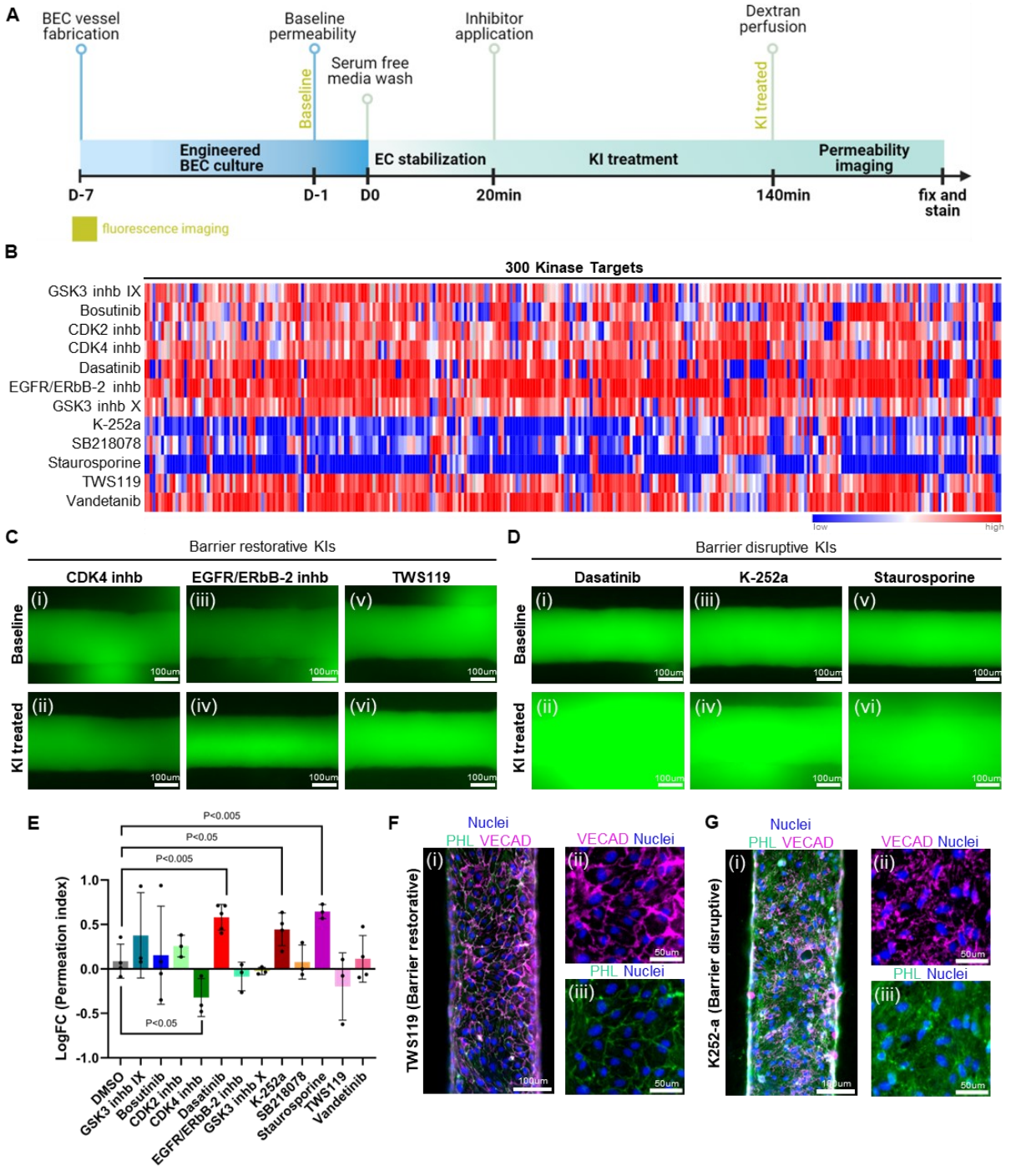


**Figure 3.2 Kinase screening in resting 3D perfusable BEB model reveals distinct barrier disruptive and restorative KIs.**

(A) Schematic diagram of permeability imaging protocol. BEB model is fabricated 1 week prior to permeability imaging. 1 day prior to KI treatment, baseline permeability is measured for resting vessels. On the day of experiment, KIs are treated in serum-absent equilibrated microvessels for 2 h and perfused with 70kDa dextran for permeability imaging. (B) Residual activity of 300 kinase targets for 12 screened KIs. Activation of kinases are colored red and inactivation of kinases are colored blue. (C) Representative fluorescence image of dextran perfused BEB microvessels after 2h KI treatment with barrier restorative KIs (i,ii) CDK4 inhb, (iii,iv) EGFR/ERbB-2 inhb and (v,vi) TWS119. (i, iii,iv) Images of initial barrier disruption in resting vessels were chosen to highlight the barrier restoration after KI treatment (ii,iv,vi). (D) Representative fluorescence image of dextran perfused BEB microvessels after 2h KI treatment with barrier disruptive KIs (i,ii) Dasatinib, (iii,iv) K252-a and (v,vi) Staurosporine. Images of (i, iii,iv) initial intact barrier formation in resting vessels were chosen to highlight the barrier disruption after (ii,iv,vi) KI treatment. (E) Log fold change values for permeability index quantified from KI treatment of BEB microvessels (n = 3-4). Compared to DMSO control, CDK4 inhb significantly improved the barrier while all barrier disruptive KIs from (D) significantly increased permeability compared to DMSO control. (F) Representative IF image of barrier restorative KI treatment in (i) BEB microvessel showing (ii) thick VECAD staining and (iii) quiescent cortical actin structure (G) Representative IF image of barrier disruptive KI treatment in (i) BEB microvessel showing (ii) truncated and punctate VECAD staining and (iii) formation of endothelial stress fibers.

### *3.4.3 TBI plasma perfusion mimics the BEB breakdown and shows potential of barrier-restorative kinase inhibitors for enhancing barrier recovery*

Secondary injury in traumatic brain injury (TBI) is initiated by the loss of the brain endothelial barrier, driven by the pro-inflammatory and pro-coagulative state of vessels triggered by the initial injury. To study barrier changes in response to the hypercoagulable and hemorrhagic states associated with TBI, we used our 3D BEB microvessels to model endothelial cell (EC) injury and barrier disruption. Following our kinase inhibitor perfusion protocol, we prepared D7 microvessels and measured baseline permeability one day prior to TBI plasma treatment. Only microvessels with intact baseline permeability were selected for perfusion and equilibrated with serum-free media to reduce the protective influence of serum on the plasma perfusate. Plasma samples from human TBI patients were then perfused through the human brain microvascular endothelial cell (HBMEC) lumens using gravity-driven flow for 6 hours (n=3), followed by an additional 2-hour kinase inhibitor treatment (Figure 3.3 **A**).

To investigate the time it took for TBI plasma to affect barrier properties, we treated the BEB microvessels with TBI patient plasma for 2 hours (n=2) and 6 hours. Permeability imaging indicated that a 2-hour perfusion of TBI and normal plasma samples resulted in no significant change in dextran leakage in either condition. However, a 6-hour perfusion of TBI plasma (Figure 3.3 **B** v and vii) led to increased permeability compared to normal plasma (Figure 3.3 **B** i and iii). Quantification of 70 kDa FITC-dextran permeability revealed a four-fold increase in dextran leakage in TBI plasma-treated vessels compared to those treated with normal plasma (Figure 3.3 **C**). This finding suggests that prolonged exposure to plasma samples is necessary for endothelial cells to respond effectively in 3D microvessels. Our results were consistent with previous findings in a TBI mouse model, where vascular permeability and cerebral hematoma occurred 6 hours after fluid percussion injury[200]. Following permeability imaging, the perfused microvessels were fixed and stained with phalloidin (actin) and von Willebrand factor (vWF). Phalloidin staining revealed cellular retraction in TBI plasma-treated microvessels (Figure 3.3 **B** vi and viii), which correlates with the observed four-fold increase in dextran leakage. vWF staining demonstrated the presence of transluminal vWF fibers across the central channel, indicating endothelial activation and the formation of a pro-thrombotic environment within the vessel lumen (Figure 3.3 **C**). Overall, TBI plasma perfusion validated the feasibility of using HBMEC microvessels to model TBI-induced hemorrhagic coagulopathy in vitro.

Next, to assess the therapeutic potential of KIs for the stabilization of BECs within the early stages of TBI, we subjected TBI plasma-perfused vessels to kinase inhibitors that were shown to significantly increase (CDK4 inhibitor) or decrease (K252a) barrier properties in resting vessels. IF images of 6-hour TBI plasma-treated microvessels show a loss of VECAD expression (Figure 3.3 **D** v-vi, arrow) and increased cellular retraction of ECs (Figure 3.3 **D** vii-viii, arrow). Two-hour

treatment with K252a, a barrier-disruptive KI, shows progressive exacerbation of the BEB, characterized by increased cell death (Figure 3.3 **D** xii and xiii) and VECAD internalization (Figure 3.3 **D** x and xi), indicating that barrier-disruptive KIs can further deteriorate EC barrier properties in TBI-mimicking conditions (Figure 3.3 **D**). Two-hour treatment with a CDK4 inhibitor offers initial restoration of VECAD junctions (Figure 3.3 **D** i and ii), suggesting that the kinase targeted by the CDK4 inhibitor may be an important therapeutic target for stabilizing and restoring the HBMEC barrier following TBI injury (Figure 3.3 **D**).

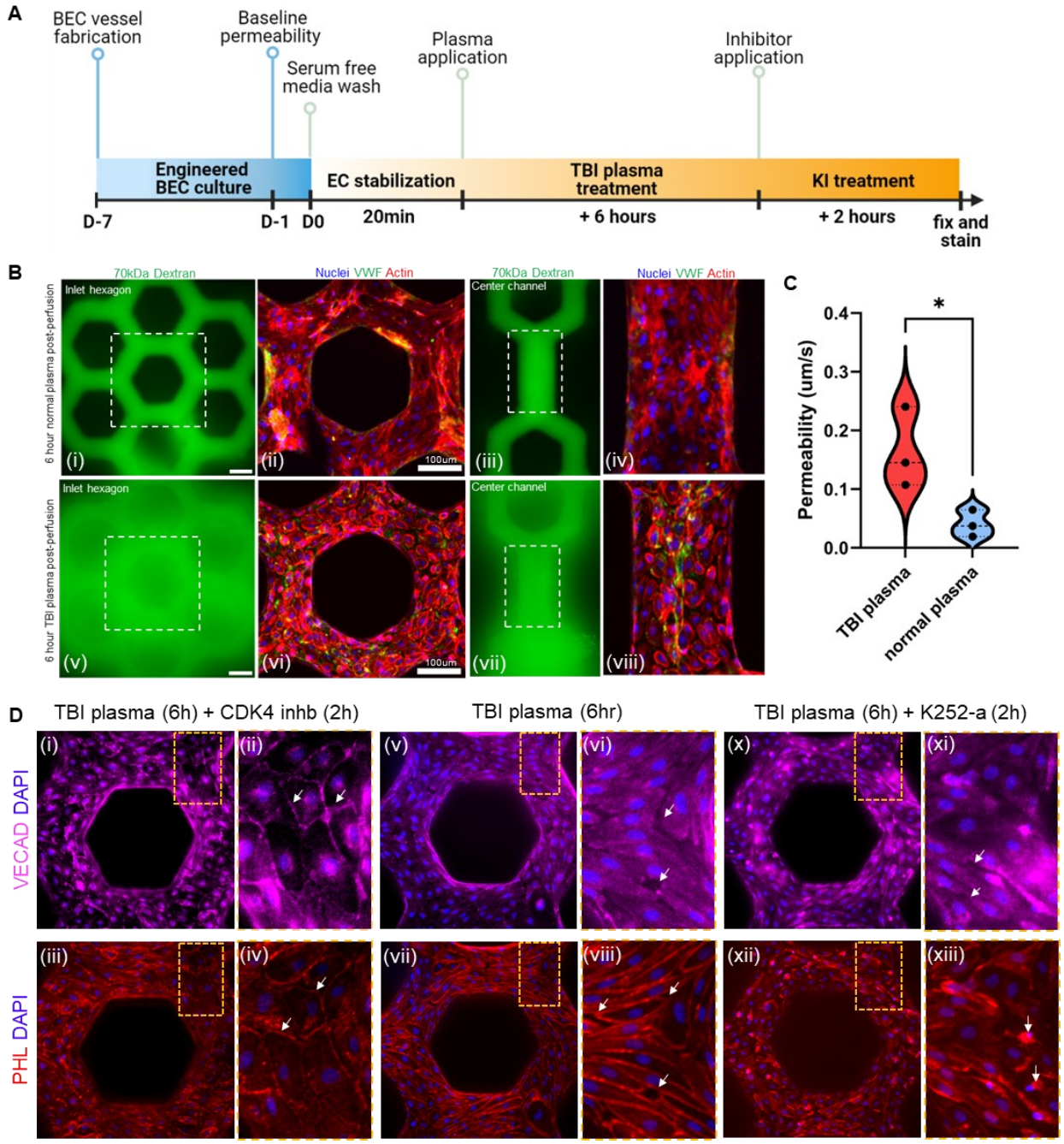


**Figure 3.3 TBI induced BEB breakdown can be modulated by two distinct class of KIs.**

(A) Schematic diagram of permeability imaging protocol after TBI patient plasma treatment. Similar approach is used as KI screening protocol with the exception of longer treatment time (6h). (B) 70kDa dextran perfusion of 3D BEC microvessels 6 hours after (i,iii) normal and (v,vii) TBI plasma perfusion. Normal plasma shows maintenance of intact barrier integrity whereas TBI plasma perfused vessels show significant leakage. Immunostaining for actin structures (phalloidin; red) and vWF (green) shows retraction of HBMECs and formation of vWF fibers in (vi, viii) TBI plasma treated BEB microvessel. Endothelial retraction and vWF fiber formation is absent in (ii,iv) normal plasma treated BEB microvessel. (C) Quantification of permeability shows 4-fold increase in permeability coefficient in TBI plasma treated microvessels. (D) IF images of (i-iv) CDK4i treatment following TBI plasma perfusion shows initial recovery of (i,ii) VECAD junctions and (iii,iv) reorganization of actin structures (white arrow). IF images of (v-viii) 6h TBI

plasma perfusion leads to (v,vi) loss of endothelial junction (VECAD; magenta) and (vii,viii) endothelial retraction (white arrow) evidence by cytoskeletal structure (phalloidin; red) in 3D microvessels perfused with (v-viii) TBI plasma for 6 hours. IF images of (x-xiii) K252-a treated microvessel shows further (x,xi) loss of junction (white arrow) and (xii,xiii) cell death (white arrow) following 6-hour perfusion of TBI plasma.

### *3.4.4 Thrombin activation is detected in TBI patient plasma and mimics barrier breakdown in 3D BEB microvessel*

Previous studies have shown that TBI injury in mice leads to an increase in brain-derived extracellular vesicles (EVs). Recently, growing literature has suggested a pathological role for disease-driven brain-derived EVs, including their involvement in inducing a systemic hypercoagulable state. To investigate whether brain-derived EVs and other pathological forms of EVs are elevated in plasma samples from TBI patients, we examined 32 patient plasma samples and quantified levels of neuronal (Figure 3.4 **A**) and glial (Figure 3.4 **B**)-derived EVs, as well as EVs expressing the anionic phospholipid phosphatidylserine (Figure 3.4 **C**) in peripheral blood. We observed a significant increase in both the total amount of brain-derived EVs and pro-coagulant forms of EVs compared to age- and gender-matched healthy controls.

Next, we investigated the coagulation profile of a mouse model of TBI by inducing severe fluid percussion injury (FPI) in the TBI mouse group and performing a sham surgery on the control group. Similar to human patient plasma, mice subjected to FPI showed increased levels of pro-coagulant PS+ EVs compared to the sham group. We also observed that mice with FPI had increased plasma fibrinogen, a substrate for thrombin, and an increased rate and level of thrombin generation. This suggests that the induction of TBI-IC is strongly correlated with increased pathological EV secretion, elevated plasma fibrinogen, and increased thrombin generation. These results show that thrombin is generated post-TBI in a high EV milieu (Figure 3.4 **F**), suggesting that thrombin activation could be used to mimic TBI-induced coagulopathy and BEB breakdown.

To study BEB disruption in the context of TBI, we mimicked thrombin activation of endothelial cells within our engineered BEB microvessel. To test whether thrombin perfusion in our 3D BEB model results in a loss of EC barrier integrity, we perfused 0.2 U/ml of thrombin through gravity-driven perfusion via an inlet reservoir in HBMEC microvessels (Figure 3.4 **G**). Fluorescent images from dextran perfusion of baseline HBMEC microvessels showed no dextran leakage into the collagen space, and scanning electron microscope (SEM) images of baseline microvessels showed tight EC junction formation between adjacent ECs (Figure 3.4 **G** i, ii, and **H**). In contrast, 15-minute thrombin activation (0.2 U/ml) resulted in increased dextran leakage and EC detachment from adjacent cells (Figure 3.4 **G** iii, iv, and **E**). A 2-hour treatment with vehicle control media in thrombin-activated (0.2 U/ml; 15 min) vessels showed that barrier disruption was sustained 2 hours after thrombin perfusion, indicating that barrier breakdown persisted (Figure 3.4 **D** v, vi, and **E**). Our data — release of BDEVs in TBI patients, increased thrombin generation in high concentrations of BDEVs in the mouse model, and disruption of the EC barrier following 15-minute thrombin exposure — strongly supports the feasibility of modeling TBI-induced BEB disruption using thrombin activation.

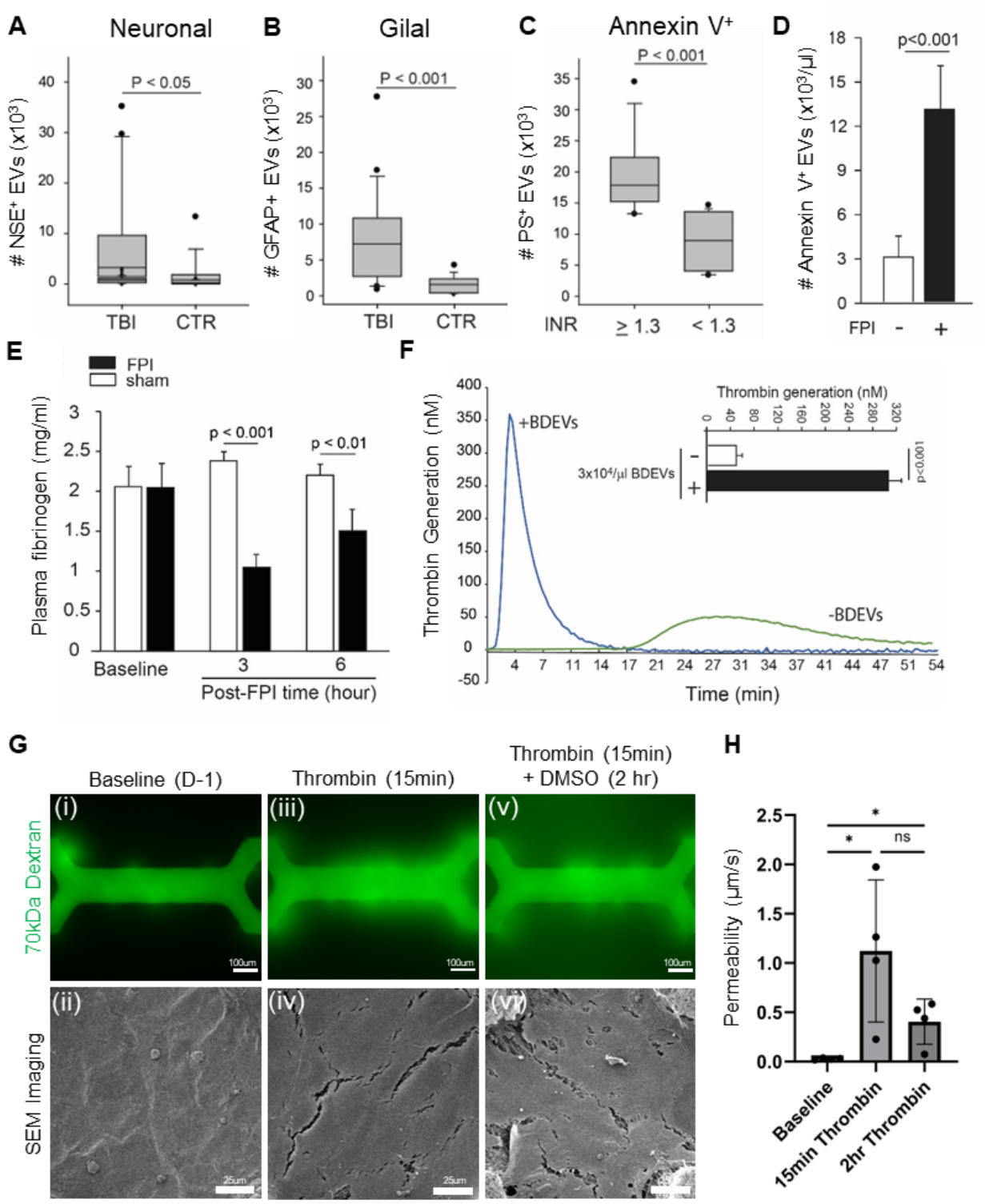


**Figure 3.4 TBI induced BEB breakdown can be modulated by two distinct class of KIs**

Plasma levels of (A) neuronal (NSE+), (B) glial (GFAP+), and (C) EVs expressing anionic phospholipid phosphatidylserine (Annexin V bound) in peripheral bloods samples from TBI patients characterized in the Table and age- and gender-matched healthy subjects (n = 32, Student t-test). The coagulation profile of mice subjected to severe fluid percussion injury or sham surgery, including plasma levels of PS+ EVs (D) and fibrinogen (the substrate of

thrombin (E) in mice subjected to severe fluid percussion injury (n=12-16, Student t-test). (F) The rate of thrombin generation of mice subjected to FPI or sham surgery (n=12, t-test). (G) Permeability and SEM analysis of endothelial barrier breakdown following thrombin (0.2U/ml) stimuli in 3D microvessels. (H) Permeability coefficient is significantly increased after 15 minutes of thrombin induction. 2hr post 15minute thrombin treatment, barrier remains leaky compared to baseline permeability.

### *3.4.5 Barrier restorative KIs ameliorate thrombin activated barrier disruption in BEB microvessels*

To assess the efficacy of kinase inhibitors (KIs) in restoring blood-brain endothelial barrier (BEB) integrity in TBI-mimicking conditions, we evaluated 12 pre-selected KIs in thrombin-activated HBMEC microvessels. We used two thrombin concentrations, 0.2 U/ml and 1 U/ml, to simulate low and high activation levels of thrombin in 3D microvessels. BEB microvessels demonstrating intact baseline permeability were selected for thrombin activation. Before thrombin perfusion, the microvessels were washed with serum-free culture media (EGM2-MV; Lonza) for 10-15 minutes. Thrombin (0.2 U/ml or 1 U/ml) was then perfused for 15 minutes to disrupt the barrier, followed by perfusion with FITC-dextran to measure the extent of disruption. Following permeability imaging, thrombin-perfused vessels were treated with KIs for 2 hours, and a second round of permeability imaging was performed to assess changes post-treatment (Figure 3.5 **A**).

Permeability quantification demonstrated that, compared to DMSO-treated control vessels (Figure 3.5 **B**), cell cycle inhibitors CDK2 (Figure 3.5 **C**) and CDK4 (Figure 3.5 **D**) consistently showed efficacy in restoring barrier integrity following thrombin-induced disruption (Figures 3.5 **E-G**; left images). Interestingly, SB218078, a Chk1 inhibitor that did not exhibit barrier-protective effects in resting vessels, provided a strong restorative effect in thrombin-activated BEB microvessels (Figure 3.5 **H**). In contrast, the GSK inhibitor and EGFR/ErbB-2 inhibitor, which were most effective in promoting restoration in resting vessels, failed to mitigate thrombin-induced barrier impairment. Similarly, as observed in resting vessels, PKC inhibitors staurosporine (Figure 3.5 **E**),

K252a (Figure 3.5 **F**), and the Src inhibitor dasatinib (Figure 3.5 **G**) exacerbated barrier disruption in thrombin-treated microvessels (Figures 3.5 **E-G**; left images). This trend was consistent across both 0.2 U/ml and 1 U/ml thrombin conditions (Figures 3.5 **B-E**). The permeability index not only measured the permeability of thrombin-activated barriers in response to the screened KIs but also served as a functional experimental readout for subsequent KiR analysis and the prediction of novel kinase targets for BBB restoration.

Next, we investigated EC morphology and junctional shape using IF confocal imaging. The DMSO vehicle control showed elongated actin structures (Figure 3.5 **I**; left image) and internalization of VECAD into the cytoplasm (Figure 3.5 **I**; right image), indicating phosphorylated VECAD and the loss of intact junctions. In BEB vessels treated with barrier-restorative KIs, CDK2 inhibitor and CDK4 inhibitor exhibited cortical actin structures (Figure 3.5 **J** and **K**; left image) as well as thick and continuous VECAD junctions (Figure 3.5 **J** and **K**; right image; Figure 3.5 **R-T**). This suggests that CDK2 inhibitor and CDK4 inhibitor successfully restored ECs into a more quiescent endothelial barrier state (Figure 3.5 **J** and **K**). Comparatively, barrier-disruptive KIs staurosporine (Figure 3.5 **L**), K252a (Figure 3.5 **M**), and dasatinib (Figure 3.5 **N**) showed different modes of barrier disruption. IF images of barrier-disruptive KIs elucidated varying modes of barrier disruption. Notably, staurosporine showed severe compaction of actin structures (Figure 3.5 **L**; left image) and a highly tortuous VECAD with evidence of active remodeling (increased vesicular transport) of the junctions (Figure 3.5 **L**; right image). In comparison, K252a-treated microvessels demonstrated reduced expression of VECAD (Figure 3.5 **M**; left image) and increased activation of ECs (Figure 3.5 **M**; right image). Alternatively, BEBs treated with dasatinib showed tapering of EC vessels from the collagen matrix with activated ECs (Figure 3.5 **N**; left image), suggesting that dasatinib may impact the focal adhesion of the integrin-collagen ECM matrix. VECAD exhibited

enhanced internalization, indicating that endothelial junctions were also impaired with dasatinib (Figure 3.5 **N**; right image) but may be less affected compared to K252a (Figure 3.5 **O-Q**).

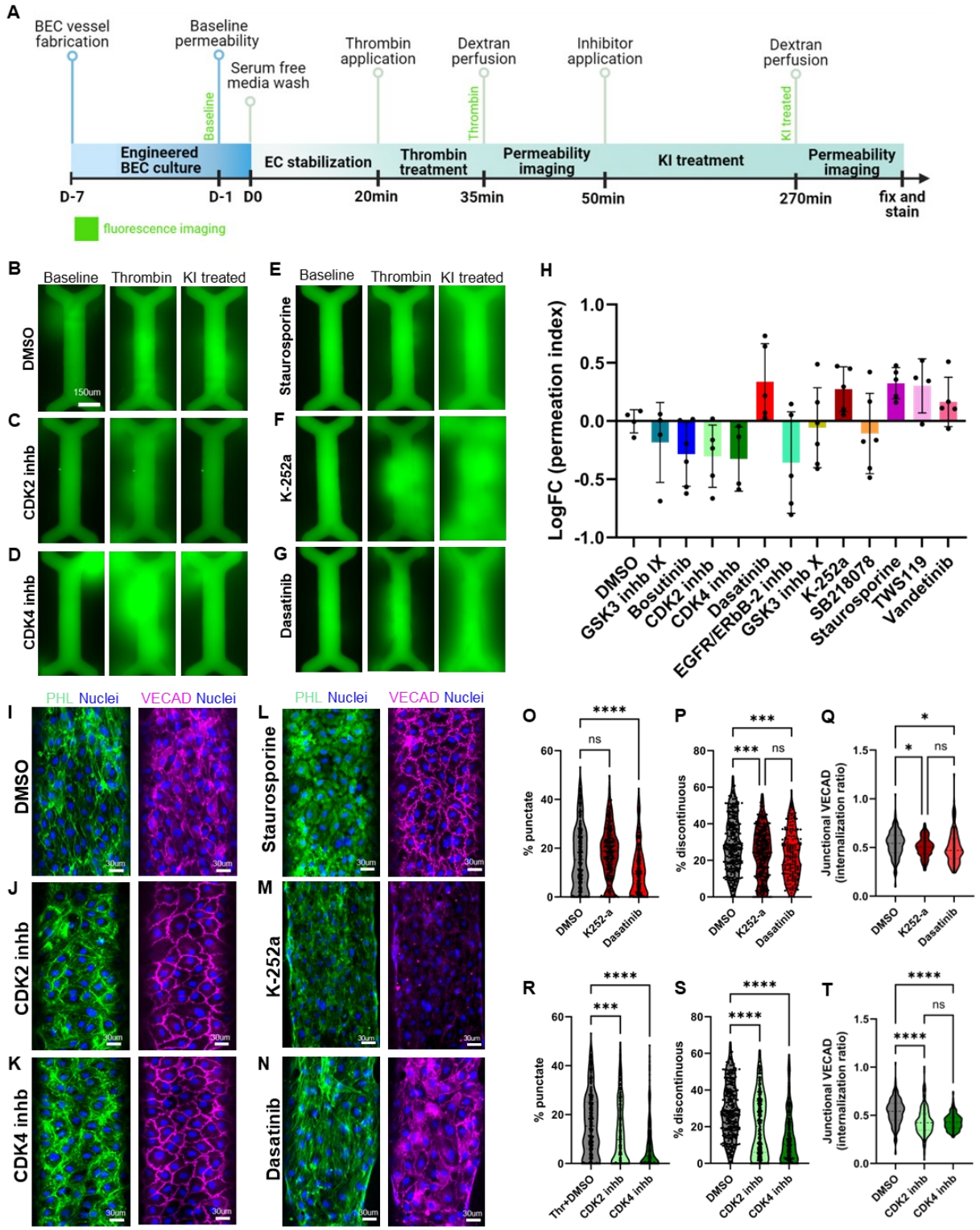


**Figure 3.5 Thrombin activated BEB microvessels show varying mode of BEB restoration and disruption in response to KIs.**

(A) schematic diagram of thrombin activation and KI treatment for permeability imaging. Protocol involves two-part imaging of permeability. Permeability is quantified immediately after thrombin treatment and KI treatment, allowing for direct comparison of how much thrombin perturbed individual vessels and how much KIs are able to modulate activated barrier. 70kDa dextran perfused images of BEB microvessels activated with 1U/ml thrombin in (B) DMSO control, barrier restorative KIS (C) CDK2 inhb and (D) CDK4 inhb and barrier disruptive KIs (E) staurosporine, (F) K252-a and (G) dasatinib. Left image shows the baseline permeability imaged D-1, middle image shows vessels after 15minute of thrombin activation and right image shows vessels after 2 hr KI treatment. (H) Permeability index quantification of 70kDa permeability imaging. Immunoflourescnece images of BEB microvessels fixed immediately after permeability imaging following 2hr KI treatment in thrombin in (I) DMSO control, barrier restorative KIS (J) CDK2 inhb and (K) CDK4 inhb and barrier disruptive KIs (L) staurosporine, (M) K252-a and (N) dasatinib. Right images show nuclei (DAPI; blue) and actin (PHL; green), left images show nuclei (DAPI; blue) and VECAD junction (magenta). Quantification of VECAD structure in barrier disruptive KIs using (O) % punctate (P) % discontinuous and (Q) internalization ratio. Quantification of VECAD structure in barrier restorative KIs treated BEB microvessesl using (R) % punctate (S) % discontinuous and (T) internalization ratio.

### *3.4.6 Ultrastructural analysis of KI induced barrier disruption and restoration*

Permeability imaging and immunofluorescence (IF) staining of VECAD provide insights into functional barrier changes and junctional alterations in response to perfused stimuli. However, these techniques do not reveal the ultrastructural morphology of junctional impacts. To investigate ultrastructural changes, we performed an in-depth investigation of BEB formation in a non-perturbed resting state and examined junctional changes in response to a barrier-restorative KI (CDK4 inhibitor), a barrier-disruptive KI (staurosporine), and the DMSO control using scanning electron microscopy (SEM; Figure 3.6 **A**, **C**, **E**, and **G**) and transmission electron microscopy (TEM; Figure 3.6 **B**, **D**, **F**, and **H**).

In resting BEB microvessels, SEM images show an absence of defined endothelial cell (EC) boundaries (Figure 3.6 A), suggesting the maintenance of quiescent EC junctions over time. TEM images of resting vessels also reveal intact endothelialization on the collagen matrix (Figure 3.6 B i) with characteristic cell-cell junction formations between neighboring ECs, secured by dense adherens and tight junctions (Figure 3.6 **B** ii and v; white arrows). Additionally, resting BEB ECs

display increased metabolic activity (Figure 3.6 **B** iii) and intact nuclear morphology (Figure 3.6 **B** iii), indicating an overall healthy barrier state.

Following thrombin activation and 2-hour DMSO vehicle control treatment, SEM images indicate disrupted endothelial barriers (Figure 3.6 **C** i and ii), with larger gaps at cell-cell junctions and an increased number of protrusions (Figure 3.6 **C** ii; white arrow) extending towards neighboring cells. This suggests that EC junctions have been disrupted and ECs are actively trying to amend the lost junctions by probing and grabbing onto neighboring cells. TEM images further reveal EC barrier breakdown (Figure 3.6 **D**), where endothelial cells partially detach from the collagen matrix (Figure 3.6 **D** i) and form gaps between neighboring ECs (Figure 3.6 **D** ii and v). An increased number of vacuoles and lysosomes is observed (Figure 3.6 **D** iii), though the nuclear structure remains intact (Figure 3.6 **D** iv).

In BEBs treated with barrier-restorative KIs, SEM imaging shows a reduced number of gaps between neighboring ECs, with pronounced cellular boundaries. Compared to the resting vessels' SEM images, the defined edges suggest active barrier restoration, though not fully returning to a quiescent, intact state without visibly defined borders (Figure 3.6 **E** i and ii). TEM images similarly show intact endothelialization on the collagen matrix (Figure 3.6 **F** i), EC tight junction formations (Figure 3.6 **F** ii), reduced gaps between neighboring ECs, and increased formation of adherens junctions (Figure 3.6 **F** v). While junctional recovery is evident, the ECs do not display the metabolically active endosomal transport seen in resting vessels (Figure 3.6 **F** iii), and CDK4 inhibition did not significantly alter nuclear morphology (Figure 3.6 **F** iv).

In BEBs treated with the barrier-disruptive KI staurosporine, SEM images reveal extensive delamination, exposing the underlying collagen structure on the abluminal side (Figure 3.6 **G** i and ii). Additionally, staurosporine treatment induces smaller membrane blebs on the EC surface

(Figure 3.6 **G** ii), suggesting the initiation of an apoptotic cascade. TEM imaging supports these findings, showing that endothelial cells lose focal attachment to both the collagen matrix and neighboring cells (Figure 3.6 **H** i and ii), with increased vacuole formation. The apoptotic pathway is further indicated by the presence of numerous autophagosomes (Figure 3.6 **H** iii and v) and nuclear condensation (Figure 3.6 **H** iv).

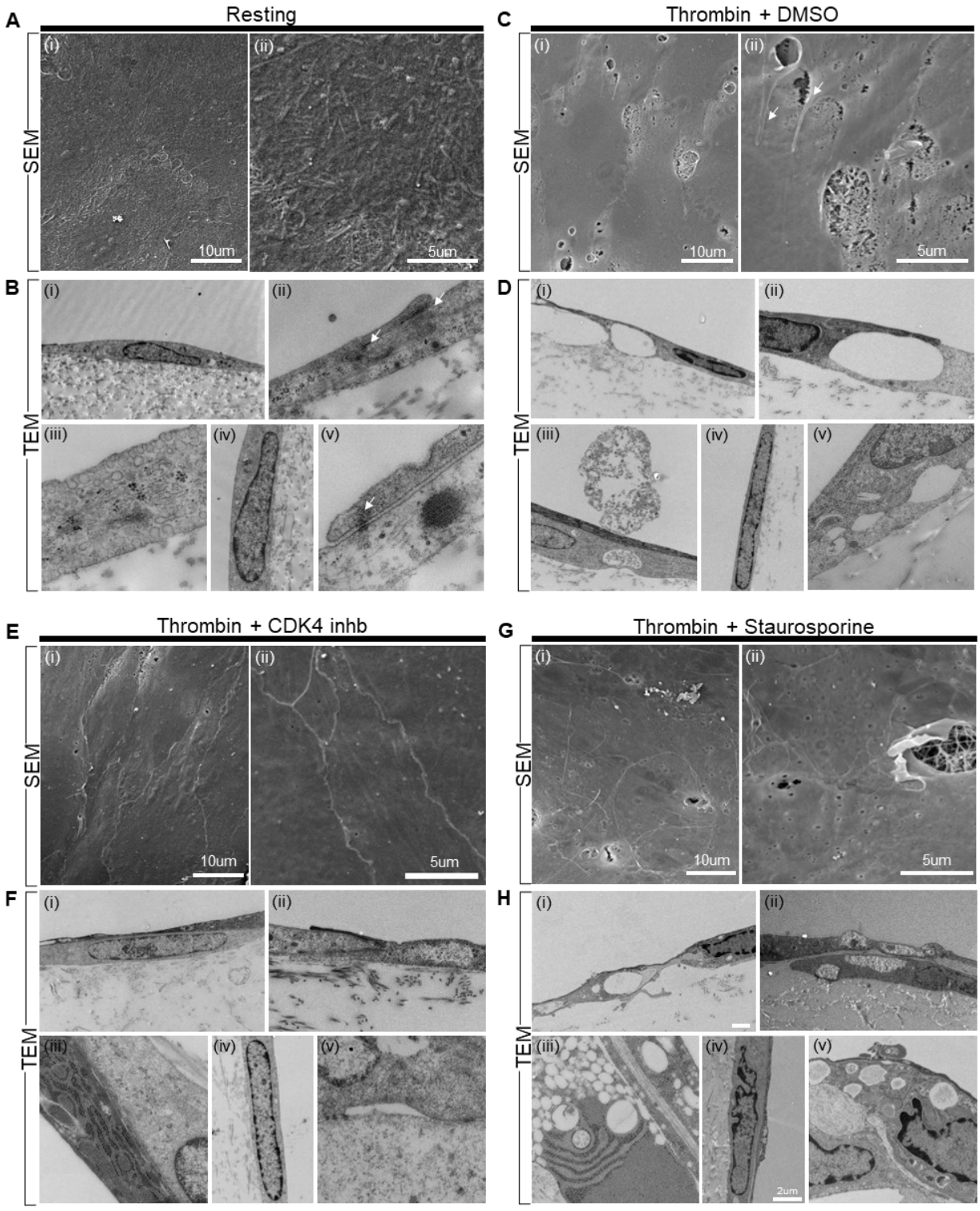


**Figure 3.6 Ultrastructural analysis reveals distinct EC barrier morphology in KI-treated 3D BEB microvessels**

SEM imaging of (A) d7 resting BEB microvessels shows (i and ii) a lack of distinct endothelial barrier in resting vessels, indicating a quiescent and intact barrier formation in d7 BEB microvessels. TEM images (B) show HBMECs are (i) tethered to the collagen matrix and (ii) form robust adherens and tight junctions with neighboring ECs. Resting vessels also exhibit increased biological activity, demonstrated by active (iii) vesicle transport cycling. Resting vessels have regular (iv) nuclear morphology. SEM imaging of (C) thrombin-activated vessels shows (i) numerous gaps near cell-cell boundaries and (ii) endothelial cell protrusions over the gap formations. (D) TEM images reveal a similar trend, where endothelial cells are (i) partially delaminated and (ii and v) show a loss of continuous junctional contact between neighboring ECs. Observations of (iii) lysosomes are noted, but nuclear structure remains normal. SEM imaging of (E) BEB microvessels treated with barrier-restorative KI following thrombin activation shows a (i and ii) pronounced junctional boundary, suggesting recovery of cell-cell junctions. (F) TEM images show (i) intact re-endothelialization of ECs along the collagen surface as well as (ii and v) re-establishment of cell-cell junctions. Although (iii) cells do not return to a biologically active state as seen in resting vessels, (iv) nuclei remain normal. SEM imaging of (G) BEB microvessels treated with barrier-disruptive KI (staurosporine) following thrombin activation shows (i and ii) pronounced delamination of endothelial cells and membrane blebbing, suggesting that staurosporine treatment induces EC apoptosis. (H) TEM images show (i) severe detachment of ECs along the collagen surface as well as (ii) formation of vacuoles and (iii and v) autophagosomes. (iv) Nuclei also exhibit significant condensation.

### *3.4.7 KIR machine learning model identifies kinase targets and kinase inhibitors potent for barrier regulation*

Using the permeation index obtained from the screening of 12 kinase inhibitors in thrombin-activated microvessels, we performed kinase regression analysis by training the KiR to predict barrier-weakening and barrier-strengthening kinases in response to coagulopathic stimuli, specifically thrombin activation, which mimics barrier disruption in TBI-IC. Permeation index values from low and high thrombin concentrations were analyzed separately. The permeation index from the 12 screened drugs predicted a total of 15 kinase targets from the 300 kinase targets on which the KiR is based. Additionally, the KiR predicted and ranked the kinase inhibitors from best (right of the vertical axis) to worst (left of the vertical axis). A heatmap of kinase targets implicated in barrier modulation and ranked kinase inhibitors showed that inhibiting kinases RIPK2, PDGFRB, BLK, FYN, EPHA1, and TXK could potentially exacerbate barrier permeability (Figure 3.7 **A**). Interestingly, no significant trend was observed in barrier-strengthening KIs with respect to predicted kinase targets. Therefore, we selected 6 KIs predicted to be among the top barrier-

strengthening KIs but with different inhibition parameters for predicted kinase targets. These included a ROCK inhibitor, AG490, a P38 inhibitor, a MEK1/2 inhibitor, Rapamycin, and a TGF-β inhibitor. Although they did not show distinct cluster profiles with respect to predicted kinase targets, when compared to the 12 KIs used to generate permeability predictions, all 6 clustered with EGFR/ErbB inhibitors (Figure 3.7 **B**).

Next, we tested the 6 predicted barrier-restorative KIs in thrombin (1 U/ml)-activated BEB microvessels. Permeability imaging revealed that three KIs — ROCK inhibitor (Figure 3.7 **D**), AG490 (Figure 3.7 **E**), and P38 inhibitor (Figure 3.7 **F**) — potentially ameliorated thrombin-activated microvessels compared to the vehicle control (Figure 3.7 **C**). Quantification of permeability showed that AG490 and the ROCK inhibitor were the most effective at enhancing the barriers, while SL237 (MEK1/2 inhibitor) and the TGF-β inhibitor showed divergent effects. Our results indicate that, despite a non-conforming residual activity profile, the KiR analysis successfully predicted a subset of KIs that would provide barrier-restorative effects.

We also demonstrated that predicted barrier-restorative KIs can induce the restoration of junctions. IF image analysis characterizing EC morphology and junctional shape in microvessels showed that DMSO vehicle control-treated BEB microvessels exhibited elongated actin structures (Figure 3.7 **H**; left image) and internalization of VECAD into the cytoplasm (Figure 3.7 **H**; right image), indicating phosphorylated VECAD and loss of intact junctions. In BEB vessels treated with predicted drugs (ROCK inhibitor, AG490, and P38 inhibitor) that ameliorated barrier permeability, all three drugs also showed enhanced VECAD recovery. ROCK inhibitor-, AG490-, and P38 inhibitor-treated BEB microvessels exhibited increased VECAD recovery; however, no striking changes in actin structure were observed (Figure 3.7 **H–K**; right image). Compared to the control, all three predicted KIs were able to repair VECAD junctions, reducing the percentage of

discontinuous VECAD boundaries (Figure 3.7 **M**) and successfully decreasing internalization of VECAD in the cytoplasm (Figure 3.7 **N**) compared to the DMSO control. However, only the ROCK inhibitor showed significant recovery of junctions (Figure 3.7 **L**). As shown by minimal changes in actin structure, the shape index (circularity) of ECs treated with predicted KIs showed no significant changes compared to DMSO-treated microvessels.

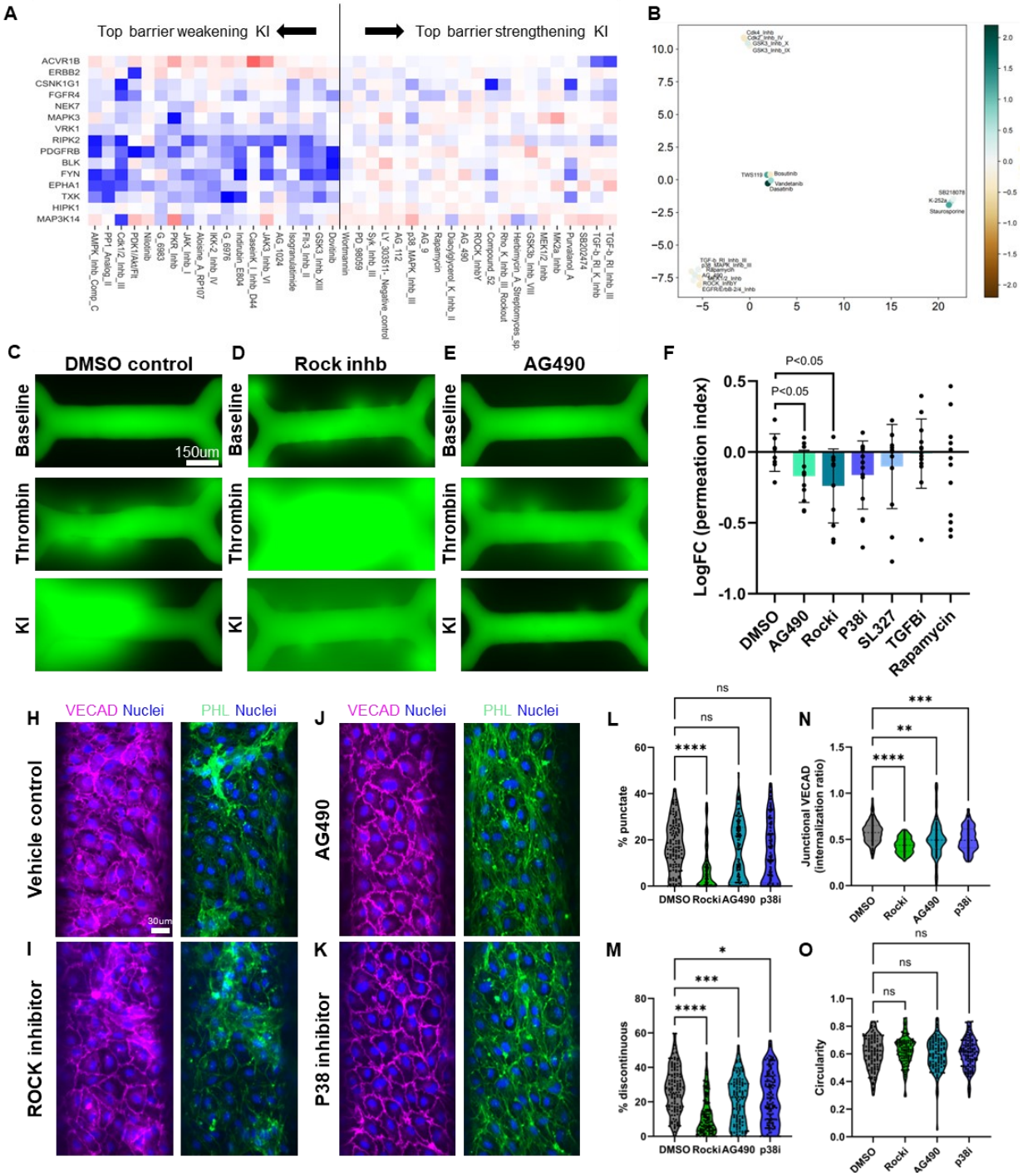


**Figure 3.7 KIR prediction of novel barrier-restorative targets.**

(A) Kinase target and kinase inhibitor predictions from KIR based on permeation index obtained from 12 KI screenings in thrombin-activated vessels. The X-axis shows a subset of kinase inhibitors predicted to be barrier-strengthening (right of vertical axis) and barrier-weakening (left of vertical axis). The Y-axis shows 15 kinase targets predicted from combined 0.2 U/ml and 1 U/ml thrombin treatment conditions. Red indicates activation of kinase

targets and blue indicates inhibition of kinase targets. (B) UMAP representation of kinase inhibitors selected from top barrier-strengthening KIs. Most of the predicted KIs clustered with EGFR/ErbB inhibitors, suggesting that most of the predicted targets have similar kinase residual activity to EGFR/ErbB inhibitors. (C–F) Validation of predicted kinase inhibitors in thrombin (1 U/ml) activated BEB microvessels. Compared to (C) vehicle control, three KIs—(D) ROCK inhibitor, and (E) AG490 —show the most promising potential for restoring the barrier following thrombin activation. (F) Normalized permeation index quantified from permeability analysis of 6 predicted kinase inhibitors, identifying the best at strengthening barriers following thrombin injury (n=8–13). (H–K) Immunofluorescence images of BEB microvessels fixed immediately after permeability imaging following 2 hours of KIR-predicted KI treatment in thrombin-activated BEB microvessels. IF images show treatment with (H) DMSO control, (I) ROCK inhibitor, (J) AG490, and (K) P38 inhibitor. Right images show nuclei (DAPI; blue) and actin (PHL; green); left images show nuclei (DAPI; blue) and VECAD junctions (magenta). Quantification of VECAD structures using % discontinuous in (L) barrier-restorative predicted KIs shows a significant decrease in the % of cells with discontinuous VECAD junctions compared to DMSO control. Quantification of VECAD structures using % punctate in (M) barrier-restorative predictions further highlights ROCK inhibitor as the best candidate with potential for junctional recovery. (N) Internatlization ratio shows that ROCK inhibitor exhibits least internalization, suggesting higher VECAD localization at the cell peripery. (O) Circularity index. Predicted drug in all cases do not exhibit significant cell shape changes.

### *3.4.8 TBI plasma predicted drug prediction*

To investigate the barrier-restorative potential of kinase inhibitors (KIs) in response to TBI patient plasma, we tested a subset of predicted KIs in TBI patient plasma-treated BEB microvessels and performed a permeability assay. TBI patient plasma samples (N = 9) were treated, simulating the conditions of barrier dysfunction observed in traumatic brain injury-induced coagulopathy (TBI-IC). Permeability was then assessed following treatment with DMSO (control) and two KIs predicted to enhance barrier integrity: ROCK inhibitor and AG490, as well as two additional KIs that were the most barrier-restorative from KI screening.

Dextran perfusion images in the DMSO control condition showed a marked increase in permeability upon plasma activation, consistent with barrier disruption (Figure 3.8 **A**). The baseline images captured one day prior to thrombin activation (D-1) demonstrated minimal dextran leakage (Figure 3.8 **A**; top panel), indicating an intact barrier. Following 6-hour treatment with TBI patient plasma (Figure 3.8 **A**; middle panel), the permeability significantly increased, evidenced by dextran leakage into the surrounding matrix. Treatment with ROCK inhibitor and

AG490 post-thrombin activation exhibited partial restoration of barrier function, as indicated by a reduction in dextran leakage after 2 hours of KI treatment (Figure 3.8 **B** and **C**; bottom panel).

To further evaluate the effect of KIs on endothelial cell (EC) junction integrity, we performed immunofluorescence staining for vascular endothelial cadherin (VECAD), a key component of endothelial adherens junctions. DMSO-treated BEB microvessels pre-treated with TBI plasma exhibited clear VECAD internalization, as indicated by cytoplasmic VECAD staining (Figure 3.8 **D**; c). However, BEB microvessels treated with ROCK inhibitor (Figure 3.8 **D**; middle image) and AG490 (Figure 3.8 **D**; right image) exhibited enhanced VECAD junction recovery, with more VECAD localized at cell junctions. This suggests that ROCK inhibitor and AG490 not only recover overall barrier integrity but also promote the relocalization of VECAD to cell-cell junctions.

To quantitatively assess the barrier-restorative effects of the KIs, we calculated the permeability index for thrombin-activated BEB microvessels treated with TBI plasma, AG490, ROCK inhibitor, P38 inhibitor, CDK2 inhibitor (KI4), and CDK4 inhibitor (KI5). Notably, ROCK inhibitor and AG490 demonstrated the greatest reduction in permeability index compared to the DMSO control, underscoring their potential as barrier-stabilizing agents in TBI plasma-disrupted microvessels (Figure 3.8 **E**). Despite the variance in TBI plasma samples, which derives from inter-patient variability and the severity of TBI-induced inflammatory effects, in the majority of TBI patient plasma-treated microvessels, barrier-restoring KIs promoted recovery of the BEB (Figure 3.8 **F**).

In summary, permeability imaging and IF analysis collectively demonstrate that ROCK inhibitor and AG490 significantly restore endothelial barrier integrity in TBI patient plasma-activated BEB microvessels. These KIs not only reduce permeability but also promote VECAD relocalization to cell junctions, indicative of enhanced junctional stability. Our findings highlight ROCK inhibitor

and AG490 as promising candidates for mitigating barrier dysfunction in thrombin-induced endothelial injury.

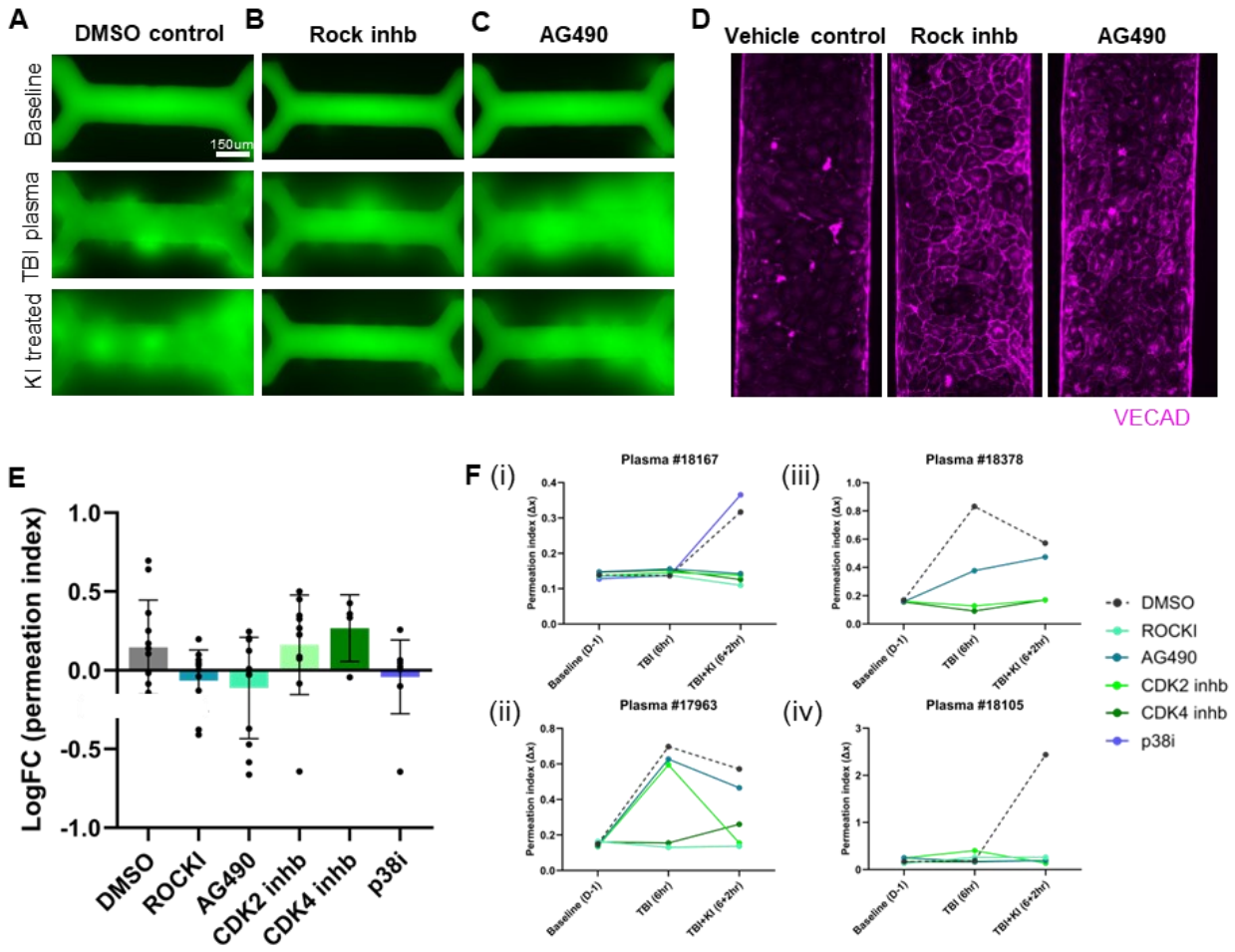


**Figure 3.8 Predicted KIs AG490 and ROCK inhb promotes barrier restorative effect in TBI patient plasma induced barrier breakdown.**

70kDa dextran perfused images of BEB microvessels activated with TBI patient plasma (n=8 plasma samples). (A) DMSO control and two predicted KIs that significantly increased permeability in thrombin-activated microvessels: (B) ROCK inhibitor and (C) AG490. Top images show baseline permeability imaged at D-1; middle images show vessels after 6 hrs of TBI patient plasma treatment; and bottom images show vessels after 2 hours of KI treatment. (D) Immunofluorescence images of BEB microvessels fixed immediately after permeability imaging following 2 hours of KI treatment in TBI patient plasma-treated BEB microvessels for (i) DMSO control, (ii) ROCK inhibitor, and (iii) AG490. Images are stained for endothelial junctions (VECAD; magenta). (E) Permeability index (Log fold change) quantification of 70kDa dextran permeability imaging for DMSO, AG490, ROCK inhibitor, p38 inhibitor, CDK2 inhibitor (KI4), and CDK4 inhibitor (KI5). KIs were treated for 2 hours in TBI patient plasma-treated BEB microvessels (F) Permeation index plot for individual TBI plasma samples at baseline (D-1), after TBI plasma treatment (6hr) and following KI treatment (6+2 hr) for (i) plasma # 18167, (ii) plasma # 17963, (iii) plasma # 18378

and (iv) plasma # 18105. Dot plot shows permeation index for vessels used for treatment of DMSO (grey; dotted), ROCK inhibitor (cyan), AG490 (turquoise), CDK2 inhb (light green), CDK4 inhb (green) and p38i (purple).

### 3.5 Discussion and conclusion

The development of a perfusable human brain endothelial cell (HBEC) model in this study represents a significant advance in modeling blood-brain barrier (BBB) function and injury response in 3D perfusable BEB microvessels. Through the fabrication of BEB microvessels, we generated a robust endothelial barrier model that can be perturbed to investigate how the EC barrier changes with injury stimuli and how the barrier recovers with therapeutic agents. The incorporation of human brain microvascular endothelial cells (HBMECs) facilitated the formation of lumenized microvessels with robust junctional protein expression, validated through immunofluorescence (IF) staining of critical junctional markers such as claudin-5, ZO-1, and VECAD. The microvessel model demonstrated an intact endothelial barrier for up to 70 kDa dextran, allowing for reliable assessment of barrier integrity under various experimental conditions.

Kinase pathways are known to regulate cell-cell junctions, cell-matrix junctions, and the reorganization of cortical actin structures, as well as the recycling of adherens junctions in endothelial cells. As such, kinase inhibitors are heavily implicated in both the disruption and restoration of endothelial cell barriers. In addition, studies have shown that human endothelial cells harbor more than 2,000 thrombin-regulated phosphorylation sites for kinases, which implies that, with correct identification methods, specific kinase inhibitors can serve as promising therapeutics for stabilizing endothelial barriers in trauma-induced coagulopathy. Previous work by Dankwa et al.[198] showed the potential of utilizing the polypharmacology of kinase inhibitors through a system-based approach known as kinase regression, a predictive computational model built on pre-existing activity profiles of kinase inhibitors to observe and predict EC cell shape changes following

inflammatory stimuli in 2D. In our study, we utilized 12 selected predictive KIs from 2D studies with the best predictive potential in KiR to investigate the use of KiR with functional permeability parameters in 3D microvessels, identifying therapeutic targets that can ameliorate barrier disruption in the early phase of TBI injury.

Our results demonstrate the utility of kinase regression analysis, which successfully predicted barrier-modulating kinases based on permeability index data from KI screenings. The predictive capacity of the KiR model allowed us to identify kinases with barrier-strengthening effects, such as the ROCK inhibitor, AG490, and the P38 inhibitor, which were validated as promising candidates for barrier restoration. The ROCK inhibitor and AG490, in particular, showed a robust capacity to reduce permeability and promote the relocalization of VECAD at cell junctions in thrombin- and TBI plasma-activated microvessels. These findings align with existing literature indicating the importance of ROCK signaling pathways in maintaining endothelial barrier stability and suggest a novel therapeutic approach for enhancing BBB integrity in the context of endothelial injury.

Moreover, our data reinforce the relevance of thrombin activation as a model for BBB disruption in conditions mimicking TBI. Thrombin, which is elevated in TBI patients, led to substantial permeability increases and endothelial junctional disruption in our 3D microvessels, providing a physiologically relevant model for studying BBB breakdown. The subsequent treatment with KIs in thrombin-activated vessels revealed that barrier-restorative agents can mitigate the permeability effects of thrombin and partially restore junctional integrity. This finding is particularly valuable for therapeutic applications targeting secondary brain injuries, where the loss of endothelial integrity exacerbates neurological outcomes.

In summary, our study highlights the potential of a 3D perfusable microvessel model to advance our understanding of BBB dynamics in diseases involving BEB breakdown. By integrating this 3D model with KI screening and KiR machine learning, we offer a scalable platform for identifying kinase targets and therapeutic inhibitors that can modulate endothelial barrier properties. Future work should aim to refine KiR predictions with larger KI libraries and investigate long-term barrier restoration outcomes in our 3D BBB model.

# Chapter 4: Guiding Vascular Cell Fate and Architecture: Developing Blood-Brain Barrier-Like Features in Human Blood Vessel Organoids.

## 4.1 Abstract

Developing an *in vitro* model that replicates the complexity of the blood-brain barrier (BBB) and neurovascular interactions is essential for advancing our understanding of brain-specific vascular functions. In this study, we leverage human vascular organoids (hVOs) to generate neurovascular organoids by incorporating key neurovascular cell types, leading to the development of BBB-like properties within the blood vessels of hVOs. Brain vasculature is known to co-develop with neurons during brain maturation, and astrocytes — major producers of retinoic acid in the developing brain — play an essential role in enhancing BBB properties by supporting tight junction expression and other BBB-specific functions.

A significant challenge in vascular biology is understanding how vasculature acquires and maintains organ-specific traits. While endothelial cells (ECs) demonstrate unique tissue-specific phenotypes *in vivo*, they tend to lose this specialization in standard culture conditions, underscoring the importance of the surrounding parenchyma in maintaining vascular identity. Within the neurovascular unit, glial cells such as astrocytes provide critical paracrine signals essential for BBB formation, maintenance, and endothelial specification. In our neurovascular organoid model, the inclusion of astrocytes and neurons supports brain-specific EC maturation, aligning with developmental processes observed in the human brain. This model offers a physiologically relevant platform for studying BBB development, homeostasis, and dysfunction,

enabling insights into neurovascular interactions and providing a robust tool for drug testing and disease modeling.

## 4.2 Introduction

The brain's unique vasculature is characterized by highly specialized endothelial cells (ECs) that form the blood-brain barrier (BBB), a critical structure for maintaining neural homeostasis and protecting the central nervous system (CNS) from toxins and pathogens. This selective barrier, formed by tight junctions between endothelial cells, is supported by interactions with astrocytes, neurons, and pericytes, collectively known as the neurovascular unit (NVU). The development of this highly regulated vascular phenotype is driven by coordinated differentiation and interaction among various cell types originating from distinct germ layers. While neurons and astrocytes arise from the ectoderm, endothelial cells are derived from the mesoderm, presenting a significant challenge for recreating neurovascular units *in vitro*, where controlled co-development of these diverse cell types is essential for the formation of a functional BBB *in vivo*.[201]

*In vivo*, brain endothelial cells acquire their unique phenotype through interactions with surrounding neuronal and glial cells, with astrocyte-derived retinoic acid signaling recognized as a key driver of brain-specific endothelial characteristics[202]. However, modeling these interactions *in vitro* remains challenging. Traditional blood vessel organoid models often lack the cellular complexity of the NVU, as they typically consist only of endothelial cells. While some co-culture approaches have integrated astrocytes or neurons separately, these models fail to replicate the full spectrum of neurovascular interactions, limiting their utility for studying brain-specific vascular function and BBB properties.

A significant challenge in vascular biology is understanding how vasculature acquires organ-specific characteristics and remodels to support each organ's unique functions. Studies have shown that endothelial cells (ECs) lose their tissue-specific phenotype when cultured outside their native environment, underscoring the importance of tissue parenchyma in maintaining vascular specificity.[38] Within the BBB, glial cells provide essential paracrine signaling that drives the formation, homeostasis, and specification of the barrier, including the regulation of endothelial tight junctions and brain EC glucose transporters. Astrocytes, in particular, are a primary source of retinoic acid, which enhances BBB properties in the developing brain. However, it remains unclear whether the incorporation of glial cells like astrocytes and neuronal cells in human vascular organoids (hVOs) would promote the acquisition of brain-specific microvascular characteristics. Mapping the transcriptomic profile of astrocyte- and neuron-co-cultured hVOs could provide crucial insights into engineering brain-specific vascular models, potentially transforming BBB modeling and enabling new opportunities to study microvascular diseases and cerebrovascular dysfunctions, such as cerebral small vessel diseases and stroke.

This study offers a novel platform for investigating neurovascular development and BBB function, providing a more physiologically relevant model for understanding the role of the NVU in health and disease. Our findings have potential implications for studying neurovascular interactions, modeling cerebrovascular complications in neurodegenerative diseases, and screening therapeutic agents targeting the BBB.

## 4.3 Methods

### *4.3.1 Human pluripotent stem cell and primary cell culture*

Primary human astrocytes (HA), human induced pluripotent stem cell derived cortical neurons (hiPSC-CN) and human induced pluripotent stem cell derived vascular organoids were used in this

study (hVOs). Primary HA (ScienCell; CC #1800) was purchased from ScienCell and used between passge between 2-4. HA was maintained in tissue culture flasks coated with poly-l-lysine (PLL; ScienCell; CC #0403) and cultured with astrocyte medium (AM; ScienCell; CC #1801) conatiang 5% fetal bovine serum (FBS; Cat #0010) and 1% astrocyte growth supplement (AGS; ScienCell; CC #1852) and 1% Penicillin/streptomycin solution (P/S; ScienCell; CC #0503), Cells were maintained at 37 °C in a 5% CO2 incubator and media was replaced every 3 days. hVOs were generated from either a male WTC-11 human induced pluripotent stem cells (Coriell, Cat# GM25256) or a MTM REUS2 embryonic stem cell line and hiPSC-CN were generated from a wild-type male stem cell line with CV background hiPSC line. Both hiPSC cell lines were maintained on Matrigel (Growth factor reduced basement membrane matrix; Corning; CC #356231) coated plates and cultured in mTeSR™ Plus medium (Stemcell Technologies; CC #100-0276) at 37°C in a 5% $CO_2$. Media replenishment for Stem cells occurred daily.

*4.3.2 Human vascular organoid differentiation*

<u>WT hVO differentiation</u>

Human induced pluripotent stem cells (hiPSCs) were differentiated into hVOs by optimizing a previously published protocol (ref). Both mTm REUS2 embryonic stem cells and WTC-11 hiPSCs were used to generate hVOs. Briefly, hVOs were differentiated from stem cell colonies cultured in Matrigel-coated plates by dissociating cells using versene (ThermoFisher; CC# 15040066) treatment for 3 minutes. Versene was aspirated, and cells were directly collected in embryonic body medium (mTeSR +) supplemented with 20 μM Y-27632 (Tocris; CC# 4423) for survival. Stem cells were plated in an ultra-low attachment six-well plate (Corning Costar; CC# CLS7007) at a seeding density of 5 × 10^5 cells per well. The next day (D0; mesoderm induction day),

embryonic bodies were induced into mesoderm aggregates via mesoderm induction medium containing N2B27 media composed of 1:1 Neurobasal media (Gibco; CC# 21103049) and DMEM/F12 media (Gibco; CC# 11330032), supplemented with N2 supplement (Gibco; CC# 17502048), vitamin A-free B27 supplement (Gibco; CC# 12587010), Glutamax, and P/S. N2B27 media was supplemented with 12 μM CHIR99021 and 30 ng/ml BMP-4 (Peprotech; CC# 120-05ET) for WNT and BMP4 activation into lateral plate mesoderm. EBs were gently stirred daily to prevent the formation of larger aggregates. On day 3 and 4 (vascular progenitor induction days), mesoderm aggregates were switched to vascular lineage induction media containing N2B27 media, 100 ng/ml VEGF-A (Peprotech; CC# 100-20-250UG), and 2 μM Forskolin (Sigma; CC# F3917). On D5 (embedding day), vascular progenitor aggregates were embedded in a collagen I-Matrigel (Col-Mat) matrix in 12-well plates. Each 12-well plate contained 30–40 organoids. Two individual layers of Col-Mat encapsulated the hVO; the bottom layer was prepared by mixing Col-Mat solution on ice and applying 500 μl in each well of a 12-well plate. The bottom layer was gelled in an incubator at 37°C for 1 hour. The top layer was prepared by creating an organoid-laden Col-Mat solution by adding vascular progenitors to ice-cold Col-Mat. 500 μl of organoid-laden Col-Mat solution was applied on top of the gelled bottom Col-Mat layer and incubated for 2 hours for gelation.

BBB-mimicking hVO differentiation

BBB-mimicking hVOs were generated by co-culturing human primary astrocytes with hVOs. The induction of vascular progenitors was conducted similar to the previously described differentiation protocol until D5. On the embedding day, primary HAs were harvested from tissue culture plates using 0.25% trypsin-EDTA and resuspended in AM media. Collected cells were diluted to adjust for a seeding density of 0.5M cells per ml to be mixed in Col-Mat solution. After calculating the

exact amount of HA needed for embedding, HA was centrifuged and resuspended in Col-Mat solution. HA-supplemented Col-Mat solution was used to generate the bottom and top layers harboring hVOs.

Neurovascular hVO differentiation

Neurovascular hVOs were generated by co-culturing human primary astrocytes and hiPSC-CNs with hVOs. The induction of vascular progenitors was conducted similar to the previously described differentiation protocol until D5. On the embedding day, primary HAs were prepared as described in the previous section. In addition to HA, hiPSC-CNs were dissociated with Accutase (Innovative Cell Tech; CC# AT104-500) and collected in Neural Differentiation media. hiPSC-CNs were diluted to adjust for a seeding density of 1M cells per ml to be mixed in Col-Mat solution. After calculating the exact amount of HA needed for embedding, HA was centrifuged and resuspended in Col-Mat solution. HA- and hiPSC-CN-supplemented Col-Mat solution was used to generate the bottom and top layers harboring hVOs.

After 7 days of vascular network formation in Col-Mat matrix (D12), the differentiated vascular networks were dissected into individual vascular networks using a dissection scope and sterile 25G needles. Individual vascular networks were transferred to a low-attachment U-bottom 96 well plates for compaction into final hVO form. Media was changed every 3 days.

*4.3.3 Embedded hVO culture media optimization*

After embedding hVOs in Col-Mat matrix, organoids were cultured in vascular organoid medium for rest of the culture period. Culture media was optimized to allow survival of neuronal cell types as well as to promote vascularization in hVOs. The original hVO medium consisted of 2 mL of

pre-warmed (37°C) StemPro-34 SFM complete medium upplemented with 15% fetal bovine serum (FBS), 100 ng/mL vascular endothelial growth factor A (VEGF-A), and 100 ng/mL fibroblast growth factor 2 (FGF-2). The optimized medium included 1:1 Stempro-34 SFM complete medium : BNMN media supplemented with 10% FBS, 100 ng/mL VEGF and 100 ng/mL FGF-2, 0.2 mg/mL brain-derived neurotrophic factor (CC# 450–02; PeproTech) and 0.2 mg/mL glial-cell-derivedneurotrophic factor (CC# 450–10; PeproTech).

*4.3.4 Cortical neuron differentiation and culture*

Human induced pluripotent stem cells (hiPSCs) were directed to neuronal differentiation as previously described by Rose et al. (2018).[163] To begin, hiPSCs were seeded at a density of 3.5 million cells per well onto 6-well plates coated with Matrigel (growth factor reduced; #356231, Corning) and maintained in Basal Neural Maintenance Medium. This medium consisted of a 1:1 mix of DMEM/F12 (#11039047, Life Technologies) and Neurobasal media (#21103049, GIBCO), with additional supplements: 0.5% N2 supplement (#17502-048, Thermo Fisher Scientific), 1% B27 supplement (#17504-044, Thermo Fisher Scientific), 0.5% GlutaMax (#35050061, Thermo Fisher Scientific), 0.5% insulin-transferrin-selenium (#41400045, Thermo Fisher Scientific), 0.5% non-essential amino acids (#11140050, Thermo Fisher Scientific), and 0.2% β-mercaptoethanol (#21985023, Life Technologies). The medium also included 10 μM SB-431542 and 0.5 μM LDN-193189 (#1062443, Biogems). The cells received fresh media daily for seven days. On day eight, the cells were treated with Versene (#15640066, GIBCO), gently detached with cell scrapers, and split at a 1:3 ratio. On day nine, the medium was changed to Basal Neural Maintenance Medium with an added 20 ng/mL FGF (R&D Systems, Minneapolis, MN), and daily feeding continued. On day sixteen, cells were passaged at a 1:3 ratio and fed daily until approximately day twenty-three.

At that point, fluorescence-activated cell sorting (FACS) was performed to select for CD184/CD24 (#557145/561646, BD PharMingen) positive and CD44/CD271 (#555479/557196, BD PharMingen) negative cells, isolating a neural precursor cell (NPC) population, as described by Yuan et al.[203] The sorted NPCs were expanded to initiate further neural differentiation. For differentiation into cortical neurons, NPCs were plated at a density of 6 million cells per 10 cm plate. After 24 hours, the cells were switched to Neural Differentiation Medium (DMEM/F12 with Glutamine, 0.5% N2 supplement, 1% B27 supplement, and 0.5% GlutaMax) containing 0.2 µg/mL brain-derived neurotrophic factor (#450-02, PeproTech), 0.2 µg/mL glial-cell-derived neurotrophic factor (#450-10, PeproTech), and 0.5 M dbcAMP (#D0260, Sigma Aldrich).

*4.3.5 Whole-organoid immunofluorescence staining and mounting.*

WT and co-cultured vascular organoids were fixed with 4% paraformaldehyde (PFA) at room temperature for 1 hour, followed by three washes in phosphate-buffered saline (PBS) for 30 minutes each. Whole-organoid immunofluorescence staining was initiated by blocking the organoids with a blocking buffer containing 3% FBS, 1% bovine serum albumin (bioWORLD; CC# 2207004), 0.5% Triton X-100 (Sigma; CC# 93420), 0.5% Tween 20 (Sigma; CC# P7949), and 0.01% (wt/vol) sodium deoxycholate solution (SD solution; prepared by adding 1 mL of 1% stock solution made by dissolving 1 g of sodium deoxycholate (Sigma; CC# D6750) in 100 mL of deionized water) for 2 hours.

Following the blocking step, primary antibodies were applied in the blocking buffer. The antibodies used in this study include ZO-1 (1:500), VECAD (conjugated-APC; 1:100), GLUT-1 (1:1000), CD31 (1:100), GFAP (conjugated; 1:500), MAP2 (1:1000), and TUJ1 (1:1000). Primary antibodies were incubated on a rocking shaker at 37°C overnight and washed three times for 20 minutes each using PBS-T solution (1% Tween in PBS). Secondary antibody staining was

conducted by incubating organoids on a 37°C shaker for 4 hours, with Hoechst 33342 added for nuclear staining. Organoids were washed twice with PBS-T and given a final wash with PBS.

Following staining, organoids were mounted on a coverslip separated by an iSpacer 0.55 mm (SUNJin Lab; CC# IS008). Organoids were mounted on the iSpacer with RapiClear 1.49 (SUNJin Lab; CC# RC149001) mounting medium to ensure full clearing of the organoid structure for confocal imaging. Cleared organoids were imaged using a Leica SP8 confocal microscope and processed using ImageJ or IMARIS imaging analysis software.

## 4.4 Results

### *4.4.1 Generating co-and tri-cultured vascular organoids towards neurovascular organoids*

Brain vasculature develops from the perineural vascular plexus, along with the development of neuroblasts into neurons, astrocytes and oligodendrocytes in the brain[204]. This synchronized development of brain endothelial and neuronal cells is crucial for establishing a brain-specific vascular phenotype. In particular, the retinoic signaling from astrocytes have been known to be a key driver of brain EC phenotype[202]. However, the distinct germ layer origins of neurons (ectoderm), astrocytes (ectoderm), and vascular networks (mesoderm) present a substantial challenge for achieving coordinated differentiation *in vitro*.

To explore whether vascular structures can adopt brain-specific characteristics and create neurovascular organoid models, we developed a novel protocol that mimics neurovascular co-development by integrating neuronal cell types into the differentiation process of human vascular organoids (hVOs) (Figure 4.1). hVOs were differentiated from the WTC-11 hiPSC line by optimizing a previously published blood vessel organoid protocol [80]. Briefly, WTC-11 hiPSCs

were plated in low-attachment well plates for embryonic body (EB) formation. Wnt agonist CHIR99021 and bone morphogenetic protein 4 (BMP4) were applied to EBs at Day 0 to induce hiPSCs into the mesoderm lineage. On Day 3, vascular endothelial growth factor-A (VEGF-A) and forskolin were administered to facilitate the differentiation of mesodermal aggregates into vascular progenitor cells. By Day 5, the developing organoids were embedded within a composite matrix of collagen I and Matrigel (Col-Mat) to promote vascular sprouting and lumen formation.

To generate a blood-brain barrier-mimicking cerebrovascular organoid, we incorporated primary human astrocytes into the Col-Mat matrix at Day 5 of the hVO differentiation protocol. Primary astrocytes, cultured on poly-L-lysine-coated tissue culture plates, were harvested and mixed into the Col-Mat at a density of 0.5 million cells per milliliter (M/ml). For neurovascular organoid formation, both primary astrocytes and hiPSC-derived cortical neurons (hiPSC-CNs) were embedded in the Col-Mat matrix at densities of 0.5 M/ml and 1 M/ml, respectively. The hiPSC-CNs were differentiated from a CV hiPSC line using dual SMAD inhibition as previously described. Briefly, CV hiPSCs were differentiated into neural progenitor cells (NPCs) over a period of three weeks, after which they underwent an additional three weeks of differentiation into neurons. At the end of the six-week protocol, cultures were enriched with cortical neurons (CNs) and maintained in neuronal maturation media for up to two weeks prior to co-culture with hVOs. Both cell types—human astrocytes (HA) and hiPSC-CNs—were incorporated into the hVO at the vascular progenitor stage, prior to the onset of angiogenesis and vascular sprouting within the matrix, thereby simulating the developmental co-differentiation of neuronal and glial cells in the formation of a mature neurovascular unit.

The embedded organoids were cultured in Col-Mat for 7 days to promote interactions between the co-cultured neuronal and glial cells and the developing vascular networks within the hVO.

The co- and tri-cultured organoids were maintained in low-serum blood vessel maturation media supplemented with neuronal growth factors—brain-derived neurotrophic factor (BDNF) and glial cell line-derived neurotrophic factor (GDNF)—for the remaining culture period. On Day 12, the organoids were dissected and transferred to suspension culture to facilitate compaction into wild-type hVOs (without co-cultured cells), BBB-mimicking hVOs (co-cultured with astrocytes only), and neurovascular organoids (co-cultured with astrocytes and hiPSC-CNs).

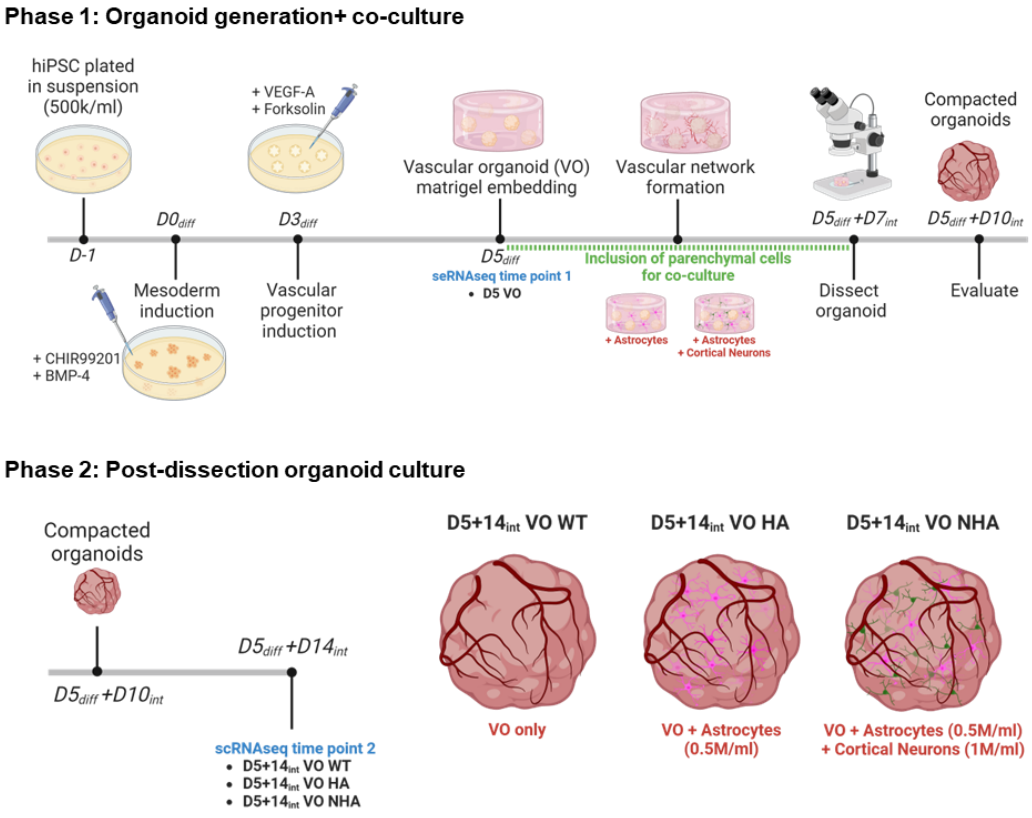


**Figure 4.1 Schematic overview of hVO differentiation and co-culture methods for generating BBB-mimicking hVOs and neurovascular hVOs.**

Organoid differentiation is divided into two phases: Phase 1 involves the induction of WTC-11 hiPSCs into the mesoderm lineage (D0; BMP-4 and CHIR99021) and further commitment into vascular progenitors (D3; VEGF-A and Forskolin). On D5 (D5diff), organoids are embedded into a matrix composed of collagen I and Matrigel. To generate a BBB-mimicking hVO, primary human astrocytes are mixed into the matrix at a density of 0.5M/ml. To generate a neurovascular hVO, both primary human astrocytes and hiPSC-CNs are mixed into the matrix at densities of 0.5M/ml and 1M/ml, respectively. hVOs are cultured in the matrix by cross-linking the matrix containing organoids in the incubator. During the 7-day culture in the Col-Mat matrix, hVOs undergo angiogenesis, forming

vascular sprouts and lumens. At D12 (D5diff +D7int), individual organoids are dissected from the gel and suspension-cultured in low-attachment 96-well plates. Phase 2 of organoid culture involves maintaining dissected organoids with media changes every 3–4 days. The culture media for maintaining organoids was optimized to promote the survival of human astrocytes and hiPSC-CNs within organoids while promoting the differentiation of vascular networks between D5–D12.

### *4.4.2 Co-cultured neuronal and glial cells interact and drive distinct angiogenic sprouting in hVOs*

To investigate the interactions between parenchymal cell types and hVOs during angiogenic sprouting and vascular differentiation, we characterized hVO sprouting within a collagen-Matrigel (Col-Mat) matrix (Figure 4.2 **A**). A few hours after embedding, co-cultured hVOs demonstrated interactions with primary human astrocytes (HAs) and hiPSC-derived cortical neurons (hiPSC-CNs), evidenced by astrocytic processes and neurite projections extending toward the periphery of the vascular progenitor spheroid (Figure 4.2 **A** ii and iii). By three days post-embedding, hVOs in co-culture conditions exhibited more pronounced differentiation and cellular remodeling (Figure 4.2 **A** v and vi) compared to hVOs cultured alone, which showed less remodeling and limited network expansion (Figure 4.2 **A** iv). These observations suggest that the presence of neuronal cells enhances angiogenesis and supports more extensive vascular network formation in co-cultured environments.

Next, we evaluated whether the neurovascular organoid media could support neuronal and glial cell viability while promoting a robust vascular network structure from vascular progenitor aggregates (Figure 4.2 **B**). Prior findings indicated that reduced serum levels in vascular organoid media decreased vascular network sprouting, leading to the presence of dense cellular aggregates of inefficiently differentiated vascular progenitors that prevented successful vascular network formation in hVOs. Conversely, serum levels in the original protocol resulted in increased neuron-

to-astrocyte conversion in hiPSC-CN cultures. Thus, evaluating cell survival, homogeneity, and vascular network integrity was essential to assess the efficacy of our protocol.

To characterize the presence of endothelial cells, astrocytes, and neurons within the neurovascular organoids, D22 organoids were fixed with 4% PFA and analyzed via immunofluorescence (IF) staining. IF imaging confirmed the presence of CD31 positive endothelial cells (Figure 4.2 **B** i), glial fibrillary acidic protein (GFAP) positive astrocytes (Figure 4.2 B ii), and microtubule-associated protein 2 (MAP2) positive neurons (Figure 4.2 **B** ii). Notably, GFAP-expressing astrocytes were predominantly localized near the organoid core, whereas MAP2-positive neurons were more abundant near the periphery (Figure 4.2 **B** ii). CD31 staining revealed a well-structured vascular network with extensive sprouts throughout the organoid volume, without evidence of a dedifferentiated core.

A closer examination of cellular interactions within the organoid demonstrated that β III-tubulin-positive neurite projections were frequently positioned near vascular structures, with both dendritic and axonal projections associating with the vasculature, suggesting potential innervation (Figure 4.2 **C**). Furthermore, GFAP positive astrocytic processes were found closely aligned with endothelial tubes, where astrocytes extended their end-feet to encapsulate the abluminal surface of capillaries (Figure 4.2 **D**). These results indicate the successful formation of a neurovascular niche within the organoids, achieved through our optimized differentiation protocol.

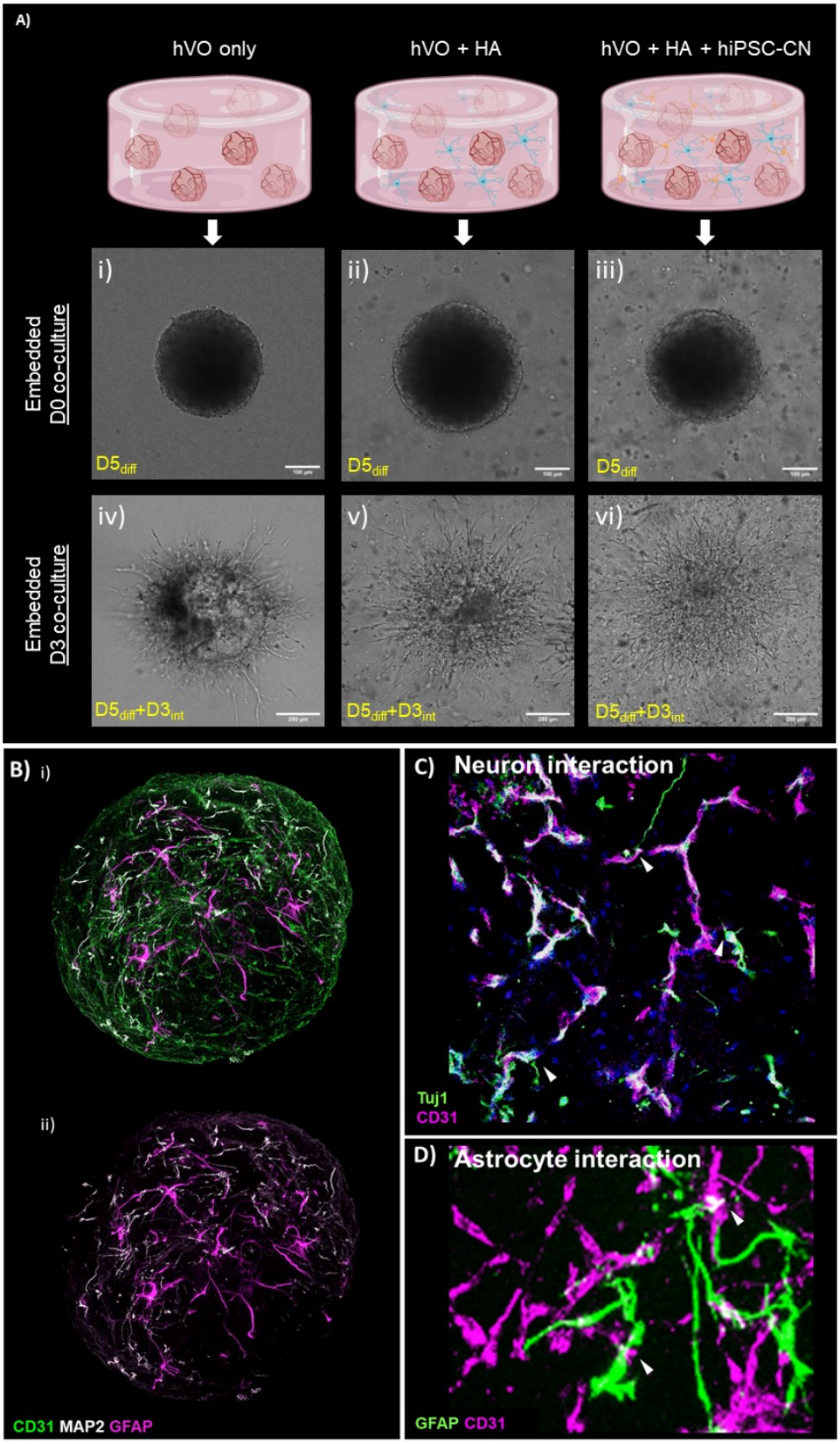


**Figure 4.2 Characterization of hVO differentiation and formation of the neurovascular unit in co-cultured hVOs.**

(A) hVOs cultured alone (WT hVO), hVO co-cultured with human primary astrocytes (BBB-mimicking hVO), and hVO tri-cultured with human primary astrocytes and hiPSC-CNs (neurovascular hVO) were imaged under a brightfield microscope to characterize the formation of vascular sprouts during the gel-embedded culture period. WT hVOs at (i) $D5_{diff}$ undergo limited vascular sprouting by (iv) $D5_{diff}+D7_{int}$, whereas (ii) $D5_{diff}$ BBB-mimicking hVO and (iii) neurovascular organoids start interacting with brain parenchymal cells starting on D0 of co-culture and have undergone extensive hVO differentiation by $D5_{diff}+D3_{int}$. (v) BBB-mimicking hVOs at $D5_{diff}+D3_{int}$ show continued interaction with co-cultured astrocytes, and (vi) neurovascular hVOs show the maintenance of both neurons and astrocytes at $D5_{diff}+D3_{int}$. (B) IF staining of hVOs at $D5_{diff}+D14_{int}$, 7 days post-dissection from the Col-Mat matrix, shows the presence of (i) vascular networks (CD31; green), astrocytes (GFAP; magenta), and hiPSC-CNs (MAP2; white). Staining confirms that culture conditions were appropriate for inducing vascular network structures while maintaining the survival of both astrocytes and hiPSC-CNs. (ii) The overall localization of astrocytes and neurons suggests that astrocytes migrate deeper within the core of the hVOs, while hiPSC-CNs remain relatively immobile near the periphery of hVOs. (C) IF image showing neuronal (TUJ1; green) interaction with vascular networks (CD31; magenta). Dendrites and axons interact closely with the vascular networks within hVOs, suggesting possible direct innervation of the microvessels within neurovascular organoids. (D) Maximum projection image reveals the formation of a characteristic neurovascular niche, where astrocytes (GFAP; green) extend their endfeet toward the capillaries (CD31; magenta) of hVOs to form the neurovascular unit.

### *4.4.3 BBB-mimicking hVOs promote cytoskeletal reorganization and acquire key brain EC specific phenotype*

Brain capillaries exhibit a unique endothelial cell (EC) phenotype that distinguishes them from microvascular ECs of other tissues. Key brain-specific features include elevated expression of tight junction proteins, which enhance the regulation of the blood-brain barrier (BBB), and higher expression of glucose transporter proteins, facilitating the efficient transfer of glucose from the bloodstream to meet the brain's heightened metabolic demands. Characterization of overall HA co-cultured organoids compared to WT organoids revealed an increased level of compaction and cytoskeletal reorganization in suspension culture (Figure 4.3 **A**). While the overall organoid structure remains similar up to 7 days after dissection from the Mat-Col matrix (Figure 4.3 **A** i and vi), the astrocyte co-cultured organoids begin to shrink faster and undergo cytoskeletal compaction (Figure 4.3 **A** ix and x), suggesting that the stromal population in co-cultured organoids may be different from that of WT organoids (Figure 4.3 **A** iv and v).

Human vascular organoids (hVOs) derived from mTm hiPSCs display notable compaction and cytoskeletal reorganization when co-cultured with parenchymal cells (Figure 4.3 **A** i-v) compared to hVOs in monoculture conditions (Figure 4.3 **A** vi-x). This preliminary observation suggests that co-culturing with parenchymal cells initiates cell fate changes within the organoids. Future analysis of hVO development will involve scRNA-seq to further examine cellular profiles and provide detailed insights into vascular development within the cell-laden hVOs during a 7-day embedded co-culture period. Notably, while wild-type (WT) hVOs do not express glucose transporter 1 (GLUT1) (Figure 4.3 **B** i) or the tight junction protein ZO-1 (Figure 4.3 **C** i), hVOs co-cultured with astrocytes show significant expression of both GLUT1 (Figure 4.3 **B** ii) and ZO-1 (Figure 4.3 **C** ii) throughout the organoid. Together, these characteristics indicate the acquisition of blood-brain barrier (BBB)-specific molecular features by endothelial cells within BBB-mimicking organoids.

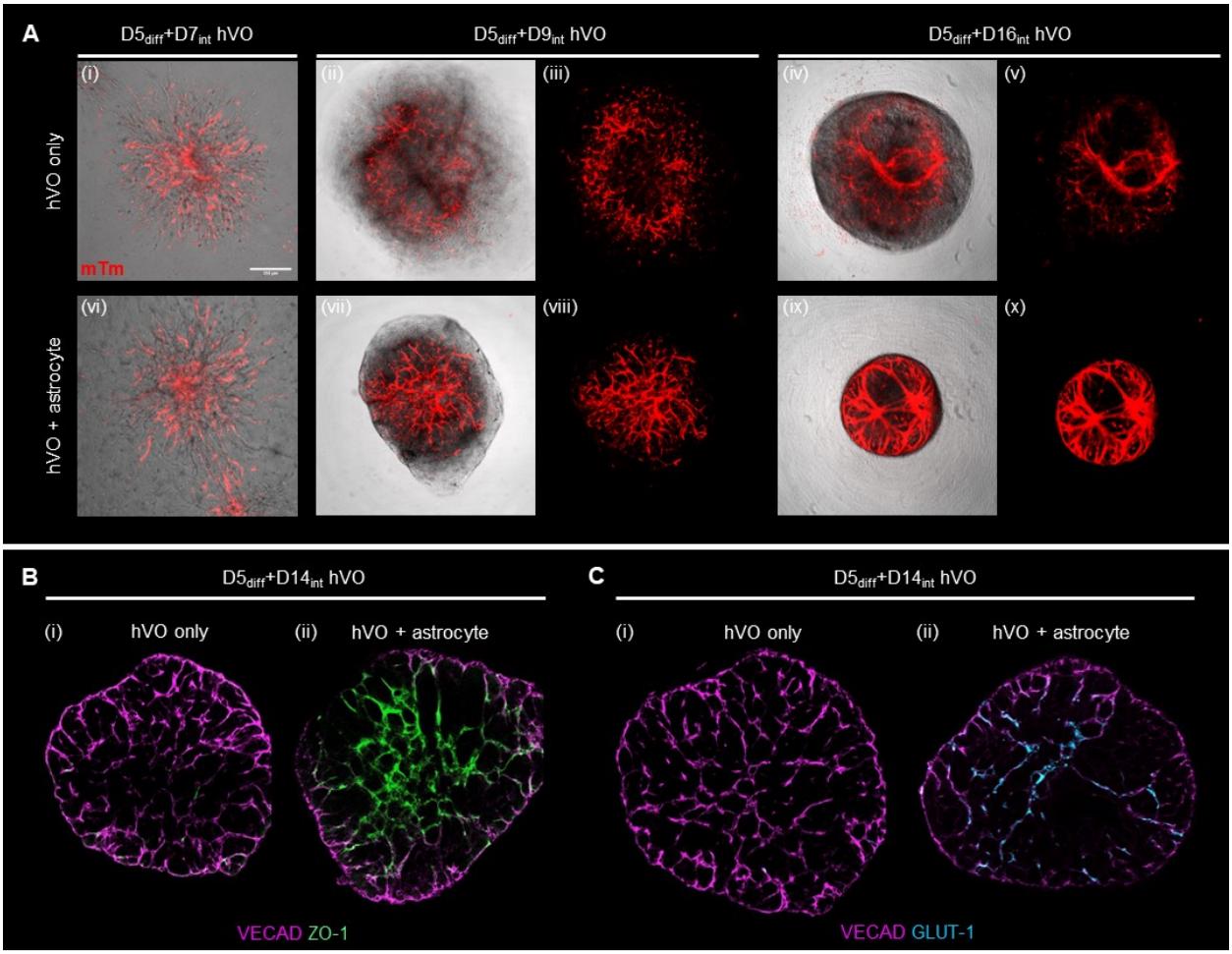


**Figure 4.3 BBB-mimicking hVOs demonstrate cytoskeletal reorganization and increased expression of BBB specific EC signatures.**

(A) hVOs differentiated from Reus2 MTM (red) embryonic stem cells show that organoids in both (i) WT and (vi) BBB-mimicking conditions exhibit similar levels of vascular network structure at D7 ($D5_{diff}$+$D7_{int}$ hVOs) of co-culture within the Col-Mat matrix exhibits similar level of vascular network structure. 2 days after dissection ($D5_{diff}$ +$D9_{int}$ hVOs), (ii and iii) WT hVOs and (vii and viii) BBB-mimicking hVOs compact into spherical organoids with intact network structure. 9 days after dissection ($D5_{diff}$+$D16_{int}$ hVOs), (iv and v) WT hVOs exhibit regression of the network structure but maintain overall size, while (ix and x) BBB-mimicking hVOs compact into smaller spherical organoids with stromal-like cells encompassing the organoid structure. Characterization of brain EC-specific markers ZO-1 and GLUT-1 revealed that (B) tight junction protein expression is significantly reduced in (i) WT hVOs, whereas (ii) BBB-mimicking hVOs show increased expression of ZO-1 (green), co-expressed with VECAD-positive vascular networks within the hVO. (C) The glucose transporter GLUT-1 (cyan) is also significantly reduced in (i) WT hVOs, while (ii) BBB-mimicking hVOs show increased GLUT-1 expression, co-expressed with VECAD-positive vascular networks. These results suggest that co-culturing astrocytes in BBB-mimicking hVOs led to the acquisition of a BBB-specific phenotype in ECs within the hVOs.

*4.4.4 scRNAseq reveals the acquisition of brain-specific endothelial cell (EC) and extracellular marix (ECM)-related transcriptomic profiles in neurovascular organoids*

To characterize and compare the cell populations present in neurovascular organoids, BBB organoids, and wild-type (WT) vascular organoids at the transcriptomic level, we conducted single-cell RNA sequencing (scRNA-seq) of $D5_{diff}$+$D14_{int}$ hVOs derived from WTC-11 hiPSCs. We pooled 4 rounds of organoid differentiation, yielding an average of approximately 600,000 cells per sample, and subsequently loaded a total of 10,000 cells for scRNA-seq analysis. The UMAP representation (Figure 4.4 **A**) of our data indicates no significant shift in the overall cell populations among wild-type (Figure 4.4 **A** i), BBB-mimicking (Figure 4.4 **A** ii), and neurovascular organoids (Figure 4.4 **A** iii). This observation suggests that co-culture at the vascular progenitor stage did not result in the emergence of novel cellular subtypes and that the addition of neuronal cell types alone was insufficient to induce cell fate changes within the vascular networks.

Initial analysis identified 11 clusters generated by the Seurat package (Figure 4.4 **B**). Specifically, clusters 9 and 7 correspond to endothelial cells, marked by *CDH5* and *PECAM1*; cluster 10 comprises neuronal and astrocytic populations, with neurons identified by *SYT1, DCX*, and NSG2, and astrocytes by AQP4, GFAP, and S100B; cluster 11 represents microglial cells, characterized by *AIF1, C1QB,* and *CD68*. Clusters 0, 1, 2, 3, 4, 5, 6, and 8 correspond to perivascular cells. Within the perivascular clusters, clusters 4 and 5 were associated with collagen-producing cells, denoted by *COL1A1, COL4A1*, and *COL25A1*; clusters 0, 2, and 3 were more closely related to fibroblast populations, indicated by *DCN* and *PDGFRA*; and clusters 1 and 8 represented a mural cell population, identified by *PDGFRB* and *CSPG4.* Despite the absence of novel cellular populations, changes in the percentage of cells within each cluster were observed (Figure 4.4 **C**). As anticipated, WT human vascular organoids (hVOs) exhibited elevated levels of CDH5 and

*PECAM1* (Figure 4.4 **D** i). However, when comparing the expression levels of genes associated with brain-specific endothelial cells (ECs), including *A2M, RGS5, APOLD1*, and *IFITM1*, we found that their expression was significantly higher in the BBB-mimicking and neurovascular organoids (Figure 4.4 **D** ii). This finding suggests that the incorporation of neuronal cell types enhances the gene expression profile of brain ECs within the hVOs

Furthermore, we noted that genes associated with fibroblast populations, such as PDGFRA and DCN (Figure 4.4 **D** iii), were upregulated in co-cultured hVOs compared to WT organoids. Conversely, a decrease in expression was observed for mural cell markers *PDGFRB* and *CSPG4* (Figure 4.4 **D** iv). Notably, while genes coding for collagen types *COL1A1* and *COL4A1* were significantly upregulated in WT hVOs, the specific subset of collagen *COL25A1*, which is known to be expressed primarily in the brain and has been linked to neurodegenerative diseases such as Alzheimer's, was preferentially upregulated in co-cultured organoids (Figure 4.4 **D** v). Additionally, the expression of metalloproteinases *MMP2* and *MMP9* was elevated in co-cultured hVOs, suggesting enhanced extracellular matrix (ECM) remodeling in these organoids (Figure 4.4 D v).

UMAP representation of our scRNA-seq data indicated that astrocyte and neuronal populations within neurovascular organoids could not be distinctly separated. Examination of neuronal marker gene expression, including *SYT1*, *DCX*, and *NSG2*, showed significantly elevated levels in neurovascular organoids compared to moderate levels in BBB-mimicking hVOs and low levels in WT organoids, confirming the successful incorporation of neurons in neurovascular organoids (Figure 4.4 **D** vi). Similarly, astrocytic markers such as *CD74, AQP4, GFAP*, and *S100B* were predominantly expressed in BBB-mimicking hVOs (Figure 4.4 **D** vii). Notably, we observed a pronounced upregulation of microglia-associated genes, including *AIF1, C1QB*, and *CD68*,

specifically in astrocyte co-cultured organoids (Figure 4.4 **D** viii). This finding may suggest either an elevated presence of microglial cells or an increased activation state, consistent with the known role of activated astrocytes in triggering immune responses that promote microglial activation.

Finally, we investigated the expression of genes associated with WNT signaling pathways and solute influx and efflux transporters. The WNT/β-catenin signaling cascade is critically implicated in the process of angiogenesis within developing brain vasculature[205]. Our findings revealed an upregulation of *WNT5A* expression specifically in astrocyte co-cultured conditions; however, the proportion of cells exhibiting differential WNT signaling activity remained comparatively low (Figure 4.4 **D** ix). The brain vasculature is characterized by a rich repertoire of solute influx and efflux transporters that are essential for the selective delivery and clearance of various molecules in and out of the brain parenchyma. Genes encoding such transporters, including *SLC6A, KCNMA1, ABCA9, ABCA1*, and *ABCA5*, displayed significantly increased expression levels in co-cultured organoids relative to WT organoids (Figure 4.4 **D** x). These results suggest that the integration of neuronal cell types contributes to the establishment of a niche that promotes the acquisition of brain-specific attributes within the vascular networks.

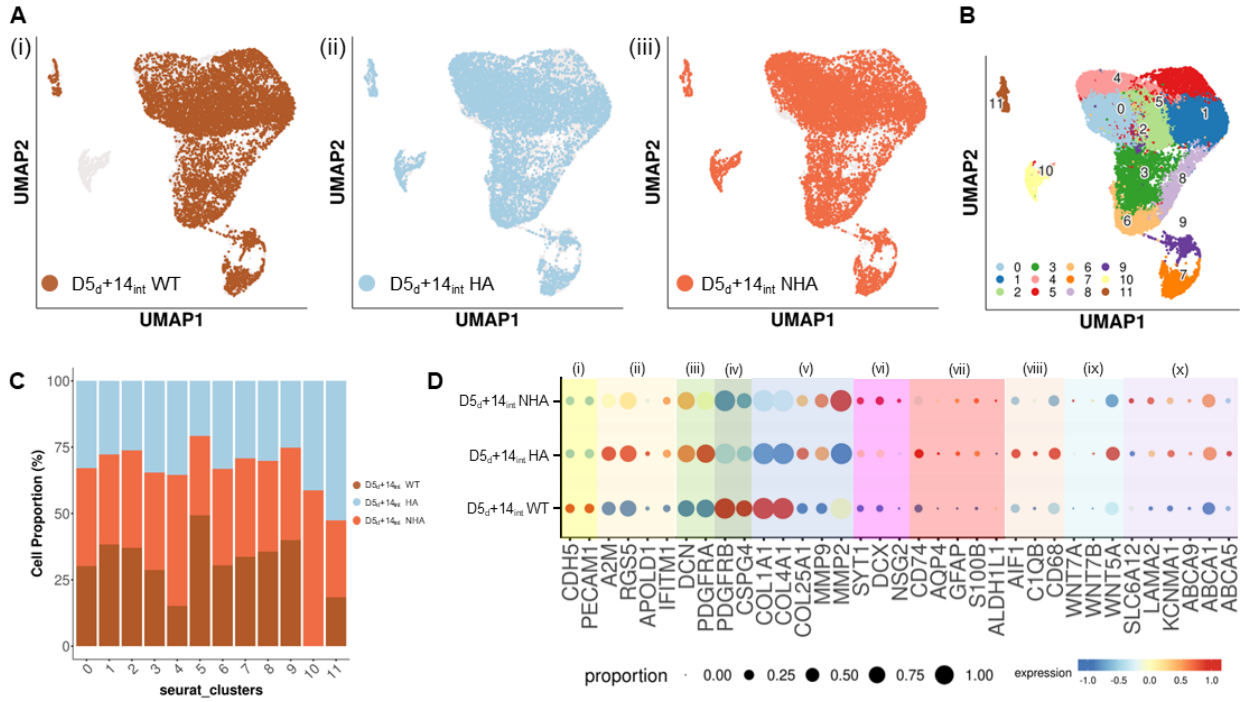


**Figure 4.4 ScRNA-seq analysis of WT, BBB-mimicking, and neurovascular organoids reveals increased production and remodeling of BBB-specific extracellular matrix (ECM) and the acquisition of brain-specific transcriptomic signatures.**

(A) UMAP visualization of cell states from (i) WT hVOs, (ii) BBB-mimicking organoids, and (iii) neurovascular organoids. (B) Seurat clustering of potential cell states across samples. (C) Proportion plot of cells in each cluster for WT, BBB-mimicking, and neurovascular hVOs. WT hVOs lack cluster 10, representing astrocyte and neuronal cell types. (D) Bubble plot showing gene expression and proportions across conditions for (i) EC-related genes, (ii) brain vascular genes, (iii) fibroblasts genes, (iv) mural cell genes, (v) ECM-related genes, (vi) neuronal genes, (vii) astrocyte genes, (viii) microglial genes, (ix) WNT pathway genes, and (x) brain-specific transporter genes.

## 4.5 Discussion and Conclusion

This study presents a novel approach to generating neurovascular organoids that emulate key features of brain vasculature by integrating neuronal and glial cell types with vascular progenitor cells derived from human induced pluripotent stem cells (hiPSCs). The findings demonstrate that co-culturing neuronal and astrocytic cells with vascular organoids supports the acquisition of brain-specific endothelial characteristics and promotes the formation of a neurovascular unit, which includes interactions between neurons, astrocytes, and endothelial cells. These results highlight the importance of cell-cell interactions in establishing a brain-specific endothelial cell phenotype and underscore the potential of this model for studying blood-brain barrier (BBB) properties and neurovascular interactions.

The integration of primary human astrocytes and hiPSC-derived cortical neurons into the vascular organoid differentiation protocol provided a microenvironment that facilitated more extensive angiogenic sprouting and vascular network formation than seen in wild-type (WT) vascular organoids. The presence of astrocytes and neurons likely contributed to the secretion of neurotrophic and angiogenic factors, enhancing endothelial cell (EC) differentiation and vascular remodeling. This aligns with prior research indicating that astrocyte-derived retinoic acid signaling is instrumental in driving brain-specific EC characteristics (reference). Our results further support the concept that co-development with parenchymal cells is necessary for vascular cells to adopt brain-specific phenotypes, as evidenced by the unique expression profiles of tight junction proteins (e.g., ZO-1) and glucose transporters (e.g., GLUT1) in the BBB-mimicking organoids.

The scRNA-seq data provide valuable insights into the cellular diversity within the neurovascular organoids and highlight significant shifts in gene expression associated with BBB-specific markers. The upregulation of brain-specific endothelial markers such as *A2M, APOLD1*, and

*IFITM1*, alongside increased expression of ECM-related genes like *COL25A1* and *MMP2/9*, suggests that co-culture conditions promote the acquisition of a BBB-like transcriptomic signature. *COL25A1*, a brain-specific collagen, has previously been linked to neurodegenerative diseases, highlighting the neurovascular organoids' potential utility for studying disease-related pathways *in vitro*. Additionally, the observed ECM remodeling likely reflects a dynamic environment conducive to neurovascular maturation and homeostasis.

Notably, neuronal and astrocytic markers were more abundantly expressed in neurovascular organoids, with astrocytes localized primarily near the organoid core and neurons near the periphery. This organization resembles the brain's native architecture, where astrocytes extend their end-feet to enclose capillaries, contributing to BBB formation and maintenance. The close association of β III-tubulin-positive neurites with vascular structures further suggests potential innervation of the vascular network, which is a characteristic feature of the neurovascular niche. The finding of elevated microglial markers in astrocyte co-cultured organoids may indicate either increased microglial presence or activation in response to astrocytic signals, consistent with their roles in immune surveillance and neuroinflammation.

Interestingly, while scRNA-seq did not reveal novel cell types resulting from co-culture, the increased percentage of cells expressing brain-specific endothelial markers in the BBB-mimicking and neurovascular organoids suggests a shift in endothelial cell identity toward a brain phenotype. The observed upregulation of *WNT5A* and solute transporters (e.g., *ABCA9, ABCA1*) in co-cultured organoids provides further evidence of brain-specific characteristics, as WNT signaling is important for brain angiogenesis in the developing CNS, and efflux transporters are essential for the removal of selective molecules from brain parenchyma to the plasma.

In conclusion, our co-culture approach effectively mimics the *in vivo* neurovascular environment, resulting in vascular organoids that exhibit brain-specific endothelial phenotypes and neurovascular unit organization. This model represents a promising platform for studying neurovascular development, BBB function, and the pathological mechanisms underlying neurodegenerative and neurovascular diseases. Future studies could further explore the effects of different neuronal and glial subtypes on vascular differentiation, as well as the impact of neurovascular interactions on disease modeling and drug screening applications.

# Chapter 5: Shaping Vascular Cell Fate through Hemodynamic Stimulation: Modeling Hierarchical Networks in Perfusable Vascular Organoids

## 5.1 Abstract

Engineering complex tissues holds promise for tissue regeneration and disease modeling. However, developing organ-specific vasculature, which plays a critical role in mediating inter-tissue communication and maintaining unique metabolic homeostasis in each organ, remains a significant challenge. Human induced pluripotent stem cell-derived vascular organoids (hVOs) offer the potential to mimic *in vivo* blood vessels with extensive remodeling capacity that, upon implantation *in vivo*, can integrate with the host vasculature and remodel into hierarchical vessels. However, achieving *in vitro* perfusion of hVOs remains challenging. Here, we combine hVOs, microvascular engineering, and co-culture models to develop a perfusable hierarchical vascular network *in vitro*. To investigate vascular remodeling in hVOs under intraluminal perfusion, we established anastomosis between hVOs and pre-patterned microvasculature seeded with primary human brain microvascular endothelial cells (HBMECs), as evidenced by dextran perfusion of hVO microvessels (hVOMVs). Capillary extensions from hVOs connected with angiogenic sprouts from HBMECs within the microchannel, and distinct remodeling features occurred when a pressure drop and constant flow were applied across the hVOMV system. Our ongoing work focuses on utilizing single-cell RNA-seq to understand the cell population and transcriptomic profile of perfusable BBB-mimicking hVOs. This advancement holds significant promise for disease modeling and tissue engineering applications in the realm of neuroscience and regenerative medicine.

## 5.2 Introduction

Vascular development is a fundamental process underlying tissue formation, growth, and repair, with successful vascularization remaining a critical challenge in engineering complex tissues. [38,39,206] During early development, endothelial cells (ECs) differentiate from mesodermal precursors, such as angioblasts in the yolk sac, to form a primitive vascular network. [207,208] This network undergoes extensive remodeling to generate a mature, hierarchical vessel tree with specific structural and functional characteristics tailored to support each organ's unique needs. This process is influenced by a combination of hemodynamic stimuli and biochemical cues, which guide ECs through distinct developmental stages, enabling them to acquire the specific identities necessary for the diverse requirements of different tissues. [209]

The establishment of a hierarchical vascular structure is essential for efficient blood flow, nutrient distribution, and waste removal in complex tissues. Vascular development progresses through both vasculogenesis—the formation of new vessels from mesodermal progenitors—and angiogenesis—the sprouting of new vessels from pre-existing ones. As development proceeds, these processes are further refined to form a structured network with arteries, veins, and capillaries in specific spatial arrangements. Within this hierarchical network, each vessel type serves distinct roles, such as high-pressure distribution in arteries, low-pressure collection in veins, and selective permeability in capillaries. Arteriovenous specification is a critical component of hierarchical vascular development, with ECs acquiring distinct arterial or venous identities based on their location, function, and molecular signaling cues. Notch signaling is a well-established pathway driving arterial differentiation, primarily activated by the initiation of blood flow during development. Increased shear stress from blood flow induces Notch activation, which promotes the expression of arterial-specific genes while repressing venous identity. In contrast, venous specification is

influenced by alternative pathways, including Ephrin-B2 and Prox1 signaling, which inhibit Notch and contribute to venous-specific gene expression. However, despite advances in understanding the molecular basis of arteriovenous specification, there remains an incomplete understanding of how endothelial cells acquire distinct transcriptomic profiles and phenotypes across different vessel types, sizes, and hemodynamic vascular beds. Hemodynamic forces regulate the differentiation and behavior of ECs, contributing to vascular patterning and hierarchy by modulating gene expression and cell behavior in response to flow. Understanding these flow-mediated mechanisms is essential for engineering vascular networks that can mimic the physiological organization and functionality of native tissue. Yet, replicating these conditions *in vitro* has proven challenging.

Recent advancements in stem cell technologies, such as human vascular organoids (hVOs), have provided new opportunities to model vascular development and disease in a controlled environment. [140,210] Vascular organoids, which consist of multiple vascular cell types, including ECs, pericytes, and mesodermal progenitors, have demonstrated the ability to self-organize into complex vascular structures. [80,81,120] Upon *in vivo* implantation, hVOs have shown the potential to form hierarchical vascular networks, driven by perfusion through host vasculature integration. These organoid-based systems provide a unique platform for studying vascular and tissue development, with applications in regenerative medicine and disease modeling. However, establishing and controlling hierarchical vascular network formation within engineered microvessels *in vitro* remains an ongoing challenge.

In this study, we aim to develop an *in vitro* model of hierarchical vascular network formation using perfusable hVO microvessel constructs (hVOMVs) subjected to controlled hemodynamic stimuli. By integrating hVOs into engineered microvessels and applying flow and pressure conditions, we

investigate the impact of hemodynamic forces on vascular remodeling, network hierarchy, and arteriovenous specification. This model has the potential to replicate aspects of *in vivo* vascular development, providing a versatile platform to study vascular biology and laying the groundwork for future applications in tissue engineering and disease modeling.

## 5.3 Methods

### *5.3.1 Human vascular organoid differentiation*

Human induced pluripotent stem cells (hiPSCs) were differentiated into hVOs by optimizing a previously published protocol (ref). Both mTm REUS2 embryonic stem cells and WTC-11 hiPSCs were used to generate hVOs. Briefly, hVOs were differentiated from stem cell colonies cultured in Matrigel-coated plates by dissociating cells using versene (ThermoFisher; CC# 15040066) treatment for 3 minutes. Versene was aspirated, and cells were directly collected in embryonic body medium (mTeSR +) supplemented with 20 μM Y-27632 (Tocris; CC# 4423) for survival. Stem cells were plated in an ultra-low attachment six-well plate (Corning Costar; CC# CLS7007) at a seeding density of 5 × 10^5 cells per well. The next day (D0; mesoderm induction day), embryonic bodies were induced into mesoderm aggregates via mesoderm induction medium containing N2B27 media composed of 1:1 Neurobasal media (Gibco; CC# 21103049) and DMEM/F12 media (Gibco; CC# 11330032), supplemented with N2 supplement (Gibco; CC# 17502048), vitamin A-free B27 supplement (Gibco; CC# 12587010), Glutamax, and P/S. N2B27 media was supplemented with 12 μM CHIR99021 and 30 ng/ml BMP-4 (Peprotech; CC# 120-05ET) for WNT and BMP4 activation into lateral plate mesoderm. EBs were gently stirred daily to prevent the formation of larger aggregates. On day 3 and 4 (vascular progenitor induction days), mesoderm aggregates were switched to vascular lineage induction media containing N2B27 media, 100 ng/ml VEGF-A (Peprotech; CC# 100-20-250UG), and 2 μM Forskolin (Sigma; CC#

F3917). On D5 (embedding day), vascular progenitor aggregates were embedded in a collagen I-Matrigel (Col-Mat) matrix in 12-well plates. Each 12-well plate contained 30–40 organoids. Two individual layers of Col-Mat encapsulated the hVO; the bottom layer was prepared by mixing Col-Mat solution on ice and applying 500 µl in each well of a 12-well plate. The bottom layer was gelled in an incubator at 37°C for 1 hour. The top layer was prepared by creating an organoid-laden Col-Mat solution by adding vascular progenitors to ice-cold Col-Mat. 500 µl of organoid-laden Col-Mat solution was applied on top of the gelled bottom Col-Mat layer and incubated for 2 hours for gelation. After 7 days of vascular network formation in Col-Mat matrix (D12), the differentiated vascular networks were dissected into individual vascular networks using a dissection scope and sterile 25G needles. Individual vascular networks were transferred to a low-attachment U-bottom 96 well plates for compaction into final hVO form. Media was changed every 3 days.

*5.3.2 hVOMV fabrication*

Engineered microvessels were fabricated using soft lithography and injection molding techniques previously described by Zheng et al. Briefly, type I rat tail collagen was dissolved in 0.1% acetic acid at a stock concentration of 15 mg/mL. The collagen was neutralized and diluted to 7.5 mg/mL on ice with 1 M NaOH (20 mM final), 10× M199 (CC# 11825015; Thermo Fisher Scientific), and EGM-2MV. A microfabricated polydimethylsiloxane (PDMS) stamp was used to define a 2mm apart hexagon vessel network with a feature height of 150 µm. Collagen was molded around this PDMS stamp through a collagen injection port. D19 hVOs were inserted into the center of hexagon vessel network using a gel loading pipette and incubated in 37 °C to allow gelation. A flat collagen gel was also generated. After gelation at 37 °C, the channels were incubated with the flat collagen gel to generate closed off microchannels that can be perfused and seeded with endothelial cells

(ECs). These two gels merged through additive bonding upon incubation at 37 °C. Once the gel was fabricated, HBMECs were lifted from culture flasks with trypsin (CC# MT-25-052-CI; Thermo Fisher Scientific) and resuspended in GM at a concentration of 7–10 × $10^6$ cells/mL. Using a gel loading pipette tip, 10 μL of this cell suspension is injected into the inlet of the microvessel and allowing them to circumferentially attach to the collagen gel under static conditions for 1 h prior to the start of gravity-driven flow. Microvessel constructs were cultured under gravity-driven flow for 5–7 days with media replenishment approximately every 12 h.

*5.3.3 Immunoflourescence staining*

At the end of each experimental time point, hVOMV were fixed with 4% paraformaldehyde (PFA) at room temperature for 1 hour followed by three washes in phosphate-buffered saline (PBS) for 30 minutes each. Whole-organoid microvessel immunofluorescence staining was initiated by blocking the organoids with a blocking buffer containing 3% FBS, 1% bovine serum albumin (bioWORLD; CC# 2207004), 0.5% Triton X-100 (Sigma; CC# 93420), 0.5% Tween 20 (Sigma; CC# P7949), and 0.01% (wt/vol) sodium deoxycholate solution (SD solution; prepared by adding 1 mL of 1% stock solution made by dissolving 1 g of sodium deoxycholate (Sigma; CC# D6750) in 100 mL of deionized water) for 2 hours. All of the reagents were introduced to the vessels via the microchannels through the inlet of acrylic jigs.

Following the blocking step, primary antibodies were applied in the blocking buffer. The antibodies used in this study include, VECAD (conjugated-APC; 1:100), phalloidin (1:100), CD31 (1:100). Primary antibodies were incubated on a rocking shaker at 37°C overnight and washed three times for 20 minutes each using PBS-T solution (1% Tween in PBS). Secondary antibody staining was conducted by incubating organoids on a 37°C shaker for 4 hours, with Hoechst 33342

added for nuclear staining. Organoids microvessels were washed twice with PBS-T and given a final wash with PBS.

Following staining, the organoids vessels were mounted on a coverslip using iSPACER (SUNJin Lab; CC# IS003) and cleared with RapiClear 1.52 (SUNJin Lab; CC# RC152001) by dismounting the collagen gel from acrylic jigs and cutting the remaining dead collagen spaces. Or the organoids vessels were directed cleared on the acrylic jig with RapiClear 1.52 (SUNJin Lab; CC# RC152001) mounting medium to ensure full clearing of the organoid microvessel structure for confocal imaging. Cleared organoids were imaged using a Leica SP8 confocal microscope. The entire collagen construct was imaged using at least a 5 by 5 large z stack image stitch (10% blending stitch) under a 10× objective with a z-step size of 1.5-2.5 μm. 3D reconstruction and cross-sectional images of the microvessels were rendered using ImageJ software.

*5.3.4 hVOMV perfusion*

Permeability measurements were conducted on D7 hVOMV assuming connection from the microchannel to organoids have been established. At D7 hVOMV, microvessels were perfused with 500 kDa FITC-dextran (100 mg/mL in EGM-2MV+VO growth media) to assess the connection of the microvessels. Dextran solution was perfused into the microvessels with a hydrostatic pressure drop c) for ~1 hr. Images of dextran perfusion was obtained using a fluorescent microscope (Nikon Eclipse Ti2).

*5.3.5 Hemodynamic application in hVOMV*

Following perfusion of hVOMV at D7, subset of hVOMV were subjected to altered pressure drop or contious flow. Pressure drop was applied by changing the direction of hydrostatic pressure drop across the organoids from inlet-outlet pressure drop. ~1 mmHg pressure drop was applied on the left inlets of the hVOMV, driving the media across the connected hVO in the center of the

microvessel. Continuous flow was applied to the microvessels via a syringe pump perfusion across the organoid by blocking the diagonal inlet and outlet of the hVOMV and connecting the inlet of the hVOMV with syringe pump (2.5 μl/min). All altered hemodynamic flow was administered for additional 3 days.

*5.3.6 Single cell RNA sequencing*

The 10X Chromium scRNA-seq outputs were de-multiplexed, mapped to the human reference genome (hg19, GRCh38) and aggregated into one single-cell object through the Cell Ranger V4.0 bioinformatics pipeline (10X Genomics). Batch effect corrections were performed as described (10.1038/nbt.4091). Dimension reduction and clustering of 10X scRNA-seq data were conducted using the Seurat package (10.1016/j.cell.2019.05.031). The pseudotime analyses were conducted through the Monocle3 package (10.1038/nbt.2859, 10.1038/nmeth.4402, 10.1038/s41586-019-0969-x). DEGs were identified using the nonparametric Wilcoxon rank sum test by FindMarkers function of Seurat package to find DEGs from each identity cluster against the remaining cells, with min.pct = 0.25, logfc.threshold = 0.25. We used default options for the analysis if not specified otherwise. FeaturePlot, DimPlot, and DotPlot functions of the Seurat package were used for visualization of selected genes. The 'VlnPlot' function of the Seurat package was used for violin plots to show the expression level of selected genes with log normalized value by default. Pathway analyses were conducted using the R package clusterProfiler (10.1089/omi.2011.0118).

## 5.4 Results

### *5.4.1 Generating perfusable vascular organoid via anastomosis with 3D perfusable microvessels*

As new blood vessels form and mature into a hierarchical vascular network, vascular cells undergo distinct fate transitions in response to hemodynamic cues and structural adaptations. To recapitulate this process and investigate the establishment of vascular hierarchy under varying hemodynamic conditions, we engineered perfusable hVO microvessels. Here, we adapted the vascular organoid protocol developed by Wimmer et al.[80] Briefly, hiPSCs were harvested two days prior to mesoderm induction and resuspended in aggregation media in low-attachment 6-well plates (plating density: 500,000 cells/well). On day 0, hiPSC aggregates underwent mesoderm induction with BMP4 and CHIR99021 in N2B27 media. By day 3, mesoderm precursors were differentiated into vascular progenitor aggregates using VEGF-A and forskolin in N2B27. On day 5, the vascular progenitors were embedded in a Matrigel-collagen gel and cultured in this matrix to promote vascular network formation. Organoids were then cultured for an additional 7 days in the Matrigel-collagen gel and dissected under a dissecting microscope on day 12. The dissected hVOs were then suspension-cultured in low-attachment 96-well plates for 3 days to allow for compaction of the vascular networks within the hVOs. The hVOs were cultured with regular media changes, reaching a maturation stage ($D5_{diff}$ + $D14_{int}$) suitable for incorporation into hVOMVs (Figure 5.1; Phase 1).

To promote perfusion within the hVO, each hVO was integrated into engineered microvessels fabricated using a soft-lithography and injection molding approach. After fabrication, the hVOMV was maintained for 7 days under gravity-driven perfusion to facilitate anastomosis between the hVO and the engineered microvessel—a critical step for ensuring functional perfusion. On day 7

of hVOMV culture ($D5_{diff}$ + $D14_{int}$ + $D7_{v}$), the anastomosed constructs were confirmed to be fully perfusable, marking the point at which controlled hemodynamic stimuli could be applied. The hVOMVs were then subjected to gravity-driven flow, a pressure gradient of 1 mmHg across the hVO, and continuous flow at a rate of 2.5 µL/min for an additional 3-day period ($D5_{diff}$ + $D14_{int}$ + $D7_{v}$ + $D3_{H}$) (Figure 5.1; Phase 2).

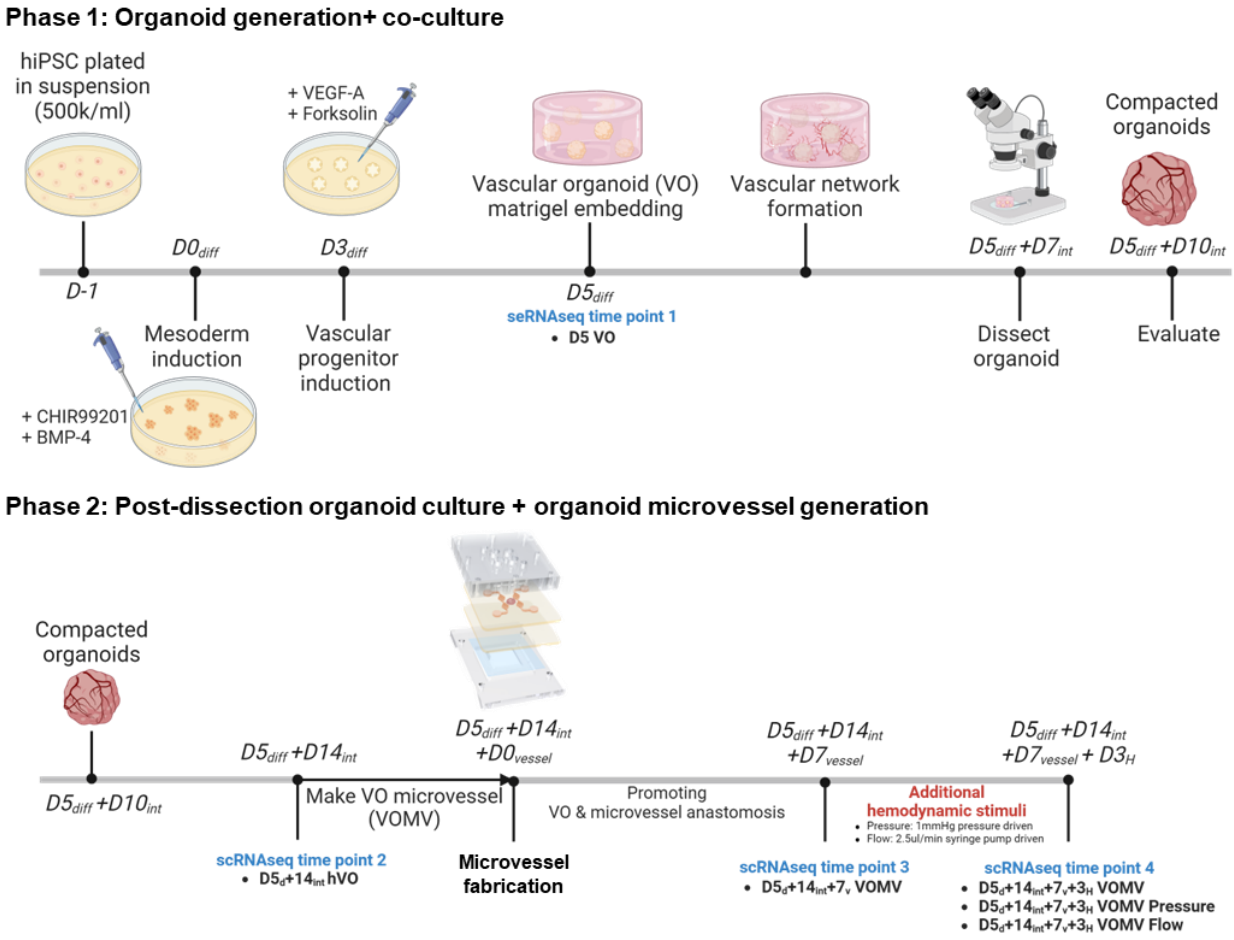


**Figure 5.1 Schematic overview of hVO differentiation, fabrication of hVOMV, and hemodynamic stimulation applied to hVOMV.**

hVO differentiation is divided into two phases: Phase 1 involves the induction of WTC-11 hiPSCs into the mesoderm lineage (D0; BMP-4 and CHIR99021) and further commitment into vascular progenitors (D3; VEGF-A and Forskolin). On D5 ($D5_{diff}$), organoids are embedded into a matrix composed of collagen I and Matrigel (Col-Mat VOs are dissected after a 7-day culture in Col-Mat ($D5_{diff}$+$D7_{int}$) and cultured in suspension as individual organoids in an

ultra-low attachment 96-well plate.. Phase 2 of organoid culture includes maintaining dissected organoids with media changes every 3–4 days. hVOs from D19 ($D5_{diff}$+$D14_{int}$) to D21 are used to fabricate hVO microvessels (hVOMV). The hVOMV is generated by incorporating hVOs in engineered microvessels created via soft lithography. hVOMV is cultured for 7 days under gravity-driven perfusion to promote anastomosis between the hVO and microvessels, enabling full perfusion of the hVO. At D7 of hVOMV culture ($D5_{diff}$+$D14_{int}$ +$D7_{v}$) hVOMV is considered perfusable and is subjected to an additional 3 days ($D5_{diff}$+$D14_{int}$ +$D7_{v}$ +$D3_{H}$) with different hemodynamic stimuli, including gravity-driven flow, a 1 mmHg pressure gradient across the hVO, and continuous flow at 2.5 μL/min.

*5.4.2 Generating perfusable vascular organoid via anastomosis with 3D perfusable microvessels*

Next, we investigated the ability of hVOs to remodel into hierarchical vascular structures by generating a perfusable vascular organoid model *in vitro*. We combined a previously described soft-lithography-based microvascular engineering approach with differentiated hVOs to promote bidirectional vascular growth and anastomosis. To introduce hVOs within engineered microvessels, we fabricated acrylic jigs with a central fifth hole to insert hVOs and enable direct feeding of the hVOs prior to connecting the microfluidic channels. Three-dimensional microvessels were generated in hexagonal patterns using methods described earlier. Before crosslinking the collagen into its final pattern in a 37°C incubator, hVOs were inserted into the center of the hexagon patterns (Figure 5.2 **A**).

To promote anastomosis between the hVOs and microvessels, the hVOMV was maintained under gravity-driven perfusion with high-VEGF-containing media for 7 days. After 3 days in culture, both hVOs and microvessels exhibited early capillary extensions toward each other (Figure 5.2 **A** i). By days 6–7, extensive network integration was evident, with hVOs and microchannels forming an anastomosed vascular network (Figure 5.2 **A** ii). The hVOMVs were fixed on day 7 and stained with phalloidin (green) and VE-Cadherin (magenta) to visualize the remodeled vascular network within the hVOMV (Figure 5.2 **B**). Maximum projection (MP) images of day 7 hVOMVs confirm connectivity within the hVOMV, where the hVO extends

toward and connects with surrounding microvessels, particularly in the lower layer of the construct near the microvessels (Figure 5.2 **B** ii and iii). As the *z*-cross-section approaches the center of the organoid, the hVO exhibits a well-organized vascular network, indicative of robust and functional integration between the hVO and the engineered microvessels (Figure 5.2 **B** iv). This indicates that the perfusion of the hVO can support and maintain the vascular network structure, which is otherwise lost in suspension culture due to endothelial cell regression in the absence of flow.

Next, we analyzed the intraluminal perfusability of the connected hVOMV using dextran perfusion (Figure 5.2 **C** and **D**). FITC-labeled 500 kDa dextran was introduced through the inlets of the microchannels. The dextran distributed throughout CD31+ (red) vascular lumens, reaching the hVO and demonstrating effective intraluminal perfusion across the network (Figure 5.2 **C**). Orthogonal views of the perfusable hVOMV show the presence of a vascular hierarchy (Figure 5.2 **E** i-iv), with a diverse range of vessel lumen sizes. These range from larger lumens near the microchannel side (*y*1; Figure 5.2 **E** ii), to capillary-sized vessels connecting the organoids to the patterned microchannels (*y*2; Figure 5.2 **E** iii), and larger sprouts toward the center of the organoid (*y*3; Figure 5.2 **E** iv), with diameters ranging from 10 μm to 150 μm. This diversity indicates the presence of a self-assembled hierarchical network within the hVOMV. Together, these results demonstrate that hVOMVs cultured under gravity-driven perfusion for 7 days exhibit functional anastomosis, effective intraluminal perfusion, and a hierarchical vascular architecture.

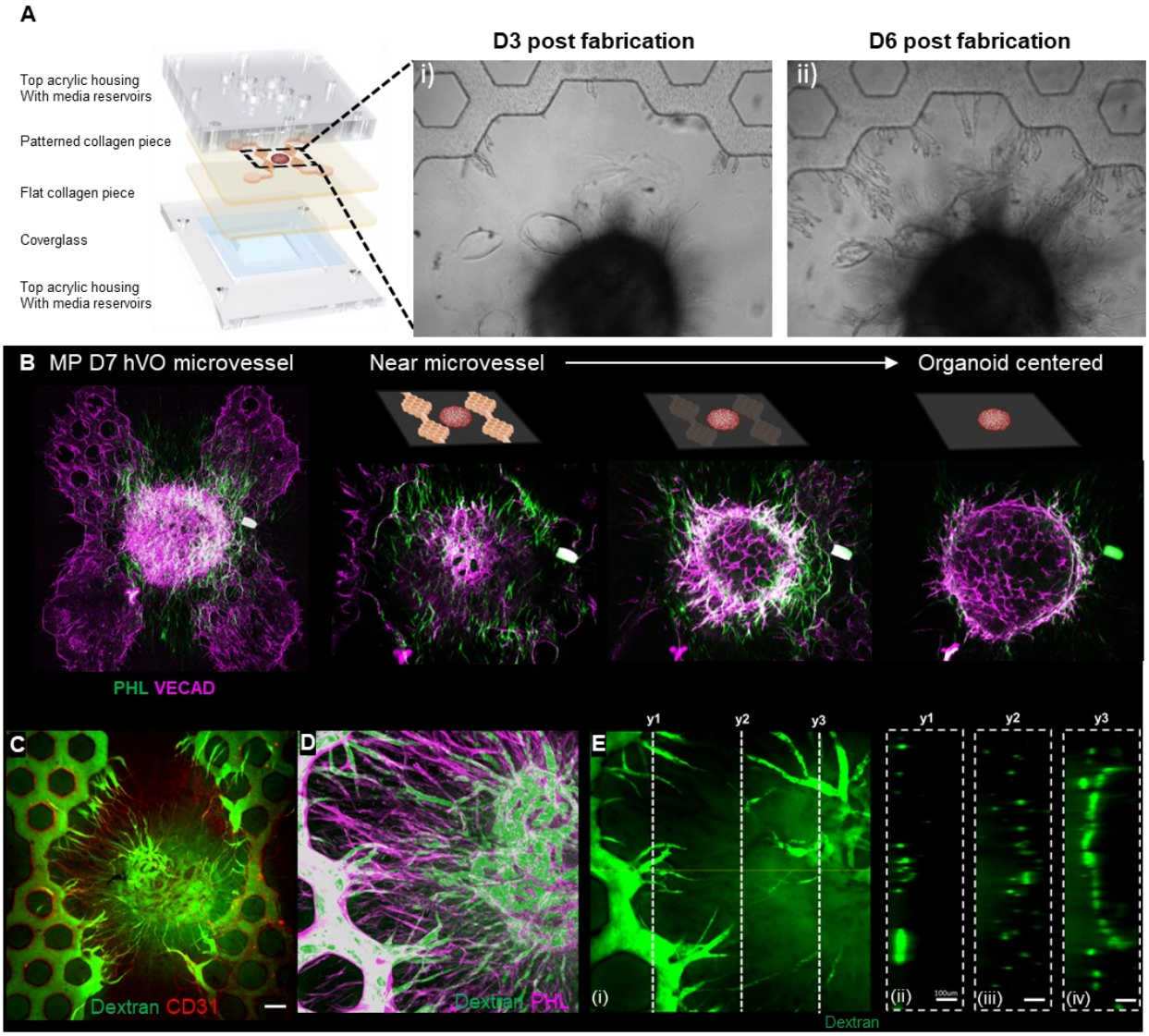


**Figure 5.2 D7 hVOMV exhibits hVO anastomosis with microchannels and intraluminal perfusion of connected hVOs**

Representative images of hVO microvessel fabrication and anastomosis during a 7-day culture period. (A) Schematic diagram of the acrylic jig housing the hVO in the center of hexagonal microvessels. Representative images show capillary extensions from organoids and vascular sprouts from microchannels at (i) day 3 and (ii) day 6 of hVOMV culture. (B) By day 7 of gravity-driven hVOMV culture, the hVO and pre-patterned microvessels connect, completing anastomosis. (i) Maximum projection (MP) images of hVOMV after 7 days of culture. The organoid extends towards microvessels near the (ii and iii) bottom layer of the hVOMV; (iv) the center of the fully connected hVOMV shows a well-structured vascular network. (C) Demonstration of hVOMV perfusability in day 7 hVOMV. FITC 500 kDa dextran (green) was perfused into the hVOMV via the inlets of the microchannels. The dextran travels through the

CD31+ (red) vascular lumens toward the hVO. (D) Maximum projection images of dextran-perfused hVOMV. Phalloidin (magenta) staining shows the presence of both perfusable lumens and perivascular cells surrounding the organoids. (E) Cross-sectional image of dextran-perfused hVOMV and orthogonal view of the perfused hVOMV. Each y cross-section represents an orthogonal view, showing (ii) larger lumens near the microchannel (y1), (iii) capillary-sized vessels connecting microchannels and the hVO (y2), and (iv) larger arteriole-sized lumens near the organoid compartment (y3). The wide range of vascular lumen diameters suggests the formation of a hierarchical vascular network.

### *5.4.3 hemodynamic driven remodeling of perfusable vascular organoids*

To investigate the impact of flow and pressure on vascular remodeling in hVO microvessel constructs, we cultured hVOMVs under various hemodynamic conditions and observed the resulting vascular structures. The differential effects of gravity-driven flow, pressure gradients, and continuous flow on the microvascular network within the D7 hVOMV over a 3-day culture period were characterized (Figure 5.3 **A-D**). hVOs within D7 hVOMVs cultured under gravity-driven flow showed minimal remodeling (Figure 5.3 **A** i and ii), likely due to the perfusion method and timing of anastomosis, which only allowed fluid to diffuse parallel to the organoids with minimal direct flow across the hVOs (Figure 5.3 **A** ii). In D10 hVOMVs maintained under continuous gravity-driven flow (Figure 5.3 **C**), vascular remodeling was more pronounced compared to the D7 hVOMVs. This is likely due to enhanced network connectivity and improved perfusion of the hVOs as the hVO-microvessel connections matured, allowing more flow into the hVOs. Cross-sectional images of D10 hVOs ($D5_{diff}$ + $D14_{int}$ + $D7_{v}$ + $D3_{H}$) reveal an increased number of vascular lumens, indicating enhanced network density and branching (Figure 5.3 **A** ii). However, without a defined pressure gradient, the vessels did not align in a specific orientation. This condition demonstrates that continuous low-shear flow promotes vascular growth and remodeling, albeit in a non-directed manner.

Directionality of hVOMVs was observed in D10 hVOMVs cultured under a pressure gradient (Figure 5.3 **B**). The pressure gradient was introduced by applying pressure to the left side of the

patterned microvessels using different media heights in the channels (Figure 5.3 **B** i). The applied pressure gradient promoted the alignment of microvessels along the direction of the pressure, as shown in cross-sectional images (Figure 5.3 **B** ii). This directional alignment indicates that the pressure gradient encouraged structured, flow-oriented growth within the microvascular network, enhancing perfusion efficiency.

The most pronounced remodeling was observed in D10 hVOMVs subjected to a continuous flow rate of 2.5 µL/min using a syringe pump (Figure 5.3 **D**). Continuous flow was directed across the hVOs, with diagonal inlets and outlets blocked by collagen plugs to prevent flow short-circuiting and ensure that flow passed through the organoids. Cross-sectional images of the hVO ($D5_{diff}$ + $D14_{int}$ + $D7_{v}$ + $D3_{H}$) cultured under continuous flow reveal a microvascular network with significantly larger lumens and improved integration within the hVO. The formation of larger, well-perfused lumens suggests that continuous flow supports both structural expansion and vascular maturation within the organoid network, potentially enhancing the functional capabilities of the hVOMV.

Together, these results demonstrate that different hemodynamic stimuli distinctly influence the structural and functional maturation of hVOMVs. Gravity-driven perfusion supported limited baseline remodeling, while a pressure gradient induced directional alignment of microvessels. Continuous gravity-driven flow promoted non-directional vascular remodeling, whereas continuous directed flow resulted in the formation of larger lumens and a more integrated vascular network. These findings underscore the importance of hemodynamic forces in shaping vascular architecture and highlight the utility of hVOMVs as a model to study vascular responses to flow and pressure in a controlled *in vitro* environment.

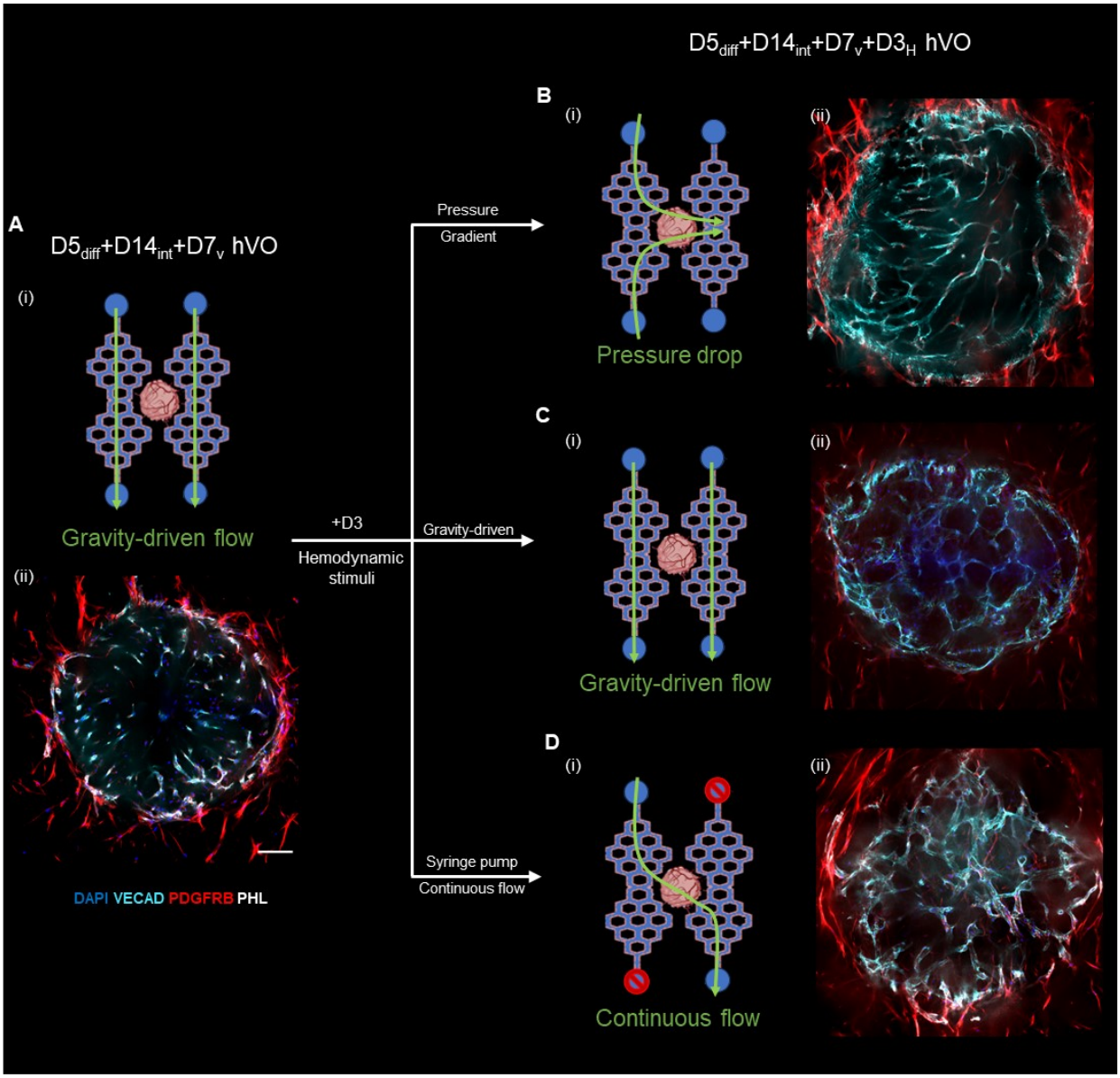


**Figure 5.3 Flow and pressure-induced remodeling of hVOMV.**

(A) Representative image and schematic of culture conditions in D7 hVOMV ($D5_{diff}$ + $D14_{int}$ + $D7_v$ hVO). (i) Schematic overview of the perfusion method used to culture hVOMV up to day 7 with gravity-driven flow. This flow runs parallel to the organoids, providing diffusion-mediated delivery with minimal direct flow across the hVO. (ii) Cross-sectional image of the $D5_{diff}$ + $D14_{int}$ + $D7_v$ hVO in the center of the D7 hVOMV, showing minimal remodeling and smaller lumen formation. Representative image and schematic of culture conditions in D10 hVOMV with distinct hemodynamic stimuli. (B) D10 hVOMV with an applied pressure gradient at D7. (i) Schematic overview showing a 1 mmHg pressure gradient applied across the organoid from the left side to the right side of the hVO ($D5_{diff}$ + $D14_{int}$ + $D7_v$ + $D3_H$). (ii) Cross-sectional image of $D5_{diff}$ + $D14_{int}$ + $D7_v$ + $D3_H$ hVO showing microvessels aligned in the direction of the pressure gradient. (C) D10 hVOMV with continuous gravity-driven flow. (i) Schematic overview showing gravity-driven flow applied parallel to the hVO ($D5_{diff}$ + $D14_{int}$ + $D7_v$ + $D3_H$). (ii) Cross-sectional image of $D5_{diff}$ + $D14_{int}$ + $D7_v$ + $D3_H$ hVO cultured under gravity-driven flow, showing more vascular remodeling compared to

the $D5_{diff}$ + $D14_{int}$ + $D7_{v}$ hVO, but without specific directionality. (D) D10 hVOMV with continuous flow applied at D7. (i) Schematic overview showing a continuous flow of 2.5 µL/min applied across the organoid through the hVO lumens using a syringe pump. Diagonal inlets and outlets were blocked with collagen plugs to prevent short-circuiting of the flow, directing it across the organoid. (ii) Cross-sectional image of $D5_{diff}$ + $D14_{int}$ + $D7_{v}$ + $D3_{H}$ hVO showing a microvascular network within the hVOs, characterized by larger lumens and an overall integration of the hVO within hVOMV construct.

### *5.4.4 scRNAseq reveals cell fate changes across developmental trajectory of vascular network from vascular progenitor ($D5_{diff}$) to hVOMV ($D5_{diff}$+$14_{int}$+$7_{v}$+$3_{H}$).*

After confirming that the co-culture conditions in hVOs and flow conditions in hVO vessels support the presence of distinct cell populations and appropriate morphology, hVOs and hVOMVs were digested and dissociated into single cells for scRNA-seq. Initial analysis revealed significant changes in cell populations from vascular progenitors ($D5_{diff}$) to D10 hVOMV ($D5_{diff}$+$14_{int}$+$7_{v}$+$3_{H}$) (Figure 5.4 **A**), with 15 clusters identified by Seurat analysis (Figure 5.4 **B**). Cell population analysis across each condition shows that the number of cells in each cluster changes markedly from vascular progenitors to D7 hVOMV, with the most substantial shifts occurring as vascular progenitors transition to hVOs ($D5_{diff}$ + $14_{int}$) forming mature vascular networks and as D7 hVOs anastomose with the microvessels ($D5_{diff}$+$14_{int}$+$7_{v}$) (Figure 5.4C).

Gene expression profiles reveal that genes associated with the lateral plate mesoderm (*TBX4* and *HAND1*) are highly expressed in vascular progenitors, confirming a correct developmental trajectory. This trajectory shows a subsequent shift toward endothelial cell commitment in hVOs, as indicated by the expression of endothelial-related genes *KDR* and *CDH5* (Figure 5.4 **D** and **E**). The mural cell marker *PDGFRB* is present throughout the developmental trajectory from $D5_{d}$+$14_{int}$ hVOs to $D5_{diff}$+$14_{int}$+$7_{v}$+$3_{H}$ hVOMV However, both endothelial and mural cell populations shift as suspension-cultured hVOs transition from progenitor populations to mature endothelial cells. The progenitor population disappears by $D5_{diff}$+$14_{int}$+$7_{v}$ while the mural cell population arises and

undergoes changes from $D5_{diff}+14_{int}+7_{v}$ hVO to $D5_{diff}+14_{int}+7_{v}+3_{H}$ hVOMV (Figure 5.4 **E**). Notably, a small population of microglial cells (marked by *AIF1* and *C1QB*) arises in $D5_{diff}+14_{int}$ hVOs and $D5_{diff}+14_{int}+7_{v}$ hVOMV but disappears over time in D10 ($D5_{diff}+14_{int}+7_{v}+3_{H}$) gravity-driven culture of hVOMV (Figure 5.4 **D**).

Furthermore, KEGG pathway analysis of upregulated pathways in D5diff vascular progenitors highlights the Wnt signaling pathway, pathways regulating the pluripotency of stem cells, and the Rap1 pathway, all of which are heavily implicated in the initial stages of vascular development (Figure 5.4 **F**). In contrast, upregulated KEGG pathways in $D5_{diff}$ + $14_{int}$ hVOs include the PI3K-Akt signaling pathway, focal adhesion, and the MAPK signaling pathway, which are more closely related to vascular angiogenesis and tubule formation. This aligns well with the formation of extensive vascular networks within hVOs and the active anastomosis of hVOs with HBMECs in microchannels.

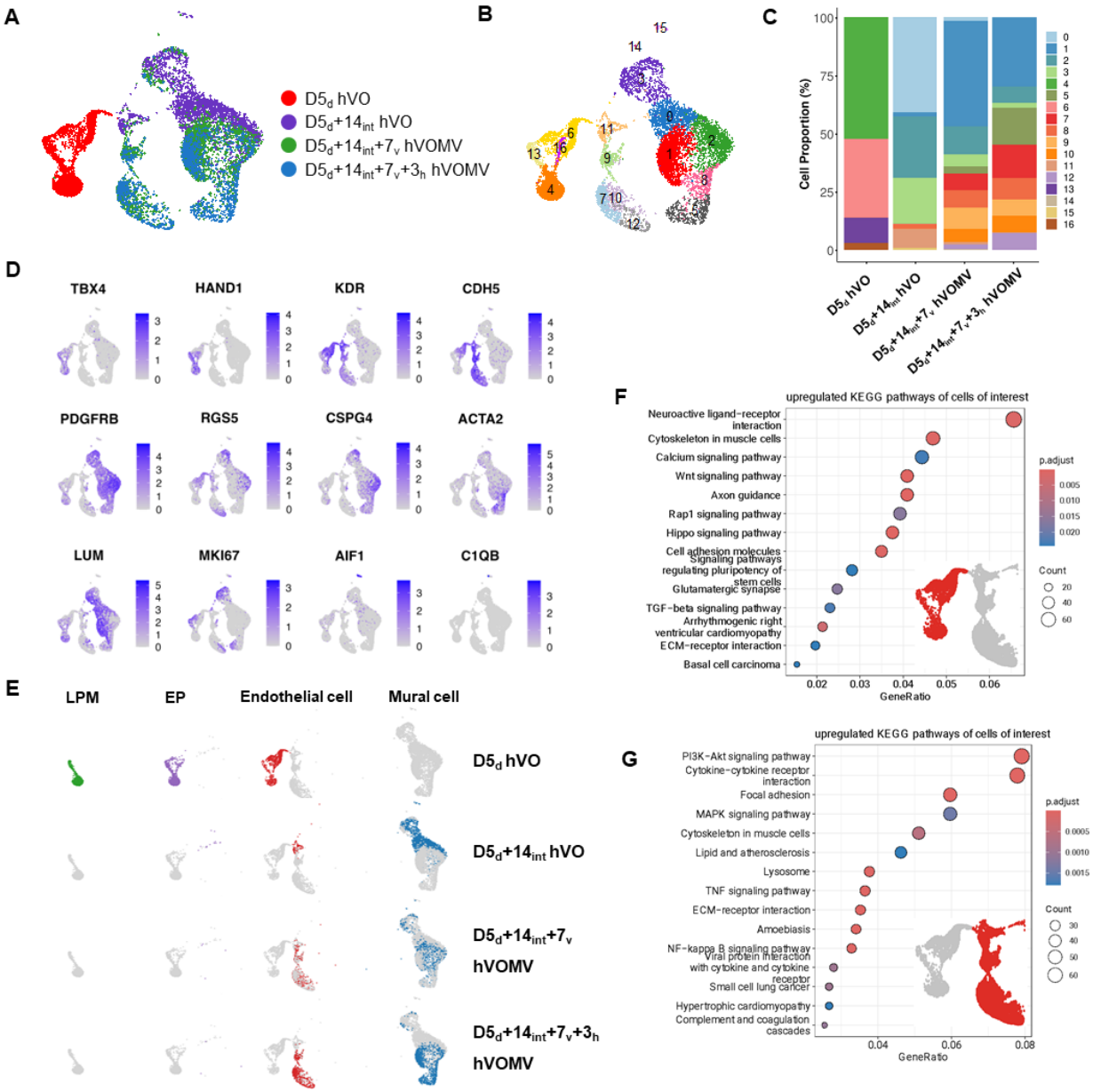


**Figure 5.4 ScRNAseq of reveals cell fate changes across developmental trajectory of vascular network from vascular progenitor (D5diff) to hVOMV (D5d+14int+7v+3h).**

(A) UMAP representation of cell populations from vascular progenitor ($D5_{diff}$) to hVO prior to integration in microvessels ($D5_{diff}$+$14_{int}$), D7 hVOMV ($D5_{diff}$+$14_{int}$+$7_{v}$) and D10 hVOMV ($D5_{diff}$+$14_{int}$+$7_{v}$+$3_{H}$ ). (B) Cell ranger analysis shows 15 clusters which appear based on Seurat clustering. (C) population changes in each cluster for 4 stages of the model. (D) Gene expression profile of cells expressing genes related to lateral plate mesoderm (TBX4, and HAND1), endothelial progenitor (KDR), endothelial cells (CDH5), mural cell (PDGFRB, RGS5, CSPG4, and ACTA2), fibroblasts (LUM), proliferation (MKI67) and microglia (AIF1, and C1QB). (E) UMAP distribution of lateral plate mesoderm (LPM), endothelial progenitors (EP), endothelial cells and mural cells showing cell fate changes. Upregulated KEGG pathway for (F) vacular progenitor population and (G) endothelial cells.

*5.4.5 Arteriovenous specification during vascular development from vascular progenitors (D5d) to hVOMV ($D5_{diff}$+$14_{int}$+$7_{v}$+$3_{H}$).*

To investigate whether hVOs are primed into arteriovenous fate prior to introduction into hVOMVs and cultured under flow, we specifically examined the endothelial cell cluster (defined as CDH5 ≥ 0), meaning any cells that did not express *CDH5* were excluded from further analysis. Our results show the presence of arteriovenous populations, as well as lymphatic and brain endothelial cells (Figure 5.5 **A**). The presence of brain endothelial cells is expected to increase in $D5_{diff}$+$14_{int}$+$7_{v}$ since the microchannels are seeded with resting HBMECs positive for vWF (Figure 5.5 **B**).

Proportion analysis of cell populations in EC clusters reveals that the majority of $D5_{d}$ cells express venous EC markers, with a smaller population of vascular progenitors enriched for arterial ECs (Figure 5.5 **B**). However, as vascular progenitors transition to $D5_{d}$+$14_{int}$ hVOs, the proportion of venous ECs decreases, while the proportion of arterial ECs increases. As hVOs are integrated with hVOMVs and anastomosis occurs, the percentage of venous ECs rapidly decreases, accompanied by an increase in the percentage of lymphatic ECs (Figure 5.5B). An investigation of the top genes implicated in each EC cluster suggests that arterial ECs express genes related to angiogenesis (*PRDN* and *IGFBP3*), while venous ECs express genes related to venous identity (*APLNR*) and BMP signaling (*CRHBP*) (Figures 5.5 **C** and **D**). Brain ECs, which primarily originate from HBMECs used in microvessel fabrication, express high levels of *vWF, ANPEP, and HHIP*, genes associated with blood-brain barrier ECs. Finally, lymphatic ECs highly express *LYVE1*, a characteristic lymphatic marker (Figures 5.5 **C** and **D**).

Next, we examined endothelial cell cluster 2 in depth to investigate if true arteriovenous signature is observed in $D5_{diff}$+$14_{int}$ hVOs. UMAP representation of EC cluster 2 shows three distinct EC

subclusters (Figure 5.5 **E**). A bubble plot of the top five genes in these clusters shows that a small subset of cells in cluster 2 expresses genes related to PBMCs (*PRC1*, *KIF18B*, and *KIF4A*) and proliferation-related genes (*FOXM1*). Cluster 1 highly expresses genes related to arterial fate (*CXCR4* and *GJA5*), while cluster 0 expresses genes related to venous fate (*LHX6*). The co-expression map of venous-related genes *APLNR*, *NR2F2*, and *LHX6* shows preferential clustering in cluster 0 (Figures 5.5 **G** and **H**). In contrast, arterial EC-related genes *GJA4*, *SOX17*, *DLL4*, and *CXCR4* are predominantly co-expressed in cluster 1 (Figures 5.5 **I** and **J**). These data suggest that, prior to the fabrication of hVOMVs, hVOs retain arteriovenous populations.

Finally, we investigated when the arteriovenous population in hVOs arises. To analyze changes specific to hVOs, we removed *vWF*+ cells, assumed to be HBMECs introduced during hVOMV fabrication. Pseudotime analysis of *vWF*-negative, *CDH5*-positive ECs from D5d vascular progenitors to $D5_{diff}+14_{int}+7_{v}+3_{H}$ D10 hVOMV vessels shows that ECs progress from lateral plate mesoderm to endothelial progenitors to hierarchical vessels (Figure 5.5 **K**). Trajectory analysis reveals that, over time, *CDH5* expression increases as arterial progenitors (*SOX17*) appear and subside, while artery-specific genes (*DLL4*) increase. Interestingly, capillary-related genes (*CLDN5*, *RGCC*, *APLNR*) begin to emerge, suggesting that the connection between the microchannel and the hVO leads to increased capillary EC formation. Toward the end of the trajectory, there is a burst of lymphatic vessel formation, suggesting that lymphatic vessels mature as the hVOMV becomes perfusable (Figure 5.5 **L**). Overall, our results show that arteriovenous ECs are primed before the introduction of perfusion, and these populations preferentially enrich into arterial, lymphatic, and capillary ECs as the hVO becomes perfusable.

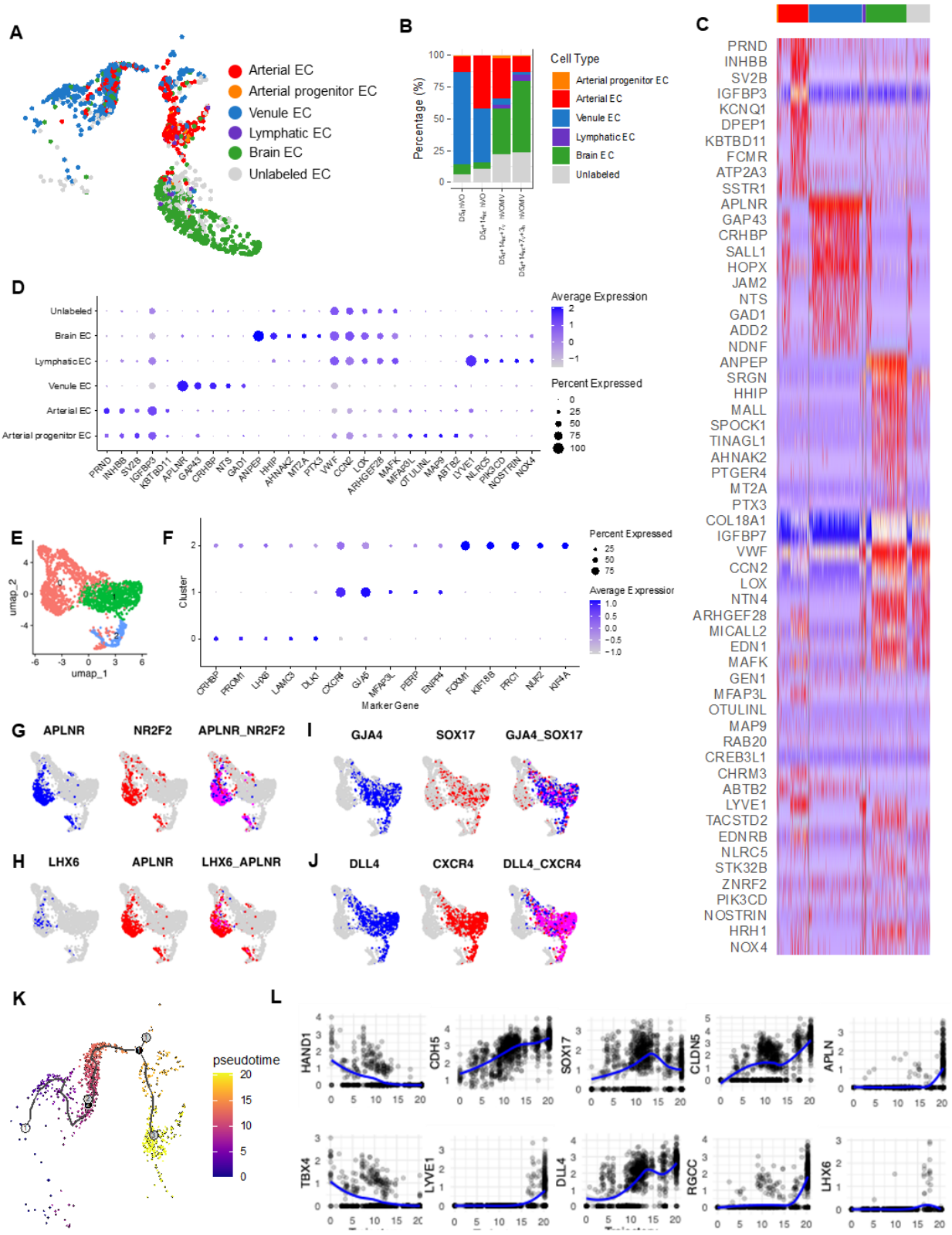


**Figure 5.5 Arteriovenous specification during vascular development from vascular progenitors (D5d) to hVOMV (D5d+14int+7v+3h).**

(A) UMAP representation of endothelial sub population in endothelial cell cluster. (B) population % map showing the changes in ratio of endothelial subpopulation from vascular progenitor to hVOMV. (C) Heatmap of differential gene expression in Each cluster (D) Bubble plot representing top genes expressed in annotated subpopulation. (E) UMAP integration of most representative EC cluster in D7 hVO ($D5_{diff}+14_{int}$ hVO). Prior to generation of organoid vessels, hVOs have committed arterio-venous specification. (F) Bubble plot representing top 5 genes in UMAP cluster from (E). Co-expression plot showing (G and H) venous specific gene and (I and J) arterial specific gene. (H) Monocle trajectory analysis for EC cluster in all 4 conditions without brain ECs (HBMEC). (K) Trajectory plot showing gene expression and regression line graph for lateral plate mesoderm (HAND1, and TBX4), general endothelial cells (CDH5), arterial ECs (SOX17, DLL4), capillary ECs (CLDN5, RGCC, and APLN), lymphatic ECs (LYVE1) and venule ECs (APLN, and LHX6).

## 5.5 Discussion and Conclusion

In this study, we successfully engineered perfusable human vascular organoid microvessels (hVOMVs) and demonstrated that different hemodynamic stimuli, including pressure gradients and continuous flow, drive distinct patterns of vascular remodeling and network maturation. These results illustrate the significance of hemodynamic cues in guiding vascular architecture, offering insights into the mechanisms by which blood vessels establish and maintain hierarchical organization in response to flow and pressure.

Our approach involved combining hVOs with 3D-patterned microvessels, creating a system capable of supporting anastomosis and subsequent intraluminal perfusion within hVOs. Successful anastomosis and intraluminal perfusion are essential steps for investigating how blood vessels develop and remodel in response to distinct hemodynamic flows. Our model allows the hVOs to remain functionally perfusable *in vitro*, addressing a critical limitation of traditional organoid cultures where the lack of flow often leads to endothelial cell regression.

Our results also demonstrate that hVOMVs can be used to model the impact of hemodynamic forces on vascular architecture in a controlled *in vitro* environment, enabling parametric studies on how different pressure and flow rates impact vessel remodeling. These findings underscore the

necessity of hemodynamic cues—such as flow directionality and pressure gradients—in driving organized, functional vascular remodeling and network hierarchy. This study provides a framework for future research aimed at replicating organ-specific vascular structures and functionalities. hVOMVs offer a versatile platform for studying flow-mediated vascular development, disease modeling, and drug screening.

In the future, refining flow conditions to more closely mimic physiological patterns may further enhance the utility of hVOMVs in biomedical research. Additionally, integrating co-cultured parenchymal cells or testing the effect of pulsatile flow could provide insights into how microenvironmental and biomechanical factors together shape vascular identity and function. By developing systems that better emulate *in vivo* vascular dynamics, we can expand the applicability of engineered vascular models for studying tissue-specific vascularization and advancing regenerative medicine.

.

# Chapter 6: Future works

## 6.1 Spatial phenotyping of endothelial cells in 3D microvessel images using pixel level clustering for comprehensive KIR prediction of barrier regulating kinases.

Endothelial cells, which form the innermost layer of blood vessels, serve as a critical barrier between the bloodstream and surrounding tissues. Altered barrier function and compromised vascular integrity are hallmarks of many vascular diseases, often reflected in morphological and structural changes. Despite rapid advancements in bioinformatics and imaging technologies that enable extensive data collection, current tools remain limited in their capacity to accurately capture and analyze intricate morphological changes. Consequently, significant delays occur in the experimental analysis phase, limiting the progress of cutting-edge research.

Chapter 3 utilized a kinase inhibition regression (KIR) model to predict barrier-regulating kinase inhibitors (KIs) from functional permeability screening. In this work, junctional analysis was employed to confirm and characterize the findings. As a direction for future work, extracting cellular features directly from immunofluorescent images would be valuable, given that kinase pathways are heavily implicated in endothelial cell (EC) junctional dynamics and morphology.

Current approaches for analyzing EC morphology rely on traditional segmentation techniques that identify individual cells based on distinct boundaries. These methods often overlook subtle yet critical morphological details, such as variations in cell shape, texture, and intercellular interactions—features essential for understanding cellular behavior and dynamics. Rigid boundary definitions can result in the loss of these nuanced features, limiting the comprehensiveness of morphological analysis. Additionally, current segmentation approaches are time-consuming,

labor-intensive, and susceptible to inter-operator variability, compromising the reproducibility and objectivity of extracted parameters. This limitation poses a significant challenge for accurate and unbiased morphological analysis of EC junctions, affecting research efforts across the scientific community.

The development of a pixel-based clustering tool for comprehensive morphological analysis of ECs cultured in 2D and 3D microvessels will provide an invaluable resource for investigating how ECs respond to different stimuli. Rather than relying on boundary-based segmentation, this tool will map intensity profiles and morphological features at the pixel level to capture subtle cellular details. The method will analyze pixel distances relative to the cell nucleus across z-stacks, enabling the detection of intensity variations and spatial relationships within and between cells.

This tool will integrate functional vessel permeability data with EC structural and morphological information, resulting in a multidimensional dataset suitable for advanced regression models. This approach will facilitate a comprehensive assessment of how specific kinases and genes regulate endothelial barrier function in response to various KIs. The successful development of this tool will significantly advance EC morphology analysis, improving objectivity and analytical potential for both our research and the broader vascular biology community. Its adaptability for 3D image analysis will enable more precise and comprehensive investigations, supporting deeper insights into EC responses to injury and therapeutic interventions.

### 6.2 Modeling CADASIL pathophysiology using hVOMV.

A major benefit of utilizing human induced pluripotent stem cells (hiPSCs) lies in their potential to model the pathophysiology of rare genetic disorders using patient-specific cells. For instance,

CADASIL, a hereditary vasculopathy that causes recurrent strokes and dementia, is characterized by the accumulation of NOTCH3 extracellular domain aggregates, leading to vascular smooth muscle cell (VSMC) degeneration. Despite the severity of CADASIL, effective treatments remain unavailable due to limited models that accurately capture its pathophysiology.

The use of patient-derived hiPSCs offers a promising path forward for creating disease-specific models to study CADASIL mechanisms and identify potential therapies. By integrating tissue engineering with hiPSC technology, researchers can construct patient-specific 3D vascular networks to examine CADASIL microvessels under physiologically relevant conditions. This approach enables detailed analysis of structural and functional abnormalities in CADASIL VSMCs and endothelial cells (ECs).

Developing CADASIL models using human vascular organoids (hVOs) derived from patient hiPSCs holds promise for uncovering disease-specific changes and potential therapeutic targets. As proof of concept, hVOs were successfully generated from hiPSCs derived from both CADASIL patients and healthy controls (Figure 6.1). Initial comparisons between control hVOs (Figure 6.1 **A**) and CADASIL hVOs (Figure 6.1 **B**) suggest an overexpression of pericytes within CADASIL hVOs. Cross-sectional analysis reveals that pericytes in CADASIL hVOs do not colocalize with $CD31^+$ ECs (~18%), whereas in control hVOs, pericytes are localized adjacent to $CD31^+$ ECs (~66%). These Initial studies have demonstrated that hVOs generated from CADASIL patients exhibit disorganized mural cell architecture compared to healthy controls, reflecting key disease characteristics. This suggests that hVOs, especially when combined with perfusable microvessels, could be valuable tools for investigating disease mechanisms and advancing drug discovery in the future.

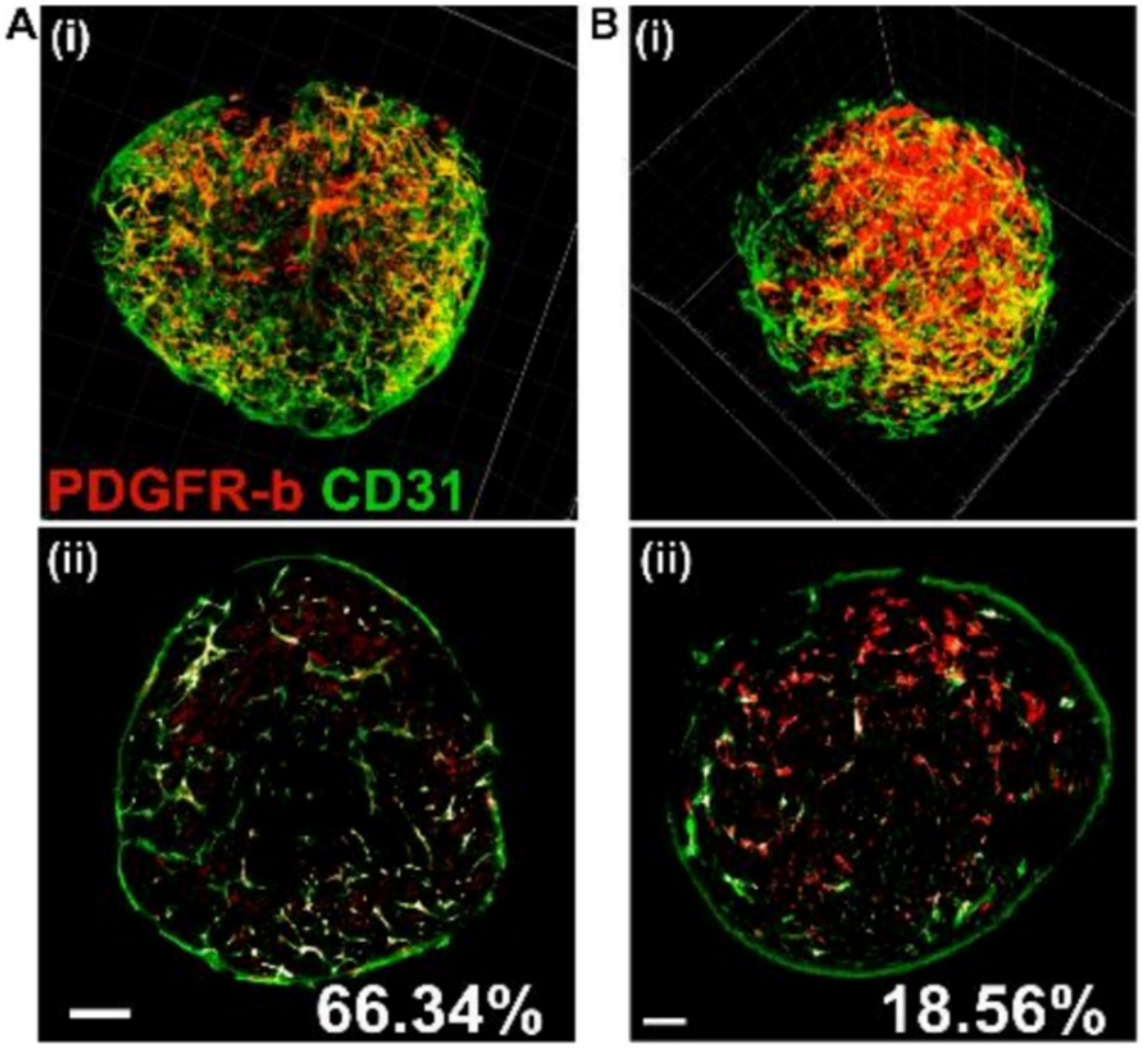


**Figure 6.1 CADASIL hVOs show disorganized pericyte localization.**

A) Control hVO and (B) CADASIL hVO. (i) 3D rendering and (ii) cross-sectional image shows higher % of pericyte co-localization with CD31+ area.

# Appendix A. 3D bioprinting of mechanically tuned bioinks derived from cardiac decellularized extracellular matrix.

*This appendix has been published in the following manuscript: Shin YJ* and Shafranek RT*, et al. "3D bioprinting of mechanically tuned bioinks derived from cardiac decellularized extracellular matrix" Acta biomaterialia, 2021. DOI: 10.1016/j.actbio.2020.11.006*

## A.1 Abstract

3D bioprinting is a powerful technique for engineering tissues used to study cell behavior and tissue properties in vitro. With the right formulation and printing parameters, bioinks can provide native biological and mechanical cues while allowing for versatile 3D structures that recapitulate tissue-level organization. Bio-based materials that support cellular adhesion, differentiation, and proliferation - including gelatin, collagen, hyaluronic acid, and alginate - have been successfully used as bioinks. In particular, decellularized extracellular matrix (dECM) has become a promising material with the unique ability to maintain both biochemical and topographical micro-environments of native tissues. However, dECM has shown technical limitations for 3D printing (3DP) applications posed by its intrinsically low mechanical stability. Herein, we report hydrogel bioinks composed of partially digested, porcine cardiac decellularized extracellular matrix (cdECM), Laponite-XLG nanoclay, and poly(ethylene glycol)-diacrylate (PEG-DA). The Laponite facilitated extrusion-based 3DP, while PEG-DA enabled photo-polymerization after printing. Improving upon previously reported bioinks derived from dECM, our bioinks combine extrudability, shape fidelity, rapid cross-linking, and cytocompatibility in a single formulation (> 97% viability of encapsulated human cardiac fibroblasts and > 94% viability of human induced pluripotent stem cell derived cardiomyocytes after 7 days). The compressive modulus of the cured hydrogel bioinks was tunable from 13.4-89 kPa by changing the concentration of PEG-DA in the

bioink formulation. Importantly, this span of mechanical stiffness encompasses ranges of tissue stiffness from healthy (compressive modulus ~5-15 kPa) to fibrotic (compressive modulus ~30-100 kPa) cardiac tissue states. The printed constructs demonstrated shape fidelity, adaptability to different printing conditions, and high cell viability following extrusion and photo-polymerization, highlighting the potential for applications in modeling both healthy and fibrotic cardiac tissue.

## A.2 Introduction

3D bioprinting technologies enable the fabrication of tissue-like constructs that aim to replicate the complexity of biological systems. These digital manufacturing processes can take advantage of imaging techniques such as CT and MRI scans to create computer-aided design (CAD) files. The digital files provide the blueprint for 3D bioprinters to fabricate a desired tissue construct. Therefore, the growth of the 3D bioprinting field provides opportunities to employ this technology for in vitro disease modeling. Such models could be utilized for applications in drug screening, disease mechanism research, and pre-clinical studies in the tissue of interest[211–220].

Recent advances in bioinks for 3D bioprinting have sought to modify the biochemical and mechanical properties of the bioink matrix for in vitro disease modeling and tissue engineering[214,221–235]. However, an existing challenge in the field is the balance between the rheological properties required for printing and the physicochemical properties required of the printed matrix. The complex relationship between rheological parameters, printability, and cell viability has been recently reviewed[236,237] for common 3D bioprinting techniques, including inkjet printing and micro-extrusion. For extrusion-based 3DP, one of the most important properties of a bioink is shear-thinning behavior, in which the material flows under high shear stress but maintains a significantly higher viscosity under low-shear conditions[238,239] (‘at rest’). In addition, the

viscoelastic properties of the bioinks have been shown to be critical for maintaining cell viability during the printing process[240–242].

Conventionally, both natural hydrogel materials (gelatin[243–245], collagen[214,244], hyaluronic acid[243,246,247], alginate[248–250]) and synthetic hydrogels (poly(lactic acid)[251], PEG-DA[252,253], Pluronic F127[254–256]) have been popular choices for bioinks. Synthetic hydrogels exhibit good gelation kinetics and mechanical tunability, which is advantageous for bioprinting. However, these materials lack the ability to closely mimic the biological cues of the native ECM micro-environment. On the other hand, naturally derived hydrogels have the ability to emulate tissue micro-environments through their biophysical and biochemical properties but can be more challenging to tune with respect to their viscoelastic properties during the printing process and the mechanical properties that arise after printing. Among the naturally derived hydrogels, dECM-derived bioinks have attracted significant attention for their enhanced tissue functionality, which is unmatched by other hydrogels. dECM bioinks are unique in that they preserve some of the growth factors, extracellular matrix (ECM) proteins, and glycosaminoglycans (GAGs) specific to the source tissue. Previous studies have demonstrated 3DP of dECM bioinks derived from a variety of sources including liver[243,257,258], heart[257,259,260], kidney[220,261], cartilage[262,263], adipose[259] and tendons[264]. However, similar to other naturally derived hydrogels, dECM gels are marked by a lack of mechanical and structural stability (with compressive, tensile, or shear moduli < 1 kPa), which is lost during both the decellularization and digestion processes[259]. Recent work has focused on tailoring the mechanical properties of dECM-based bioinks to match the properties of a particular tissue. For example, one recent study reported the improvement of mechanical stability through a two-step gelation process requiring both temperature control and UV cross-linking using vitamin B to engineer a physiologically relevant cardiac tissue compressive modulus (~15 kPa)[263].

While multiple approaches have enabled dECM-based bioinks to recapitulate the modulus of native cardiac tissues, current methods have not fully investigated strategies for modeling diseased cardiac tissues, which manifest a higher tissue stiffness (compressive modulus between 30-100 kPa)[265,266]. For instance, cardiac fibrosis is one of the hallmarks of cardiac disease, accompanied by many cardiomyopathies such as hypertrophic cardiomyopathy, idiosyncratic dilated cardiomyopathy, and myocardial infarction[267]. Therefore, introducing technologies to recapitulate mechanical properties of fibrotic cardiac tissue in 3D platforms is valuable for modeling cardiac diseases. A key event in cardiac fibrosis, a process marked by disproportionate deposition of collagen and abnormal proliferation of fibroblasts, is the differentiation of fibroblasts to myofibroblasts[268–270]. While many factors influence activation of myofibroblasts, one of the most important is substrate stiffness[271–274]. However, the mechanism by which myofibroblasts recognize and respond to substrate elasticity is not well understood. Therefore, there is a need to develop in vitro systems with precisely tunable mechanical properties that mimic the extracellular environment.

Herein, we report a cdECM-based bioink that has been modified with Laponite and PEG-DA to afford bioinks that can be extrusion-printed to fabricate constructs with tunable mechanical properties. To the best of our knowledge, this is the first report of a bioink that uses dECM, Laponite, and PEG-DA concurrently to afford a single bioink capable of extrusion and rapid photo-polymerization. This naturally derived bioink can print without supports, cure quickly, and promote high viability of encapsulated cells. To date, there are few examples of dECM-derived bioinks that can be photo-cross-linked in 1 minute or less while simultaneously preserving shape fidelity and cell viability. Specifically, we show that the desired mechanical stiffness of cross-linked cdECM bio-constructs can be achieved by varying the concentration of PEG-DA, covering

all physiological compressive stiffness ranges from healthy (5-15 kPa) to pathological (30-100 kPa) conditions. Additionally, Laponite has been shown to provide necessary rheological properties[275] and print fidelity[276–279] while providing the biocompatibility that is crucial for bioinks[280]. Therefore, our bioinks satisfy the need for high-stiffness bio-constructs without sacrificing biocompatibility or the capacity to fabricate complex 3D structures. Our work improves upon a previous report[259] in which dECM-based bioinks, both with and without living cells, were extrusion printed into a poly(caprolactone) support framework, then thermally cured at 37 °C for 30 minutes. In particular, the current strategy eliminates the need for both support frameworks and long thermal gelation periods by adding Laponite to facilitate stacking of filaments and PEG-DA to promote rapid photo-polymerization (1 minute or less). Other bioinks require support frameworks or fugitive inks (like Pluronic F127) for mechanical reinforcement[281,282], while our bioinks are free-standing and self-supporting. Our bioinks cross-link rapidly and irreversibly due to the photo-polymerization of PEG-DA, while bioinks that use alginate[281–283] or dECM without a photo-cross-linker[282] require replenishment of exogenous cations to preserve cross-linking interactions or long thermal curing times that may result in loss of shape fidelity. Finally, our bioinks require mild processing and printing conditions, in contrast to bioink formulations that require higher extrusion pressures (like collagen, ECM, and tannic acid[284]) or freeze-drying, harsh chemical cross-linking, and solvent treatment[285]. Whereas harsh processing and printing conditions are acceptable for applications wherein cells are seeded onto printed constructs, it is critical to avoid conditions that cause cell death for bioinks with encapsulated cells. Overall, the all-in-one bioinks reported herein simplify the extrusion-printing process, requiring no support frameworks, no long gelation periods, and no harsh chemical treatments or printing pressures that damage embedded cells.

With the ability to rapidly photo-polymerize filaments, 3D-printed constructs maintain structural integrity in contrast to constructs that are cured slowly, which often collapse due to destabilization of the underlying layers. Furthermore, varying the concentration of PEG-DA affords more precise control over the final stiffness of printed constructs compared to thermal gelation. Through incorporation of both Laponite and PEG-DA, we show that the printed cdECM bio-constructs have the potential to be used for disease modeling of cardiac fibrosis by controlling the mechanical properties to afford compressive moduli that mimic both native and diseased cardiac tissue. Additionally, the cdECM bioinks demonstrate high cell viability of human cardiac fibroblasts (> 97% viability) and human induced pluripotent stem cell derived cardiomyocytes (> 94% viability) after 7 days. These are promising results for the fabrication of functional 3D-printed constructs containing active cardiac cells.

## A.3 Materials and Methods

### *A.3.1 Decellularization of porcine cardiac tissue*

Cardiac tissues were obtained from porcine hearts, purchased from a local butcher. Left ventricles were specifically harvested from porcine hearts and stored at -20°C, up to 6 months. Cardiac tissues were thawed, diced, washed in deionized (DI) water for 2 h and decellularized using multiple chemical detergents, following a published protocol[259]. Briefly, the rinsed cardiac tissues were immersed in 1% sodium lauryl sulfate (Fisher Scientific; SDS) in phosphate buffered saline (PBS, Invitrogen) for 72 h. Following SDS treatment, porcine heart cubes were treated with 1% Triton X-100 (Sigma-Aldrich) in PBS for 1 h, then washed in PBS for 72 h. All rinsing and detergent washing steps involved stirring of the solution on stir plates at 200 rpm. Solution changes for 1% SDS (in PBS) and PBS occurred daily to ensure efficient removal of cellular debris and

thorough washing of remaining detergents. After PBS washes, the decellularized scaffold tissues were collected in tubes and stored at -80°C until lyophilization.

*A.3.2 Composite cdECM bioink preparation*

Fabrication of the cdECM pre-gel was conducted by lyophilizing frozen samples of cdECM for 72 h. Lyophilized cdECMs were stored at 4°C up to 3 months prior to pepsin digestion. Upon digestion, lyophilized cdECM was shredded and finely chopped into flakes using razor blades. To prepare the cdECM pre-gel, cdECM flakes were massed in a glass vial for digestion at ~9-10% w/v; typically, 500 mg of cdECM was combined with 50 mg of pepsin (P7000, from porcine gastric mucosa, Sigma-Aldrich) and 4.3 mL of 0.1 M aqueous HCl at room temperature for one week. Following digestion, solubilized 10% cdECM pre-gel was diluted with 0.5 mL of 10X RPMI to account for ionic balance. The remaining volume (200 μL) was used to adjust final pH to 7.4 using 10 M aqueous NaOH. A pH meter was used to monitor the change during pH adjustment. cdECM pre-gels were stored at 4°C up to 2 weeks.

The solubilized cdECM was combined with a nanoclay viscosity modifier, Laponite-XLG (BYK Additives & Instruments), a photo-curable cross-linker, PEG-DA (Mn = 700 g mol−1, Sigma-Aldrich), and a photo-initiator, lithium phenyl-2,4,6-trimethylbenzoylphosphinate (LAP; Sigma-Aldrich). Laponite powder was pre-dissolved in DI water at 9.1% w/w to prevent separation of Laponite and cdECM and to help form a homogeneous gel. All gels were formulated by mass/weight. Typical bioink preparation was as follows: First, the LAP photo-initiator was added to a clean glass vial. Next, the appropriate mass of cdECM pre-gel was added to the glass vial, followed by 9.1% w/w Laponite gel. A small volume of 10X RPMI 1640 media was then added to ensure final 1X concentration. This was followed by DI water, and finally by PEG-DA (liquid at room temperature). The final concentrations of each component were 0.4% w/w LAP, 1X RPMI,

4.6% w/w cdECM, 2.3% w/w Laponite, and 6.0, 8.25, or 10.5% w/w PEG-DA, with DI water constituting the remaining mass. The final composite bioinks were briefly vortexed, then centrifuged for ~30 s at 2 000 rpm to ensure collection of all components at the bottom of the vial. Finally, the bioinks were covered with reflective foil and stirred at room temperature until visually homogeneous, at least 18 h.

*A.3.3 Rheological analysis*

All rheological experiments were performed on a TA Instruments Discovery HR-2 hybrid rheometer equipped with a Peltier temperature-control accessory. All experiments utilized a flat-plate 8 mm stainless steel geometry and were conducted at 21 °C. First, strain amplitude sweep experiments were conducted for each cdECM ink formulation to establish the linear viscoelastic region (LVR). All strain amplitude sweeps were conducted at a constant angular frequency (ω) of 1 Hz (6.28 rad s−1). Then, frequency amplitude sweeps were performed at constant 1% oscillatory strain (γ) to determine the viscoelastic behavior of the gels at both short and long time scales. To help quantify printability, shear-thinning experiments were carried out during which samples were subjected to increasing rates of shear (0.005-50 s−1). To further establish the reversible mechanical yielding and recovery of the bioinks, short oscillatory step-strain experiments were conducted at constant frequency (1 Hz) with alternating cycles of 1% and 100% strain amplitude. Finally, blue-light (405 nm) photo-curing at 28 mW cm−2 intensity was performed using a Mightex BLS-series BioLED analog control module coupled to a Mightex WLS-series WheeLEDTM light source. These curing experiments demonstrated rapid photo-curing of the bioinks. It should be noted that these rheological curing experiments provided measures of the shear modulus (G'), which is a different parameter from the compressive modulus measured on a load frame. Moreover, the intensity of light used to cure rheological samples (28

mW cm−2) may not have been the same intensity as the light used for curing compressive samples, which could not be accurately quantified. The purpose of the rheological curing experiments was simply to demonstrate rapid photo-curing and to provide an estimate of the range of material stiffness that could be achieved.

*A.3.4 Compressive modulus testing*

Cylindrical samples for compression testing, approximately 9 mm in diameter by 5 mm in height, were cast in PDMS molds. Samples were cured under 395-400 nm irradiation (QUANS UV LED flood light, 20 W) at a distance of 15 cm from the light for 60 s. Uniaxial compression testing was performed on an Instron 5585H load frame using a 50 N load cell at a rate of 1.3 mm min−1. Uniaxial compressive force was applied to the hydrogel constructs until the point of failure. The compressive modulus was calculated using linear regression analysis of the stress-strain curve between 0-10% strain. Each bioink formulation was measured at least in triplicate.

*A.3.5 Characterization of bioink printability*

Allevi 2, a two-syringe 3D bioprinter with a pneumatic pressure system, was used to print the cdECM-Laponite-PEG-DA 'composite' bioink. Testing of the bioink printability was conducted for all formulations (6.0%, 8.25% and 10% w/w PEG-DA) by printing a square CAD model (10 mm x 10 mm). Prior to printing, the cdECM composite bioink was loaded into a 10-mL syringe by filtering through a 25G needle to ensure successful printing. The syringe was then connected to an external pressure source to enable pneumatic extrusion. Various ranges of pneumatic pressure (6, 7, 8 and 9 psi) and the diameter of the nozzle (25G: 260 μm and 27G: 210 μm) were used to optimize best printing parameters as well as to demonstrate the versatility and adaptability of the cdECM composite bioink. After each print, an external blue-light module (405 nm) located under the extruder head was turned on for 60 s to immediately cross-link the printed bioink. Photographs

of printed constructs were analyzed using ImageJ software to quantify the print linewidth measurements and to analyze overall printability of the cdECM bioinks.

Demonstration of the cdECM composite bioink printability was further validated by creating and printing CAD models harboring complex geometries. Three different designs, the UW husky logo, University of Washington acronym, and concentric circles with varying diameters, were prepared. For visualization, 1 μL of yellow food dye (Whole Foods 365 Brand; based on vegetable glycerin and turmeric) was incorporated into the final gel formulation. The husky logo was 2 cm x 3 cm with infill density of 30%, and the concentric circles consisted of 4 different circles (1, 2, 3, and 4 cm in diameter). All prints were demonstrated using the cdECM composite bioink comprised of 6.0% PEG-DA and 2.3% Laponite. A 25G nozzle at 9 psi was used to print each design at room temperature. After printing, each design was photocured using a blue-light module for 30 s. Confirmation of the stability of our printed material was conducted using the 6.0% PEG-DA bioink, which was printed, photo-cured and immersed in Hank's buffered solution for 1 week.

The ability to print a multi-layer construct was analyzed by layering square prints to create a z-construct of 18 layers. To test printability in the z-direction, the cdECM-Laponite-PEG-DA 'composite' bioink (6.0% PEG-DA) was printed using both a 25G nozzle at 9 psi and a 22G nozzle at 8 psi. Z-stacks were created through a layer-by-layer method whereby each layer was extruded then cross-linked using 405 nm irradiation for 30 s before a subsequent layer was printed on top of the previous cured layer. The thickness of each layer was measured from each side of the printed 3D construct and was used to quantify the structural durability of the z-stack.

*A.3.6 Cell culture*

Human cardiac fibroblasts (HCFs), human induced pluripotent stem cell (hiPSC) derived cardiomyocytes, and HS27A human bone marrow derived stromal cells (ATCC) were

cultured for use in assessing the biocompatibility of the cdECM-Laponite-PEG-DA composite bioink. Briefly, HCFs were cultured in Fibroblast Medium-2 (ScienCell) supplemented with 5% Fetal Bovine Serum (ScienCell), fibroblast growth supplement-2 (ScienCell; FGS-2) and 1% Penicillin/Streptomycin (ScienCell). Media was changed every 2 days, and cells between passage 3-5 were utilized. HS27As were cultured and maintained in high-glucose DMEM (Invitrogen) supplemented with 10% fetal bovine serum.

UC 3-4 urine-derived hiPSCs[286] were cultured and differentiated into cardiomyocytes following an adaptation of a previously published method[287]. In brief, hiPSCs were induced with RPMI 1640 medium (Invitrogen) supplemented with B-27 without insulin (Invitrogen) and 10 μM CHIR-99021 (Selleck Chemicals). After 18 h, the medium was replaced with fresh RPMI/B-27 without insulin for 48 h. The medium was then replaced with RPMI/B-27 without insulin supplemented with 5 μM IWP-4 (REPROCELL) for 48 h, after which the medium was once again replaced with fresh RPMI/B-27 without insulin for 48 h. Finally, medium was replaced with RPMI/B-27 with insulin (Invitrogen). Spontaneously beating cells are typically observed 10-12 days after induction.

*A.3.7 Fabrication of engineered heart tissue constructs*

The design and fabrication of the hardware utilized for both generating the engineered heart tissues (EHTs) and measuring forces in situ has been previously described[288]. In brief, post pair arrays were fabricated by pouring polydimethylsiloxane (PDMS; Sylgard 184, Dow Chemical) at a 10:1 base to curing agent ratio into an acrylic mold. A glass capillary tube was inserted into one post of each pair to impart rigidity to that post. Molds were then placed into a 65°C oven overnight to cure the PDMS. Cured post pair arrays were then removed from the mold. Each post was 12.5 mm long and 1.5 mm in diameter and featured a cap structure 0.5 mm thick and 2 mm in diameter to assist with tissue attachment. Post-to-post spacing was 8 mm. Wells for tissue casting were

fabricated by pouring approximately 1 mL of PDMS into the wells of a 24-well culture plate before inserting custom 3D printed spacers that would form rectangular wells with dimensions of 12 mm x 4 mm x 4mm (length x width x depth). After curing the PDMS overnight, molds were removed. hiPSC-CMs and HS-27A stromal cells were mixed in the cdECM-Laponite-PEG-DA composite bioink (6.0% PEG-DA) at cell densities of 20 × 106 cells/mL and 10 × 106 cells/mL, respectively. 70 μL of this cell-hydrogel mixture was then pipetted into each cast PDMS well, after which PDMS post arrays were positioned upside-down into the wells, ensuring that each post tip was immersed in the cell-hydrogel solution. The 24-well plate was then exposed to blue light for 30 seconds before it was placed into an incubator at 37°C and 5% CO2 for approximately 60 min. 1 mL of RPMI/B-27 with insulin (supplemented with Y-27632 dihydrochloride ROCK inhibitor and 1% penicillin/streptomycin) was then added to each well. After 24 h, the media was replaced with fresh RPMI/B-27 with insulin, and media changes were conducted every other day.

*4.3.8 Cell viability testing*

Cell viability was assessed on a thin disc of cdECM-Laponite-PEG-DA hydrogel (0.1 mm thick x 1 mm in diameter) containing HCFs and on EHTs containing hiPSC-CMs and ATCCs. HCFs were resuspended into respective bioink formulations at a density of 2.0 × 106 cells/mL Each formulation was syringe-extruded into thin discs (7mm x 7mm x 1mm). After 1 day and 7 day culture periods, cell viability analysis was performed using a live/dead cell assay kit (Invitrogen Life Technologies, USA) following the protocol provided by the manufacturer. Stained samples were imaged using 10X magnification through a confocal microscope (Spinning disk, Nikon Instruments, NY, USA) and quantified using ImageJ image processing software (National Institutes of Health, MD, USA). Green fluorescence signals indicated live cells (calcein-AM excitation/emission: 488/515 nm) whereas red fluorescence signals indicated dead cells (ethidium

homodimer-1 excitation/emission: 570/602 nm). Viability analysis was conducted by quantifying the number of live cells in each culture condition using ImageJ software.

#### *4.3.9 Statistical analysis.*

All data are reported as mean ± standard deviation. Statistical significance was determined via a one-way analysis of variance (ANOVA) test for all the quantification measurements, including comparisons of compressive modulus, storage modulus, tan δ, and yield stress (σy). Pairwise f-tests and two tailed Student's t-tests were subsequently conducted for pairs of data sets.

## A.4 Results and Discussion

#### *4.4.1 Preparation of composite cdECM-Laponite-PEG-DA bioinks*

Fabrication and printing of the cdECM bioink required multiple processing steps (Figure A.1). Initially, left ventricular tissues harvested from porcine hearts were decellularized with chemical detergents to effectively remove cellular components and to preserve the cardiac ventricular ECM. The cdECM harbors many of the biophysical and biochemical cues present in the native cardiac micro-environment and therefore provides some of the crucial intrinsic features (i.e. morphological similarities, specific cell-matrix interactions, tissue specificity) that cannot be replicated by other materials[289,290]. We have previously shown that porcine cardiac tissues could be effectively decellularized (~98% removal of cellular content) while maintaining major ECM components (such as collagen and GAGs) using a combination of chemical detergents: 1% SDS and 1% Triton X-100[259,291]. The cdECM was then digested with gastric pepsin at low pH to create a concentrated, soluble form of cdECM that could be utilized in the extrudable composite bioinks.

An important consideration throughout optimization of the bioink included the ability for the hydrogel to maintain its shape after extrusion. To date, one of the challenges of using dECM-based

bioinks has been the poor intrinsic mechanical properties – such as low modulus, viscosity, and yield stress – which prevent a high-fidelity print, especially in the z-direction. Our formulation with 4.6% cdECM alone was too low in shear modulus and viscosity to be suitable for extrusion-based 3DP. To address this challenge, we introduced a clay-based bioceramic, Laponite-XLG, to enhance the printability of the bioink. Laponite, a disc-like crystalline colloid, has been previously used for modification of rheological properties[275,292]. Studies showed that incorporation of Laponite enabled high print fidelity and exhibited the biocompatibility required for bioinks[283]. Combining rheological experiments (Section 4.4.2) with qualitative manual extrusion, it was determined that a concentration of 2.3% w/w Laponite was sufficient to impart the desired rheological properties to the cdECM bioink.

Furthermore, the tunability of mechanical properties - via introduction of cross-linking agents - can afford a wider array of bioinks for engineering stiffness. In cardiac tissue, the myocardium stiffness is regulated by different cardiac cellular subtypes such as cardiomyocytes, cardiac fibroblasts, and endothelial cells that regulate the ECM. Therefore, the interplay between resident cardiac cells and paracrine signaling within their micro-environment can result in modification of ECM stiffness. In particular, various forms of cardiac myopathies that lead to inflammation and scar tissue formation, such as myocardial infarction and ventricular ischemia, can trigger progressive fibrosis and excessive deposition of ECM. Many cdECM based bioink studies have so far recapitulated the tissue stiffness of the healthy myocardium (compressive; ~5-15 kPa) through thermal and photo-initiated cross-linking but have not emulated the material stiffness required for modeling cardiac diseases that are closely associated with tissue ECM stiffness. To address this issue, we incorporated different concentrations of a PEG-DA cross-linker to afford constructs with

a range of stiffness following photo-polymerization. Iterative rheological photo-curing (Section 4.4.3) was used to determine the range of PEG-DA concentrations that could accurately represent the stiffness of different cardiac disease states.

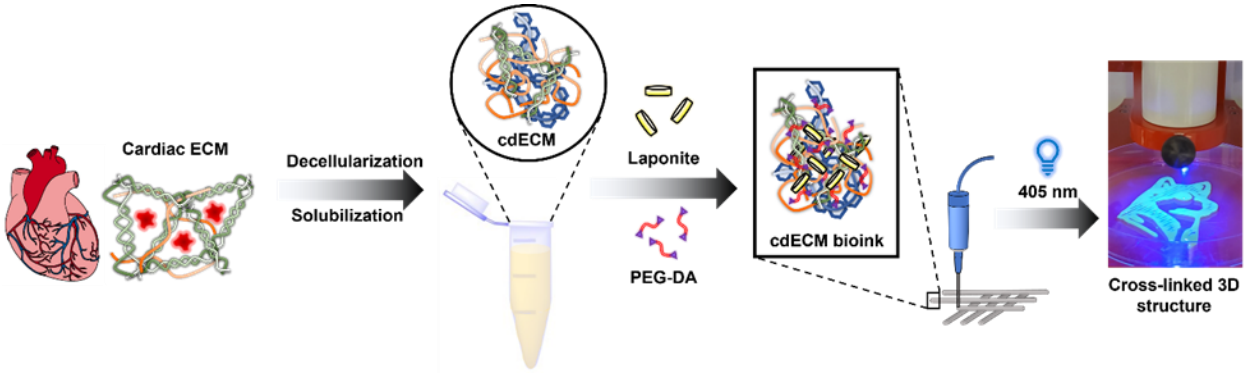


**Figure A.1 Schematic overview of the cdECM bioink preparation and fabrication of 3D bio-printed constructs.**

Schematic overview of the fabrication and printing of engineered cdECM bioinks. Fabrication of the bioink involved decellularization and solubilization of cardiac tissues into pre-gels which were modified with Laponite to afford a viscoelastic bioink capable of providing a high-fidelity print. Incorporation of the cross-linker PEG-DA and a photo-initiator, lithium phenyl-2,4,6-trimethylbenzoylphosphinate, allowed tunable mechanical properties by changing PEG-DA concentration.

### *4.4.2 Rheological characterization of cdECM-Laponite-PEG-DA bioinks*

With the necessary components of the bioinks in hand, we attempted to quantify printability using rheological experiments. For the remainder of the manuscript, bioink formulations are referred to by weight percentage, using the general formula cdECM-Laponite-PEG-DA%. To validate the use of each bioink component, we prepared a full range of six bioink formulations: cdECM alone (4.6-0-0% w/w), cdECM with PEG-DA (4.6-0-6.0% w/w), cdECM with Laponite (4.6-2.3-0% w/w), and three 'printable' formulations, each containing 4.6% w/w cdECM, 2.3% w/w Laponite, and 6.0, 8.25, or 10.5% w/w PEG-DA. For a bioink to be suitable for direct-write extrusion 3DP, it must exhibit several desirable viscoelastic properties. Some rheological parameters that have been shown to impact printability include yield stress, $\sigma y$[238,239,293,294], loss factor, tan $\delta$ (G"/G')[295], and viscosity, $\eta$[276,296]. Specifically, bioinks with gel character (G' >G") tend to exhibit high shape

fidelity after extrusion-based 3DP. It is also important for such materials to be shear-thinning, which facilitates pneumatic extrusion. With these parameters in mind, three rheological experiments were performed on each cdECM bioink formulation. Each test was performed for each of the six different formulations, with comparisons made against the control 4.6-0-0% ink.

The first test was an oscillatory strain amplitude sweep from 0.01 to 100% strain (Supplementary Figure. SA.1 **a** and **b**). The primary purpose of this test was to determine the equilibrium shear moduli and to establish the linear viscoelastic region (LVR) for each formulation to ensure that all subsequent oscillatory measurements would occur without irreversible deformation. Based on this experiment, 1% strain was chosen as the standard for all subsequent oscillatory measurements. Additionally, the strain amplitude sweep allowed estimation of σy by calculating oscillatory stress from the applied strain and then plotting shear moduli vs. stress (Figure A.2 **a** and **b**). Yield stresses were estimated by determining the onset point of G' decrease using regression techniques in Trios software (TA Instruments).

For viscoelastic gels, σy is a critical stress value below which any deformation is small and reversible[297]. Above σy, the gel network breaks down, the material flows and becomes deformed. Therefore, higher values for σy suggest better stackability of printed filaments in the z-direction and better shape fidelity. There was only one statistically significant difference in σy (Figure A.3 **c**) compared to the control formulation consisting only of cdECM (4.6-0-0%), likely due to difficulty with reproducibility of experiments. This makes it difficult to draw any conclusions about the effects of Laponite and PEG-DA on the σy values for the cdECM bioinks; however, the statistically significant difference ($p < 0.05$) between the 4.6-2.3-10.5% and 4.6-0-0% formulations, together with analysis of G' and tan δ, imply that Laponite may be responsible for

any increase in the yield stress of the bioink. The effects of Laponite on the rheological characteristics of the bioink are discussed further in analysis of G' and tan δ.

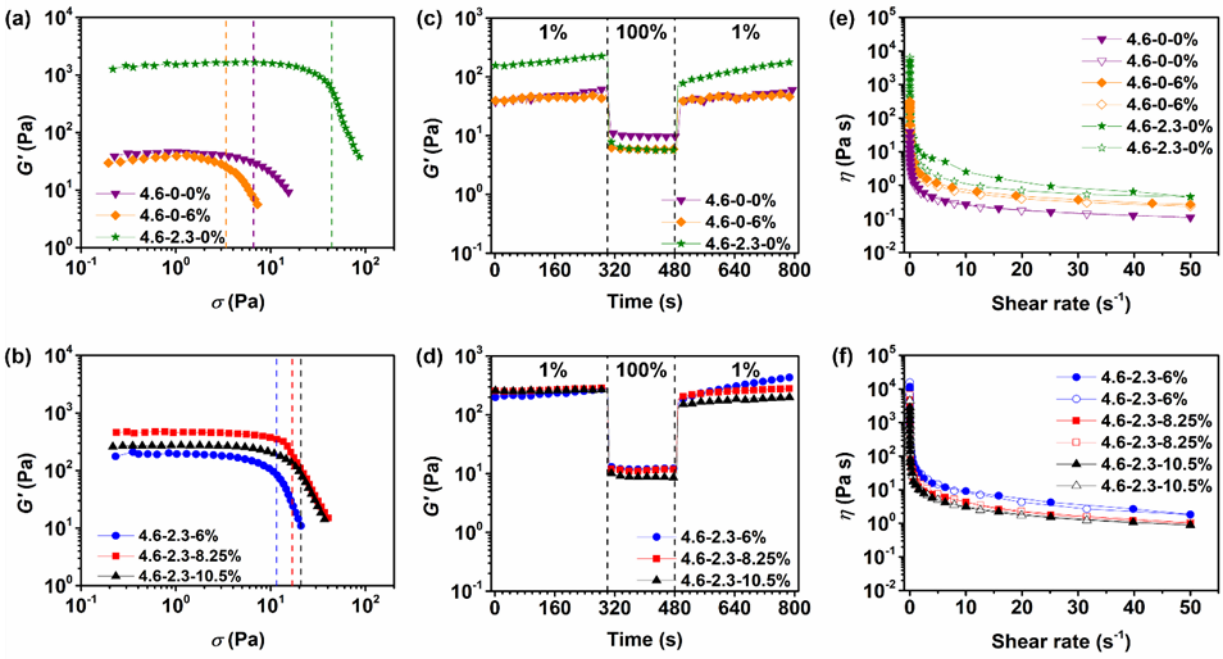


**Figure A.2 Rheometric characterization of different formulations of cdECM-Laponite-PEG-DA bioink.**

(a,b) Oscillatory stress sweep experiments conducted at 1 Hz angular frequency for (a) control formulations and (b) printable formulations. The onset of *G'* decrease was reported as the apparent yield stress, $\sigma_y$. The mean yield stress for each formulation is plotted as a dashed vertical line. All plots are the mean of 3 tests. (c,d) Dynamic oscillatory strain experiments conducted at 1 Hz angular frequency for (c) control formulations and (d) printable formulations. Strain amplitude alternated between 1 and 100%. All plots are the mean of 3-4 tests. (e,f) Plots of viscosity *vs.* shear rate for control formulations (e) and printable formulations (f) demonstrated the shear-thinning behavior and different viscosities of each formulation. Filled symbols indicate increasing shear rate, while open symbols indicate decreasing shear rate. All plots shown are the mean of 3-4 tests.

Next, dynamic oscillatory strain experiments (Figure A.2 **c** and **d**), in which samples were subjected to alternating periods of 1% and 100% strain at constant angular frequency, were performed. These tests provided estimates of the shear storage and loss (G") moduli, as well as the loss factor, tan δ. More importantly, the tests provided information about the mechanical recovery of inks following periods of high strain well outside of the LVR. The tests demonstrated that all

formulations behave as low-modulus viscoelastic solids with G' >G" and tan δ< 1 under low-strain conditions, which are meant to model behavior of the inks at rest. At high strain, all formulations exhibited a rapid decrease in G' and tan δ> 1, characteristic of fluid-like materials. Upon reversion to low strain, all formulations recovered nearly to the initial plateau value of G'. Many replicates showed a sloping curve for G' which made a plateau value difficult to estimate. Therefore, the exact time required for G' to reach the plateau value following high strain could not be determined. In general, formulations with Laponite were stiffer than those without, reflected by higher G' values (Figure A.3 **a**). Indeed, G' was higher for all formulations compared to the cdECM alone, excluding the 4.6-0-6.0% formulation that did not contain Laponite. This is likely due to the formation of a non-covalent Laponite gel network. Laponite, a disc-like platelet composed of sodium-magnesium-lithium silicates, is known to bear a negative charge on the face of the disc and a positive charge on the edges. At concentrations above ~ 1% w/w in aqueous solution and at pH < 9, the platelets may aggregate to form a so-called "house-of-cards" gel network, with the positively-charged edges of one disc interacting with the negatively-charged face of another[298,299]. The pH of the cdECM bioinks was maintained at ~ 7.4, and the concentration of Laponite was 2.3% w/w, meaning conditions were favorable for the formation of an ionic gel network. It is almost certain that Laponite discs interact not only with themselves, but also with partially-digested cdECM proteins. Indeed, strong electrostatic interactions between Laponite and collagen or type A gelatin[300–302] have been well-characterized. The additional structure afforded by Laponite and Laponite-protein networks increased the solid-like characteristics of the bioink by providing cross-links, thereby increasing the storage modulus and rendering the bioinks stiffer. PEG-DA alone (4.6-0-6.0% formulation) had no significant effect on G' compared to the control. This is unsurprising, given that the interaction between PEG-DA of relatively low molecular

weight (Mn = 700 g mol−1) and cdECM proteins is expected to be minimal. At this molecular weight, PEG is quite hydrophilic and does not present enough amphiphilic character to interact with hydrophobic residues in proteins.

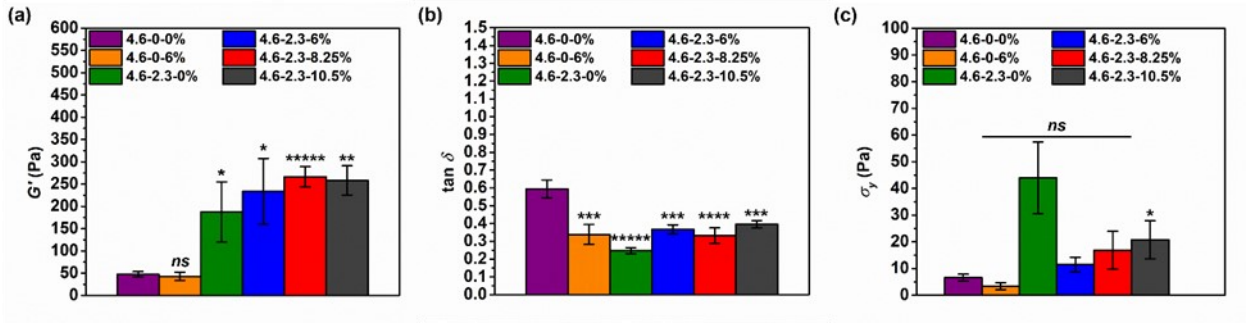


**Figure A.3 Laponite increases the plateau shear storage modulus (G') and decreases the loss factor (tan δ) of the cdECM bioinks.**

Statistically significant differences were determined *via* one-way analysis of variance (ANOVA), followed by pairwise *f*-tests and two-tailed Student's *t*-tests. All formulations were compared to the 4.6-0-0% bioink formulation as a control. Asterisks indicate significance levels: *$p < 0.05$; **$p < 0.01$; ***$p < 0.001$; ****$p < 0.0001$; *****$p < 0.00001$; *ns* = not significant. (a) Formulations containing Laponite exhibited significantly greater plateau *G'* values, largely due to the formation of a Laponite gel network. The addition of PEG-DA alone (4.6-0-6%, orange) had no significant effect on measured *G'* values. $N = 4$-5 for each measurement. (b) The loss factor, tan $\delta$, was lower compared to the control (4.6-0-0%, purple) for all formulations. This is an expected result for inks containing Laponite, but somewhat unexpected for the 4.6-0-6% formulation. $N = 4$-5 for each measurement. (c) The yield stress, $\sigma_y$, showed too much variability in measurement to assess any significant differences; however, the trend appeared to be an increase in yield stress in the presence of Laponite. $N = 3$ for each measurement.

Moreover, non-cross-linked PEG-DA in water is not expected to self-assemble into a gel network. The values of tan δ for our cdECM bioinks were significantly lower for all formulations compared to the control formulation comprised solely of cdECM (Figure A.3 **b**). This result is expected for inks containing Laponite, since the cross-linking interactions in the gel network impart a greater proportion of solid-like properties to the inks. As such, the ratio G" / G' becomes smaller. It is unclear why tan δ for the 4.6-0-6.0% formulation is significantly lower than the control, since PEG-DA is not expected to participate in any gel network formation that could alter tan δ. It is possible that the observed effect is simply due to the slight reduction in water content for the 4.6-

0-6.0% formulation compared to the control: The loose network of cdECM components occupies a slightly smaller volume of water and may not interact significantly with the PEG-DA, thereby increasing the measured solid-like behavior of the ink. Of course, if true, this reduction in water content could partially account for the reduction in tan δ for the other formulations as well. For bioinks that must be extruded and maintain shape fidelity, the value of tan δ should be between zero and one. Theoretically, inks with tan δ closer to one extrude uniformly and require only gentle pressure but exhibit poor shape fidelity and limited stackability. Inks with tan δ closer to zero are robust and self-supporting but require higher printing pressures and may be too brittle to extrude uniformly. These observations are rationalized by considering the physical meaning of tan δ, which is an expression of the ratio of fluid, viscous behavior (G") to solid, elastic behavior (G') in a viscoelastic material. If this ratio is ≥1, the material is mostly fluid and behaves correspondingly, meaning it tends to spread and flow and should not exhibit a yield stress. If the ratio is < 1, the material is mostly solid; this regime is typical for hydrogels. The closer tan δ is to 0, the more likely a material is to be self-supporting, but also more brittle due to the increased solid-like, elastic character of the material. Tan δ is also an important factor for measuring the glass transition temperature (Tg) of amorphous polymers via dynamic mechanical analysis: Below the Tg, tan δ << 1, and the polymer is brittle, while at and above the Tg, tan δ increases to reflect rubbery, elastomeric character. Therefore, a bioink with tan δ ~ 1 is likely to be fluid and runny, while a bioink with tan δ ~ 0 is likely to be rigid and brittle. Using a gelatin-alginate bioink, Lee and co-workers[295] found that a range of tan δ values between 0.25-0.45 were optimal for balancing smooth extrusion, shape fidelity, and cell viability. Additionally, bioinks with relatively low moduli (G' < 5 kPa) required lower extrusion pressure and were therefore better for cell viability. While these parameters were determined for a different bioink composition than the present study, it is

nevertheless interesting to note that tan δ for each of our extrudable cdECM bioink formulations (i.e., formulations containing all three components cdECM, PEG-DA, and Laponite) is between 0.25-0.45. Overall, the results of the dynamic strain experiments indicate that all inks are capable of mechanical recovery following deformation beyond the LVR, while inks containing Laponite are higher-modulus and lower in tan δ compared to the control cdECM-only formulation.

The shear-thinning behavior of the bioinks was evaluated by rotational shear rate sweep experiments (Figure A.2 **e** and **f**). All ink formulations exhibited shear-thinning behavior, wherein the viscosity decreased with increasing shear rate. Formulations without Laponite had relatively low viscosity (< 500 Pa•s) at low shear rates, while all formulations containing Laponite had viscosity above 5 000 Pa•s under low-shear conditions. The higher viscosity of the Laponite-containing inks (compared to the control cdECM-only formulation) might indicate more favorable printability. If the viscosity of an ink is too low, extruded filaments may spread or collapse upon contact with the printing stage or the previous layer of a printed object. However, to determine viscosity more accurately at a specific shear rate, it would be necessary to make repeated measurements at the shear rate of interest. Thus, the absolute values reported for viscosity may be inaccurate, although the trends between different formulations are expected to hold. Furthermore, the shear rate sweep experiments provided another estimate of σy. Indeed, flow curves of stress vs. shear rate (Supplementary Figure. SA.1 **e** and **f**) indicate that all ink formulations had a non-zero yield stress when fit to Herschel-Bulkley curves (fits not shown). However, the oscillatory strain amplitude sweeps were preferred for calculation of σy due to the gel-like nature of the bioinks[297].

Finally, a frequency amplitude sweep was performed to evaluate the frequency dependence of the moduli for each bioink formulation (Supplementary Figure. SA.1 **c** and **d**). A noticeable frequency

dependence of the moduli was observed for bioinks formulated without Laponite, wherein the moduli values increased with increasing angular frequency. This trend is characteristic of weakly interacting or weakly cross-linked polymer chains, wherein the material is more fluid-like at lower frequencies, while more solid-like at higher frequencies[297]. However, inks formulated with Laponite showed no apparent frequency dependence. This trend is observed for solid-like materials with fairly strong cross-linking interactions and a stress relaxation time that must be greater than the inverse of the lowest applied frequency (0.1 rad s−1). Thus, Laponite imparts structural stability to the bioinks through non-covalent interactions.

Overall, the rheological data demonstrate that, in principle, any of the cdECM bioinks could be suitable for extrusion-based 3DP. They are all hydrogels at rest, with measurable yield stresses. However, bioink formulations without Laponite were not printable in practice. Rheological experiments showed that cdECM bioinks formulated with Laponite are higher-modulus, have lower tan δ, and are more viscous, both at rest and when flowing, than inks without. Physically, this means that inks containing Laponite should have better extrudability, shape fidelity, and stackability in the z-dimension.

### *4.4.3 Characterization of PEG-DA-mediated mechanical tunability in composite cdECM bioinks*

The precise tunability of the mechanical properties of 3D-printed bioinks is critical to the development of tissue models that can replicate native structure and function with a high degree of fidelity. Therefore, an important consideration in the gelation/cross-linking process of engineered bioinks is the curing of the printed construct to reach a target modulus. As such, most dECM-based bioinks have utilized thermal gelation kinetics, wherein the printing process takes advantage of the change in temperature to induce physical cross-linking of abundant collagen

within the dECM. However, the rate of thermal gelation is insufficient for extrusion-based bioprinting processes that do not involve the use of a temporary support gel[303], especially as additional layers are stacked in the z-direction. To overcome such challenges, multifaceted cross-linking schemes have been introduced, from two-step thermal gelation approaches[260] to incorporation of photo-polymerizable cross-linkers[263], which have successfully enhanced the mechanical properties of the cdECM-based bioinks to recapitulate representative cardiac tissue compressive moduli in the range of 5-15 kPa. However, there is still a lack of tissue-derived 3D bioinks that can recapitulate the mechanical properties of pathological cardiac conditions observed in the fibrotic heart. To take full advantage of the opportunities provided by 3D bioprinting (i.e., in vitro disease modeling, drug-screening applications) it is beneficial to create mechanically versatile bioinks that can be tuned to match specific tissue compressive moduli found in both healthy (5-15 kPa) and diseased states (30-100 kPa).

PEG-DA is a common synthetic polymer for hydrogel biomaterials with tunable elastic properties, solute permeability, and biocompatibility[304,305]. Therefore, we sought to incorporate different concentrations of PEG-DA to fabricate a mechanically tunable bioink that can recapitulate a wide range of cardiac tissue compressive moduli. LAP was employed as a water-soluble photo-initiator to rapidly initiate polymerization of the PEG-DA; a prompt polymerization of PEG-DA was desired as rapid cross-linking kinetics are necessary to maintain pattern fidelity of the bio-construct. LAP has also been shown to permit high survival of the encapsulated cells, an important property required to engineer a bioink[306]. Thus, the cdECM composite bioinks in this investigation comprised cdECM-Laponite hydrogels with PEG-DA (6.0%, 8.25%, or 10.5% w/w) and 0.4% w/w LAP.

To quantify both the gelation kinetics and the ability to formulate hydrogels with distinct mechanical properties, we performed oscillatory time sweep measurements with photo-curing (405 nm, 28 mW cm−2) for three printable formulations of our composite cdECM bioink. Each formulation consisted of 4.6% w/w digested cdECM, 2.3% Laponite, and 0.4% LAP, with PEG-DA concentrations of 6.0%, 8.25%, or 10.5%. For the first 120 s of the test, G' and G" were measured at 1 Hz and 1% strain to obtain baseline moduli prior to photo-polymerization. Irradiation started at 120 s and lasted for 60 s, resulting in fast and stable cross-linking of the bioink (Figure A.4 **a** and **b**). The photo-polymerization was rapid for all formulations, with the ink reaching 95% of the final plateau modulus in approximately 14 s (10.5% PEG-DA), 17 s (8.25%) and 20 s (6.0%). These blue-light curing tests also validated the ability to optimize and control material stiffness by varying PEG-DA concentration. As expected, the final stiffness of each bioink increased with increasing PEG-DA concentration from G' = 0.761 kPa (6.0% PEG-DA) to 5.23 kPa (8.25%) to 36.9 kPa (10.5%) (Figure A.4 **c**). The substantial increase in G' corresponding to a relatively small increase in PEG-DA concentration is likely due to a considerable increase in cross-link density (ρx) and decrease in molecular weight between cross-links (Mc). The relationship between moduli (shear, compressive, and tensile) and PEG-DA molecular weight/concentration has been well-characterized in the literature[307–311].

Next, uniaxial compression testing was performed on cured hydrogels generated from each composite cdECM bioink formulation. Each formulation was photo-cross-linked in a cylindrical PDMS mold. A representative stress-strain curve was obtained for each composite cdECM bioink (Figure A.4 **d**). The linear region of the stress-strain curve between 0-10% strain was used to calculate the compressive modulus (Figure A.4 **e**). The compressive moduli of the three printable formulations were 13.4 ± 0.4 kPa (6.0% PEG-DA), 39 ± 8 kPa (8.25%), and 89 ± 7 kPa (10.5%)

(Figure A.4 **f**). Importantly, all the printable formulations mimicked either the compressive modulus of healthy (5-15 kPa) or fibrotic (30-100 kPa) cardiac tissues[265,266]. Thus, our low-modulus bioink (6.0% PEG-DA) can be cured to a stiffness that approximates healthy tissue while the intermediate (8.25% PEG-DA) and high-modulus (10.5% PEG-DA) bioinks may be suitable for recapitulating fibrotic tissue.

(a) Oscillatory time sweep analysis ($\gamma$ = 1%, $\omega$ = 1 Hz) of each gel formulation before and after photo-cross-linking. The light was turned on at 120 s and turned off at 180 s. (b) Zoomed time sweep plot between 110-190 s, demonstrating rapid increase in *G'* upon photo-curing. (c) Analysis of *G'* after photo-induced cross-linking (60 s) for different PEG-DA concentrations in cdECM bioinks. Error bars are ± one standard deviation. (d) Stress-strain curves from uniaxial compression testing showing characteristic behavior of hydrogels. All plots are the mean of 3-4 tests. (e) Zoomed stress-strain plot between 0-10% strain, showing linear regions from which compressive moduli were calculated. (f)

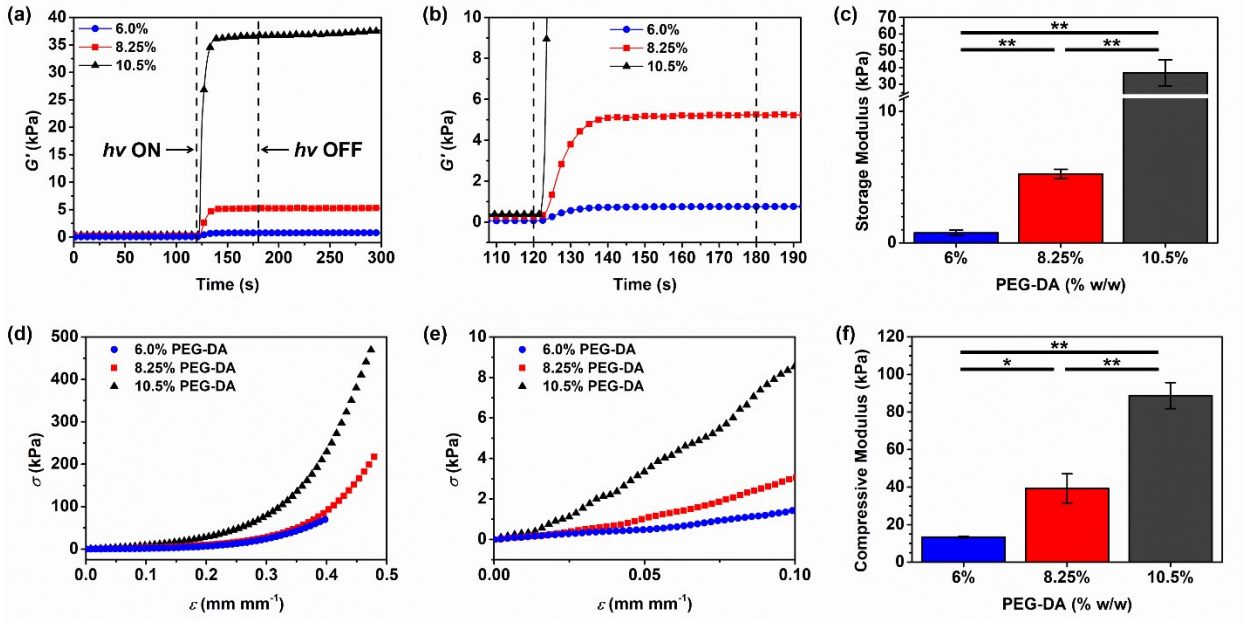


**Figure A.4 Tunable mechanical properties by incorporation of PEG-DA (Mn= 700 g mol-1) into the cdECM bioink.**

Analysis of compressive moduli for each PEG-DA concentration between 0-10% strain, showing that the different formulations can be used to recapitulate cardiac tissue stiffness associated with normal (blue) and diseased conditions (red and grey). Error bars are ± one standard deviation. Statistically significant differences were determined via one-way analysis of variance (ANOVA), followed by two-tailed Student's *t*-tests. Asterisks indicate significance levels: *$p < 0.01$; **$p < 0.005$.

*4.4.4 3D printing of composite cdECM bioinks*

3DP of intricate tissue constructs requires precise control of optimal printing parameters. Extrusion-based printing offers a high degree of freedom wherein print parameters can be manipulated to determine the dimensions of the extruded bioink, allowing enhanced linewidth resolution and shape fidelity. However, the resolution and fidelity of the print in extrusion-based 3D bioprinting is limited by the inherent properties of the bioink itself. Rheological experiments (Figure A.2) showed that our printable formulations harbor the necessary characteristics of an extrudable bioink, which inspired confidence in the ability for our bioink to extrude and maintain the intended shape. To further assess the feasibility and versatility of our composite cdECM bioink for extrusion-based printing, we created a simple square CAD design and subjected our bioinks to various printing conditions.

All our printable composite cdECM bioinks were tested using different nozzle sizes and pressures. Two nozzle sizes with distinct inner diameters (25G: 260 μm and 27G: 210 μm), four print pressures (6, 7, 8 and 9 psi), and three PEG-DA concentrations (6.0%, 8.25%, and 10.5% w/w) were correlated to the linewidth of the extruded filament (Figure A.5). The printing parameters (i.e., nozzle sizes and print pressures) used to assess printability were chosen based on the ability to reproducibly generate prints with good shape fidelity. The linewidth measurements from 24 different conditions showed that the width of the line can be adjusted from 370 μm to 3 mm. The range of linewidth dimension allows use of lower pressures and smaller nozzle diameters to print constructs with structural detail, while higher pressures and larger nozzle diameters will enable efficient printing of larger structures. The width of the measurement was mostly dependent upon the nozzle diameter, except for the low-modulus bioink (6.0% PEG-DA) which was not as affected by the size of the nozzle (Figure A.5 **d**). We observed that an increase in the extrusion pressure

corresponded with larger linewidth measurements for both nozzle sizes. Interestingly, the concentration of PEG-DA within the bioink was one of the governing factors for linewidth. With the low-modulus bioink (6.0% PEG-DA) (Figure A.5 **a**), the printed lines were comparably thinner than the intermediate (8.25%) (Figure A.5 **b**) and high (10.5%) modulus bioinks (Figure A.5 **c**). This is likely due to the lower viscosity values observed for the intermediate and high-modulus bioinks. While G', tan δ, and σy values were similar for the 6.0%, 8.25%, and 10.5% PEG-DA bioinks, the viscosity appeared to decrease from 6.0% to 8.25% to 10.5%. It should be noted that, for the experiments performed, it is difficult to accurately determine statistically significant differences in viscosity values between formulations.

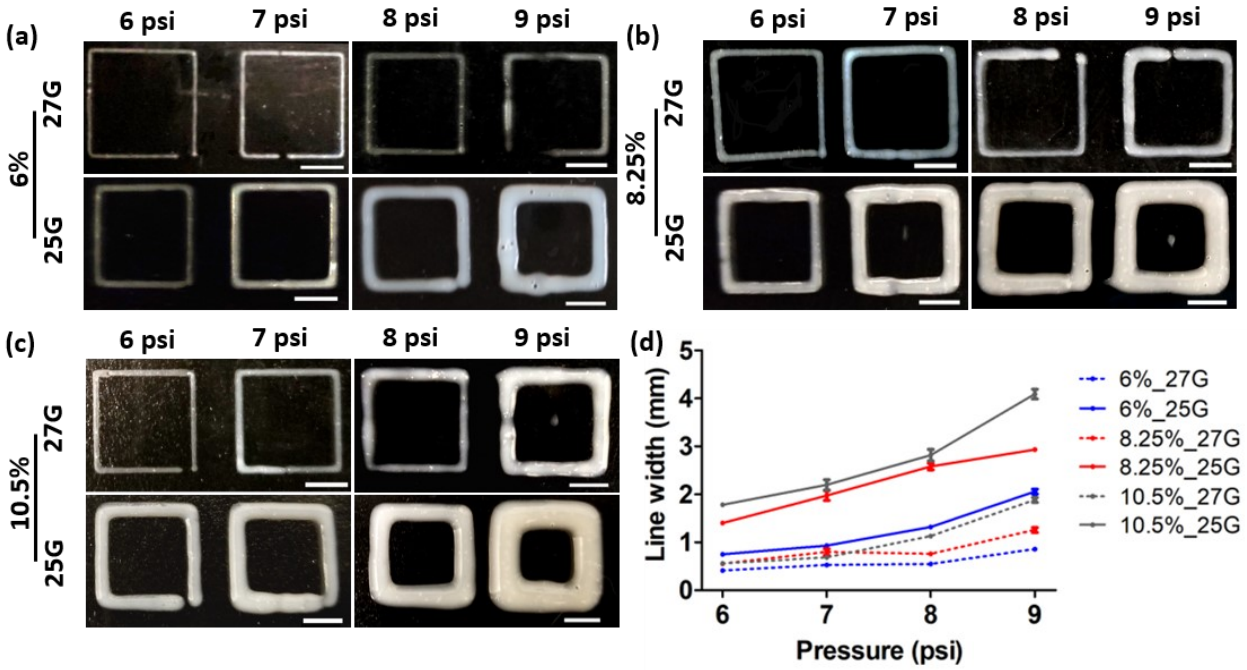


**Figure A.5 Demonstration of printed line fidelity of cdECM-Laponite-PEG-DA bioinks.**

3D printing of a square CAD model demonstrates adaptability of the bioink for different formulations. The size of the nozzle (25G: 260 μm and 27G: 210 μm) and the feed pressure were varied to generate 8 different print conditions for all three (a) low modulus bioink, (b) intermediate modulus bioink, and (c) high modulus bioink (total of 24 print parameters). The analysis of printability was conducted by quantifying the width of each line print ($n$ = 4). (d) Linewidth measurement graph showing the trend of linewidth with respect to nozzle size, print pressure and composite cdECM bioink formulations. Scale bars: 5 mm.

Furthermore, we prepared a line print using our low-modulus bioink (6.0% PEG-DA) and tested our bioink stability by measuring the width of our print immediately and 7 days after immersion in a salt- balanced aqueous solution. The results showed that the width of our line print is maintained at 2 mm at both time points, indicating that our composite bioinks do not undergo swelling (Supplementary Figure. SA.3). Next, we created more complex CAD models to demonstrate that our bioink could be applied to print more versatile structures with intricate geometries. We created three distinct designs: an acronym representing the University of Washington (UW) (Figure A.6 **a**), a concentric circular design (Figure A.6 **b**), and a UW husky logo (Figure A.6 **c**). The low-modulus bioink (4.6% w/w cdECM, 2.3% Laponite, 6.0% PEG-DA) was chosen based on its ability to create higher-resolution prints. Each design was printed at 9 psi and cross-linked immediately after with a 405 nm light module located on the print head (Fig. 6(d)). All the designs were printed with high fidelity with respect to the sliced CAD model. Specifically, there was no bleeding of printed bioink, resulting in crisp borders, no disparity in the resolution of different diameters of concentric circles, and high shape fidelity with respect to infill patterns and infill density within the husky logo.

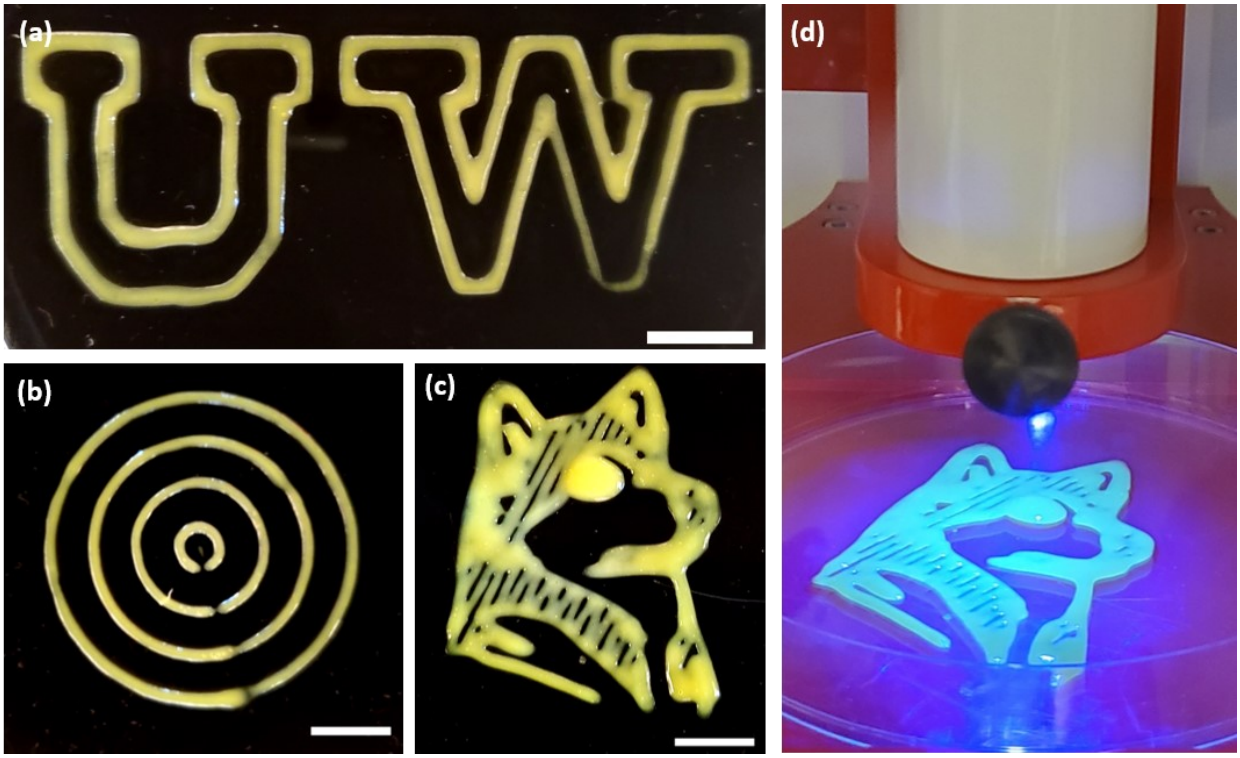


**Figure A.6 Demonstration of printability of complex geometries using cdECM-Laponite-PEG-DA bioink.**

3D printing of complex geometries demonstrates adaptability of the bioink to create complex structures. cdECM composite bioink with 6.0% PEG-DA was used to print (a) the alphabetic acronym of the University of Washington, (b) a concentric circle and (c) the UW husky logo. (d) Demonstration of blue-light (405 nm) mediated cross-linking for the cdECM composite bioink post-print. Scale bars: 1 cm.

Finally, we tested the feasibility of our composite cdECM bioink to generate a multi-layered 3D construct. Demonstration of stacking of filaments in the z-direction was performed via layer-by-layer printing of the low-modulus (6.0% PEG-DA) bioink). To improve the durability of the overall construct, 30 s photo-cross-linking (405 nm) of each construct was performed before a subsequent layer was printed on top (Figure A.7 **a**). The layer-by-layer 3D extrusion printing of the composite bioink afforded a multi-layered construct up to 18 layers (Figure A.7 **b**). The resulting structure was a flexible elastomer that could be picked up with forceps and maintained its structure over one month. A multi-layered construct printed using a smaller nozzle size (25G at 9 psi) shows that extruded filaments maintain their shape prior to cross-linking and enhance the

fidelity of each print in the z-direction (Figure A.7 **b** and **c**). The top view image, especially, validates that the material did not collapse as more ink was deposited, suggesting high durability and structural integrity of the bioink (Figure A.7 **d**). The printability of our bioink in the z-direction was quantitatively validated through measurement of each layer width at different z-positions (heights) of the construct. Indeed, the linewidths were relatively similar throughout the entire multi-layered construct, which further validated the high fidelity and mechanical durability enabled by our composite cdECM bioink (Figure A.7 **c**).

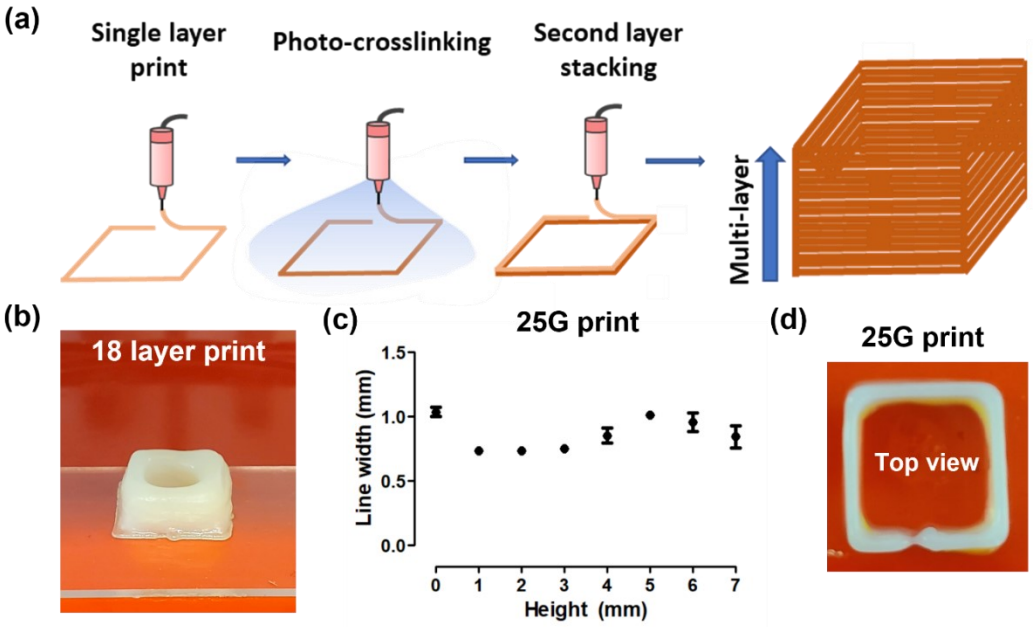


**Figure A.7 Demonstration of 3D printability of cdECM composite bioink in the z-direction.**

3D printing of multiple stacks of square prints was conducted to demonstrate the ability to fabricate a mechanically stable, layered 3D construct in the (vertical) *z*-direction. (a) Schematic of the 3DP process involved in an 18-layered tower. Each print was conducted using a 25G nozzle at 9 psi or a 22G nozzle at 8 psi with the low-modulus bioink (6.0% PEG-DA) and immediately cross-linked using blue-light (405 nm) irradiation for 30 s. This process was repeated 18 times to create a stable, 18-layered construct. (b) Picture of an 18-layered construct printed with a 22G nozzle at 8 psi. (c) Analysis of the linewidth quantified for different heights of the 18-layered construct printed with a 25G nozzle at 9 psi post-print ($n$ = 4) and (d) top view of the construct printed with a 25G nozzle at 9 psi. The measurements were taken using calipers every 1 mm until the final layer.

### *4.4.5 Biocompatibility assessment of composite cdECM bioinks*

To demonstrate the feasibility of utilizing our engineered cdECM composite bioink as a tissue engineering scaffold, we tested the biocompatibility of various control and printable bioink formulations. Previous studies have shown that bioinks comprised of cdECM were able to support cellular survival up to 7 days post-print, indicating that the cdECM-based bioinks were not only biocompatible but also able to withstand shear conditions during the pneumatic printing process[257,259]. To test whether the incorporation of Laponite, high concentrations of PEG-DA, and LAP photo-initiator diminishes the biocompatibility of our bioink, we demonstrated cell viability using primary human cardiac fibroblasts (HCFs) and human induced pluripotent stem cell derived cardiomyocytes (hiPSC-CMs). HCFs were chosen based on previous studies that have investigated the effect of substrate stiffness on trans-differentiation of myofibroblasts. As myofibroblast trans-differentiation manifests in cardiac fibrosis through mechano-transduction of stiffening cardiac ECM, HCFs serve as an ideal cell type to investigate a potential mechano-transduction pathway involved in cardiac fibrosis, a potential application of the mechanically tunable composite bioink[268,312,313]. Characterization of cell survival was conducted through a Live/Dead Assay kit on varying formulations of cdECM, Laponite and PEG-DA containing gels. Initially, we tested the viability of cells in a 0-0-6% (PEG-DA only) gel, a 0-2.3-6% (Laponite and PEG-DA) gel, and a 4.6-0-6% (cdECM and PEG-DA) gel (Supplementary Figure. SA.4). Viability results showed that addition of Laponite and cdECM significantly increased the cellular survival after 7 days. In particular, Laponite enabled the highest survival of HCFs cultured within the gels, maintaining viability above 98% throughout a 7-day long culture period. This finding aligns well with previous reports of cdECM-based hydrogels and Laponite-containing hydrogels that exhibit excellent biocompatibility both in vitro and in vivo[283,314].

Next, we tested the viability of HCFs within our composite printable bioink formulations with varying concentrations of PEG-DA (6.0%, 8.25% and 10.5% w/w) and compared the results to the 4.6-0-0% (cdECM only) gel. To better understand the possible effects of synthetic additives (i.e. Laponite, PEG-DA, and LAP photoinitiator) on cell viability, we performed hand extrusion of cell-laden bioinks using the exact syringes and needles required for 3D printing. This method was chosen because: 1) the printing pressure required to print our material is similar to the pressure applied during hand extrusion and 2) it avoids variability that may arise from printing parameters. To ensure the consistency of shear stress applied to the cells within the bioink, we utilized the same needle gauge used to 3D print our cell-laden bioinks. Therefore, we do not expect to observe significant changes between the overall viability of the cells within hand extruded bioinks and 3D printed bioinks, aside from larger variations in the standard error caused by the variability of print parameters used in the 3D printing system. Our composite bioink exhibited high cellular survival 1 day and 7 days after printing and cross-linking (> 97% viability), indicating that the PEG-DA concentrations used in our hydrogels do not cause any deleterious effects (Figure A.8). Moreover, compared to the cdECM-only formulation, our printable formulations (i.e., those containing Laponite) showed reduced cellular cytotoxicity, suggesting that the addition of Laponite drastically enhanced the viability of the cells. In addition, comparing the viability results of cells in cdECM-only gels (Figure A.8) with cells in cdECM and PEG-DA gels show that introduction of PEG-DA-mediated cross-linking increased cellular survival. Because PEG-DA photo-polymerization occurred within 30 s, cured constructs were immersed in culture media quickly after printing. By contrast, the thermally cured cdECM-only gels required 30 minutes of gelation time, depriving encapsulated HCFs of media for a long period of time and decreasing cellular survival.

One drawback to our printable formulation, however, is the inability of HCFs to spread out and assume their native fibroblast morphology as observed in the cdECM-only gel. This is likely a direct result of diminished biochemical cues and the presence of dense, non-biodegradable PEG-DA networks that prevented the cells from enzymatically degrading and remodeling the matrix. Similarly, unlike the normal EHT tissues, which are able to compact and generate functional cardiomyocyte beating within one week, EHTs generated from our bioinks showed limited compaction (data not shown), re-confirming our hypothesis that cell-cell interaction between the stromal cells responsible for contraction of EHT was limited by the dense, cross-linked PEG-DA network within our gels that reduced cellular ability to remodel the matrix. Nevertheless, the incorporation of Laponite and PEG-DA were necessary for high-fidelity extrusion 3D printing and for recapitulating the mechanical properties that we are aiming to model. Furthermore, previous studies showed that Laponite and gold nanoparticles incorporated into an injectable dECM hydrogel allowed enhanced functionality of cardiac tissues, suggesting that Laponite may not significantly impair the functionality of cardiac cells[315]. Our results also show that all four EHTs harboring hiPSC-CMs exhibited high viability (> 94%) after 7 days of culture, thus validating that additives within our printable bioink formulations can support the survival of less robust cells such as hiPSC-CMs. However, we recognize that further analysis of cellular activity needs to be addressed for application of the bioinks in disease modeling. One possibility is the inclusion of enzymatically cleavable bonds within the cross-linkers for facile degradation of the surrounding matrix, which would further support functional activity of cardiac cells within the system.

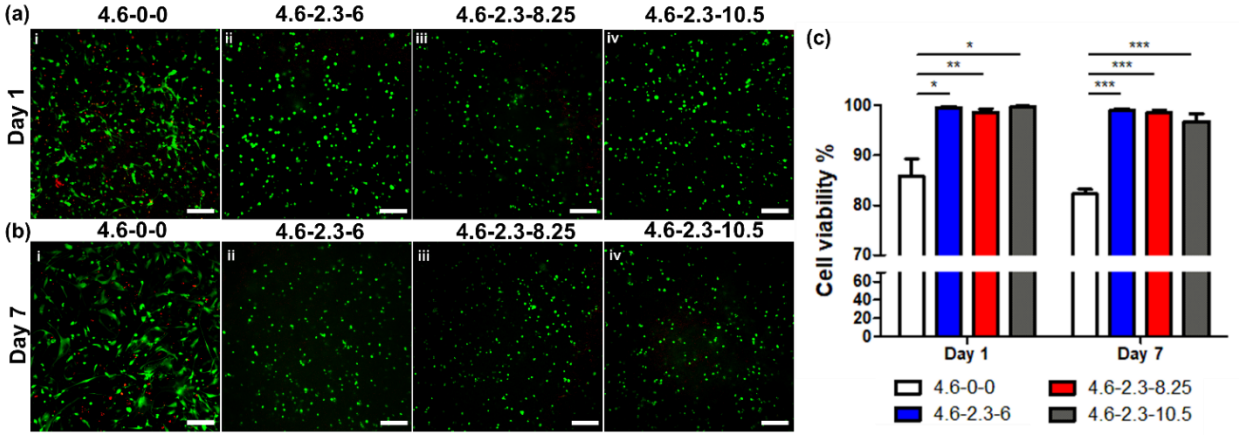


**Figure A.8 Cell viability of primary human cardiac fibroblasts (HCFs) after 1 day and 7 days of culture within composite bioinks.**

Live/Dead cell viability was performed on HCFs encapsulated within composite bioinks. x-y-z numbers in the legends refer to x: cdECM % w/w, y: Laponite %, and z: PEG-DA % within the bioink. (a,b) Representative fluorescence images with live/dead viability staining at (a) day 1 and (b) day 7 of culture. Cellular survival was higher in all composite bioink formulations with (ii) 6.0% PEG-DA; (iii) 8.25% PEG-DA; and (iv) 10.5% PEG-DA compared to (i) cdECM only (4.6-0-0%) gels. (c) Quantification of cell viability showed that HCFs maintained high viability (> 97%) within all bioink formulations compared to the cdECM-only gel. Although viability was lower in the cdECM-only gel, HCFs exhibited more spreading, suggesting that cdECM only was more favorable for enzymatic degradation by HCFs. Scale bar: 200 μm. Statistically significant differences were determined via one-way analysis of variance (ANOVA), followed by two-tailed Student's *t*-tests. Asterisks indicate significance levels: *$p < 0.001$; **$p < 0.05$; ***$p < 0.0005$.

## A.5 Conclusion

Composite bioinks derived from porcine cdECM were engineered for extrusion-based 3DP of constructs with tunable elasticity. Laponite-XLG nanoclay enabled shape fidelity and high resolution by increasing the shear storage modulus and viscosity of the cdECM-based hydrogels. The final compressive modulus of the photo-polymerized hydrogels was adjustable from 13.4-89 kPa according to the concentration of PEG-DA in the bioink formulation. This range of moduli encompasses the stiffness of both healthy and fibrotic cardiac tissue and shows that our printed constructs could be viable models of cardiac disease states. The linewidths of the extruded cdECM bioink filaments were correlated to both extrusion pressure and nozzle diameter, demonstrating

quantification of print resolution and shape fidelity. Complex and multi-layer structures could also be printed, which are important considerations for future printing of biologically relevant 3D bio-constructs. Finally, encapsulated human cardiac fibroblasts survived both extrusion and photo-polymerization to show > 97% viability after 7 days, demonstrating the cytocompatibility of the cdECM composite bioinks. Additional viability testing with human induced pluripotent stem cell derived cardiomyocytes also showed that our bioinks could support the survival of less robust cardiac cells. This study lays the groundwork for 3D bioprinting of constructs intended to model both healthy and fibrotic cardiac tissue states by recapitulating biological cues and biomechanical properties.

## A.6 Supplementary Figures

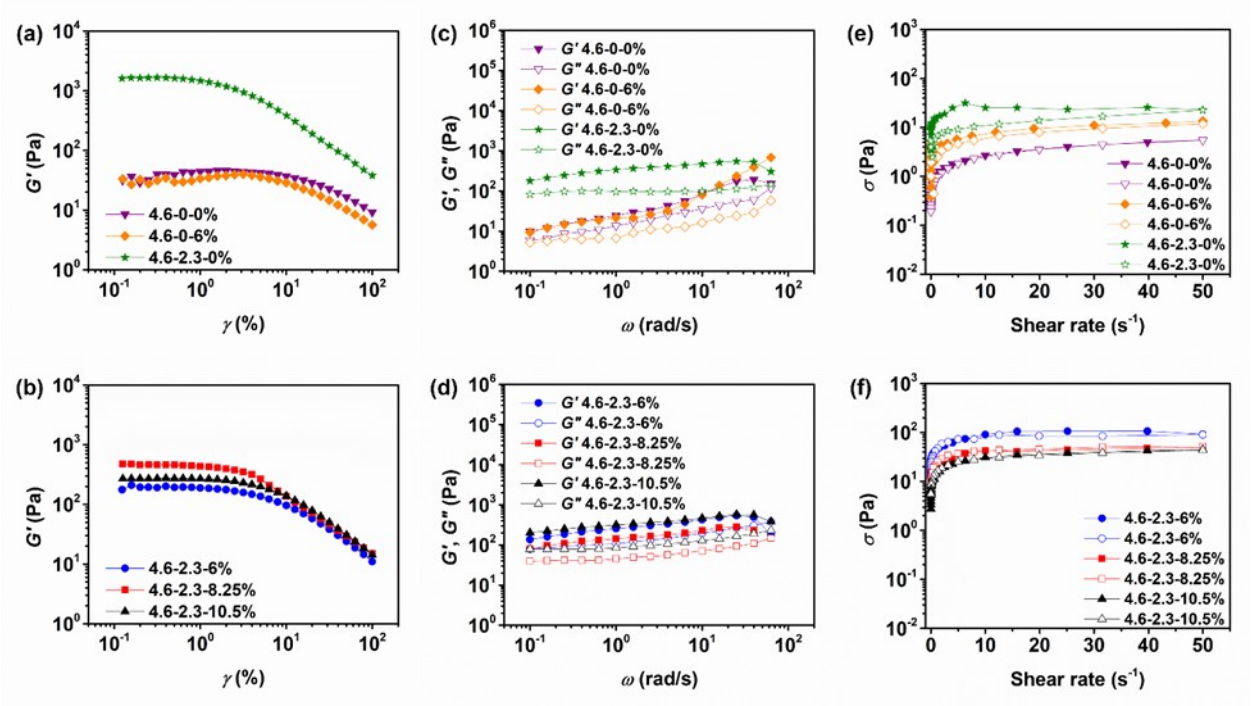


**Supplementary Figure A.1 Further rheological characterization of composite cdECM bioinks.**

(a,b) Oscillatory strain amplitude sweeps performed at 1 Hz (6.28 rad $s^{-1}$) angular frequency for (a) control and (b) printable formulations. Data between 0.01-0.1% strain has been omitted due to inconsistency and instrument sensitivity issues. All plots are the mean of three experiments. (c,d) Frequency amplitude sweeps from 0.1-100 rad $s^{-1}$ conducted at 1% strain for (c) control and (d) printable formulations. The final data point at 100 rad $s^{-1}$ has been omitted due to wall slippage effects. (e,f) Plots of stress vs. shear rate for (e) control and (f) printable formulations. Filled symbols indicate increasing shear rate, while open symbols indicate decreasing shear rate. The shape of the flow curves is characteristic of shear-thinning viscoelastic materials with a measurable yield stress. Herschel-Bulkley curve fitting (not shown) resulted in inconsistent and sometimes invalid estimates of yield stress.

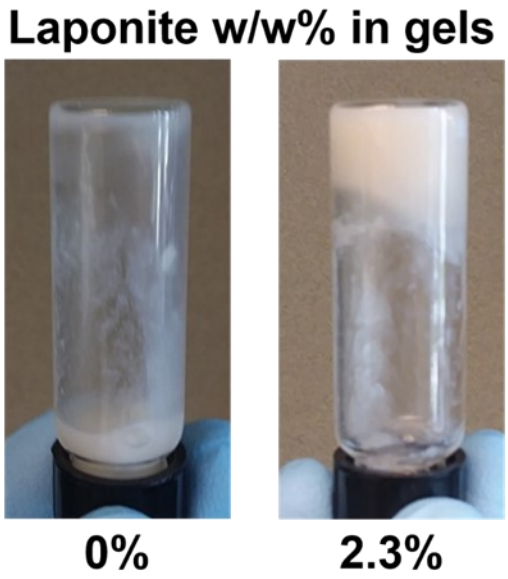


**Supplementary Figure A.2 Laponite increases viscosity and shear storage modulus of the cdECM bioinks.**

Composite cdECM gel formulations without (left) and with (right) Laponite-XLG, demonstrating difference in flow behavior when the vial is inverted. The addition of Laponite enhances the apparent viscosity of the gel.

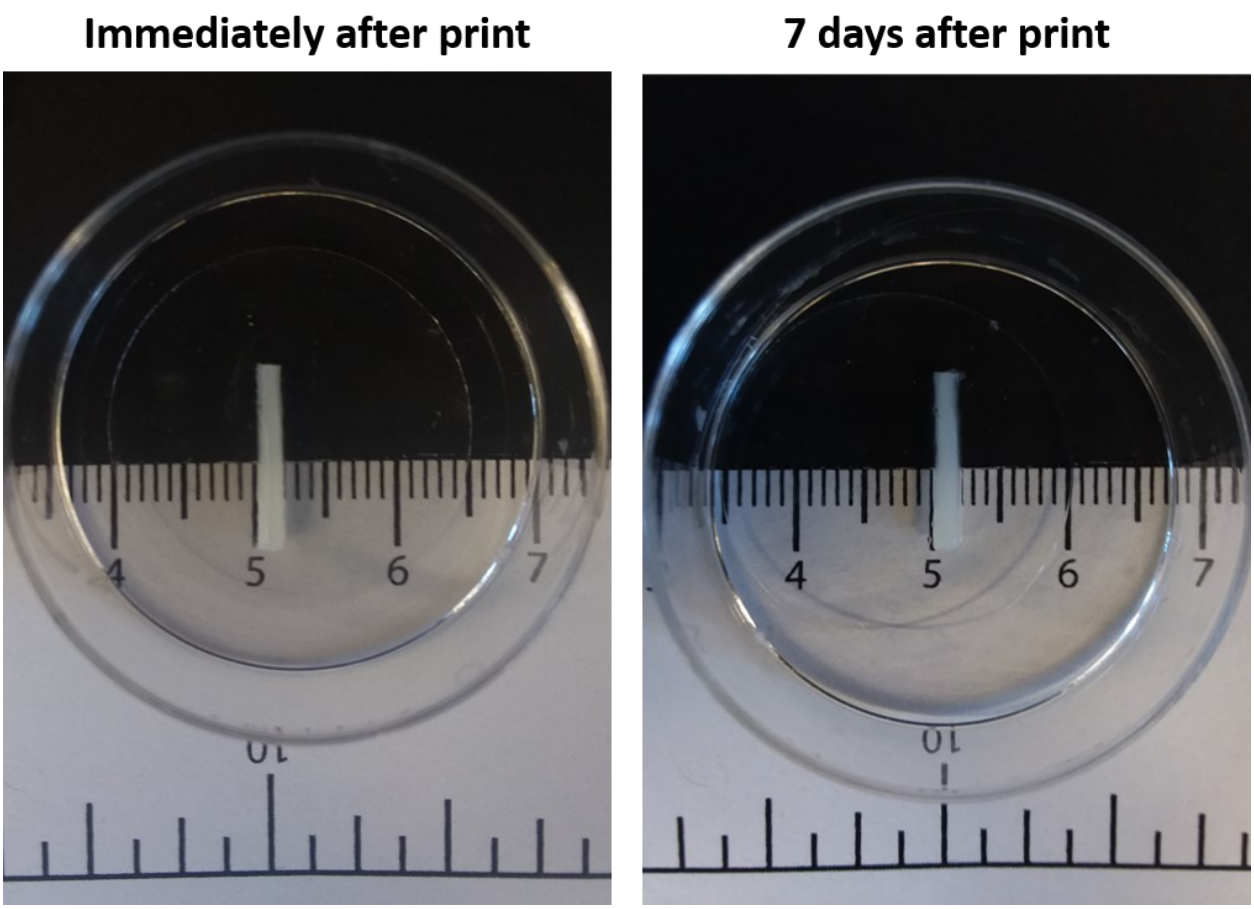


**Supplementary Figure A.3 Cross-linked, printed structures do not swell in aqueous media.**

Images of line prints immediately after (left) and 7 days after (right) incubation in PBS. The print was conducted using the low-modulus composite bioink (6.0% PEG-DA, 2.3% Laponite). The material did not undergo swelling over a one-week period and maintained its structural integrity.

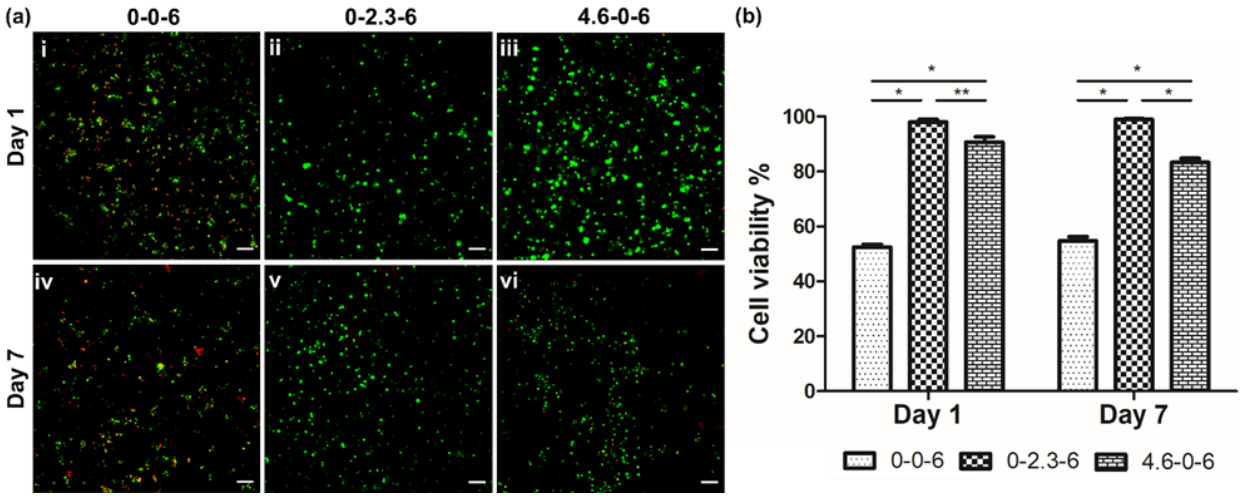


**Supplementary Figure A.4 Laponite and dECM support the viability of cardiac cells encapsulated within the bioink.**

(a) Images of live/dead staining of human cardiac fibroblasts in the (i,iv) PEG-DA (0-0-6%) gel, (ii,v) Laponite/PEG-DA (0-2.3-6%) gel, and (iii,vi) cdECM/PEG-DA (4.6-0-6%) gel. Scale bars: 100 µm. (b) Quantification of cell viability shows that Laponite/PEG-DA gels support > 95% cell survival, suggesting that Laponite significantly enhances the viability of encapsulated cells. Asterisks indicate significance levels: *$p < 0.001$; **$p < 0.01$.

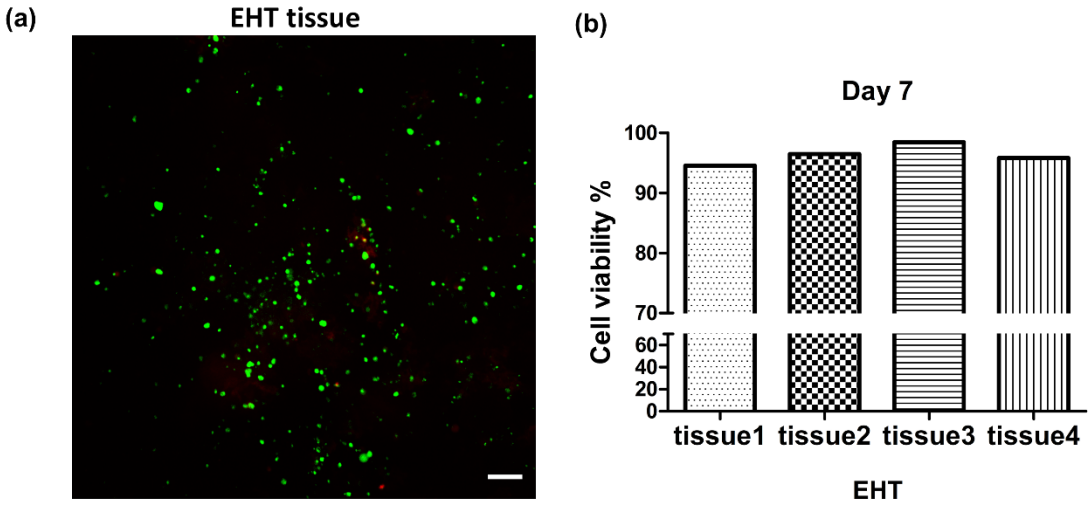


**Supplementary Figure A.5 Engineered heart tissue (EHT) fabricated from cdECM/Laponite/PEG-DA bioink supports the survival of human induced pluripotent stem cell derived cardiomyocytes (hiPSC-CMs).**

(a) Live/dead stained images of hiPSC-CMs within engineered heart tissue generated from cdECM composite bioinks. Scale bar: 100 μm. (b) Quantification of percent viability of cells after a 7-day culture shows > 94% of survival in all four tissues.

# References


1. Qiu, J. & Hirschi, K. K. Endothelial Cell Development and Its Application to Regenerative Medicine. *Circ. Res.* **125**, 489–501 (2019).

2. Carmeliet, P. *et al.* Abnormal blood vessel development and lethality in embryos lacking a single VEGF allele. *Nature* **380**, 435–439 (1996).

3. Miquerol, L., Langille, B. L. & Nagy, A. Embryonic development is disrupted by modest increases in vascular endothelial growth factor gene expression. *Development* **127**, 3941–3946 (2000).

4. Lee, S. *et al.* Autocrine VEGF Signaling Is Required for Vascular Homeostasis. *Cell* **130**, 691–703 (2007).

5. W., G. N. *et al.* Haploinsufficiency of delta-like 4 ligand results in embryonic lethality due to major defects in arterial and vascular development. *Proc. Natl. Acad. Sci.* **101**, 15949–15954 (2004).

6. Hellström, M. *et al.* Dll4 signalling through Notch1 regulates formation of tip cells during angiogenesis. *Nature* **445**, 776–780 (2007).

7. Gerhardt, H. *et al.* VEGF guides angiogenic sprouting utilizing endothelial tip cell filopodia . *J. Cell Biol.* **161**, 1163–1177 (2003).

8. Cao, Y. *et al.* PFKFB3-mediated endothelial glycolysis promotes pulmonary hypertension. *Proc. Natl. Acad. Sci.* **116**, 13394–13403 (2019).

9. De Bock, K. *et al.* Role of PFKFB3-Driven Glycolysis in Vessel Sprouting. *Cell* **154**, 651–663 (2013).

10. Stratman, A. N., Schwindt, A. E., Malotte, K. M. & Davis, G. E. Endothelial-derived PDGF-BB and HB-EGF coordinately regulate pericyte recruitment during vasculogenic tube assembly and stabilization. *Blood* **116**, 4720–4730 (2010).

11. Stenzel, D. *et al.* Peripheral mural cell recruitment requires cell-autonomous heparan sulfate. *Blood* **114**, 915–924 (2009).

12. Hellström, M. *et al.* Lack of Pericytes Leads to Endothelial Hyperplasia and Abnormal Vascular Morphogenesis. *J. Cell Biol.* **153**, 543–554 (2001).

13. Zhao-Jun, L. *et al.* Regulation of Notch1 and Dll4 by Vascular Endothelial Growth Factor in Arterial Endothelial Cells: Implications for Modulating Arteriogenesis and Angiogenesis. *Mol. Cell. Biol.* **23**, 14–25 (2003).

14. Quillien, A. *et al.* Distinct Notch signaling outputs pattern the developing arterial system. *Development* **141**, 1544–1552 (2014).

15. Coultas, L. *et al.* Hedgehog regulates distinct vascular patterning events through VEGF-dependent and -independent mechanisms. *Blood* **116**, 653–660 (2010).

16. Corada, M. *et al.* The Wnt/β-Catenin Pathway Modulates Vascular Remodeling and Specification by Upregulating Dll4/Notch Signaling. *Dev. Cell* **18**, 938–949 (2010).

17. Wythe, J. D. *et al.* ETS Factors Regulate Vegf-Dependent Arterial Specification. *Dev. Cell* **26**, 45–

58 (2013).

18. Stalmans, I. *et al.* Arteriolar and venular patterning in retinas of mice selectively expressing VEGF isoforms. *J. Clin. Invest.* **109**, 327–336 (2002).

19. Seo, S. & Kume, T. Forkhead transcription factors, Foxc1 and Foxc2, are required for the morphogenesis of the cardiac outflow tract. *Dev. Biol.* **296**, 421–436 (2006).

20. You, L.-R. *et al.* Suppression of Notch signalling by the COUP-TFII transcription factor regulates vein identity. *Nature* **435**, 98–104 (2005).

21. le Noble, F. *et al.* Control of arterial branching morphogenesis in embryogenesis: go with the flow. *Cardiovasc. Res.* **65**, 619–628 (2005).

22. PEIRCE, S. M. & SKALAK, T. C. Microvascular Remodeling: A Complex Continuum Spanning Angiogenesis to Arteriogenesis. *Microcirculation* **10**, 99–111 (2003).

23. Fang, J. S. *et al.* Shear-induced Notch-Cx37-p27 axis arrests endothelial cell cycle to enable arterial specification. *Nat. Commun.* **8**, 2149 (2017).

24. Noseda, M. *et al.* Notch Activation Induces Endothelial Cell Cycle Arrest and Participates in Contact Inhibition: Role of p21Cip1 Repression. *Mol. Cell. Biol.* **24**, 8813–8822 (2004).

25. Kao, C.-Y. *et al.* Elevated COUP-TFII expression in dopaminergic neurons accelerates the progression of Parkinson's disease through mitochondrial dysfunction. *PLOS Genet.* **16**, e1008868 (2020).

26. Xie, X., Tang, K., Yu, C.-T., Tsai, S. Y. & Tsai, M.-J. Regulatory potential of COUP-TFs in development: Stem/progenitor cells. *Semin. Cell Dev. Biol.* **24**, 687–693 (2013).

27. Chavkin, N. W. *et al.* Endothelial cell cycle state determines propensity for arterial-venous fate. *Nat. Commun.* **13**, 5891 (2022).

28. Kadry, H., Noorani, B. & Cucullo, L. A blood–brain barrier overview on structure, function, impairment, and biomarkers of integrity. *Fluids Barriers CNS* **17**, 69 (2020).

29. Lochhead, J. J., Yang, J., Ronaldson, P. T. & Davis, T. P. Structure, Function, and Regulation of the Blood-Brain Barrier Tight Junction in Central Nervous System Disorders. *Front. Physiol.* **11**, (2020).

30. Schupp, J. C. *et al.* Integrated Single-Cell Atlas of Endothelial Cells of the Human Lung. *Circulation* **144**, 286–302 (2021).

31. Schimmel, K., Ichimura, K., Reddy, S., Haddad, F. & Spiekerkoetter, E. Cardiac Fibrosis in the Pressure Overloaded Left and Right Ventricle as a Therapeutic Target. *Front. Cardiovasc. Med.* **9**, (2022).

32. Droste, P. *et al.* Semiautomated pipeline for quantitative analysis of heart histopathology. *J. Transl. Med.* **21**, 666 (2023).

33. Rodriguez, P. Q. *et al.* Inactivation of mediator complex protein 22 in podocytes results in intracellular vacuole formation, podocyte loss and premature death. *Sci. Rep.* **10**, 20037 (2020).

34. Kumaran, G. K. & Hanukoglu, I. Mapping the cytoskeletal architecture of renal tubules and surrounding peritubular capillaries in the kidney. *Cytoskeleton* **81**, 227–237 (2024).

35. Szafranska, K., Kruse, L. D., Holte, C. F., McCourt, P. & Zapotoczny, B. The wHole Story About

Fenestrations in LSEC. *Front. Physiol.* **12**, (2021).

36. Schaum, N. *et al.* Ageing hallmarks exhibit organ-specific temporal signatures. *Nature* **583**, 596–602 (2020).

37. Paik, D. T. *et al.* Single-Cell RNA Sequencing Unveils Unique Transcriptomic Signatures of Organ-Specific Endothelial Cells. *Circulation* **142**, 1848–1862 (2020).

38. Marcu, R. *et al.* Human Organ-Specific Endothelial Cell Heterogeneity. *iScience* **4**, 20–35 (2018).

39. Kalucka, J. *et al.* Single-Cell Transcriptome Atlas of Murine Endothelial Cells. *Cell* **180**, 764-779.e20 (2020).

40. Barry, D. M. *et al.* Molecular determinants of nephron vascular specialization in the kidney. *Nat. Commun.* **10**, 5705 (2019).

41. Yang, A. C. *et al.* A human brain vascular atlas reveals diverse mediators of Alzheimer's risk. *Nature* **603**, 885–892 (2022).

42. Vanlandewijck, M. *et al.* A molecular atlas of cell types and zonation in the brain vasculature. *Nature* **554**, 475–480 (2018).

43. Inverso, D. *et al.* A spatial vascular transcriptomic, proteomic, and phosphoproteomic atlas unveils an angiocrine Tie–Wnt signaling axis in the liver. *Dev. Cell* **56**, 1677-1693.e10 (2021).

44. Sabbagh, M. F. *et al.* Transcriptional and epigenomic landscapes of CNS and non-CNS vascular endothelial cells. *Elife* **7**, e36187 (2018).

45. Hunter, J. M. *et al.* Morphological and Pathological Evolution of the Brain Microcirculation in Aging and Alzheimer's Disease. *PLoS One* **7**, e36893 (2012).

46. Govindpani, K. *et al.* Vascular Dysfunction in Alzheimer's Disease: A Prelude to the Pathological Process or a Consequence of It? *J. Clin. Med.* **8**, (2019).

47. Moore, E. E. *et al.* Trauma-induced coagulopathy. *Nat. Rev. Dis. Prim.* **7**, 30 (2021).

48. Sloos, P. H. *et al.* Platelet dysfunction after trauma: From mechanisms to targeted treatment. *Transfusion* **62**, S281–S300 (2022).

49. Della-Morte, D., Pacifici, F. & Rundek, T. Genetic susceptibility to cerebrovascular disease. *Curr. Opin. Lipidol.* **27**, (2016).

50. Davis, G. E., Stratman, A. N., Sacharidou, A. & Koh, W. Chapter Three - Molecular Basis for Endothelial Lumen Formation and Tubulogenesis During Vasculogenesis and Angiogenic Sprouting. in (ed. Jeon, K. W. B. T.-I. R. of C. and M. B.) vol. 288 101–165 (Academic Press, 2011).

51. Davis, G. E. *et al.* Control of Vascular Tube Morphogenesis and Maturation in 3D Extracellular Matrices by Endothelial Cells and Pericytes BT - Cell-Cell Interactions: Methods and Protocols. in (ed. Baudino, T. A.) 17–28 (Humana Press, 2013). doi:10.1007/978-1-62703-604-7_2.

52. Kamei, M. *et al.* Endothelial tubes assemble from intracellular vacuoles in vivo. *Nature* **442**, 453–456 (2006).

53. Xu, K. & Cleaver, O. Tubulogenesis during blood vessel formation. *Semin. Cell Dev. Biol.* **22**, 993–1004 (2011).

54. Sacharidou, A. *et al.* Endothelial lumen signaling complexes control 3D matrix–specific

tubulogenesis through interdependent Cdc42- and MT1-MMP–mediated events. *Blood* **115**, 5259–5269 (2010).

55. Stratman, A. N., Davis, M. J. & Davis, G. E. VEGF and FGF prime vascular tube morphogenesis and sprouting directed by hematopoietic stem cell cytokines. *Blood* **117**, 3709–3719 (2011).

56. Stratman, A. N., Malotte, K. M., Mahan, R. D., Davis, M. J. & Davis, G. E. Pericyte recruitment during vasculogenic tube assembly stimulates endothelial basement membrane matrix formation. *Blood* **114**, 5091–5101 (2009).

57. Whisler, J. A., Chen, M. B. & Kamm, R. D. Control of Perfusable Microvascular Network Morphology Using a Multiculture Microfluidic System. *Tissue Eng. Part C Methods* **20**, 543–552 (2012).

58. Hsu, Y.-H. *et al.* Full range physiological mass transport control in 3D tissue cultures. *Lab Chip* **13**, 81–89 (2013).

59. Phan, D. T. T. *et al.* A vascularized and perfused organ-on-a-chip platform for large-scale drug screening applications. *Lab Chip* **17**, 511–520 (2017).

60. Phan, D. T. T. *et al.* Blood–brain barrier-on-a-chip: Microphysiological systems that capture the complexity of the blood–central nervous system interface. *Exp. Biol. Med.* **242**, 1669–1678 (2017).

61. Hachey, S. J. *et al.* An in vitro vascularized micro-tumor model of human colorectal cancer recapitulates in vivo responses to standard-of-care therapy. *Lab Chip* **21**, 1333–1351 (2021).

62. Liu, Y. *et al.* Human in vitro vascularized micro-organ and micro-tumor models are reproducible organ-on-a-chip platforms for studies of anticancer drugs. *Toxicology* **445**, 152601 (2020).

63. Palikuqi, B. *et al.* Adaptable haemodynamic endothelial cells for organogenesis and tumorigenesis. *Nature* **585**, 426–432 (2020).

64. Jeon, J. S. *et al.* Human 3D vascularized organotypic microfluidic assays to study breast cancer cell extravasation. *Proc. Natl. Acad. Sci.* **112**, 214–219 (2015).

65. Campisi, M. *et al.* 3D self-organized microvascular model of the human blood-brain barrier with endothelial cells, pericytes and astrocytes. *Biomaterials* **180**, 117–129 (2018).

66. Hofer, M. & Lutolf, M. P. Engineering organoids. *Nat. Rev. Mater.* **6**, 402–420 (2021).

67. Kim, J., Koo, B.-K. & Knoblich, J. A. Human organoids: model systems for human biology and medicine. *Nat. Rev. Mol. Cell Biol.* **21**, 571–584 (2020).

68. Sheridan, M. A. *et al.* Establishment and differentiation of long-term trophoblast organoid cultures from the human placenta. *Nat. Protoc.* **15**, 3441–3463 (2020).

69. Unbekandt, M. & Davies, J. A. Dissociation of embryonic kidneys followed by reaggregation allows the formation of renal tissues. *Kidney Int.* **77**, 407–416 (2010).

70. Takasato, M. *et al.* Directing human embryonic stem cell differentiation towards a renal lineage generates a self-organizing kidney. *Nat. Cell Biol.* **16**, 118–126 (2014).

71. Puschhof, J. *et al.* Intestinal organoid cocultures with microbes. *Nat. Protoc.* **16**, 4633–4649 (2021).

72. Giandomenico, S. L., Sutcliffe, M. & Lancaster, M. A. Generation and long-term culture of

advanced cerebral organoids for studying later stages of neural development. *Nat. Protoc.* **16**, 579–602 (2021).

73. Broutier, L. *et al.* Culture and establishment of self-renewing human and mouse adult liver and pancreas 3D organoids and their genetic manipulation. *Nat. Protoc.* **11**, 1724–1743 (2016).

74. Koike, H. *et al.* Engineering human hepato-biliary-pancreatic organoids from pluripotent stem cells. *Nat. Protoc.* **16**, 919–936 (2021).

75. Miller, A. J. *et al.* Generation of lung organoids from human pluripotent stem cells in vitro. *Nat. Protoc.* **14**, 518–540 (2019).

76. Drakhlis, L., Devadas, S. B. & Zweigerdt, R. Generation of heart-forming organoids from human pluripotent stem cells. *Nat. Protoc.* **16**, 5652–5672 (2021).

77. Low, J. H. *et al.* Generation of Human PSC-Derived Kidney Organoids with Patterned Nephron Segments and a De Novo Vascular Network. *Cell Stem Cell* **25**, 373-387.e9 (2019).

78. Homan, K. A. *et al.* Flow-enhanced vascularization and maturation of kidney organoids in vitro. *Nat. Methods* **16**, 255–262 (2019).

79. Ham, O., Jin, Y. B., Kim, J. & Lee, M.-O. Blood vessel formation in cerebral organoids formed from human embryonic stem cells. *Biochem. Biophys. Res. Commun.* **521**, 84–90 (2020).

80. Wimmer, R. A., Leopoldi, A., Aichinger, M., Kerjaschki, D. & Penninger, J. M. Generation of blood vessel organoids from human pluripotent stem cells. *Nat. Protoc.* **14**, 3082–3100 (2019).

81. Monteil, V. *et al.* Inhibition of SARS-CoV-2 Infections in Engineered Human Tissues Using Clinical-Grade Soluble Human ACE2. *Cell* **181**, 905-913.e7 (2020).

82. Holloway, E. M. *et al.* Differentiation of Human Intestinal Organoids with Endogenous Vascular Endothelial Cells. *Dev. Cell* **54**, 516-528.e7 (2020).

83. Cakir, B. *et al.* Engineering of human brain organoids with a functional vascular-like system. *Nat. Methods* **16**, 1169–1175 (2019).

84. Jeon, J. S. *et al.* Generation of 3D functional microvascular networks with human mesenchymal stem cells in microfluidic systems. *Integr. Biol.* **6**, 555–563 (2014).

85. Sun, X.-Y. *et al.* Generation of vascularized brain organoids to study neurovascular interactions. *Elife* **11**, e76707 (2022).

86. Rayner, S. G. & Zheng, Y. Engineered Microvessels for the Study of Human Disease. *J. Biomech. Eng.* **138**, (2016).

87. Griffith, L. G. & Naughton, G. Tissue Engineering--Current Challenges and Expanding Opportunities. *Science (80-. ).* **295**, 1009–1014 (2002).

88. Pober, J. S. & Sessa, W. C. Evolving functions of endothelial cells in inflammation. *Nat. Rev. Immunol.* **7**, 803–815 (2007).

89. Yau, J. W., Teoh, H. & Verma, S. Endothelial cell control of thrombosis. *BMC Cardiovasc. Disord.* **15**, 130 (2015).

90. Rodrigues, M., Kosaric, N., Bonham, C. A. & Gurtner, G. C. Wound Healing: A Cellular Perspective. *Physiol. Rev.* **99**, 665–706 (2018).

91. Song, H.-H. G., Rumma, R. T., Ozaki, C. K., Edelman, E. R. & Chen, C. S. Vascular Tissue

Engineering: Progress, Challenges, and Clinical Promise. *Cell Stem Cell* **22**, 340–354 (2018).

92. Fleischer, S., Tavakol, D. N. & Vunjak-Novakovic, G. From Arteries to Capillaries: Approaches to Engineering Human Vasculature. *Adv. Funct. Mater.* **30**, 1910811 (2020).

93. Mandrycky, C., Hadland, B. & Zheng, Y. 3D curvature-instructed endothelial flow response and tissue vascularization. *Sci. Adv.* **6**, eabb3629 (2024).

94. Schot, M. *et al.* Photoannealing of Microtissues Creates High-Density Capillary Network Containing Living Matter in a Volumetric-Independent Manner. *Adv. Mater.* **36**, 2308949 (2024).

95. Zheng, Y. *et al.* In vitro microvessels for the study of angiogenesis and thrombosis. *Proc. Natl. Acad. Sci.* **109**, 9342–9347 (2012).

96. Kotha, S. *et al.* Microvasculature-directed thrombopoiesis in a 3D in vitro marrow microenvironment. *PLoS One* **13**, e0195082 (2018).

97. Redd, M. A. *et al.* Patterned human microvascular grafts enable rapid vascularization and increase perfusion in infarcted rat hearts. *Nat. Commun.* **10**, 584 (2019).

98. Roberts, M. A. *et al.* Stromal Cells in Dense Collagen Promote Cardiomyocyte and Microvascular Patterning in Engineered Human Heart Tissue. *Tissue Eng. Part A* **22**, 633–644 (2016).

99. Shin, Y. J. *et al.* Amyloid beta peptides (Aβ) from Alzheimer's disease neuronal secretome induce endothelial activation in a human cerebral microvessel model. *Neurobiol. Dis.* **181**, 106125 (2023).

100. Maria, B. *et al.* Binding Heterogeneity of Plasmodium falciparum to Engineered 3D Brain Microvessels Is Mediated by EPCR and ICAM-1. *MBio* **10**, 10.1128/mbio.00420-19 (2019).

101. Rayner, S. G. *et al.* Reconstructing the Human Renal Vascular–Tubular Unit In Vitro. *Adv. Healthc. Mater.* **7**, 1801120 (2018).

102. Zeinstra, N. *et al.* Stacking thick perfusable human microvascular grafts enables dense vascularity and rapid integration into infarcted rat hearts. *Biomaterials* **301**, 122250 (2023).

103. Zhang, B. *et al.* Biodegradable scaffold with built-in vasculature for organ-on-a-chip engineering and direct surgical anastomosis. *Nat. Mater.* **15**, 669–678 (2016).

104. Nguyen, D.-H. T. *et al.* Biomimetic model to reconstitute angiogenic sprouting morphogenesis in vitro. *Proc. Natl. Acad. Sci.* **110**, 6712–6717 (2013).

105. Howard, C., Joof, F., Hu, R., Smith, J. D. & Zheng, Y. Probing cerebral malaria inflammation in 3D human brain microvessels. *Cell Rep.* **42**, 113253 (2023).

106. Rizzo, R. *et al.* Multiscale Hybrid Fabrication: Volumetric Printing Meets Two-Photon Ablation. *Adv. Mater. Technol.* **8**, 2201871 (2023).

107. Rayner, S. G. *et al.* Multiphoton-Guided Creation of Complex Organ-Specific Microvasculature. *Adv. Healthc. Mater.* **10**, 2100031 (2021).

108. Song, H.-H. G. *et al.* Transient Support from Fibroblasts is Sufficient to Drive Functional Vascularization in Engineered Tissues. *Adv. Funct. Mater.* **30**, 2003777 (2020).

109. Szklanny, A. A. *et al.* 3D Bioprinting of Engineered Tissue Flaps with Hierarchical Vessel Networks (VesselNet) for Direct Host-To-Implant Perfusion. *Adv. Mater.* **33**, 2102661 (2021).

110. Quintard, C. *et al.* A microfluidic platform integrating functional vascularized organoids-on-chip.

*Nat. Commun.* **15**, 1452 (2024).

111. Debbi, L. *et al.* Integrating engineered macro vessels with self-assembled capillaries in 3D implantable tissue for promoting vascular integration in-vivo. *Biomaterials* **280**, 121286 (2022).

112. Margolis, E. A., Choi, L. S., Friend, N. E. & Putnam, A. J. Engineering primitive multiscale chimeric vasculature by combining human microvessels with explanted murine vessels. *Sci. Rep.* **14**, 4036 (2024).

113. Orellano, I. *et al.* Engineering Vascular Self-Assembly by Controlled 3D-Printed Cell Placement. *Adv. Funct. Mater.* **32**, 2208325 (2022).

114. Duong, V. T. & Lin, C.-C. Digital Light Processing 3D Bioprinting of Gelatin-Norbornene Hydrogel for Enhanced Vascularization. *Macromol. Biosci.* **23**, 2300213 (2023).

115. Mazari-Arrighi, E. *et al.* Self-Organization of Long-Lasting Human Endothelial Capillary-Like Networks Guided by DLP Bioprinting. *Adv. Healthc. Mater.* **13**, 2302830 (2024).

116. Zohar, B. *et al.* A micro-channel array in a tissue engineered vessel graft guides vascular morphogenesis for anastomosis with self-assembled vascular networks. *Acta Biomater.* **163**, 182–193 (2023).

117. Strobel, H. A., Moss, S. M. & Hoying, J. B. Methods for vascularization and perfusion of tissue organoids. *Mamm. Genome* **33**, 437–450 (2022).

118. Grebenyuk, S. *et al.* Large-scale perfused tissues via synthetic 3D soft microfluidics. *Nat. Commun.* **14**, 193 (2023).

119. Cochrane, A. *et al.* Advanced in vitro models of vascular biology: Human induced pluripotent stem cells and organ-on-chip technology. *Adv. Drug Deliv. Rev.* **140**, 68–77 (2019).

120. Wimmer, R. A. *et al.* Human blood vessel organoids as a model of diabetic vasculopathy. *Nature* **565**, 505–510 (2019).

121. 2021 Alzheimer's disease facts and figures. *Alzheimers. Dement.* **17**, 327–406 (2021).

122. Brookmeyer, R., Johnson, E., Ziegler-Graham, K. & Arrighi, H. M. Forecasting the global burden of Alzheimer's disease. *Alzheimer's Dement.* **3**, 186–191 (2007).

123. Behl, T. *et al.* The road to precision medicine: Eliminating the "One Size Fits All" approach in Alzheimer's disease. *Biomed. Pharmacother.* **153**, 113337 (2022).

124. Guerreiro, R. & Bras, J. The age factor in Alzheimer's disease. *Genome Med.* **7**, 106 (2015).

125. DeTure, M. A. & Dickson, D. W. The neuropathological diagnosis of Alzheimer's disease. *Mol. Neurodegener.* **14**, 32 (2019).

126. Kuchibhotla, K. V *et al.* Neurofibrillary tangle-bearing neurons are functionally integrated in cortical circuits in vivo. *Proc. Natl. Acad. Sci.* **111**, 510–514 (2014).

127. Spires-Jones, T. L. & Hyman, B. T. The Intersection of Amyloid Beta and Tau at Synapses in Alzheimer's Disease. *Neuron* **82**, 756–771 (2014).

128. Grammas, P. Neurovascular dysfunction, inflammation and endothelial activation: Implications for the pathogenesis of Alzheimer's disease. *J. Neuroinflammation* **8**, 26 (2011).

129. Blanchard, J. W. *et al.* Reconstruction of the human blood–brain barrier in vitro reveals a pathogenic mechanism of APOE4 in pericytes. *Nat. Med.* **26**, 952–963 (2020).

130. Ringman, J. M. *et al.* Clinical Predictors of Severe Cerebral Amyloid Angiopathy and Influence of APOE Genotype in Persons With Pathologically Verified Alzheimer Disease. *JAMA Neurol.* **71**, 878–883 (2014).

131. Vidoni, E. D. *et al.* Cerebral β-Amyloid Angiopathy Is Associated with Earlier Dementia Onset in Alzheimer's Disease. *Neurodegener. Dis.* **16**, 218–224 (2016).

132. Weller, R. O., Preston, S. D., Subash, M. & Carare, R. O. Cerebral amyloid angiopathy in the aetiology and immunotherapy of Alzheimer disease. *Alzheimers. Res. Ther.* **1**, 6 (2009).

133. Behl, T., Kaur, I., Fratila, O., Brata, R. & Bungau, S. Exploring the Potential of Therapeutic Agents Targeted towards Mitigating the Events Associated with Amyloid-β Cascade in Alzheimer's Disease. *Int. J. Mol. Sci.* **21**, (2020).

134. Tietz, S. & Engelhardt, B. Brain barriers: Crosstalk between complex tight junctions and adherens junctions. *J. Cell Biol.* **209**, 493–506 (2015).

135. Gupta, A. *et al.* Coagulation and inflammatory markers in Alzheimer's and vascular dementia. *Int. J. Clin. Pract.* **59**, 52–57 (2005).

136. Lip, G. Y. H. & Blann, A. von Willebrand factor: a marker of endothelial dysfunction in vascular disorders? *Cardiovasc. Res.* **34**, 255–265 (1997).

137. Peng, Z., Shu, B., Zhang, Y. & Wang, M. Endothelial Response to Pathophysiological Stress. *Arterioscler. Thromb. Vasc. Biol.* **39**, e233–e243 (2019).

138. Borroni, B. *et al.* Peripheral Blood Abnormalities in Alzheimer Disease: Evidence for Early Endothelial Dysfunction. *Alzheimer Dis. Assoc. Disord.* **16**, (2002).

139. Järemo, P., Milovanovic, M., Buller, C., Nilsson, S. & Winblad, B. P-selectin paradox and dementia of the Alzheimer type: Circulating P-selectin is increased but platelet-bound P-selectin after agonist provocation is compromised. *Scand. J. Clin. Lab. Invest.* **73**, 170–174 (2013).

140. Kelleher, R. J. & Soiza, R. L. Evidence of endothelial dysfunction in the development of Alzheimer's disease: Is Alzheimer's a vascular disorder? *Am. J. Cardiovasc. Dis.* **3**, 197–226 (2013).

141. Wolters, F. *et al.* Von Willebrand Factor and the Risk of Dementia: A Population-Based Study (P1.092). *Neurology* **86**, (2016).

142. Zuliani, G. *et al.* Markers of endothelial dysfunction in older subjects with late onset Alzheimer's disease or vascular dementia. *J. Neurol. Sci.* **272**, 164–170 (2008).

143. Cook-Mills, J. M., Marchese, M. E. & Abdala-Valencia, H. Vascular Cell Adhesion Molecule-1 Expression and Signaling During Disease: Regulation by Reactive Oxygen Species and Antioxidants. *Antioxid. Redox Signal.* **15**, 1607–1638 (2010).

144. Zenaro, E., Piacentino, G. & Constantin, G. The blood-brain barrier in Alzheimer's disease. *Neurobiol. Dis.* **107**, 41–56 (2017).

145. Zenaro, E. *et al.* Neutrophils promote Alzheimer's disease–like pathology and cognitive decline via LFA-1 integrin. *Nat. Med.* **21**, 880–886 (2015).

146. Suhara, T. *et al.* Aβ42 generation is toxic to endothelial cells and inhibits eNOS function through an Akt/GSK-3β signaling-dependent mechanism. *Neurobiol. Aging* **24**, 437–451 (2003).

147. Xu, J. *et al.* Amyloid β Peptide–Induced Cerebral Endothelial Cell Death Involves Mitochondrial

Dysfunction and Caspase Activation. *J. Cereb. Blood Flow Metab.* **21**, 702–710 (2001).

148. Bhatia, R., Lin, H. & Lal, R. Fresh and globular amyloid β protein (1–42) induces rapid cellular degeneration: evidence for AβP channel-mediated cellular toxicity. *FASEB J.* **14**, 1233–1243 (2000).

149. Kass, B. *et al.* Aβ oligomer concentration in mouse and human brain and its drug-induced reduction ex vivo. *Cell Reports Med.* **3**, 100630 (2022).

150. Szu, J. I. & Obenaus, A. Cerebrovascular phenotypes in mouse models of Alzheimer's disease. *J. Cereb. blood flow Metab. Off. J. Int. Soc. Cereb. Blood Flow Metab.* **41**, 1821–1841 (2021).

151. Shin, Y. *et al.* Blood–Brain Barrier Dysfunction in a 3D In Vitro Model of Alzheimer's Disease. *Adv. Sci.* **6**, 1900962 (2019).

152. Zheng, Y., Chen, J. & López, J. A. Flow-driven assembly of VWF fibres and webs in in vitro microvessels. *Nat. Commun.* **6**, 7858 (2015).

153. Choublier, N. *et al.* Exposure of human cerebral microvascular endothelial cells hCMEC/D3 to laminar shear stress induces vascular protective responses. *Fluids Barriers CNS* **19**, 41 (2022).

154. Helle, E., Ampuja, M., Antola, L. & Kivelä, R. Flow-Induced Transcriptomic Remodeling of Endothelial Cells Derived From Human Induced Pluripotent Stem Cells . *Frontiers in Physiology* vol. 11 (2020).

155. Cucullo, L. *et al.* Immortalized Human Brain Endothelial Cells and Flow-Based Vascular Modeling: A Marriage of Convenience for Rational Neurovascular Studies. *J. Cereb. Blood Flow Metab.* **28**, 312–328 (2007).

156. Haass, C. *et al.* The Swedish mutation causes early-onset Alzheimer's disease by β-secretase cleavage within the secretory pathway. *Nat. Med.* **1**, 1291–1296 (1995).

157. Young, J. E. *et al.* Stabilizing the Retromer Complex in a Human Stem Cell Model of Alzheimer's Disease Reduces TAU Phosphorylation Independently of Amyloid Precursor Protein. *Stem cell reports* **10**, 1046–1058 (2018).

158. Park, J. *et al.* A 3D human triculture system modeling neurodegeneration and neuroinflammation in Alzheimer's disease. *Nat. Neurosci.* **21**, 941–951 (2018).

159. Penney, J., Ralvenius, W. T. & Tsai, L.-H. Modeling Alzheimer's disease with iPSC-derived brain cells. *Mol. Psychiatry* **25**, 148–167 (2020).

160. Williams, L. M. *et al.* Prolonged culturing of iPSC-derived brain endothelial-like cells is associated with quiescence, downregulation of glycolysis, and resistance to disruption by an Alzheimer's brain milieu. *Fluids Barriers CNS* **19**, 10 (2022).

161. Knupp, A. *et al.* Depletion of the AD Risk Gene SORL1 Selectively Impairs Neuronal Endosomal Traffic Independent of Amyloidogenic APP Processing. *Cell Rep.* **31**, 107719 (2020).

162. Levy, S. *et al.* The Diploid Genome Sequence of an Individual Human. *PLOS Biol.* **5**, e254 (2007).

163. Rose, S. E. *et al.* Leptomeninges-Derived Induced Pluripotent Stem Cells and Directly Converted Neurons From Autopsy Cases With Varying Neuropathologic Backgrounds. *J. Neuropathol. Exp. Neurol.* **77**, 353–360 (2018).

164. Dewji, N. N., Mukhopadhyay, D. & Singer, S. J. An early specific cell-cell interaction occurs in

the production of β-amyloid in cell cultures. *Proc. Natl. Acad. Sci.* **103**, 1540–1545 (2006).

165. Oberstein, T. J. *et al.* The Role of Cathepsin B in the Degradation of Aβ and in the Production of Aβ Peptides Starting With Ala2 in Cultured Astrocytes. *Front. Mol. Neurosci.* **13**, (2021).

166. Welzel, A. T. *et al.* Secreted Amyloid β-Proteins in a Cell Culture Model Include N-Terminally Extended Peptides That Impair Synaptic Plasticity. *Biochemistry* **53**, 3908–3921 (2014).

167. Young, J. E. *et al.* Elucidating molecular phenotypes caused by the SORL1 Alzheimer's disease genetic risk factor using human induced pluripotent stem cells. *Cell Stem Cell* **16**, 373–385 (2015).

168. Na, H.-J. *et al.* TSPYL5-mediated inhibition of p53 promotes human endothelial cell function. *Angiogenesis* **22**, 281–293 (2019).

169. Drakeford, C. & O'Donnell, J. S. Targeting von Willebrand Factor–Mediated Inflammation. *Arterioscler. Thromb. Vasc. Biol.* **37**, 1590–1591 (2017).

170. Chow, V. W., Mattson, M. P., Wong, P. C. & Gleichmann, M. An Overview of APP Processing Enzymes and Products. *NeuroMolecular Med.* **12**, 1–12 (2010).

171. Satir, T. M. *et al.* Partial reduction of amyloid β production by β-secretase inhibitors does not decrease synaptic transmission. *Alzheimers. Res. Ther.* **12**, 63 (2020).

172. Janelidze, S. *et al.* Plasma β-amyloid in Alzheimer's disease and vascular disease. *Sci. Rep.* **6**, 26801 (2016).

173. Lim, Y. Y. *et al.* Plasma Amyloid-β Biomarker Associated with Cognitive Decline in Preclinical Alzheimer's Disease. *J. Alzheimer's Dis.* **77**, 1057–1065 (2020).

174. Nakamura, A. *et al.* High performance plasma amyloid-β biomarkers for Alzheimer's disease. *Nature* **554**, 249–254 (2018).

175. Rissman, R. A., Trojanowski, J. Q., Shaw, L. M. & Aisen, P. S. Longitudinal plasma amyloid beta as a biomarker of Alzheimer's disease. *J. Neural Transm.* **119**, 843–850 (2012).

176. Hansson, O., Lehmann, S., Otto, M., Zetterberg, H. & Lewczuk, P. Advantages and disadvantages of the use of the CSF Amyloid β (Aβ) 42/40 ratio in the diagnosis of Alzheimer's Disease. *Alzheimers. Res. Ther.* **11**, 34 (2019).

177. Mehta, P. D. *et al.* Plasma and Cerebrospinal Fluid Levels of Amyloid β Proteins 1-40 and 1-42 in Alzheimer Disease. *Arch. Neurol.* **57**, 100–105 (2000).

178. Chen, M. B. *et al.* Brain Endothelial Cells Are Exquisite Sensors of Age-Related Circulatory Cues. *Cell Rep.* **30**, 4418-4432.e4 (2020).

179. Propson, N. E., Roy, E. R., Litvinchuk, A., Köhl, J. & Zheng, H. Endothelial C3a receptor mediates vascular inflammation and blood-brain barrier permeability during aging. *J. Clin. Invest.* **131**, (2021).

180. Yousef, H. *et al.* Aged blood impairs hippocampal neural precursor activity and activates microglia via brain endothelial cell VCAM1. *Nat. Med.* **25**, 988–1000 (2019).

181. Gate, D. *et al.* Clonally expanded CD8 T cells patrol the cerebrospinal fluid in Alzheimer's disease. *Nature* **577**, 399–404 (2020).

182. Lee, W.-J. *et al.* Plasma MCP-1 and Cognitive Decline in Patients with Alzheimer's Disease and Mild Cognitive Impairment: A Two-year Follow-up Study. *Sci. Rep.* **8**, 1280 (2018).

183. Chui, R. & Dorovini-Zis, K. Regulation of CCL2 and CCL3 expression in human brain endothelial cells by cytokines and lipopolysaccharide. *J. Neuroinflammation* **7**, 1 (2010).

184. Michaux, G. & Cutler, D. F. How to roll an endothelial cigar: the biogenesis of Weibel-Palade bodies. *Traffic* **5**, 69–78 (2004).

185. Fu, H. *et al.* Flow-induced elongation of von Willebrand factor precedes tension-dependent activation. *Nat. Commun.* **8**, 324 (2017).

186. Fonseca, A. C. R. G. *et al.* Amyloid-beta disrupts calcium and redox homeostasis in brain endothelial cells. *Mol. Neurobiol.* **51**, 610–622 (2015).

187. Kook, S.-Y. *et al.* Aβ<sub>1–42</sub>-RAGE Interaction Disrupts Tight Junctions of the Blood–Brain Barrier Via Ca<sup>2+</sup>-Calcineurin Signaling. *J. Neurosci.* **32**, 8845 LP – 8854 (2012).

188. Parodi-Rullán, R., Sone, J. Y. & Fossati, S. Endothelial Mitochondrial Dysfunction in Cerebral Amyloid Angiopathy and Alzheimer's Disease. *J. Alzheimers. Dis.* **72**, 1019–1039 (2019).

189. Cleator, J. H., Zhu, W. Q., Vaughan, D. E. & Hamm, H. E. Differential regulation of endothelial exocytosis of P-selectin and von Willebrand factor by protease-activated receptors and cAMP. *Blood* **107**, 2736–2744 (2006).

190. Mietkowska, M., Schuberth, C., Wedlich-Söldner, R. & Gerke, V. Actin dynamics during Ca(2+)-dependent exocytosis of endothelial Weibel-Palade bodies. *Biochim. Biophys. acta. Mol. cell Res.* **1866**, 1218–1229 (2019).

191. Chen, S.-C. *et al.* Cross-linking of P-selectin glycoprotein ligand-1 induces death of activated T cells. *Blood* **104**, 3233–3242 (2004).

192. Petri, B. *et al.* von Willebrand factor promotes leukocyte extravasation. *Blood* **116**, 4712–4719 (2010).

193. Deane, R., Bell, R. D., Sagare, A. & Zlokovic, B. V. Clearance of amyloid-beta peptide across the blood-brain barrier: implication for therapies in Alzheimer's disease. *CNS Neurol. Disord. Drug Targets* **8**, 16–30 (2009).

194. Zlokovic, B. V, Deane, R., Sagare, A. P., Bell, R. D. & Winkler, E. A. Low-density lipoprotein receptor-related protein-1: a serial clearance homeostatic mechanism controlling Alzheimer's amyloid β-peptide elimination from the brain. *J. Neurochem.* **115**, 1077–1089 (2010).

195. Hartz, A. M. S. *et al.* Amyloid-β contributes to blood-brain barrier leakage in transgenic human amyloid precursor protein mice and in humans with cerebral amyloid angiopathy. *Stroke* **43**, 514–523 (2012).

196. d'Uscio, L. V, He, T. & Katusic, Z. S. Expression and Processing of Amyloid Precursor Protein in Vascular Endothelium. *Physiology (Bethesda).* **32**, 20–32 (2017).

197. Ristori, E., Donnini, S. & Ziche, M. New Insights Into Blood-Brain Barrier Maintenance: The Homeostatic Role of β-Amyloid Precursor Protein in Cerebral Vasculature. *Front. Physiol.* **11**, 1056 (2020).

198. Dankwa, S. *et al.* Exploiting polypharmacology to dissect host kinases and kinase inhibitors that modulate endothelial barrier integrity. *Cell Chem. Biol.* **28**, 1679-1692.e4 (2021).

199. Anastassiadis, T., Deacon, S. W., Devarajan, K., Ma, H. & Peterson, J. R. Comprehensive assay of kinase catalytic activity reveals features of kinase inhibitor selectivity. *Nat. Biotechnol.* **29**, 1039–

1045 (2011).

200. Dong, X. *et al.* Anticoagulation targeting membrane-bound anionic phospholipids improves outcomes of traumatic brain injury in mice. *Blood* **138**, 2714–2726 (2021).

201. Brown, L. S. *et al.* Pericytes and Neurovascular Function in the Healthy and Diseased Brain. *Front. Cell. Neurosci.* **13**, (2019).

202. Mizee, M. R. *et al.* Retinoic Acid Induces Blood–Brain Barrier Development. *J. Neurosci.* **33**, 1660 LP – 1671 (2013).

203. Yuan, F. *et al.* Efficient generation of region-specific forebrain neurons from human pluripotent stem cells under highly defined condition. *Sci. Rep.* **5**, 18550 (2015).

204. Paredes, I., Himmels, P. & Ruiz de Almodóvar, C. Neurovascular Communication during CNS Development. *Dev. Cell* **45**, 10–32 (2018).

205. Guérit, S. *et al.* Astrocyte-derived Wnt growth factors are required for endothelial blood-brain barrier maintenance. *Prog. Neurobiol.* **199**, 101937 (2021).

206. Deanfield, J. E., Halcox, J. P. & Rabelink, T. J. Endothelial Function and Dysfunction. *Circulation* **115**, 1285–1295 (2007).

207. Risau, W. Mechanisms of angiogenesis. *Nature* **386**, 671–674 (1997).

208. Yamashita, J. *et al.* Flk1-positive cells derived from embryonic stem cells serve as vascular progenitors. *Nature* **408**, 92–96 (2000).

209. Patsch, C. *et al.* Generation of vascular endothelial and smooth muscle cells from human pluripotent stem cells. *Nat. Cell Biol.* **17**, 994–1003 (2015).

210. Dao, L. *et al.* Modeling blood-brain barrier formation and cerebral cavernous malformations in human PSC-derived organoids. *Cell Stem Cell* **31**, 818-833.e11 (2024).

211. Kang, H. W. *et al.* A 3D bioprinting system to produce human-scale tissue constructs with structural integrity. *Nat. Biotechnol.* **34**, 312–319 (2016).

212. Bejleri, D. & Davis, M. E. Decellularized Extracellular Matrix Materials for Cardiac Repair and Regeneration. *Adv. Healthc. Mater.* **8**, 1–29 (2019).

213. Choi, Y. J. *et al.* A 3D cell printed muscle construct with tissue-derived bioink for the treatment of volumetric muscle loss. *Biomaterials* **206**, 160–169 (2019).

214. Lee, A. *et al.* 3D bioprinting of collagen to rebuild components of the human heart. *Science (80-. ).* **365**, 482–487 (2019).

215. Wang, L. L. *et al.* Three-dimensional extrusion bioprinting of single- and double-network hydrogels containing dynamic covalent crosslinks. *J. Biomed. Mater. Res. - Part A* **106**, 865–875 (2018).

216. Song, K. H., Highley, C. B., Rouff, A. & Burdick, J. A. Complex 3D-Printed Microchannels within Cell-Degradable Hydrogels. *Adv. Funct. Mater.* **28**, 1–10 (2018).

217. Ouyang, L., Highley, C. B., Rodell, C. B., Sun, W. & Burdick, J. A. 3D Printing of Shear-Thinning Hyaluronic Acid Hydrogels with Secondary Cross-Linking. *ACS Biomater. Sci. Eng.* **2**, 1743–1751 (2016).

218. Farzin, A. *et al.* 3D-Printed Sugar-Based Stents Facilitating Vascular Anastomosis. *Adv. Healthc.*

*Mater.* **7**, 1–9 (2018).

219. Zhu, K. *et al.* Gold Nanocomposite Bioink for Printing 3D Cardiac Constructs. *Adv. Funct. Mater.* **27**, (2017).

220. Homan, K. A. *et al.* Bioprinting of 3D Convoluted Renal Proximal Tubules on Perfusable Chips. *Sci. Rep.* **6**, 1–13 (2016).

221. Highley, C. B., Song, K. H., Daly, A. C. & Burdick, J. A. Jammed Microgel Inks for 3D Printing Applications. *Adv. Sci.* **6**, (2019).

222. Kolesky, D. B. *et al.* 3D bioprinting of vascularized, heterogeneous cell-laden tissue constructs. *Adv. Mater.* **26**, 3124–3130 (2014).

223. Barry, R. A. *et al.* Direct-write assembly of 3D hydrogel scaffolds for guided cell growth. *Adv. Mater.* **21**, 2407–2410 (2009).

224. Shin, M., Galarraga, J. H., Kwon, M. Y., Lee, H. & Burdick, J. A. Gallol-derived ECM-mimetic adhesive bioinks exhibiting temporal shear-thinning and stabilization behavior. *Acta Biomater.* **95**, 165–175 (2019).

225. Jeon, O., Lee, Y. B., Hinton, T. J., Feinberg, A. W. & Alsberg, E. Cryopreserved cell-laden alginate microgel bioink for 3D bioprinting of living tissues. *Mater. Today Chem.* **12**, 61–70 (2019).

226. Motealleh, A. *et al.* 3D printing of step-gradient nanocomposite hydrogels for controlled cell migration. *Biofabrication* **11**, (2019).

227. Pi, Q. *et al.* Digitally Tunable Microfluidic Bioprinting of Multilayered Cannular Tissues. *Adv. Mater.* **30**, 1–10 (2018).

228. Skylar-Scott, M. A. *et al.* Biomanufacturing of organ-specific tissues with high cellular density and embedded vascular channels. *Sci. Adv.* **5**, (2019).

229. Kolesky, D. B., Homan, K. A., Skylar-Scott, M. A. & Lewis, J. A. Three-dimensional bioprinting of thick vascularized tissues. *Proc. Natl. Acad. Sci. U. S. A.* **113**, 3179–3184 (2016).

230. Lind, J. U. *et al.* Instrumented cardiac microphysiological devices via multimaterial three-dimensional printing. *Nat. Mater.* **16**, 303–308 (2017).

231. Trachsel, L., Johnbosco, C., Lang, T., Benetti, E. M. & Zenobi-Wong, M. Double-Network Hydrogels including Enzymatically Crosslinked Poly-(2-alkyl-2-oxazoline)s for 3D Bioprinting of Cartilage-Engineering Constructs. *Biomacromolecules* **20**, 4502–4511 (2019).

232. Murphy, S. V & Atala, A. 3D bioprinting of tissues and organs. *Nat. Biotechnol.* **32**, 773–785 (2014).

233. Schaum, N. *et al.* Single-cell transcriptomics of 20 mouse organs creates a Tabula Muris. *Nature* **562**, 367–372 (2018).

234. Lee, M. *et al.* Exploitation of Cationic Silica Nanoparticles for Bioprinting of Large-Scale Constructs with High Printing Fidelity. *ACS Appl. Mater. Interfaces* **10**, 37820–37828 (2018).

235. Gauvin, R. *et al.* Microfabrication of complex porous tissue engineering scaffolds using 3D projection stereolithography. *Biomaterials* **33**, 3824–3834 (2012).

236. Yin, J., Zhao, D. & Liu, J. Trends on physical understanding of bioink printability. *Bio-Design*

*Manuf.* **2**, 50–54 (2019).

237. Zhang, Z. *et al.* Evaluation of bioink printability for bioprinting applications. *Appl. Phys. Rev.* **5**, (2018).

238. Smith, P. T., Basu, A., Saha, A. & Nelson, A. Chemical modification and printability of shear-thinning hydrogel inks for direct-write 3D printing. *Polymer (Guildf).* **152**, 42–50 (2018).

239. Paxton, N. *et al.* Proposal to assess printability of bioinks for extrusion-based bioprinting and evaluation of rheological properties governing bioprintability. *Biofabrication* **9**, (2017).

240. Dubbin, K., Hori, Y., Lewis, K. K. & Heilshorn, S. C. Dual-Stage Crosslinking of a Gel-Phase Bioink Improves Cell Viability and Homogeneity for 3D Bioprinting. *Adv. Healthc. Mater.* **5**, 2488–2492 (2016).

241. Dubbin, K., Tabet, A. & Heilshorn, S. C. Quantitative criteria to benchmark new and existing bio-inks for cell compatibility. *Biofabrication* **9**, (2017).

242. Lopez Hernandez, H., Grosskopf, A. K., Stapleton, L. M., Agmon, G. & Appel, E. A. Non-Newtonian Polymer–Nanoparticle Hydrogels Enhance Cell Viability during Injection. *Macromol. Biosci.* **19**, 1–7 (2019).

243. Skardal, A. *et al.* A hydrogel bioink toolkit for mimicking native tissue biochemical and mechanical properties in bioprinted tissue constructs. *Acta Biomater.* **25**, 24–34 (2015).

244. Mazzocchi, A., Devarasetty, M., Huntwork, R., Soker, S. & Skardal, A. Optimization of collagen type I-hyaluronan hybrid bioink for 3D bioprinted liver microenvironments. *Biofabrication* **11**, (2019).

245. Bertassoni, L. E. *et al.* Direct-write bioprinting of cell-laden methacrylated gelatin hydrogels. *Biofabrication* **6**, (2014).

246. Stichler, S. *et al.* Double printing of hyaluronic acid/poly(glycidol) hybrid hydrogels with poly(ε-caprolactone) for MSC chondrogenesis. *Biofabrication* **9**, 44108 (2017).

247. Noh, I., Kim, N., Tran, H. N., Lee, J. & Lee, C. 3D printable hyaluronic acid-based hydrogel for its potential application as a bioink in tissue engineering. *Biomater. Res.* **23**, 1–9 (2019).

248. Freeman, F. E. & Kelly, D. J. Tuning alginate bioink stiffness and composition for controlled growth factor delivery and to spatially direct MSC Fate within bioprinted tissues. *Sci. Rep.* **7**, 1–12 (2017).

249. Nguyen, D. *et al.* Cartilage Tissue Engineering by the 3D Bioprinting of iPS Cells in a Nanocellulose/Alginate Bioink. *Sci. Rep.* **7**, 1–10 (2017).

250. Wüst, S., Godla, M. E., Müller, R. & Hofmann, S. Tunable hydrogel composite with two-step processing in combination with innovative hardware upgrade for cell-based three-dimensional bioprinting. *Acta Biomater.* **10**, 630–640 (2014).

251. Narayanan, L. K. *et al.* 3D-Bioprinting of Polylactic Acid (PLA) Nanofiber-Alginate Hydrogel Bioink Containing Human Adipose-Derived Stem Cells. *ACS Biomater. Sci. Eng.* **2**, 1732–1742 (2016).

252. Frost, B., Sutliff, B. P., Thayer, P., Bortner, M. J. & Foster, E. J. Gradient poly(Ethylene glycol) diacrylate and cellulose nanocrystals tissue engineering composite scaffolds via extrusion bioprinting. *Front. Bioeng. Biotechnol.* **7**, 1–14 (2019).

253. Xin, S., Chimene, D., Garza, J. E., Gaharwar, A. K. & Alge, D. L. Clickable PEG hydrogel microspheres as building blocks for 3D bioprinting. *Biomater. Sci.* **7**, 1179–1187 (2019).

254. Müller, M., Becher, J., Schnabelrauch, M. & Zenobi-Wong, M. Nanostructured Pluronic hydrogels as bioinks for 3D bioprinting. *Biofabrication* **7**, (2015).

255. Saha, A. *et al.* Additive Manufacturing of Catalytically Active Living Materials. *ACS Appl. Mater. Interfaces* **10**, 13373–13380 (2018).

256. Millik, S. C. *et al.* 3D printed coaxial nozzles for the extrusion of hydrogel tubes toward modeling vascular endothelium. *Biofabrication* **11**, (2019).

257. Yu, C. *et al.* Scanningless and continuous 3D bioprinting of human tissues with decellularized extracellular matrix. *Biomaterials* **194**, 1–13 (2019).

258. Lee, H. *et al.* Development of Liver Decellularized Extracellular Matrix Bioink for Three-Dimensional Cell Printing-Based Liver Tissue Engineering. *Biomacromolecules* **18**, 1229–1237 (2017).

259. Pati, F. *et al.* Printing three-dimensional tissue analogues with decellularized extracellular matrix bioink. *Nat. Commun.* **5**, 1–11 (2014).

260. Ahn, G. *et al.* Precise stacking of decellularized extracellular matrix based 3D cell-laden constructs by a 3D cell printing system equipped with heating modules. *Sci. Rep.* **7**, 1–11 (2017).

261. Ali, M. *et al.* A Photo-Crosslinkable Kidney ECM-Derived Bioink Accelerates Renal Tissue Formation. *Adv. Healthc. Mater.* **8**, 1800992 (2019).

262. Kang, H. *et al.* In vivo cartilage repair using adipose-derived stem cell-loaded decellularized cartilage ECM scaffolds. *J. Tissue Eng. Regen. Med.* **8**, 442–453 (2014).

263. Jang, J. *et al.* Tailoring mechanical properties of decellularized extracellular matrix bioink by vitamin B2-induced photo-crosslinking. *Acta Biomater.* **33**, 88–95 (2016).

264. Toprakhisar, B. *et al.* Development of Bioink from Decellularized Tendon Extracellular Matrix for 3D Bioprinting. *Macromol. Biosci.* **18**, 1–12 (2018).

265. Thum, T. *et al.* MicroRNA-21 contributes to myocardial disease by stimulating MAP kinase signalling in fibroblasts. *Nature* **456**, 980–984 (2008).

266. Dixon, I. M. C., Cunnington, R. H., Rattan, S. G. & Wigle, J. T. Cardiac Fibrosis and Heart Failure—Cause or Effect? BT - Cardiac Fibrosis and Heart Failure: Cause or Effect? in (eds. Dixon, I. M. C. & Wigle, J. T.) 1–4 (Springer International Publishing, 2015). doi:10.1007/978-3-319-17437-2_1.

267. Hinderer, S. & Schenke-Layland, K. Cardiac fibrosis – A short review of causes and therapeutic strategies. *Adv. Drug Deliv. Rev.* **146**, 77–82 (2019).

268. Kim, P., Chu, N., Davis, J. & Kim, D. H. Mechanoregulation of Myofibroblast Fate and Cardiac Fibrosis. *Adv. Biosyst.* **2**, 1–11 (2018).

269. Yong, K. W. *et al.* Paracrine effects of adipose-derived stem cells on matrix stiffness-induced cardiac myofibroblast differentiation via angiotensin II type 1 receptor and smad7. *Sci. Rep.* **6**, 1–13 (2016).

270. Van Den Borne, S. W. M. *et al.* Myocardial remodeling after infarction: The role of myofibroblasts. *Nat. Rev. Cardiol.* **7**, 30–37 (2010).

271. Stempien-Otero, A., Kim, D. H. & Davis, J. Molecular networks underlying myofibroblast fate and fibrosis. *J. Mol. Cell. Cardiol.* **97**, 153–161 (2016).

272. Meyer-ter-Vehn, T., Han, H., Grehn, F. & Schlunck, G. Extracellular Matrix Elasticity Modulates TGF-β–Induced p38 Activation and Myofibroblast Transdifferentiation in Human Tenon Fibroblasts. *Invest. Ophthalmol. Vis. Sci.* **52**, 9149–9155 (2011).

273. Huang, X. *et al.* Matrix stiffness-induced myofibroblast differentiation is mediated by intrinsic mechanotransduction. *Am. J. Respir. Cell Mol. Biol.* **47**, 340–348 (2012).

274. Godbout, C. *et al.* The Mechanical Environment Modulates Intracellular Calcium Oscillation Activities of Myofibroblasts. *PLoS One* **8**, (2013).

275. Dávila, J. L. & d'Ávila, M. A. Laponite as a rheology modifier of alginate solutions: Physical gelation and aging evolution. *Carbohydr. Polym.* **157**, 1–8 (2017).

276. Faes, M., Valkenaers, H., Vogeler, F., Vleugels, J. & Ferraris, E. Extrusion-based 3D printing of ceramic components. *Procedia CIRP* **28**, 76–81 (2015).

277. Jin, Y., Zhao, D. & Huang, Y. Study of extrudability and standoff distance effect during nanoclay-enabled direct printing. *Bio-Design Manuf.* **1**, 123–134 (2018).

278. Hong, S. *et al.* 3D Printing of Highly Stretchable and Tough Hydrogels into Complex, Cellularized Structures. *Adv. Mater.* **27**, 4035–4040 (2015).

279. Jin, Y., Liu, C., Chai, W., Compaan, A. & Huang, Y. Self-Supporting Nanoclay as Internal Scaffold Material for Direct Printing of Soft Hydrogel Composite Structures in Air. *ACS Appl. Mater. Interfaces* **9**, 17456–17465 (2017).

280. Gungor-Ozkerim, P. S., Inci, I., Zhang, Y. S., Khademhosseini, A. & Dokmeci, M. R. Bioinks for 3D bioprinting: An overview. *Biomater. Sci.* **6**, 915–946 (2018).

281. Rathan, S. *et al.* Fiber Reinforced Cartilage ECM Functionalized Bioinks for Functional Cartilage Tissue Engineering. *Adv. Healthc. Mater.* **8**, 1801501 (2019).

282. Gao, G. *et al.* Tissue Engineered Bio-Blood-Vessels Constructed Using a Tissue-Specific Bioink and 3D Coaxial Cell Printing Technique: A Novel Therapy for Ischemic Disease. *Adv. Funct. Mater.* **27**, 1700798 (2017).

283. Ahlfeld, T. *et al.* Development of a clay based bioink for 3D cell printing for skeletal application. *Biofabrication* **9**, (2017).

284. Kim, W. & Kim, G. H. An intestinal model with a finger-like villus structure fabricated using a bioprinting process and collagen/SIS-based cell-laden bioink. *Theranostics* **10**, 2495–2508 (2020).

285. Lee, H. *et al.* Fabrication of micro/nanoporous collagen/dECM/silk-fibroin biocomposite scaffolds using a low temperature 3D printing process for bone tissue regeneration. *Mater. Sci. Eng. C* **84**, 140–147 (2018).

286. Guan, X. *et al.* Dystrophin-deficient cardiomyocytes derived from human urine: New biologic reagents for drug discovery. *Stem Cell Res.* **12**, 467–480 (2014).

287. Lian, X. *et al.* Directed cardiomyocyte differentiation from human pluripotent stem cells by modulating Wnt/β-catenin signaling under fully defined conditions. *Nat. Protoc.* **8**, 162–175 (2013).

288. Bielawski, K. S., Leonard, A., Bhandari, S., Murry, C. E. & Sniadecki, N. J. Real-Time Force and

Frequency Analysis of Engineered Human Heart Tissue Derived from Induced Pluripotent Stem Cells Using Magnetic Sensing. *Tissue Eng. Part C Methods* **22**, 932–940 (2016).

289. Tsui, J. H. *et al.* Functional maturation of human iPSC-based cardiac microphysiological systems with tunable electroconductive decellularized extracellular matrices. *bioRxiv* 786657 (2019).

290. Choudhury, D., Tun, H. W., Wang, T. & Naing, M. W. Organ-Derived Decellularized Extracellular Matrix: A Game Changer for Bioink Manufacturing? *Trends Biotechnol.* **36**, 787–805 (2018).

291. Hodgson, M. J., Knutson, C. C., Momtahan, N. & Cook, A. D. Extracellular Matrix from Whole Porcine Heart Decellularization for Cardiac Tissue Engineering BT - Decellularized Scaffolds and Organogenesis: Methods and Protocols. in (ed. Turksen, K.) 95–102 (Springer New York, 2018). doi:10.1007/7651_2017_31.

292. Sydney Gladman, A., Matsumoto, E. A., Nuzzo, R. G., Mahadevan, L. & Lewis, J. A. Biomimetic 4D printing. *Nat. Mater.* **15**, 413–418 (2016).

293. Ribeiro, A. *et al.* Assessing bioink shape fidelity to aid material development in 3D bioprinting. *Biofabrication* **10**, (2018).

294. Mouser, V. H. M. *et al.* Yield stress determines bioprintability of hydrogels based on gelatin-methacryloyl and gellan gum for cartilage bioprinting. *Biofabrication* **8**, (2016).

295. Gao, T. *et al.* Optimization of gelatin-alginate composite bioink printability using rheological parameters: A systematic approach. *Biofabrication* **10**, (2018).

296. He, Y. *et al.* Research on the printability of hydrogels in 3D bioprinting. *Sci. Rep.* **6**, 1–13 (2016).

297. Mezger, T. G. The Rheology Handbook. *Pigment Resin Technol.* **38**, 790–797 (2009).

298. Dijkstra, M., Hansen, J. P. & Madden, P. A. Gelation of a clay colloid suspension. *Phys. Rev. Lett.* **75**, 2236–2239 (1995).

299. Ruzicka, B. & Zaccarelli, E. A fresh look at the Laponite phase diagram. *Soft Matter* **7**, 1268–1286 (2011).

300. Shi, J., Wang, C., Ngai, T. & Lin, W. Diffusion and Binding of Laponite Clay Nanoparticles into Collagen Fibers for the Formation of Leather Matrix. *Langmuir* **34**, 7379–7385 (2018).

301. Pawar, N. & Bohidar, H. B. Surface selective binding of nanoclay particles to polyampholyte protein chains. *J. Chem. Phys.* **131**, (2009).

302. Li, C., Mu, C., Lin, W. & Ngai, T. Gelatin Effects on the Physicochemical and Hemocompatible Properties of Gelatin/PAAm/Laponite Nanocomposite Hydrogels. *ACS Appl. Mater. Interfaces* **7**, 18732–18741 (2015).

303. Hinton, T. J. *et al.* Three-dimensional printing of complex biological structures by freeform reversible embedding of suspended hydrogels. *Sci. Adv.* **1**, (2015).

304. Beamish, J. A., Zhu, J., Kottke-Marchant, K. & Marchant, R. E. The effects of monoacrylated poly(ethylene glycol) on the properties of poly(ethylene glycol) diacrylate hydrogels used for tissue engineering. *J. Biomed. Mater. Res. - Part A* **92**, 441–450 (2010).

305. Buxton, A. N. *et al.* Design and Characterization of Poly(Ethylene Glycol) Photopolymerizable Semi-Interpenetrating Networks for Chondrogenesis of Human Mesenchymal Stem Cells. *Tissue Eng.* **13**, 2549–2560 (2007).

306. Fairbanks, B. D., Schwartz, M. P., Bowman, C. N. & Anseth, K. S. Photoinitiated polymerization of PEG-diacrylate with lithium phenyl-2,4,6-trimethylbenzoylphosphinate: polymerization rate and cytocompatibility. *Biomaterials* **30**, 6702–6707 (2009).

307. Jimenez-Vergara, A. C., Lewis, J., Hahn, M. S. & Munoz-Pinto, D. J. An improved correlation to predict molecular weight between crosslinks based on equilibrium degree of swelling of hydrogel networks. *J. Biomed. Mater. Res. - Part B Appl. Biomater.* **106**, 1339–1348 (2018).

308. Nguyen, Q. T., Hwang, Y., Chen, A. C., Varghese, S. & Sah, R. L. Cartilage-like mechanical properties of poly (ethylene glycol)-diacrylate hydrogels. *Biomaterials* **33**, 6682–6690 (2012).

309. Bryant, S. J., Anseth, K. S., Lee, D. A. & Bader, D. L. Crosslinking density influences the morphology of chondrocytes photoencapsulated in PEG hydrogels during the application of compressive strain. *J. Orthop. Res.* **22**, 1143–1149 (2004).

310. Lee, S., Tong, X. & Yang, F. The effects of varying poly(ethylene glycol) hydrogel crosslinking density and the crosslinking mechanism on protein accumulation in three-dimensional hydrogels. *Acta Biomater.* **10**, 4167–4174 (2014).

311. Mazzoccoli, J. P., Feke, D. L., Baskaran, H. & Pintauro, P. N. Mechanical and cell viability properties of crosslinked low- And high-molecular weight poly(ethylene glycol) diacrylate blends. *J. Biomed. Mater. Res. - Part A* **93**, 558–566 (2010).

312. Herum, K. M., Lunde, I. G., McCulloch, A. D. & Christensen, G. The Soft- and Hard-Heartedness of Cardiac Fibroblasts: Mechanotransduction Signaling Pathways in Fibrosis of the Heart. *Journal of Clinical Medicine* vol. 6 (2017).

313. Kim, W. *et al.* Hippo signaling is intrinsically regulated during cell cycle progression by APC/CCdh1. *Proc. Natl. Acad. Sci.* **116**, 9423–9432 (2019).

314. Peak, C. W., Stein, J., Gold, K. A. & Gaharwar, A. K. Nanoengineered Colloidal Inks for 3D Bioprinting. *Langmuir* **34**, 917–925 (2018).

315. Zhang, Y. *et al.* Novel preparation of Au nanoparticles loaded Laponite nanoparticles/ECM injectable hydrogel on cardiac differentiation of resident cardiac stem cells to cardiomyocytes. *J. Photochem. Photobiol. B Biol.* **192**, 49–54 (2019).